This electronic thesis or dissertation has been downloaded from Explore Bristol Research, http://research-information.bristol.ac.uk

Author:
Peccin Da Silva, Anderson

Title:
Macro-element modelling of plate anchors for floating offshore structures accounting for capacity changes during operational conditions

General rights
Access to the thesis is subject to the Creative Commons Attribution - NonCommercial-No Derivatives 4.0 International Public License. A copy of this may be found at https://creativecommons.org/licenses/by-nc-nd/4.0/legalcode This license sets out your rights and the restrictions that apply to your access to the thesis so it is important you read this before proceeding.

Take down policy
Some pages of this thesis may have been removed for copyright restrictions prior to having it been deposited in Explore Bristol Research. However, if you have discovered material within the thesis that you consider to be unlawful e.g. breaches of copyright (either yours or that of a third party) or any other law, including but not limited to those relating to patent, trademark, confidentiality, data protection, obscenity, defamation, libel, then please contact collections-metadata@bristol.ac.uk and include the following information in your message:

- Your contact details
- Bibliographic details for the item, including a URL
- An outline nature of the complaint

Your claim will be investigated and, where appropriate, the item in question will be removed from public view as soon as possible.

Macro-element modelling of plate anchors for floating offshore structures accounting for capacity changes during operational conditions

By

Anderson Peccin da Silva

Department of Civil Engineering

University of Bristol

A dissertation submitted to the University of Bristol in accordance with the requirements of the degree of DOCTOR OF PHILOSOPHY in the Faculty of Engineering, Department of Civil Engineering

December 2021

Word count: 62680

Abstract

Within the context of offshore structures for renewable energy and oil & gas, anchoring systems play an important role in the stability of floating devices. Plate anchors can be used to moor floating structures both in taut-leg and catenary configurations. So far, no well-established anchor design criterium capable of predicting the 'whole-life' anchor behaviour has been developed. In parallel to that, macro-element models are a time-effective approach that has been used for several geotechnical applications, though limited work has been done on macro-element for anchors. Furthermore, few macro-element models have considered the effect of pore pressure generation and dissipation, as most of them have been developed for either drained or undrained cases. In that context, this thesis presents a macro-element framework that combines an advanced macro-element model for anchors with a representative soil element that captures the behaviour of the whole soil mass around the anchor. The representative soil element tracks the effects of changes of effective stress on the soil strength, which in turn governs the anchor capacity in the macro-element model. The two modelling components are linked through a mobilised capacity compatibility condition. The modelling framework is challenged to simulate the behaviour of plate anchors in cohesive soils subjected to long-term cyclic and maintained loading and compared with centrifuge test results published in the literature. In addition, the model is assessed by comparison with centrifuge data in plate anchors subjected to different loading rates in non-cohesive soils. It is shown that the model is able to predict the evolution of anchor capacity under different loading conditions, provided that calibration of model parameters with a limited number of centrifuge tests is carried out.

Acknowledgements

I would like to express my gratitude to my supervisor, Dr Andrea Diambra, for his continuous support, availability and guidance throughout my PhD. His patience, enthusiasm and active participation on my research were essential to the conclusion of this thesis. He was the main reason why I chose Bristol for my PhD and working with him made me sure I made the right decision.

I would like to extend my gratitude to Dr Dimitris Karamitros for the interesting discussions on the model development, and to Dr Shiaohuey Chow for providing experimental data and for contributing to the papers published during my studies.

I extend my thanks to Frederico Dias Paulino da Costa, for always being open for discussions, for his help with my MATLAB code, and for the friendship during my time in Bristol. I would also like to express my gratitude to the great people I met in Bristol, from friends I made during my journey and also to colleagues who shared the office 1.80 with me or who helped me at some point during my time in Bristol: Malu Carvalho, Chrys Paschou, Hannah Louise, Alex Ashford, Mimi Pedragosa, Joel Ovonlen, Edward Yap, Sabriye Özkan, Asmaa Shafee, Lawrence De Leeuw, Jamie Crispin, Alessandro Mandolini, Elpida Katsiveli, Luca Lombardi, Luana Maciel Cesar, Kaleb Bass, Franziska Cengiz, Lucas Festugato, Marina Bellaver Corte, and all people who helped me along the way.

In particular, I would like to thank Eva Frese for her support, love and understanding especially during the last months of my PhD, and for all the great moments spent together. Ik hou zoveel van jou!

Finally, I want to thank my family, in particular my loving parents Alaor, Marines, and my sister Caroline, for their continuous support, and for always making enormous sacrifices to invest in my education. Amo vocês, família!

Last, but not least, I am grateful for the financial support from the University of Bristol throughout the past years.

Author's declaration

I declare that the work in this dissertation was carried out in accordance with the requirements of the University's Regulations and Code of Practice for Research Degree Programmes and that it has not been submitted for any other academic award. Except where indicated by specific reference in the text, the work is the candidate's own work. Work done in collaboration with, or with the assistance of, others, is indicated as such. Any views expressed in the dissertation are those of the author.

SIGNED: .... December 2021
Anderson Peccin da Silva

Table of contents

List of figures

List of tables

List of symbols and abbreviations

A	Flow rule multiplier in Severn-Trent model
A_p	Area of the plate anchor
a	Pore pressure dissipation rate parameter
B	Anchor breadth
b	distance between the stress state and its image on the bounding surface
b_{max}	Maximum value that b can assume
C	Parameter controlling hyperbolic stiffness relationship in Severn-Trent model
c_v	Coefficient of consolidation
D	Anchor diameter
D_R	Relative density of soil
d	Displacement of the chain measured at the actuator or padeye travel distance
d_{peak}	Displacement of the chain (or of the anchor padeye) at peak load
d_s	Soil dilatancy
d_{bar}	Diameter of the chain
E	Young's modulus of the soil
E_n	Multiplier giving the effective chain width in the normal direction to the chain
e	Void ratio of the soil
e_n	Load eccentricity normal to the anchor fluke
e_p	Load eccentricity parallel to the anchor fluke
f	Loading surface of the anchor
F	Capacity surface of the anchor
F_s	Bounding surface of the soil
F_u	Ultimate force

g	Plastic potential of the anchor
G	Shear modulus of the soil
G_s	Specific gravity of the solids
H	Force parallel to the plate anchor
H_b	hardening term of the image stress on the bounding surface
H_f	arbitrary term of the hardening modulus
H_M	Sliding capacity of the anchor
H_m	Hardening modulus of the soil element
I_σ	Boussinesq's influence factor (stress transfer from anchor to soil)
K	Rate of change in pore pressure (or effective stress) with specific volume, i.e. slope of stress path in υ-ln(σ_v') plane
K_0	Lateral earth pressure coefficient
K_e	Bulk modulus of the soil
k	Permeability of the soil
k_d	State parameter contribution in flow rule for Severn-Trent model
k_r	Parameter defining link between the current state parameter and the soil strength
k_{su}	rate of increase of s_u with depth
m	Shape factors of the loading surface f
$\mathbf{m}$	Vector determining the unit direction of plastic flow $[m_\sigma; m_\tau]^T$
L	Anchor length
M	Moment load on the plate anchor
M_M	Rotational capacity of the anchor
N_c	Bearing capacity factor for the chain
N_{cyc}	Number of cycles
N_h	Capacity factor (sliding)
N_v	Capacity factor (normal)
N_m	Capacity factor (rotational)
N_γ	Normal capacity factor as defined in the literature for sands $N_\gamma = F_u/(A_p\,\gamma'\,Y)$

n	Shape factor of the loading surface f
$\boldsymbol{n}$	Vector determining the direction of plastic loading $[n_\sigma; n_\tau]^T$
p	Fitting parameter controlling the slope of the back-bone curve
q	Shape factor of the loading surface f
$\boldsymbol{q}$	Vector representing the plastic displacement components of the anchor $[w, u, \beta]^T$
$\boldsymbol{Q}$	Vector representing the chain load components $[V, H, M]^T$
q_a	Stress transferred from the anchor to a soil element immediately in front of anchor
q_u	Anchor capacity (T_a / A_p)
$q_{u,p}$	Anchor peak capacity
R_0	Non-dimensional hardening parameter of the anchor
R_1, R_2	Model parameters controlling the dependency of R_0 on soil strength τ_c
$\boldsymbol{S}$	Vector of shear and normal stresses $[\tau, \sigma]^T$
s_{u0}	soil shear strength at the mudline
T	Dimensionless time factor
T_{50}	Dimensionless time factor for 50% dissipation of the excess pore pressure
T_a	Chain load acting on the anchor padeye
T_p	Anchor capacity (peak load)
$T_{p,dr}$	Drained capacity of the anchor
$T_{p,max}$	Maximum capacity of the anchor in the drainage domain
$T_{p,un}$	Undrained capacity of the anchor
T_{cons}	Dimensionless time factor of consolidation
t_a	Thickness of the anchor
t_c	Time allowed for consolidation
u	Displacement parallel to the plate anchor
u_e	Excess pore water pressure
$u_{e,i}$	Initial excess pore water pressure
u_w	Pore water pressure

v	Anchor velocity of pull
V	Force perpendicular to the plate anchor
V^*	Normalised velocity
V_{50}	Dimensionless velocity for 50% dissipation of the excess pore pressure
V_M	Normal capacity of the anchor
w	Displacement perpendicular to the plate anchor
W_a	Submerged weight of the anchor
x	Horizontal displacement of the anchor
Y	Initial embedment depth
z_p	current vertical depth of the padeye
z	Vertical displacement of the anchor

α	Anchor inclination with the horizontal $= 90^\circ - \beta$
α_a	Adhesion factor between soil and anchor
β	Rotation of the anchor from the initial position
ε	Volumetric strain
ξ	Plastic potential parameter (controlling surface size in direction V)
φ_{cs}	Critical state friction angle
γ	Shear strain
γ'	Effective unit weight of the soil
γ_w	Unit weight of water
κ	Slope of the URL line
λ	Slope of the NCL and CSL lines
μ	Plastic multiplier
μ_c	Chain-soil friction coefficient
Ω	Conversion factor between K and V^*
ω	Plastic potential parameter (controlling surface size in direction M)
ψ	State parameter
ρ_c	Mobilisation of anchor capacity (anchor's hardening rule)

ρ_{cM}	Maximum mobilisation of anchor capacity on the Memory Surface
ρ_g	Parameter controlling the size of the plastic potential surface g
σ_h	Total horizontal stress on the soil
σ_v	Total vertical stress on the soil
σ_v'	Vertical effective stress on the soil
$\sigma'_{v,CSL}$	Vertical effective stress on the CSL
$\Delta\sigma'$	Additional effective stress applied to the soil by the loaded anchor
Γ_{NCL}	Intercept of the NCL with $\sigma_v' = 1$ kPa
τ	Shear stress
τ_c	Current shear strength of the soil
τ_{CSL}	Shear strength at CSL
τ_p	Peak shear stress
$\tau_{c,ref}$	Reference value of current shear strength = 100 kPa
θ_a	Direction of chain load on the anchor padeye
θ_0	Direction of chain load at the mudline
υ	Specific volume of the soil = 1 + e
χ	Plastic potential parameter (controlling surface size in direction H)

CASPA	Chain and SEPLA Plasticity Analysis
CPT	Cone penetration test
CSL	Critical state line
DSS	Direct simple shear
LCOE	Levelized cost of energy
LDFE	Large-deformation finite-element analysis
LP	Loading packet
NCL	Normal compression line
OCR	Overconsolidation ratio
PIV	Particle image velocimetry
SEPLA	Suction-embedded plate anchor
URL	Unloading-reloading line

CHAPTER 1. Introduction

1.1. Background

Studies in offshore engineering have increased significantly over the last few decades. This can be explained not only by its relevance to oil and gas industry, but mainly due to the growing interest in offshore wind with a view to generating electricity from wind turbines, as well as the recent development of floating facilities for wave and tidal energy. The UK is the world leader in offshore wind, with an installed capacity of 10.5 GW in 2020, which is sufficient to power approximately 4.5 million homes. This figure is expected to increase to 27.5 GW in 2026, overtaking the installed capacity of onshore wind, which is expected to be around 24.3 GW in the same year (Rystad Energy, 2020). In 2020, 32% of the wind power generation comes from offshore wind farms which represents 10% of UK electricity (Renewable UK, 2020). Recent advances in research and technology have significantly dropped the levelized cost of energy (LCOE) for offshore wind, and prices are expected to be lower than gas-fired plants by 2023 (Evans, 2019), as shown in Figure 1.1. Furthermore, recent reports from the International Energy Agency (IEA, 2019) indicate that offshore wind has the technical potential to generate almost 8 times the current electricity demand in the European Union (EU). On the other hand, the same report also shows that at present the installed wind energy capacity represents as low as only 0.81% of the potential generation.

Currently, the UK still has the highest installed offshore wind capacity in the world, with 29% of the world's installations in 2020, against 28% for China and 22% for Germany. However, in 2020, new installations in China accounted for 50% of the total new installations in the world, followed by the Netherlands (25%), Belgium (12%) and the UK (8%) (GWEC, 2021).

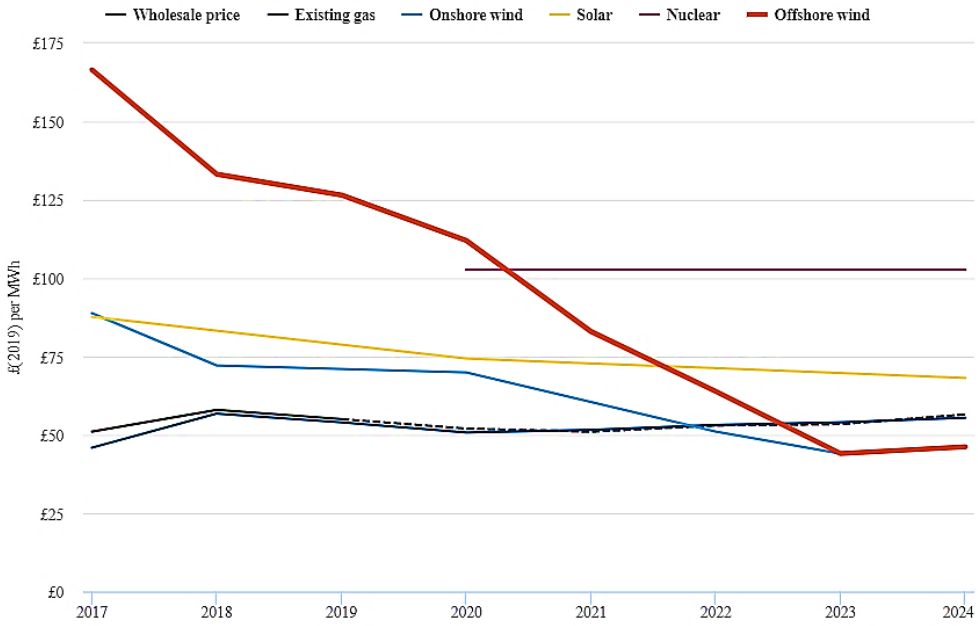

Figure 1.1 - Cost of UK electricity generation in £/MWh (current prices) for various technologies (Evans, 2019)

While most of the installed wind farms in the world are situated in shallow water (usually up to 30m depth), approximately 80% of the European offshore wind resources are located in places with water depths greater than 60 m (James & Ros, 2015). This equals a potential capacity of 4000 GW in sites for which fixed wind farm foundation devices, such as monopiles, become unattractive due to cost and operational limits. In the US, nearly 60% of offshore wind potential is located in water deeper than 60 m, according to the National Renewable Energy Laboratory (NREL) (Gerdes, 2021). The use of floating structures anchored to the seabed through mooring lines is thus an appealing solution.

Despite the great potential for floating offshore wind installations in the near future, currently less than 1% of the installed capacity offshore accounts for floating wind turbines (Gerdes, 2021), which accounts for less than 100 MW worldwide. The two largest floating wind farms are the Hywind in Scotland, with 30 MW of installed capacity, and WindFloat Atlantic in Portugal, with 25 MW. Other floating projects have less than 5 MW of installed capacity, and are mainly operating as demonstrators.

The main challenge for the floating wind sector at the moment is to decrease capital expenditures (CapEx) costs and the levelized cost of energy (LCOE). Currently, these costs are significantly higher for floating wind than for fixed-bottom wind. However, a recent study conducted by Lawrence Berkeley National Laboratory (Wiser et al., 2021) showed that the prices are likely to converge in the next few decades, as shown in Figure 1.2.

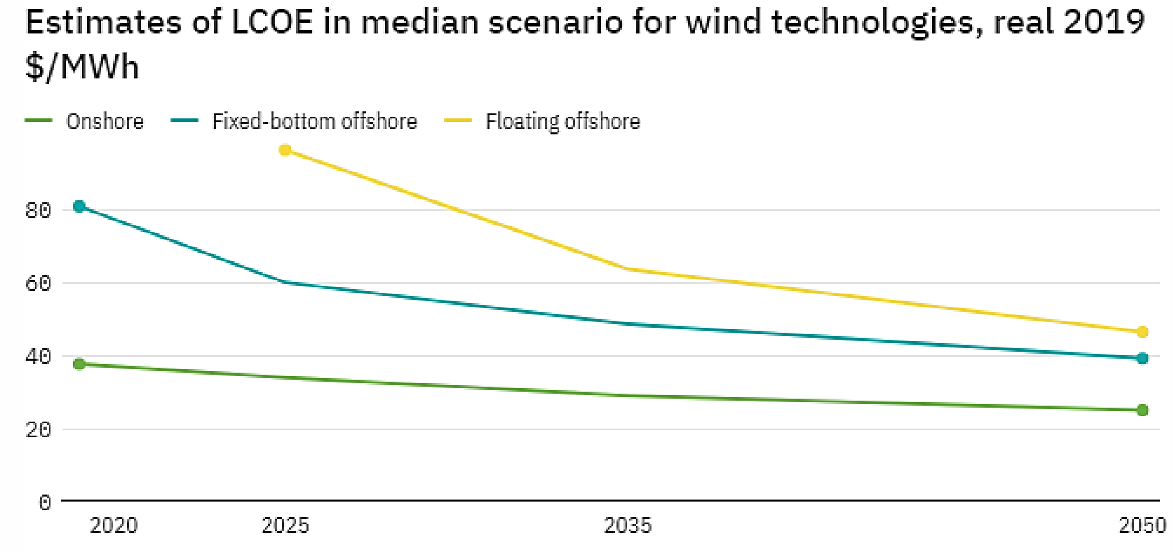

Figure 1.2 – Estimated levelized cost of energy (LCOE) for onshore, fixed-bottom offshore and floating offshore wind in the next decades (Wiser et al., 2021).

In that context, improving knowledge on anchoring solutions and mooring systems is essential to reduce the cost of floating wind energy. Research efforts have been put into developing optimal anchoring and dynamic cable systems, such as in the FLOTANT project (European Union, 2020) funded by the EU Research and Innovation programme Horizon 2020.

So far, several anchoring types of foundations for bottom-fixed and floating structures have been developed, notably monopiles, gravity and drag embedment anchors, screw anchors and, more recently, suction caissons and plate anchors. Extensive research has been carried out especially for monopile foundations (e.g. Page et al., 2018; Byrne et al., 2020; Burd et al., 2020) and suction caissons (e.g. Yin et al., 2020; Kay et al., 2021). However, research in anchoring systems for floating structures such as plate anchors has focused mainly on centrifuge modelling and in large-deformation finite element (LDFE) simulations (e.g. Merifield et al., 2001; Merifield & Sloan, 2006; Song et al., 2009; Wang et al., 2010, 2013; Tian et al., 2014), which can be time-consuming and not suitable for extended assessments.

In the interest of simplicity, macro-element modelling techniques can represent a valuable tool for exploring the mechanical response of soil-anchor interaction problems at very low computational costs while accounting for all the key problem variables (e.g. anchor geometry, embedment, soil properties, loading conditions). Macro-element models have already been successfully employed to predict the mechanical response of shallow foundations (e.g. Nova and Montrasio 1991; Cremer et al. 2001), spudcans (e.g. Martin & Houlsby 2001), monopiles (Page et al., 2018) and bucket foundations (e.g. Skau et al., 2018), but limited work has been done on macro-element modelling for plate anchors, with the exception of Cassidy et al. (2012) and Yang et al. (2012). However, macro-element models for anchors focused on static capacity under undrained conditions and did not account for changes in soil strength during operational conditions.

In addition, the current design codes used in practice (e.g. American Petroleum Institute, 2015, DNVGL-RP-E302, 2017) and design charts of anchor manufacturers (e.g. Vryhof, 2021) also provide only static and cyclic capacity of the anchor. To date, there is not a well-established anchor design criterion capable of predicting full anchor behaviour (i.e. forces, displacements and rotations) for long-term operative loading condition and accounting for the changes in soil strength during operational loadings. Considering the need to advance this matter and the growing importance of anchoring systems for offshore facilities, further research is required. This thesis aims to contribute to this knowledge gap by proposing a new modelling framework that captures anchor behaviour during 'whole-life' operation and accounting for the evolution of soil strength.

1.2. Research Problem

Currently, the most commonly used design code (DNVGL-RP-E302, 2017) provides static and cyclic capacity, focusing on soil resistance to anchor pull-out. However, there is not a well-established 'whole-life' anchor design criterion that is capable of predicting full anchor behaviour for long-term operational conditions such as cyclic loading, maintained loading and different loading rates, providing not only the pull-out capacity, but also forces, displacements and rotations and accounting for changes in soil strength due to pore pressure and consolidation effects.

1.3. Objective and research scope

Within the context of the research problem, the main objective of this research is to develop a macro-element model for plate anchors which can accurately predict anchor behaviour for operational loading conditions in both cohesive and non-cohesive soils, providing both cyclic and static capacity, cyclic displacements, and rotations, and improving the current design of these devices. This is achieved through the proposition of a macro-element modelling framework that relates the strength of a representative soil element subjected to direct simple shear conditions to the capacity of the anchor. The specific objectives are summarised below:

a) To improve current macro-element models for plate anchors under monotonic loading and compare them with a benchmark model.
b) To compare the results from the improved macro-element model with published results from finite-element (FE) and centrifuge modelling.
c) To propose a macro-element modelling framework that accounts for the evolution of soil strength due to pore pressure generation and consolidation.
d) To apply the proposed modelling framework to plate anchors in distinct types of soil (sand and clay) and under distinct loading conditions (static and cyclic loads).
e) To compare the model results with both numerical (FE) and experimental (centrifuge) analyses available in the literature.

1.4. Thesis outline

This thesis consists of seven chapters. The outline of the thesis is presented below.

Following this introductory chapter, Chapter 2 presents an overview of relevant published work on plate anchors, as well as macro-element modelling developments for several applications. The chapter introduces the main types of anchors for floating structures, followed by the main finite-element, macro-element and experimental studies on plate anchors. The chapter also includes an overview of macro-element models used for other geotechnical applications, such as shallow foundations and monopiles.

Chapter 3 presents an improved macro-element model for plate anchors in clay subjected to undrained monotonic loading. The results are compared with published work on 3D FE analyses as well as with centrifuge testing data. The improved model is also compared with a benchmark model which was used as a starting point for the new model development.

Chapter 4 introduces a new macro-element modelling framework which includes the evolution of soil strength due to pore pressure generation and dissipation. The modelling ingredients and mathematical formulations are presented and analysed.

Chapter 5 applies the modelling framework introduced in Chapter 4 to cohesive soils subjected to cyclic and maintained loading. The effect of relevant model parameters is analysed, and a calibration procedure is proposed. The results are compared with centrifuge tests from two published studies, which involve long-term cyclic loading and maintained loading.

Chapter 6 applies the modelling framework to non-cohesive soils subjected to different loading rates, which induces different drainage behaviour. The results are compared to previously published results from centrifuge tests.

Finally, Chapter 7 summarises the main conclusions from the previous chapters and indicates the main findings and limitations of the proposed macro-element model. Suggestions for future research are also presented and discussed.

1.5. List of supporting publication

Listed below are the supporting publications for the thesis with the respective bibliographic details, as well as the chapter that incorporate some of this material.

(1) Peccin da Silva, A.; Diambra, A.; Karamitros, D. (2019). Macro-element modelling of suction-embedded plate anchors for floating offshore structures. In: *Proceedings of the 7th International Symposium on Deformation Characteristics of Geomaterials (IS-Glasgow 2019)*, E3S Web of Conferences 92, 16009.

The candidate developed the new macro-element model with guidance of the second author, Dr Andrea Diambra. The implementation of the model into coding language, model calibration, and analyses, were conducted by the candidate, with inputs from all co-authors. The candidate prepared the first draft of the paper and co-authors revised and contributed to the final version. Some extracts of this paper are incorporated into Chapter 3 of this thesis.

(2) Peccin da Silva, A.; Diambra, A.; Karamitros, D.; Chow, S.H. (2020). Macro-element modelling of plate anchor kinematics under cyclic loading in clay. In: *Proceedings of the 4th International Symposium on Frontiers in Offshore Geotechnics (ISFOG),* DFI, pp. 382-391.

The candidate developed the new macro-element model with guidance of the second author, Dr Andrea Diambra. The implementation of the model into coding language, model calibration, and analyses, were conducted by the candidate, with inputs from all co-authors. The candidate prepared the first draft of the paper and co-authors revised and contributed to the final version. Some extracts of this paper are incorporated into Chapter 3 of this thesis.

(3) Peccin da Silva, A.; Diambra, A.; Karamitros, D.; Chow, S.H. (2021). A non-associative macro-element model for vertical plate anchors in clay. *Canadian Geotechnical Journal*, 58(11), 1703-1715.

The candidate developed the new macro-element model with guidance of the second author, Dr Andrea Diambra. The implementation of the model into coding language, model calibration, and analyses, were conducted by the candidate, with inputs from all co-authors. The candidate prepared the first draft of the paper and co-authors revised and contributed to the final version. Most of this paper is incorporated into Chapter 3 of this thesis.

(4) Peccin da Silva, A.; Diambra, A.; Karamitros, D.; Chow, S.H. (2021). A cyclic macro-element framework for consolidation-dependent three-dimensional capacity of plate anchors. *Journal of Marine Science and Engineering*, 9(2), 199.

The candidate developed the new macro-element model with guidance of the second author, Dr Andrea Diambra. The implementation of the model into coding language, model calibration, and analyses, were conducted by the candidate, with inputs from all co-authors. The candidate prepared the first draft of the paper and co-authors revised and contributed to the final version. Most of this paper is incorporated into Chapters 4 and 5 of this thesis.

CHAPTER 2. Literature Review

Objectives

- To present a summary of anchoring systems in offshore applications
- To present the types of anchors and their advantages and disadvantages
- To present previous macro-models developed to assess the behaviour of plate anchors and other geotechnical structures
- To present results from numerical simulations and experimental studies on anchoring systems
- To present the behaviour of anchors installed in different soils and under different loading conditions

2.1. Introduction

Anchoring systems have become increasingly relevant in the last several years, mainly due to the increase in the number of wind farms in offshore environment as well as the growing interest of oil and gas industry. Since the first offshore oil rig was installed in 1947, 18 miles from the coast of Louisiana in the United States, more than 7,000 offshore platforms have been built worldwide (Randolph & Gourvenec, 2011). On the other hand, the global installed offshore wind power capacity keeps increasing year after year and is expected to reach 27.5 GW in 2026 (Rystad Energy, 2020). Wind power in Europe overtook coal for the first time in 2016 as the second largest form of power generation (CarbonBrief, 2017) and became cheaper than new nuclear energy in 2017 (Sauven, 2017).

Although the monopile is the most common foundation type for offshore wind turbines (OWTs), their use is usually limited to water depths of up to 40m (Golightly, 2018), beyond which such foundations become unattractive due to cost of installation and operational limits. On the other hand, floating structures can be installed in much deeper water, which opens much greater possibilities and less limitations for floating wind in terms of water depth.

This chapter presents the types of anchoring systems that have been developed and that are currently in use for floating structures, as well as the main recent floating renewable energy devices in operation. Current design criteria are also presented, as well as experimental and modelling studies on plate anchors. Finally, macro-element models for several geotechnical applications are presented, and their main features are analysed.

2.2. Types of anchors

Floating – or buoyant – structures are usually linked to the seabed by mooring systems, mainly by catenary, taut line or vertical systems (Figure 2.1). The mooring system consists of lines connecting the surface structure to anchors or piles on the seabed (Brown, 2005). Vertical moorings are applicable only to tension-leg platforms and involve taut steel cables applying tension between the seabed and a platform (Richardson, 2008). Catenary moorings, on the contrary, arrive horizontally at the seabed, such that the anchor is subjected mainly to horizontal forces. In a catenary system, most of the restoring forces are generated by the self-weight of the mooring line (Randolph & Gourvenec, 2011). Taut or semi-taut line moorings, in turn, arrive at the seabed at angles of 30°-45°, with little change in angle over the length of the line. As opposed to catenary moorings, the restoring forces for taut-leg mooring systems are provided by the elasticity of the mooring lines. Taut and semi-taut lines are, therefore, restricted to deep waters where the mooring line is long enough to ensure that it is capable of providing the required elasticity (Richardson, 2008).

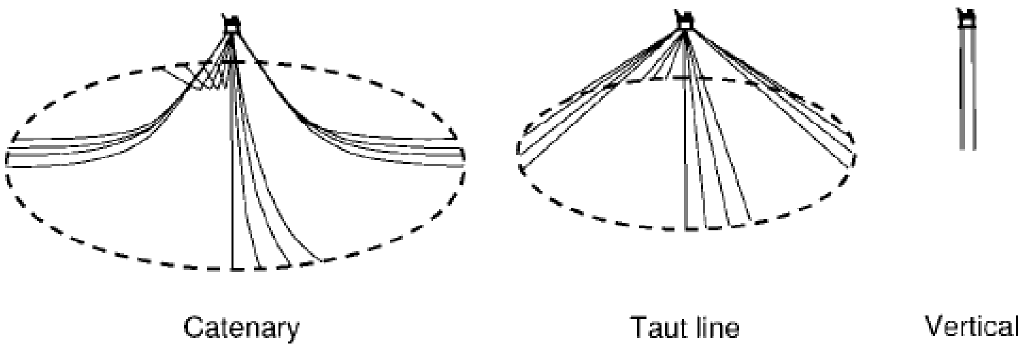

Figure 2.1 – Mooring configurations (Randolph & Gourvenec, 2011).

All the aforementioned mooring systems are fixed to the seabed by anchoring systems. The main types of anchors for floating offshore structure are suction caissons (commonly referred to as bucket foundations), drag-embedment anchors, vertically-loaded anchors (VLA), suction-embedded plate anchors (SEPLA) and dynamically-embedded plate anchors (DEPLA), as described in the next sections.

2.2.1. Suction caisson anchors

Suction caissons consist of large-diameter stiffened cylindrical shells open at the bottom and closed at the top. The water is pumped out through a hole near the top, establishing a pressure differential resulting in a downward force, in such a way that the caisson is sucked into the seabed (Figure 2.2). Two advantages of suction caissons with respect to other types of anchors is that their location can be determined with great accuracy and that they do not need to be dragged to be proof loaded (Diab & Tahan, 2005). Furthermore, their ability to resist both horizontal and vertical loads allow their use in catenary, taut lines and vertical mooring systems – although use in vertical anchorage is discouraged (Aubeny, 2018). In addition, an important advantage of suction caissons over piles is that the former does not require heavy underwater hammers and auxiliary platforms to support the installation operation (Aubeny, 2018). However, the installation process of suction caissons may make it difficult for these types of anchors to penetrate hard layers in heterogeneous soil profiles (Richardson, 2008). Additionally, the high pressure required to penetrate in certain sands may cause failure by rigid body motion due to the failure of soil plug within the anchor (Watson et al., 2006).

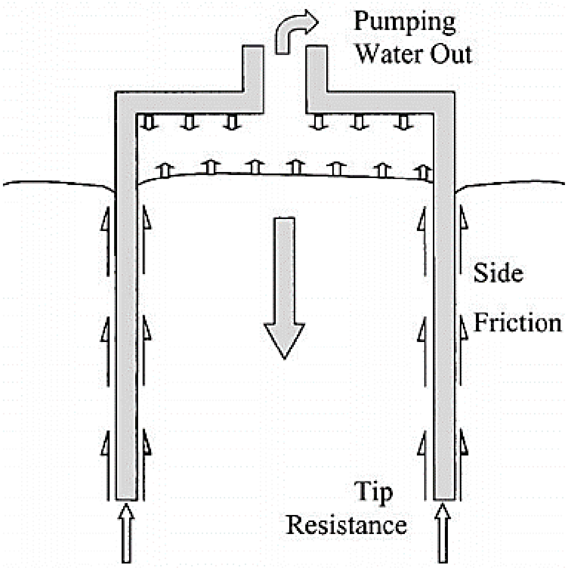

Figure 2.2 – Suction caisson schematic (Diab & Tahan, 2005).

2.2.2. Anchor piles

Anchor piles are steel tubes with a mooring line attached at some point below the mudline. They are either driven or drilled into the seabed, in the same manner as piles used for fixed structures. Anchor piles' holding capacity is given predominantly by shaft (axial) friction between the pile surface and the surrounding soil (Randolph & Gourvenec, 2011). This anchoring system can be installed in a wide range of seabed soil conditions and can resist both horizontal and vertical loads, making them adequate for all types of mooring configurations (Richardson, 2008). Moreover, whilst heterogeneous profiles are usually not feasible for other types of anchors, such as suction caissons, they are not particularly problematic for driven pile installation (Aubeny, 2018). Despite the versatility of anchor piles, installation costs are extremely high mainly due to driving equipment required. These installation costs increase significantly with water depth (Clewes & Micheel, 2007). Most operations are limited to 1500 m, making it unattractive in very deep water (Randolph & Gourvenec, 2011). Aubeny (2018) also draws attention to potential environmental concerns associated to acoustic emissions caused by pile driving.

2.2.3. Screw anchors

While conventional anchor piles produce high levels of underwater noise, the use of screw piles in offshore jacket structures arose as an alternative, mainly due to the strict mitigation measures to reduce noise emissions during installation in Europe (Koschinski & Ludemann, 2013). Most of the work done in these piles was undertaken at the University of Dundee, where research on the topic started in 2007 (Brown et al., 2020).

Besides the advantage in terms of noise emissions, screw anchors exhibit large tensile capacity for offshore applications, and are more efficient than piles when subjected to tensile loading (Cerfontaine et al., 2020, 2021). The main challenge for this type of anchors is related to the torque and force required for installation (Cerfontaine et al., 2021). Recently, an offshore contractor company joined efforts with the University of Dundee to develop large helical anchors. The company states that helical anchors can also be more easily removed from the seabed through reversing the installation process, allowing low-cost decommissioning of the foundations (Huisman, 2021).

2.2.4. Drag-embedded anchors

Drag-embedded anchors (DEAs) comprise a broad fluke rigidly connected to a shank (Figure 2.3). This type of anchor evolved from conventional ship anchors (Randolph & Gourvenec, 2011). The flukes are designed to cut through the soil during embedment and are responsible for the major proportion of resistance. The shank is able to rotate and orientate drag direction (Dean, 2010). Drag anchors capacity – which may exceed 10 MN – derives from both the bearing resistance of the plate and the friction along the anchor shank (Richardson, 2008). The low cost of installation is the main attractive to the use of these anchors (Aubeny, 2018). The main limitations of drag anchors concern the low resistance to vertical loads as a consequence of minimal penetration experienced in sands and stiff clays – therefore they are suitable only for catenary moorings but not for deep water applications using taut and semi-taut lines (Randolph & Gourvenec, 2011). Furthermore, there is a high level of uncertainty over the trajectory and final position of the anchor during installation (Liu et al., 2012). In addition, significant anchor drag distances may be necessary to mobilise the final capacity (Richardson, 2008).

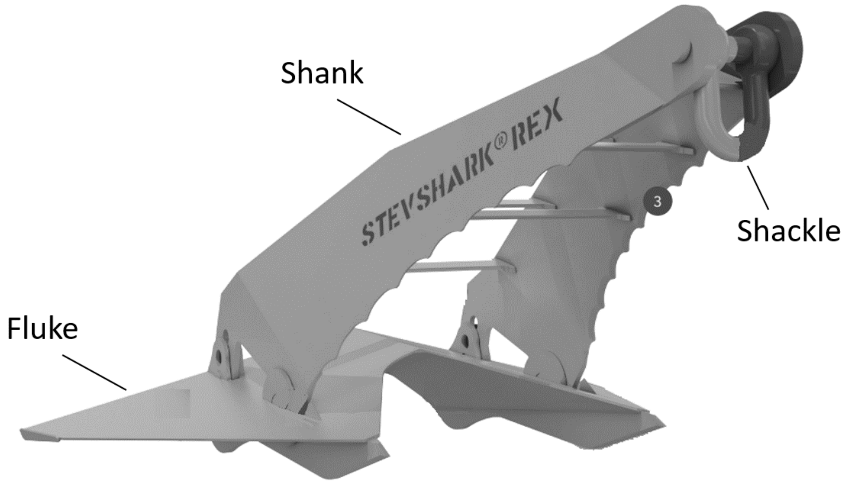

Figure 2.3 – Components of a Stevshark drag anchor (adapted from Vryhof, 2021).

DEAs have been widely used in temporary moorings solutions in deep water mainly due to their low installation cost and high holding capacity (Aubeny & Chi, 2010).

Aubeny & Chi (2010) presented a predictive model for the trajectory and capacity of DEAs for different fluke and shank geometries, soil properties and chain angle at the mudline. The model was based on limit-equilibrium analysis and proposed an interaction relationship (yield function) between vertical, horizontal and moment loads.

O'Neill & Randolph (2001) carried out centrifuge tests with DEAs in normally consolidated clay and developed an analytical model to calculate anchor embedment and holding capacity, and the results from the model predictions were shown to be consistent with published design charts for Vryhof Stevpris anchor. A different model (based on macro-element modelling concepts) was developed by Bransby & O'Neill (1999), in which an expression for a yield locus (referred to as 'capacity surface' in this thesis) in a normalised *V-H-M* space (vertical, horizontal and moment loads, respectively) based on finite-element analyses was proposed. The form of this expression would be used later in other publications for different anchor types, as will be further shown in 2.6.2. The yield locus formulation presented in Bransby & O'Neill (1999) was further expanded to a plasticity model that described the kinematics of the anchor, including forces and plastic displacements.

In summary, significant research has been done on drag-embedded anchors, including experimental investigations and the development of (analytical and numerical) models. As will be shown throughout this thesis, much of the knowledge acquired from research with drag-embedded anchors was later used in research with other anchor types. Of particular relevance for this thesis is the model developments presented in O'Neill et al. (2003), whose yield locus and plasticity framework were the basis for the development of the CASPA model in Cassidy et al. (2012), as further explained in section 2.6.2.

2.2.5. Vertically-loaded plate anchors (VLA)

An example of vertically-loaded anchor (VLA) is manufactured by Vryhof Anchors and commercially referred to as Stevmanta VLA. (Figure 2.4). VLAs are installed in a similar manner to DEAs, but the anchor shank (or the chain, in the case of the anchor in Figure 2.4) is released to a position subnormal to the fluke after drag installation (Aubeny & Chi, 2014). The main difference is that after penetrating to the expected depth, VLAs can be reconfigured so the anchor line becomes nearly perpendicular to fluke, thus maximising the uplift capacity (Liu, 2012). Other advantages of VLAs are that they are among the lightest anchors used for floating structures (Zimmerman et al., 2009) as well as having low cost of installation (Aubeny & Chi, 2014). As VLAs can be regarded as a type of drag anchor, the problems and limitations of VLAs and drag anchors are common, notably the prediction of the trajectory (Murff et al., 2005) as well as difficult prediction of final depth and position.

In terms of modelling of this type of anchors, Aubeny & Chi (2014) extended their previous model for DEAs (Aubeny & Chi, 2010) to account for some critical aspects of VLA behaviour, including anchor rotation during shank release, realignment of the free shank and continuation of the anchor embedment under free shank conditions. The model was developed within the plastic limit interaction equations proposed by O'Neill et al. (2003) and used the chain solution proposed by Neubecker & Randolph (1995). A parametric analysis was conducted and the model results were compared to a few sets of field data in terms of anchor trajectory and force-displacement behaviour, but a broader validation is still needed due to the limited availability of experimental and field data.

Figure 2.4 – Vertically-loaded anchor Stevmanta (Vryhof Anchors, 2020).

Even though most of the research development around VLAs was based on previous knowledge gained from DEAs, the number of studies on the previous is much more limited than on the latter.

2.2.6. Dynamically installed anchors

Dynamically-installed anchors were developed to overcome the high cost of installing anchors in deep water. This type of anchor is able to embed into the seabed under free-fall, reducing the installation costs (Lieng et al., 1999). They are released from a predefined height above the seabed, gaining velocity during free fall through the water before impacting on and embedding within the soil sediments (O'Loughlin et al., 2013). These anchors were initially developed with a torpedo shape, but alternative geometries have been proposed throughout the years (Figure 2.5).

Several studies on torpedo-shaped anchors have been conducted over the last three decades, including field tests in clay and calcareous sand (Medeiros, 2002), centrifuge tests and geotechnical model with viscous effects (O'Loughlin et al., 2004), calibration of bearing and frictional factors in calcareous sand (Richardson et al., 2005) and effect of anchors setup (Richardson et al., 2009) using centrifuge tests, and the derivation of a relationship between the final tip embedment of the anchors and the total energy with which it reaches the mudline (O'Loughlin et al., 2013). Torpedo anchors have been widely employed by Brazilian Oil Company Petrobras (Martins, 2020). Its use has been reported over the last two decades in the Campos Basin, offshore the state of Rio de Janeiro in Brazil (Passini et al., 2017). The typical penetration depth ranges from two to three times the anchor length in soft clays, and the holding capacity is usually between three and six times the weight of the anchor (Aubeny, 2018). While this capacity is low compared to other sorts of anchors, the ability to resist both vertical and horizontal loads as well as the low cost of fabrication and installation make this solution an attractive anchoring system.

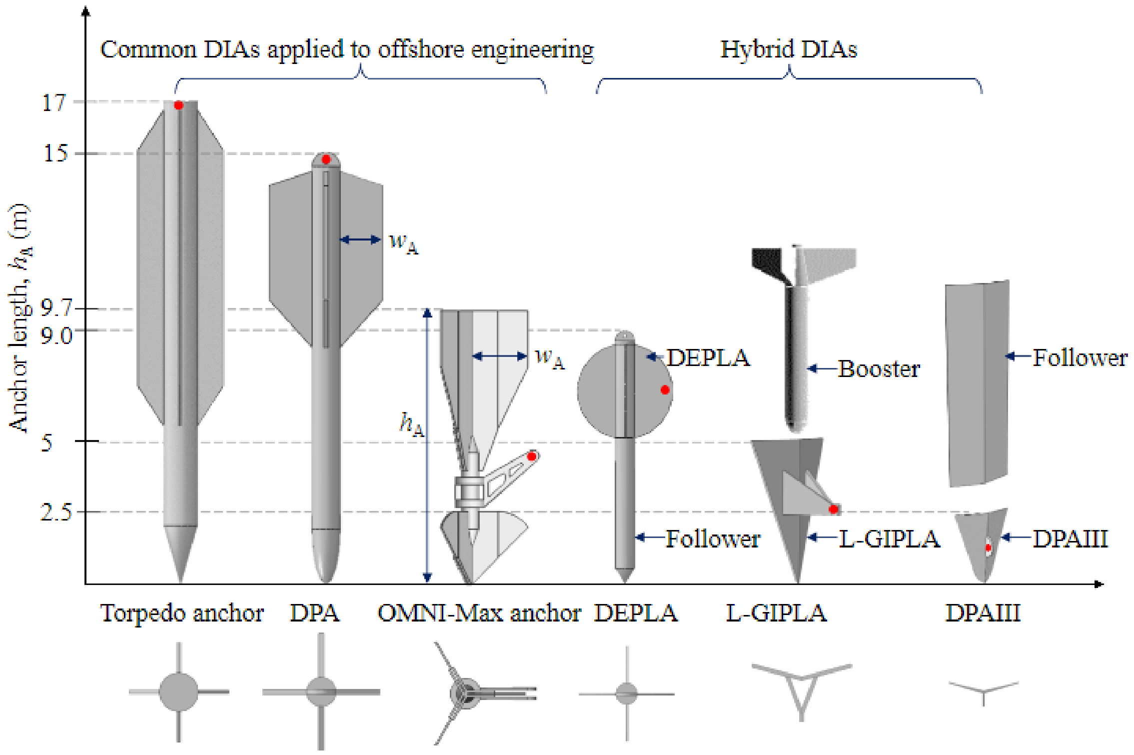

Figure 2.5 – Varied types of dynamically-installed anchors (Han & Liu, 2020).

An alternative type of gravity-installed anchor called the OMNI-Max was presented by Shelton (2007, p. 2), who described this solution as multi-directional, and self-inserting. The advantages listed by the author included "relatively small size, omni-directional mooring arm, adjustable fluke fins" and residual capacity after peak capacity is reached. A broad review on dynamically-installed anchors was carried out by Han & Liu (2020).

More recently, anchoring systems that combine dynamic installation with plate anchors were proposed, such as dynamically-installed plate anchors (DEPLA). These anchors are presented in the next section, with conventional plate anchors.

2.2.7. Plate anchors

The use of plate anchors has been reported in the last five decades. The earliest publications in this matter, though, focused on anchors for footings (e.g. Douglas & Davis, 1964; Ladanyi & Johnston, 1974), diaphragm walls (Akinmusuru, 1978) and retaining walls (Rowe & Davis, 1982), i.e. all of them in onshore applications. Whereas for onshore applications the prediction of plate behaviour is focused on the limiting conditions of small displacements, for offshore facilities the main design purpose is to provide a sufficient holding capacity, which is generally associated with large displacement that may cause plastic soil response (Han, 2016).

The first studies conducted on plate anchors for offshore applications only happened in late 1990s and early 2000s. Dove et al. (1998) and Wilde et al. (2001) introduced a new type of plate anchor, the Suction Embedded Plate Anchor (SEPLA), which comprises a rectangular thin fluke, a shank connecting the fluke to the padeye (i.e. the loading point) and, in some cases, a full-length keying flap at its edge (Figure 2.6a).

A suction caisson (the follower) is employed to install the plate anchor to its design embedment depth. The plate is initially positioned at the tip of the follower (Figure 2.6b) and is subsequently penetrated into the soil through the pressure inside the suction caisson. The suction caisson is then retrieved, leaving the SEPLA at the target depth (Han, 2016). The mooring line attached to the padeye is then tensioned by a vessel on the surface, making the anchor rotate from its initial vertical position to an inclined position, approximately normal to the load applied by the mooring line (Dove et al., 1998). This process of rotation during the pulling process is called keying, during which the anchor experiences vertical motion, resulting in loss of embedment (Gaudin et al., 2015).

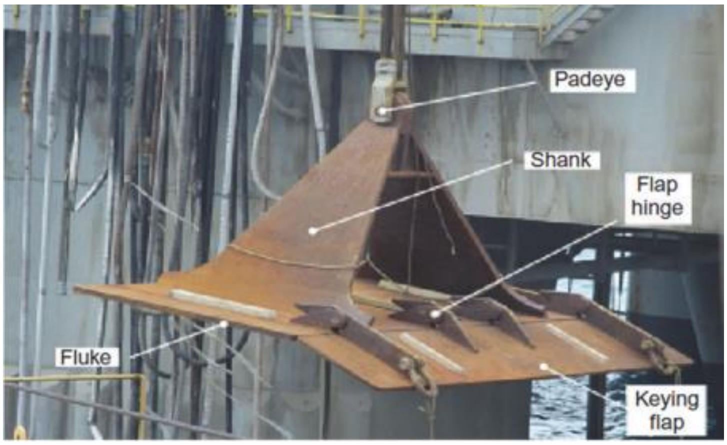

(a)

(b)

Figure 2.6 – Photographs of (a) a SEPLA anchor and (b) a SEPLA anchor at the tip of a suction follower (Han, 2016).

SEPLA's can achieve high holding capacities under both horizontal and vertical loading, allowing them to be used in catenary and taut mooring systems. The installation process allows an accurate prediction of anchor depth after installation. Some SEPLAs incorporate a keying flap which aims to reduce the loss of embedment during keying, which was shown to reduce backwards movement, slightly increase loss of embedment and increase the ultimate capacity (Yang et al., 2012). Nevertheless, since offshore marine deposits usually exhibit an increase of strength with depth, the major concern associated with SEPLA's (and offshore plate anchors in general) is the loss of embedment, which results in an unrecoverable loss of capacity (Gaudin et al., 2006; Song et al., 2009; Yang et al., 2012). Moreover, high installation and transport costs – mainly due to the size of suction caissons – are cited by Aubeny (2018) as another disadvantage of SEPLA's.

Recently, a new type of anchor similar to the plate anchor was developed: the dynamically embedded plate anchor (DEPLA), which combines the installation benefits of dynamically installed anchors with the high holding capacity of plate anchors. The DEPLA comprises a torpedo-shaped follower that penetrates the seabed through free-fall and a set of four flukes. After embedment, the follower is retrieved, and the flukes are left vertically embedded in the seabed. A mooring line attached to the flukes is then tensioned, making the flukes rotate to an orientation normal to the direction of loading (Gaudin, et al., Advances in offshore and onshore anchoring solutions, 2014). The main attractive of this type of solution is the low cost: O'Loughlin et al. (2015) estimate that the fabrication costs of DEPLAs are reduced by 70-80% relative to suction caissons.

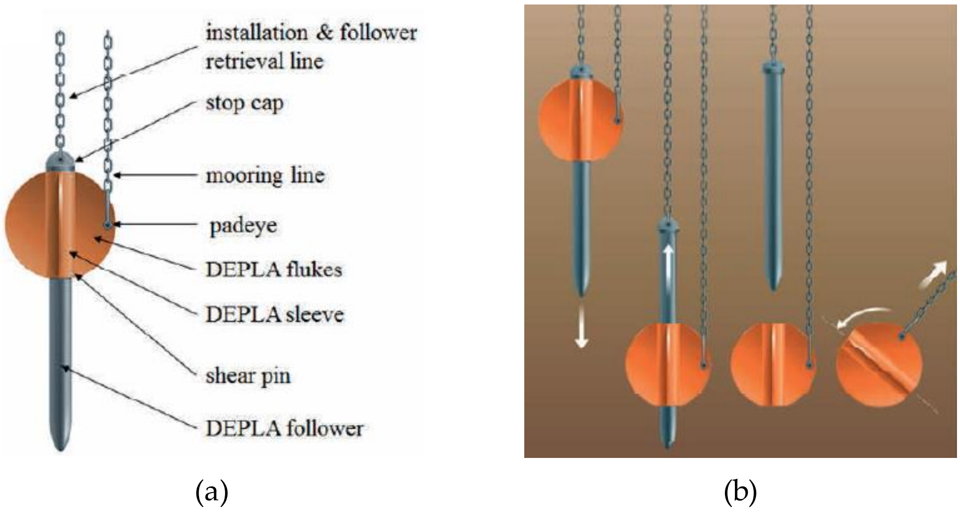

(a) (b)

Figure 2.7 – Dynamically embedded plate anchor: (a) DEPLA schematic and (b) installation and keying (Gaudin, et al., Advances in offshore and onshore anchoring solutions, 2014).

The main disadvantages of DEPLA's are the same associated with SEPLA's – loss of embedment resulting in loss of holding capacity. Furthermore, both SEPLAs and DEPLAs have additional risk associated with their use in sand (Knappett, et al., 2015).

Another type of dynamically-installed plate anchor concept, shown in Figure 2.8 and referred to as DPAIII, was proposed by Chow et al. (2017). The thin blade-like shape of the anchor increases its penetration in sand compared with existing cylindrical shafts with conical tips. The DPAIII installation is similar to previous dynamically-installed plate anchors, with the follower being retrieved to the vessel for reuse in following installations.

Centrifuge tests under drained monotonic and cyclic loading conditions for this type of anchor were carried out by Chow et al. (2018).

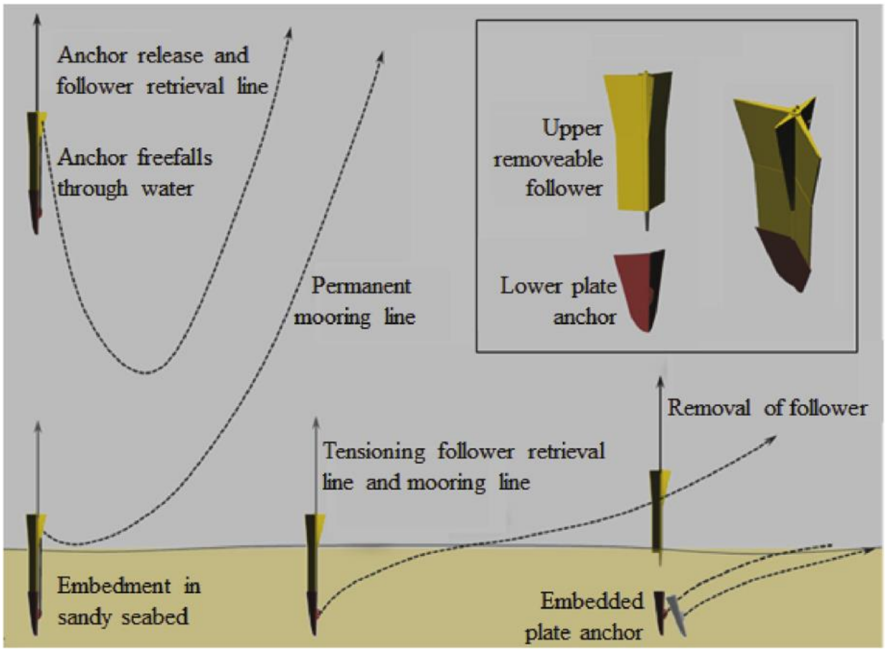

Figure 2.8 – Dynamically-installed plate anchor concept (Chow et al., 2018b).

The results from the centrifuge tests in Chow et al. (2018b) showed that the capacity of the anchor is higher under catenary mooring than under vertical mooring. It was also shown that, under drained conditions, the anchor's cyclic capacity does not degrade, and even increases, in comparison with the monotonic capacity. However, the study warned that the effect of partially drained cyclic loading needed further investigation, as these effects were still unclear and hence not accounted for (Chow et al., 2018b). These partial drainage effects in anchors were studied later by the same researchers, as detailed in section 2.5.5.

2.3. Past, current and future use

The first pilot project for floating wind was Hywind Demo, installed in 2009 offshore Karmoy, Norway (Equinor, 2019). For eight years, the 2.3 MW turbine produced more than 40 GWh and the system proved effective even with wind speeds of 40 m/s and wave heights of 19 m (Equinor, 2019). Following the success of the Demo, Hywind installed the first commercial floating wind farm about 15 miles off the coast of Peterhead in Aberdeenshire, northeast of Scotland. The wind farm started operating in 2017 and consisted of five 6 MW wind turbines with a total capacity of 30 MW. Fifteen 16-metre-tall suction anchors (three for each turbine) were used to connect the 780-metre-tall mooring lines to the clayey seabed under water depths of up to 120 m (Equinor, 2019). An illustration of the Hywind concept is displayed in Figure 2.9.

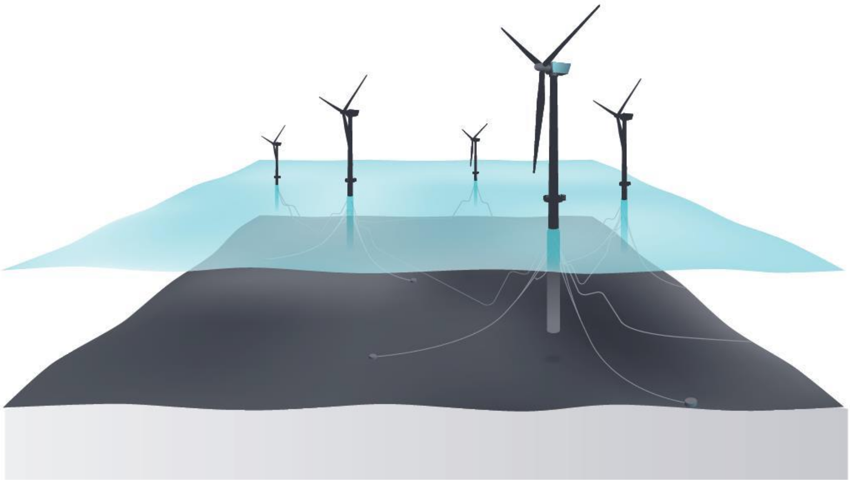

Figure 2.9 – Illustration of Hywind, the first floating offshore wind farm (Equinor, 2019).

Following pioneer Hywind, Ideol's Floatgen wind turbine was installed 22 km off the Atlantic coast of France near Le Croisic, in water depths of 33 m, and became fully operational in September 2018. The 2 MW turbine currently supplies electricity to 5000 inhabitants (Floatgen, 2018) and achieved a total of 6 GW power production in 2019 (Floatgen, 2020), exceeding the initial expectations. Six synthetic fibre (nylon) mooring lines connected the floating structure to drag-embedment anchors (Figure 2.10).

(a) (b)

Figure 2.10 – Ideol Floatgen project: (a) wind turbine after installation (Floatgen, 2019); (b) drag-embedment anchors used for Floatgen (Ideol, 2016).

Ideol's second demonstrator Hibiki has been installed since 2018, located 5 km off the cost of Kitakyushu (Japan) in water depths of 55 m (BW Ideol, 2021). The 3 MW turbine has supplied electricity to 8000 inhabitants. The anchoring system used for Hibiki was drag-embedment anchors (Itoh, 2019), similarly to Floatgen.

Recently, a commercial floating wind farm was installed 20 km off the coast of Viana do Castelo in Portugal, where the water depth reaches 100 m. WindFloat Atlantic (Figure 2.11) includes three turbines with a total installed capacity of 25 MW, which is enough to supply electricity to approximately 60,000 households a year once the three turbines are fully operational (Principle Power, 2021). Each platform will have three catenary mooring lines connected to drag embedded anchors (Lankhorst Offshore, 2021). The installation of the first wind turbine was completed in October 2019 and connected to the grid in January 2020, and it is currently the largest turbine ever to be installed on a floating platform (Principle Power, 2021).

Figure 2.11 – WindFloat Atlantic wind turbine (EDP Renewables)

Another relevant floating offshore wind project is Kincardine off the coast of Aberdeen in Scotland. The first of five 9.6 MW turbines was towed out in December 2020 (Durakovic, 2020), and, as in WindFloat Atlantic, the catenary mooring lines were connected to drag embedded anchors (Augusteijn & Buitendijk, 2021).

In addition to the developments in floating wind over the last years, advance has been made in floating wave and tidal energy devices in recent years. For example, the Orbital Marine

O2 tidal-powered turbine was sailed out of Dundee in May 2021 and started generating electricity in July 2021 (Orbital Marine, 2021). The 2 MW floating offshore unit was installed in the Fall of Warness in Scotland and is expected to produce electricity for 2,000 homes over the next 15 years (BBC, 2021). The Pelamis energy converter in Portugal was the first commercial wave energy project, which operated in 2006 until 2014 and provided energy to 1,500 homes (Power Technology, 2021).

Although less loading capacity is required for such devices, plate anchors could still be an option with future (larger) developments. The details of the anchoring systems used in such projects were not found in available literature.

2.4. Design criteria for plate anchors in offshore applications

Few studies have provided recommendations on the design of plate anchors for floating facilities, most of them focused on oil industry and not many are dedicated to offshore renewable energy devices. Most of them provide general guidelines whilst the lack of a well-stablished procedure is evident.

Early studies on embedded plate anchors for ocean construction were conducted by the US Naval Construction Battalion Center in California (Beard, 1980), providing procedures for calculating the allowable design loads under static and dynamic loading conditions in sediment seafloors. Five loading conditions were studied: short-term loading, long-term loading, impulse loading, cyclic loading and earthquake loading.

The short-term loading capacity in Beard (1980) was calculated based on anchor geometry and on a single value of soil strength: undrained shear strength (s_u) for cohesive soils and effective friction angle (φ') for granular soils, although a correction factor for soil disturbance was applied for cohesive soils.

On the other hand, long-term static capacity calculation in cohesive soils in Beard (1980) was based on the soil's effective stress strength parameters: the friction angle (φ') and the cohesion intercept (*c′*). In granular soils, as drainage occurs within a shorter period of time, the long-term capacity was assumed to be the same as the short-term holding capacity.

Beard (1980) also provides recommendations on the design of plate anchors under cyclic loading. The guidance provided applies for cases when the cyclic loads are of relatively uniform magnitude (at least one-third of the loads). The cyclic capacity is given as a percentage of the static capacity, and the procedure is limited to cases where the average load is less than 33% of the static capacity.

The procedure in Beard (1980) basically consists of determining a certain time t_c required for excess pore pressure dissipation, which depends on the soil's permeability (Figure 2.12). The number of cycles during a period of time t_c is found and limiting design bounds are then obtained from Figure 2.13.

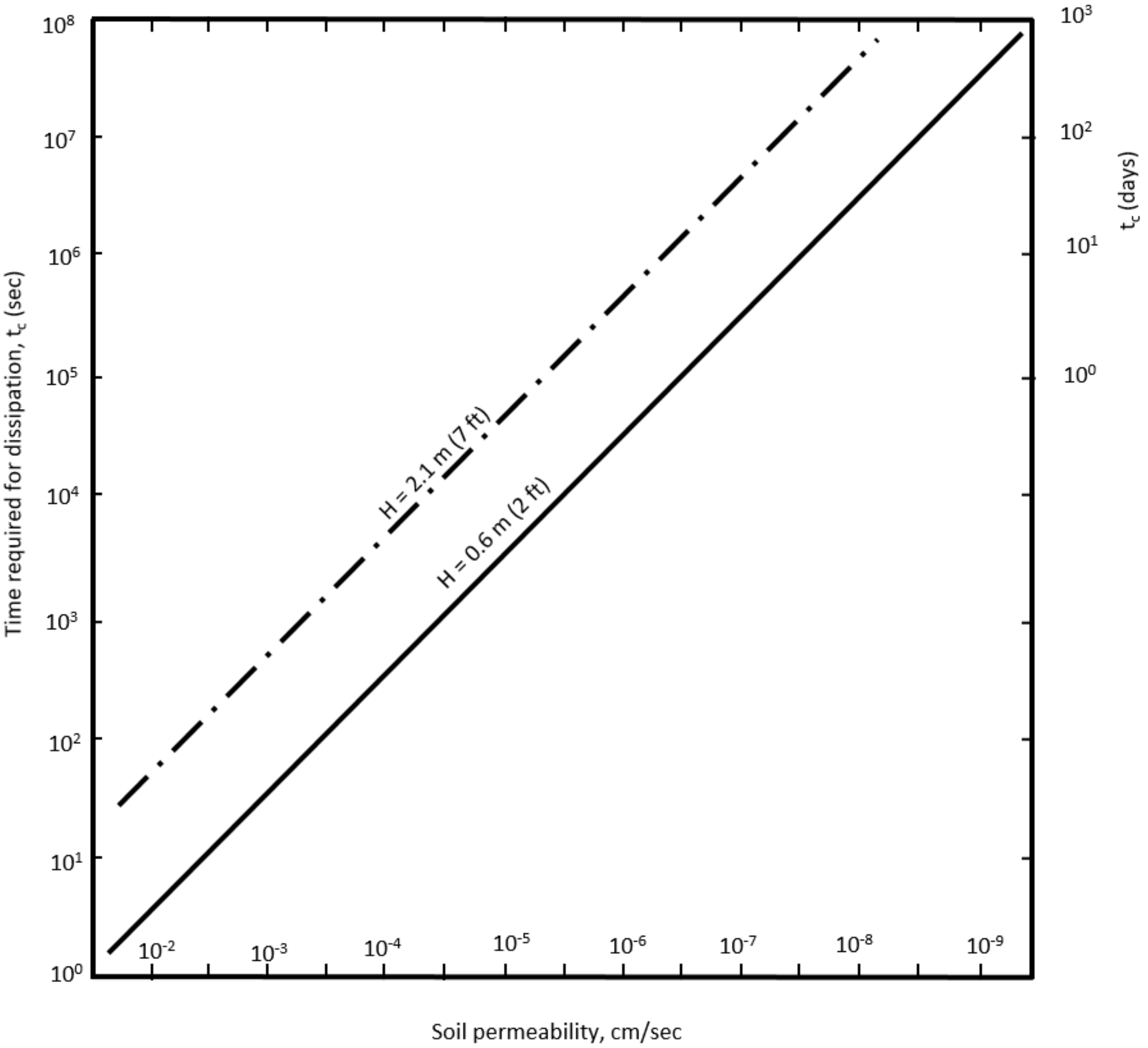

Figure 2.12 – Time required for pore pressure dissipation (adapted from Beard, 1980)

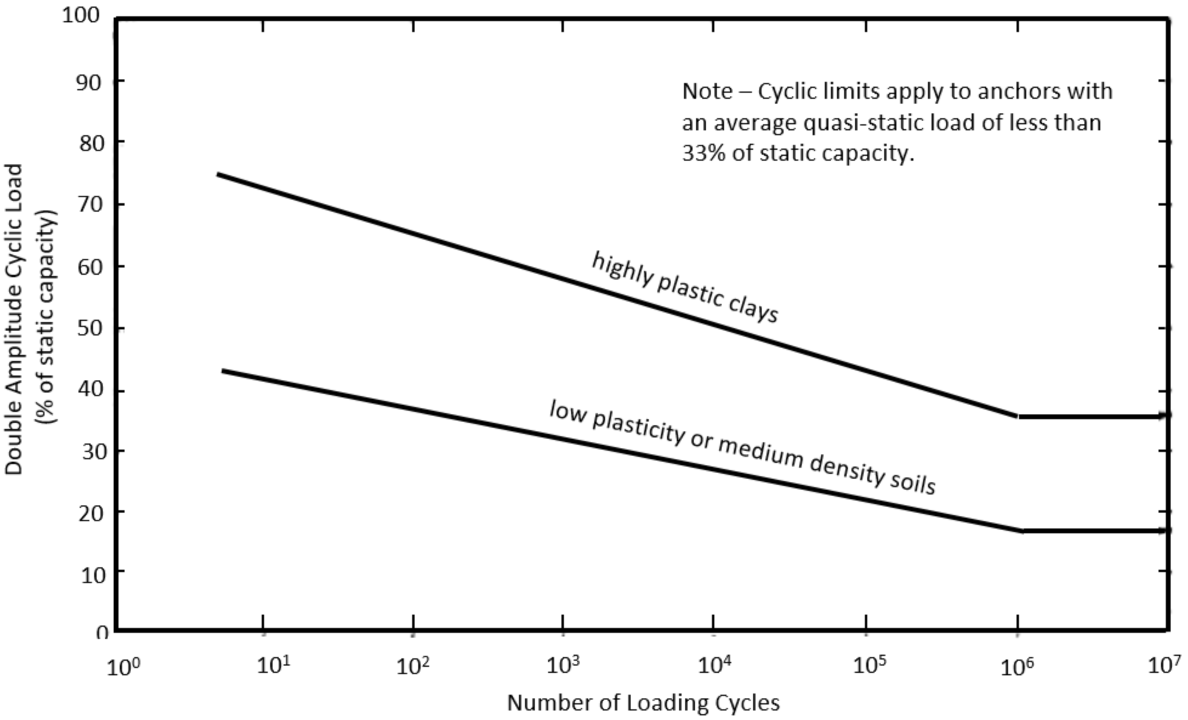

Figure 2.13 – Cyclic capacity without pore pressure dissipation (adapted from Beard, 1980)

It can be observed from Figure 2.13 that it is assumed that the cyclic capacity is always lower than the static capacity, as the percentages are all lower than 100%.

Besides the US Naval report presented previously (Beard, 1980), DNV has developed a design code for plate anchors in clay. The DNV design codes are still widely used in engineering practice.

The standard DNV-OS-J103 (2014) provides general guidance for design, construction and inspection for floating wind turbines, covering structural aspects and some geotechnical considerations. Section 9 deals with the geotechnical design of the anchoring systems, providing general guidelines for pile anchors, gravity anchors, suction anchors, fluke anchors and plate anchors. The standard DNVGL-RP-E302 (2017) is then indicated for calculation of ultimate and accidental limit states (ULS and ALS, respectively). The ULS refers to the individual anchor resistance in the case of extreme environmental actions, whereas the ALS refers to the anchor resistance when the failure of another anchor/mooring line occurs.

The static capacity in DNVGL-RP-E302 (2017) is given as a function of the penetration depth, and the cyclic capacity is calculated through the number of cycles at a certain shear stress amplitude $\tau_{f,cy}$ required to cause failure in cyclic loading. The cyclic load amplitude of the anchor is related to the cyclic shear stress amplitude of a clay sample subjected to direct simple shear (DSS) test. The cyclic diagram contours developed by e.g. Andersen et al. (2015) for Drammen clay is used to relate the shear stress levels with the cyclic loading factor to the anchor capacity. These contour diagrams (Figure 2.14) have been developed by Prof. Knut Andersen and co-workers at the Norwegian Geotechnical Institute (NGI). The Drammen clay is a soft marine clay with plasticity index of approximately 27%, and its characteristics are similar to those of many other clays encountered offshore. Since the contour diagrams normalise the cyclic shear stress (τ_{cy}) and the average shear stress (τ_a) by the undrained shear strength (s_u), as shown in Figure 2.14, the DNV code (DNVGL-RP-E302, 2017) suggests that the cyclic contours from one-way DSS tests in Drammen clay can be used for other clays, but that site-specific two-way DSS tests should be conducted to complement the Drammen diagrams.

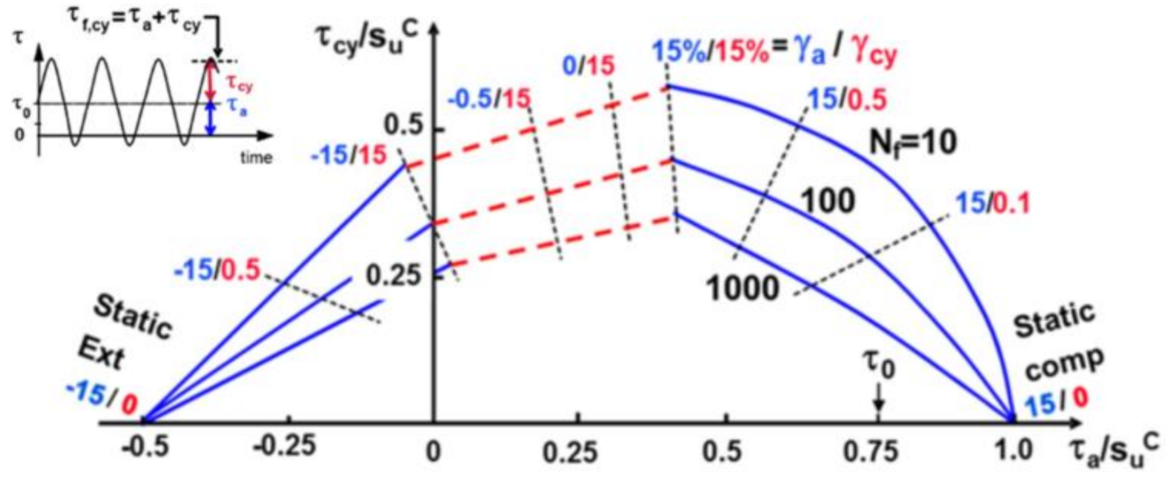

Figure 2.14 – Cyclic contour diagram (adapted from Andersen, 2015)

In terms of safety factors to be applied to the anchor design, both DNV standards mentioned above use partial load factors on the mooring line load combined with a material factor on anchor capacity. These partial load factors also depend on whether the anchors are used for temporary or permanent floaters (Zhang et al., 2022).

On the other hand, the API standard (American Petroleum Institute, 2015) developed for floating drilling and production platforms, uses lumped safety factors for the anchors, whose values depend on certain factors, such as on whether the mooring is permanent or mobile and whether the mooring condition is intact. A few basic recommendations include ensuring that the anchor's penetration depth is reached during installation and that the anchor rotation is established such that a maximum projected area is achieved, i.e. with a direction nearly perpendicular to that of the applied load. Another recommendation is that the anchor capacities should be reduced to account for long-term cyclic degradation and creep. The expression for the ultimate holding capacity in the API code is given by Equation (2.1).

$$F_u = N_c \, A_{eff} \, \eta \, s_u \tag{2.1}$$

where F_u is the ultimate holding capacity, A_{eff} is the projected area of the anchor, N_c is the bearing capacity factor determined, for example, from finite-element analysis, η is a reduction for soil disturbance during penetration and keying, and s_u is the undrained shear strength of the soil at the design penetration depth.

Despite being a simple expression, the API code mentions that the main difficulty of its application is to accurately determine the penetration depth. Furthermore, another limitation of the method is that the design is based on a single value of soil strength, hence variations during the operational life are not directly accounted for.

Besides the DNV and API codes mentioned above, anchor design can also be by means of design charts provided by anchor manufacturers. An example is the design chart of the Stevshark Rex drag-embedded anchor (Vryhof, 2021), as shown in Figure 2.15. It can be observed that the design chart does not make any distinction between drained or undrained behaviour, static or cyclic loading or even sand density. The definition of the anchor size is given by a single value of ultimate holding capacity.

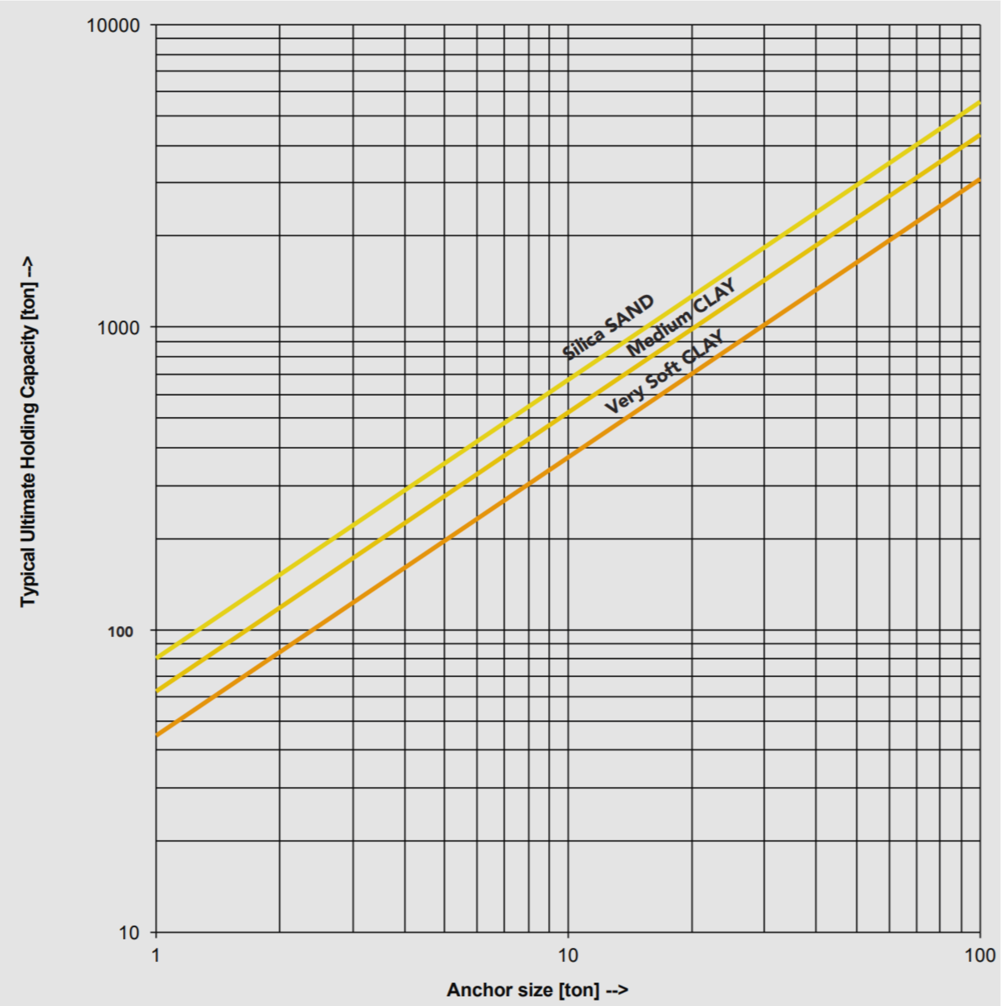

Figure 2.15 – Design chart for Vryhof's Stevshark Rex anchor (Vryhof, 2021)

In summary, design methods either focus on a single value of holding capacity for the anchor or account for cyclic capacity be means of a degradation factor. However, these methods lack an accurate prediction of anchor trajectory during keying and hence penetration depth, which is essential for an appropriate prediction of soil strength at design depth. Furthermore, full anchor behaviour during operational conditions such as cyclic and maintained loading is not accounted for. Anchor displacements and rotation is of significant interest (Cassidy et al., 2020) as well as the evolution of soil strength during the design life (Zhou et al., 2020), which is further explored in next chapters of this thesis.

2.5. Experimental studies on plate anchors

2.5.1. Introduction - Experimental techniques used

Plate anchors are usually heavy and large devices. Their length exceed 10 metres and they can weight several tons. Thus, conducting experiments with anchors in full-scale would be very expensive and time-consuming. In that sense, the behaviour of anchors is usually assessed through scale tests, notably 1g model tests and centrifuge model tests.

Through centrifuge testing, the stress dependent behaviour of soils can be captured when a sample or a geotechnical problem is scaled down. Since the soil response is largely dependent on stress levels, scaling laws are necessary to ensure stress similarity between model and prototype (Taylor, 2005). For instance, two samples with the same density can have completely different behaviour, depending on whether they are above or below the critical state line, for example (Figure 2.16). A soil sample A, below the critical state line, dilates towards the CSL, whereas a sample B, with the same void ratio as sample A but with a higher mean effective stress p', is above the CSL and therefore contracts. By scaling down a geotechnical problem, the stress level of the soil could decrease from B to A, for example, leading to completely opposite behaviour, i.e. dilatant instead of contractive (Ng, 2014).

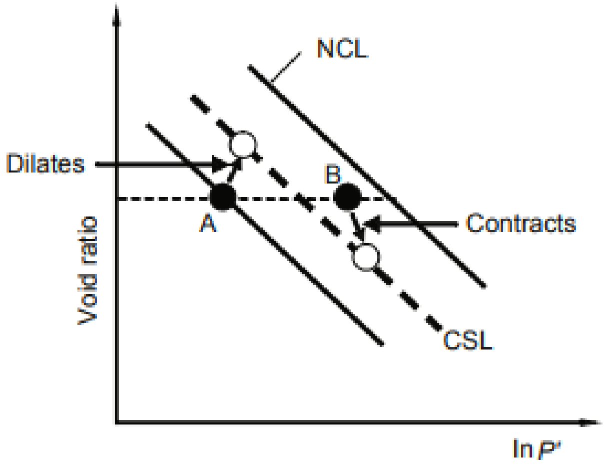

Figure 2.16 – Stress dependent behaviour of soils (Ng, 2014).

The principle of a centrifuge device consists of applying a radial acceleration field which feels like a gravitational field to the model, but many times stronger than Earth's acceleration g. Hence, if an acceleration field of N times the Earth's gravity g is applied, the vertical stress at depth h_m will be the same as that at depth h_p at prototype (full) scale. In other words, scaling down a model by N times needs to be compensated by scaling gravity up by N times in such a way that stress levels are the same at model and prototype. The scaling factor N is related to the swept angular velocity of the centrifuge equipment (ω) through the relationship $N = r\omega^2/g$, where r is the radius of rotation (Muir Wood, 2004).

Small scale 1g tests, on the other hand, do not consider the effect of gravity on soil behaviour (Song et al., 2006). Despite this limitation, 1g tests are still widely in soil-structure interaction models, mainly because such tests are generally more economical compared to centrifuge modelling (Al Heib et al., 2020). Furthermore, 1g models, while not obeying the governing laws of similitude, are used sometimes to obtain an adequate model which maintains 'first order similarity' and with proper consideration of failure mechanisms (see Muir Wood, 2004, p. 248). However, while the scaling factors for length and mass density are the same as for centrifuge test, many other quantities – including stress, force, stiffness and time – need to be correctly scaled as the scaling laws are different from those of centrifuge modelling (Muir Wood, 2004).

The follow sections show a selection of 1g and centrifuge tests performed on plate anchors, including unidirectional loading and three-dimensional loading subjected to monotonic and/or cyclic loading.

2.5.2. Unidirectional capacity

Several experimental studies on plate anchors were conducted mainly after the 1960s, though not all were focused on offshore applications. Most studies involved model (1g) tests and attempted to develop semi-empirical relationships or charts to estimate the normal capacity of plate anchors for different embedment ratios and soil properties (Rowe and Davis, 1982a,b). As will be presented in section 2.6, the experimental results were later used to develop and validate theoretical and numerical models for anchor capacity in both granular and cohesive soils.

The unidirectional (normal, tangential and rotational) capacities of plate anchors are particularly important even for cases in which the three-dimensional capacity (i.e. anchor subjected to rotation) of the anchors is studied, as most capacity surfaces are defined as a function of the normal (V_{max}), tangential (H_{max}) and rotational (M_{max}) capacities when acting independently on the anchor. Most studies, though, used flat circular, rectangular or square plates, unlike most plate anchors currently in use, which usually have different shapes and geometries (see previous section 2.2). The capacities of plate anchors with more complex geometries will be further discussed throughout the thesis when appropriate.

2.5.2.1. Unidirectional capacity in sand

A broad background of experimental studies on plate anchors in frictional soils is presented by Das (1990) and by Merifield & Sloan (2006). Several laboratory model tests (mostly calibration chamber testing) in both horizontal and vertical anchors analysed the effect of peak friction angle, anchor shape, anchor roughness and embedment ratio (e.g. Neely et al, 1973; Das & Seeley, 1975; Murray & Geddes, 1987; Murray & Geddes, 1989). These studies reported an increase of anchor capacity with friction angle, and with depth up to a certain embedment ratio, after which the capacity remains constant as the anchor behaves as a deep anchor. It was also shown that vertical anchors exhibit higher normal capacity than horizontal anchors. Soil dilatancy was found to have a significant influence on anchor response for both horizontal and vertical anchors, while roughness was shown to have little effect on horizontal anchors but a significant effect on vertical anchors.

An extensive experimental study on the uplift of circular plate anchors in sand was also reported by Ilamparuthi et al. (2002). This study included tests on circular anchors with diameters much larger than those used in previous publications. The diameters ranged from 100 to 400 mm, whereas most previous studies tested plates with diameters ranging between 25 and 75 mm.

More recently, Chow et al. (2018a) carried out 1g tests to quantify the capacity of plate anchors in sand. Unlike the previous studies, both normal and shear (tangential) capacities were studied. The tests were conducted in vertically and horizontally-installed rectangular plates under both vertical and horizontal monotonic pull. It was shown that both normal and shear capacities are highly influenced by the initial anchor orientation as well as by the embedment ratio. The results are displayed in Figure 2.17 below.

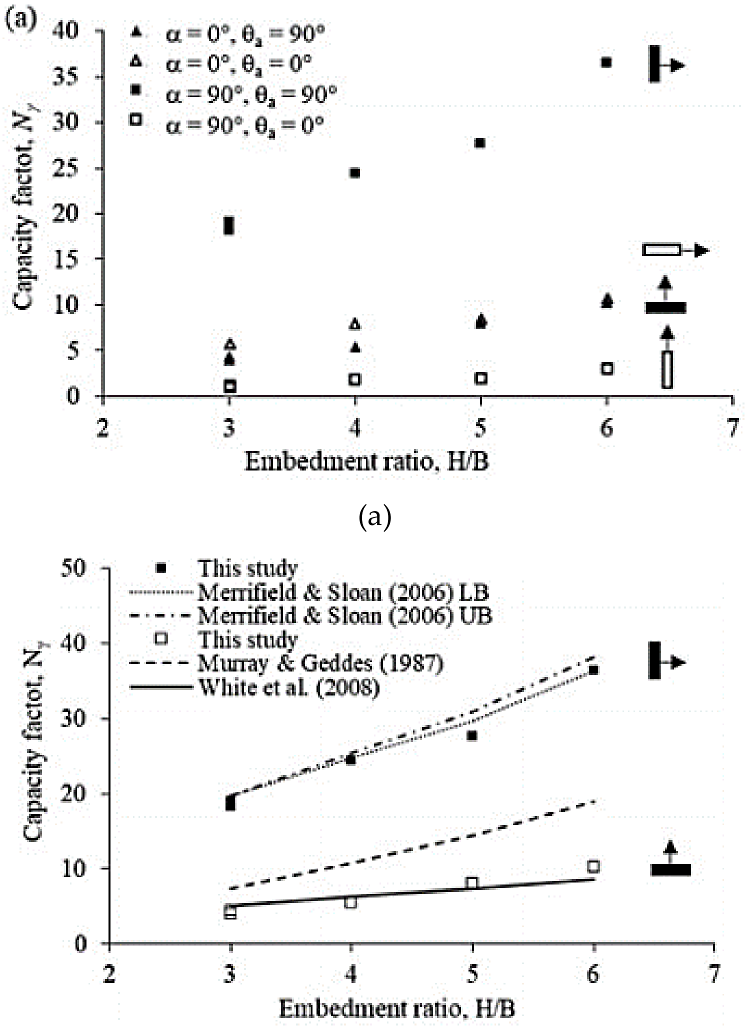

(a)

(b)

Figure 2.17 – (a) Normal and shear capacity factors for rectangular plate anchors in sand for different embedment ratios and (b) comparison of experimental and theoretical anchor capacity factors (Chow et al., 2018a). – Notation: *H* in the figure refers to the depth *Y* in the list of symbols of this thesis.

It is clear that the capacity factors (usually defined in the literature as $N_\gamma = F_u/(A_p\,\gamma'\,Y)$ for sands, where F_u is the ultimate load, A_p is the plate loading area, γ' is the sand unit weight and Y is the embedment depth) increase with increasing embedment ratio, though the gain in capacity with depth is more significant when the anchor is loaded horizontally (both for vertically and horizontally-installed plates). Another remark is that, for horizontal anchors, the shear capacity is equal or slightly higher than the normal capacity, whereas for vertical anchors the normal capacity is significantly higher than the shear capacity. These experimental results also confirmed the findings of Rowe and Davis (1982a) that the normal capacity is higher for anchors installed vertically than for those installed horizontally. In contrast to plate anchors installed in clay, anchor capacity in sand is more affected by plate orientation, direction of loading and embedment ratio (Chow et al., 2018a).

Up to date, no experimental studies on the purely rotational capacity of plate anchors in clay have been found in the literature.

2.5.2.2. Unidirectional capacity in clay

Besides the publications on the capacity of plate anchors in sand mentioned in the previous section, numerous experimental studies on the capacity in clay have been carried out.

Das (1978, 1980) conducted extensive testing programmes on square and rectangular anchors installed horizontally at different depths and pulled out vertically. Rowe & Davis (1982b) also presented a comprehensive set of experimental data – including results from previous studies – for different shapes (circular and rectangular/strip) and orientations (vertical and horizontal) of anchors subjected to normal load. Initial anchor depth seemed to play an important role in the capacity. The test results showed that the capacity of shallow circular anchors was up to twice that of strip anchors, but the difference between their capacities decreased with increasing anchor depth. Similarly, anchor roughness increased the capacity of vertically installed shallow anchors, but no significant difference was observed for those horizontally installed. In many cases, the definition of the failure was given in terms of load at a certain displacement, as the anchor experienced high deformations before reaching failure (Rowe & Davis, 1982a, 1982b).

2.5.3. Three-dimensional loading

Certain types of plate anchors, including suction embedded plate anchors (SEPLA) and dynamically installed plate anchors (DEPLA) are often installed vertically. When load is applied to the padeye, the anchor rotates to an inclination approximately normal to the local chain orientation (Cassidy et al., 2012). This process of rotation during the application of an eccentric load is known as keying, and it is illustrated in Figure 2.18 for a generic anchor.

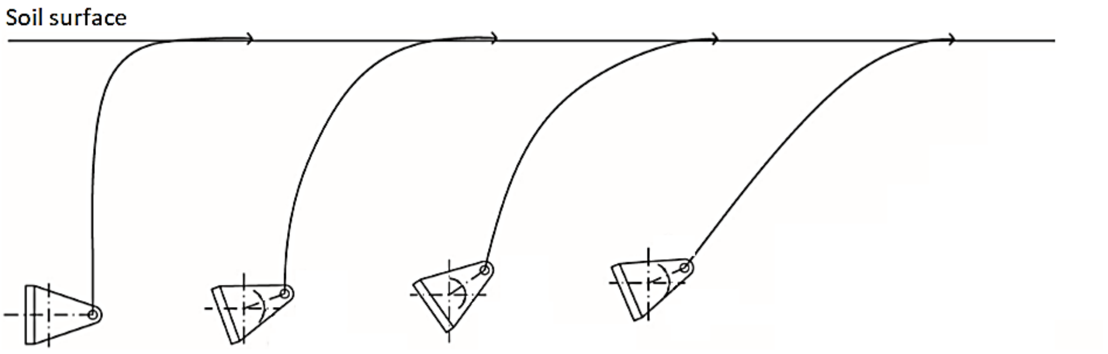

Figure 2.18 – Keying process of a vertically installed plate anchor (adapted from Chow et al., 2015).

Typical force-displacement behaviour of such anchors, illustrated in Figure 2.19 for square anchors installed in uniform clay (Song et al., 2006), usually involves an initial stiff behaviour followed by a softer response – or even a sort of ‘plateau’ – and a final stiff behaviour up to the peak load. After recovering the initial slack of the mooring line (which sometimes shows as an initial horizontal line with nearly zero load), the initial stage (1 and 1′ in Figure 2.19) usually corresponds to a stiff pre-keying mobilisation, during which the chain cuts through the soil. The following stage, the ‘plateau’ (2′ to 3′) is typical mainly for vertical load. This plateau is often not observed for inclined loading, as shown in the centrifuge test result for a load at 60° with the horizontal (Figure 2.19). From points 3 and 3′, full anchor rotation is mobilised, and the capacity quickly develops to the peak load.

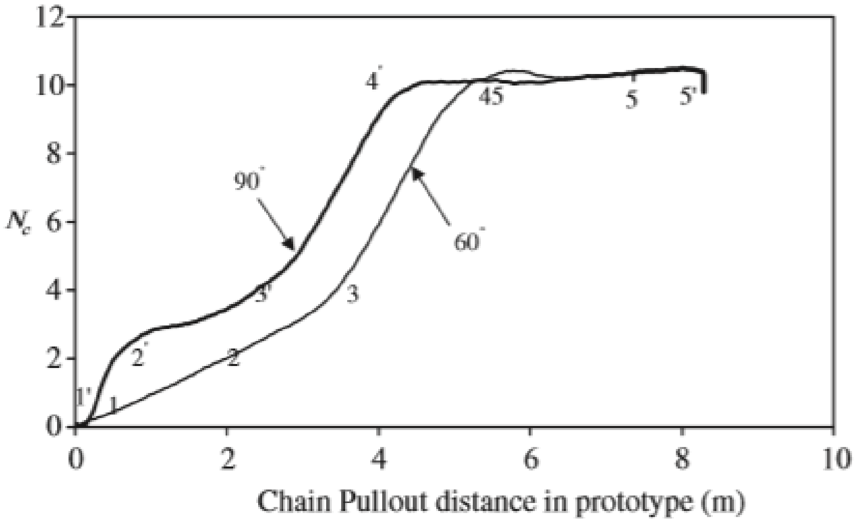

Figure 2.19 – Typical force-displacement curve for vertically-installed plate anchors (Song et al., 2006). – Notation: N_c in the figure refers to the bearing capacity factor of the anchor, given by F_u / (A_p s_u).

Similar behaviour was reported by O'Loughlin et al. (2014) who conducted centrifuge tests on DEPLA anchors of different shapes and installed in kaolin clay with different methods

(Figure 2.20). The same pattern was verified by Blake et al. (2015) in field tests conducted in DEPLA anchors for distinct reduced scales (Figure 2.21) after installation in soft clay.

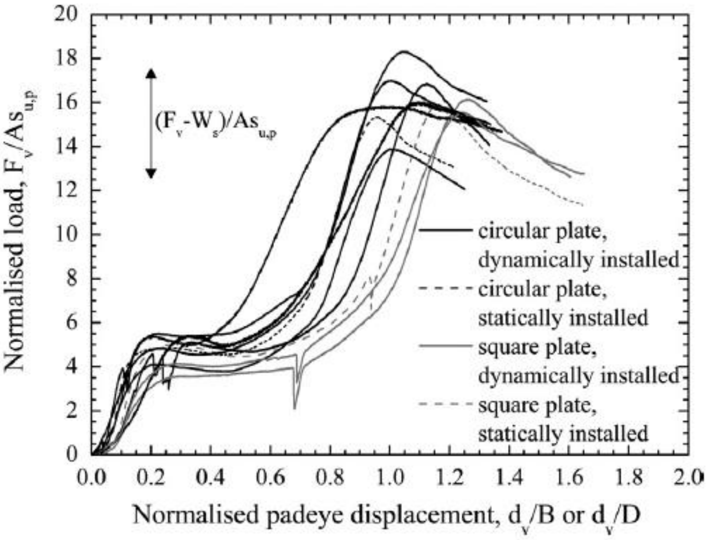

Figure 2.20 – Dimensionless load-displacement curves of DEPLA's with different shapes and installation methods (O'Loughlin et al., 2014). – Notation: F_v in the figure refers to the chain load T_a; A in the figure refers to the plate area A_p; and d_v in the figure refers to the padeye displacement d in the list of symbols of this thesis.

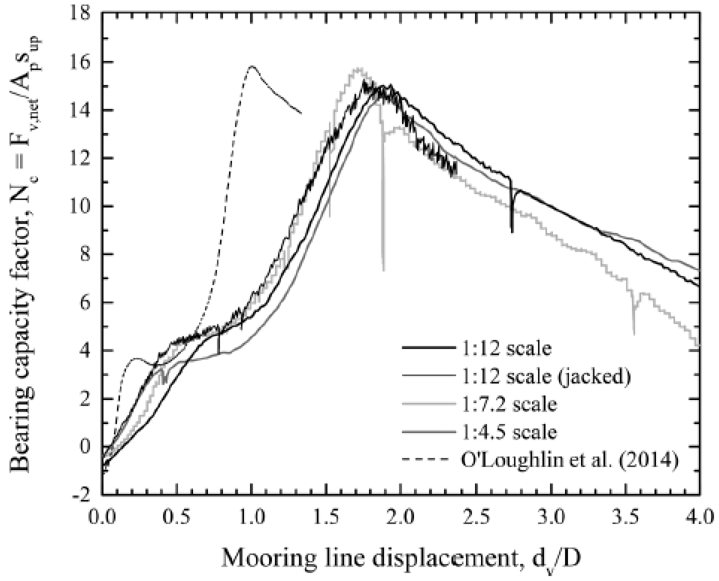

Figure 2.21 – Dimensionless load-displacement response of DEPLA's in clay for different reducing scales (Blake et al., 2015) – Notation: $F_{v,net}$ in the figure refers to the chain load T_a; A in the figure refers to the plate area A_p; and d_v in the figure refers to the padeye displacement d in the list of symbols of this thesis.

Since anchor rotation plays an important role in the mobilisation of anchor capacity, it is worth analysing the evolution of anchor rotation during loading. The rate of rotation is largely dependent on the padeye eccentricity e_n/B (where e_n is the normal eccentricity and B is the anchor breadth – see Figure 2.46), as shown through centrifuge tests conducted by

O'Loughlin et al. (2006) (Figure 2.22). For higher eccentricities (e_n/B = 0.5 and 1.0), full rotation up to an inclination approximately normal to the chain orientation is mobilised fairly quickly, as the moment load is high. For a much lower eccentricity (e_n/B = 0.17), the rate of rotation is much lower, as the anchor initially undergoes large displacement with minimal plate rotation (O'Loughlin et al., 2006).

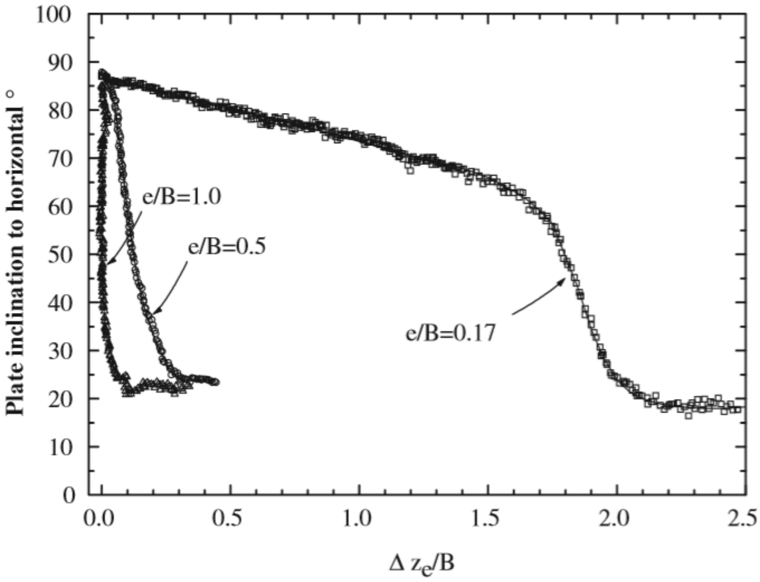

Figure 2.22 – Effect of padeye eccentricity on the rotation of a plate anchor (O'Loughlin et al., 2006) – Notation: e in the figure refers to e_n; and Δz_e in the figure refers to z in the list of symbols of this thesis.

The same behaviour was observed through centrifuge tests carried out by Gaudin et al. (2010), who showed that a SEPLA anchor with e_n/B=0.4 experienced a smaller rotation rate in comparison to an anchor with e_n/B=0.625.

The trajectory of plate anchors also play an important role, as one of the major concerns associated with offshore plate anchors is the loss of embedment during keying and the operational loading, which may result in an unrecoverable loss of capacity (Gaudin et al., 2006; Song et al., 2009; Yang et al., 2012). The trajectory of a SEPLA anchor during keying was assessed by Cassidy et al. (2012) through centrifuge PIV (Particle Image Velocimetry) tests in clay under inclined load (θ_0 = 40°). The results (Figure 2.23) showed that the anchor initially tends to move backwards (i.e. in the opposite direction of pulling) as a consequence of anchor rotation. However, after the initial rotation, relatively steady displacement in the direction of pulling is observed.

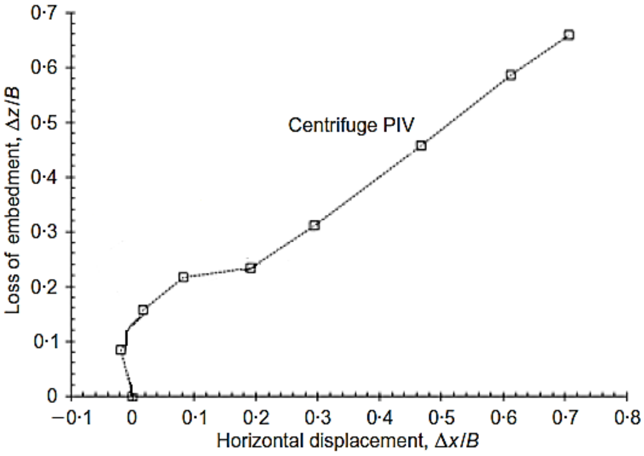

Figure 2.23 – Trajectory of SEPLA in clay assessed through PIV measurements in centrifuge test for e_p = - 0.492 m (adapted from: Cassidy et al., 2012).

The initial motion in the negative direction of x (away from the padeye position) was also observed by O'Loughlin & Barron (2012) for plate anchors in sand subjected to vertical pull (Figure 2.24). The researchers showed that after the initial rotation, the anchor's trajectory was relatively steady in the direction of pulling, confirming the behaviour previously shown by Cassidy et al. (2012).

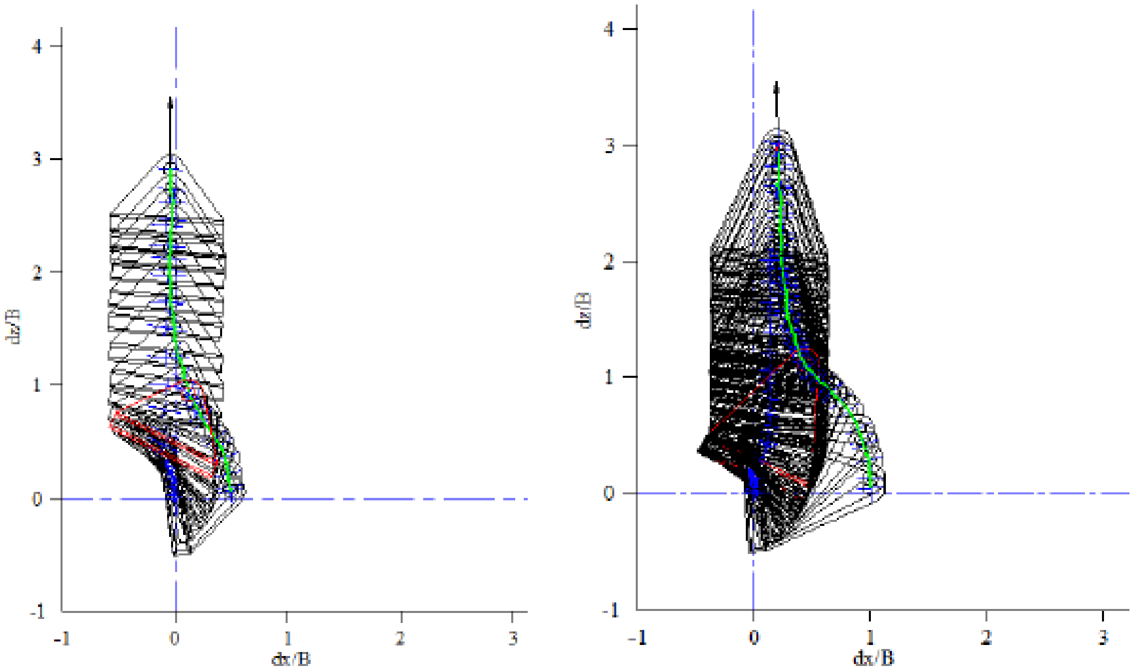

(a)

(b)

Figure 2.24 – Trajectory of the anchor subjected to vertical pull-out in sand: (a) e_n/B = 0.5 and (b) e_n/B = 1.0 (adapted from: O'Loughlin & Barron, 2012). – Notation: *dz* in the figure refers to the vertical displacement z; *dx* in the figure refers to the horizontal displacement x in the list of symbols of this thesis.

2.5.4. Cyclic behaviour of plate anchors

When installed offshore, plate anchors are subjected to long-term cyclic loading induced by wind and wave loads acting on the floating structure. In that context, understanding the behaviour of these anchoring systems under cyclic loading is essential.

Both beneficial (e.g. Chow et al. 2015, 2020) and detrimental (e.g. Andersen, 2015) effects of cyclic loading on soil strength and anchor capacity have been reported in the literature.

Chow et al. (2015) analysed the effect of cyclic loading on plate anchors installed vertically in dry dense sand. A series of centrifuge tests at an acceleration of 50g were carried out after initial installation of the anchor at 1g to an initial embedment of $5B$, as illustrated in Figure 2.25.

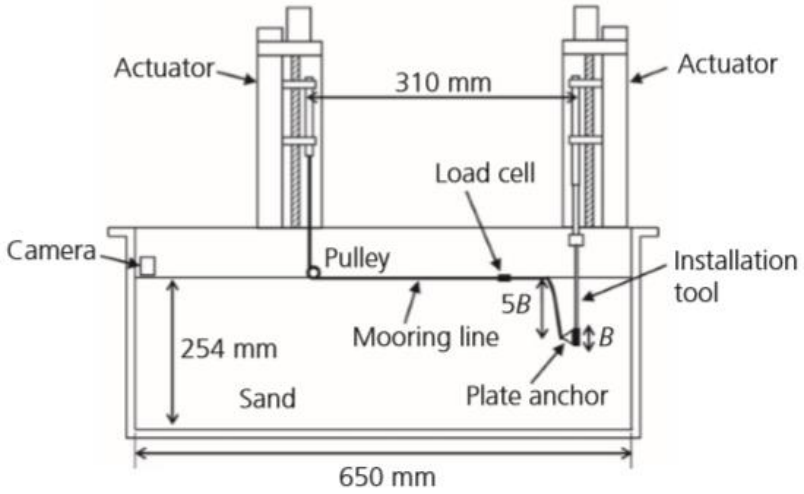

Figure 2.25 – Experimental set-up for the centrifuge tests (Chow et al., 2015)

The experimental results revealed that load-displacement and anchor rotation behaviour are similar under both monotonic and cyclic loading (Chow et al., 2015). However, it was shown that the ultimate capacity for cyclic loading may increase by 13% in comparison with the monotonic capacity, depending on the magnitude of the peak cyclic load. For cyclic loads with magnitudes close to or higher than the monotonic capacity, the soil is predominantly subjected to shear and the monotonic force-displacement curve bounds the curve from the cyclic tests. When the cyclic magnitude is lower, the cyclic load–displacement response overshot the response from the monotonic test. This effect was explained by the increase in stiffness (strength) due to sand densification effects outweighing shearing mechanisms observed near failure. The force-displacement and rotational behaviour of the plate anchor is shown in Figure 2.26.

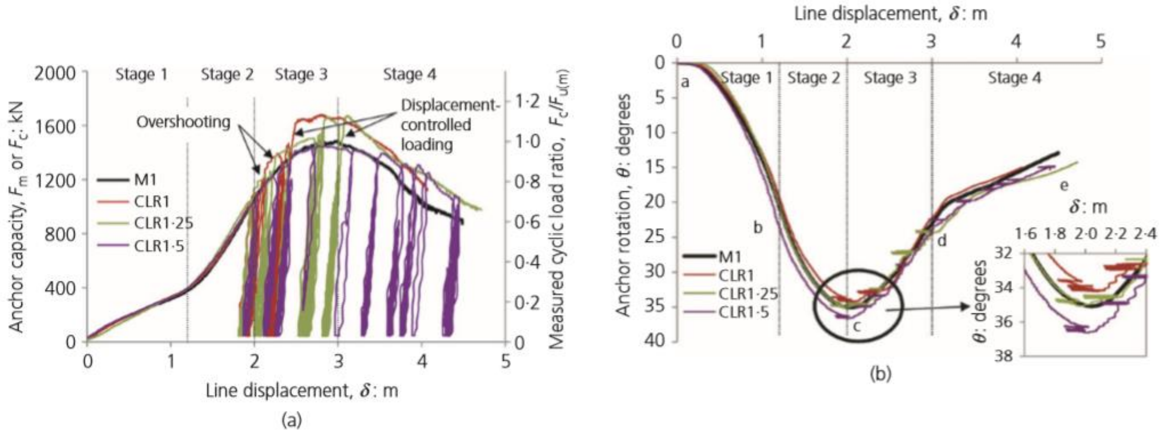

Figure 2.26 – Experimental results: (a) load-displacement; (b) rotation-displacement response (Chow et al., 2015) – Notation: F_m and F_c in the figure refers to the chain load T_a; δ in the figure refers to the chain displacement d; and θ in the figure refers to the anchor rotation β in the list of symbols of this thesis.

Similar experiments conducted by Chow et al. (2018b) with a blade-shaped anchor (as shown previously in Figure 2.8) in medium dense sand showed that the drained cyclic loading improves anchor capacity by up to 43% for both regular and irregular cyclic loading. Higher gains in capacity were observed for tests that involved lower magnitudes of cyclic loading. The force-displacement and rotation curves for monotonic and irregular cyclic loading can be visualised in Figure 2.27.

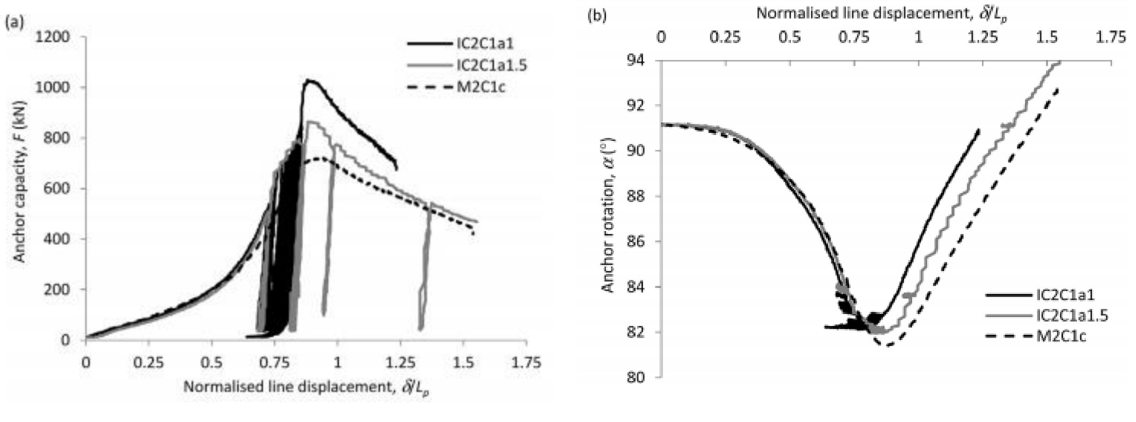

Figure 2.27 – Experimental results: (a) load-displacement; (b) rotation-displacement response for a blade-like anchor (Chow et al., 2018b). – Notation: F in the figure refers to the chain load T_a; δ in the figure refers to the chain displacement d; and L_p in the figure refers to the anchor length L in the list of symbols of this thesis.

Both studies presented above were carried out in sands with a velocity of pull that produced an expected drained response. The effects of partially-drained cyclic loading was not analysed (Chow et al., 2018b), and soil consolidation was assumed to be negligible. The consolidation-dependent behaviour of anchors is explored in the following section.

2.5.5. Consolidation-dependent behaviour of embedded structures

The detrimental effect of cyclic loading on soil strength has been widely reported by Andersen's studies. Andersen (2015) reported an extensive database of element tests (mainly DSS and cyclic triaxial tests) in cohesive soils, notably Drammen clay. The weakening of the soil strength during these cyclic tests was found to be mainly related to pore water pressure generation. Therefore, understanding the evolution of pore pressure and consolidation during not only cyclic loading but also due to partial drainage effects is essential for the assessment of the long-term response of plate anchors. In this section, previous literature on consolidation effects on plate anchors but also on other embedded structures is presented.

2.5.5.1. Consolidation-dependent of plate anchors

Yu et al. (2015) and Singh & Ramaswamy (2008) found that the vertical post-cyclic capacity of horizontal anchors in clay was lower than the monotonic capacity, but the capacity reduction was less pronounced for lower loading frequencies. Ponniah and Finlay (1988) demonstrated that long periods of unload after long-term cycles increased the anchor capacity during recycling.

Blake et al. (2011) analysed the effect of different periods of consolidation after keying (i.e. after the ' keying plateau' in force-displacement curves) through centrifuge tests in square anchors embedded in kaolin clay, as shown in Figure 2.28. After the consolidation period, the anchor was loaded up to peak load. The tests showed that the short-term capacity (i.e. without any consolidation time allowed) is about 75% of the long-term capacity (i.e. after a consolidation period of 2.7 days, equivalent to 75 years in prototype scale). This ratio between short-term and long-term capacities is considerably higher than corresponding values for piles and suction caissons (25-45%) and for torpedo anchors (6%) as reported in previous studies (Esrig et al. 1977, Chen & Randolph, 2007, Richardson et al. 2009).

Studies by Chow et al. (2020) demonstrated that the loading capacity of vertical plate anchors in sand is dependent on the rate of loading owing to the consolidation taking place during the loading process. With an experimental set-up similar to the presented in Figure 2.25, several centrifuge tests were carried out at varying loading rates in sand, under both monotonic and cyclic loading. For a low rate of pull, the capacity was approximately 440 kPa (Figure 2.29a). When the same test was performed with a much faster rate of pull, the capacity increased to values higher than 1200 kPa. This can be explained by the different levels of drainage between tests, as shown in the pore pressure profiles presented in Figure 2.29b. For a non-dimensional velocity $V^* = vd/c_v = 1349$, dilation-induced suction (negative pore pressure) was generated, increasing the soil strength and hence the anchor capacity. For a near-zero non-dimensional velocity $V^* = 0.02$, instead, most of the excess pore pressure generated was dissipated during loading, leading to insignificant changes in soil strength.

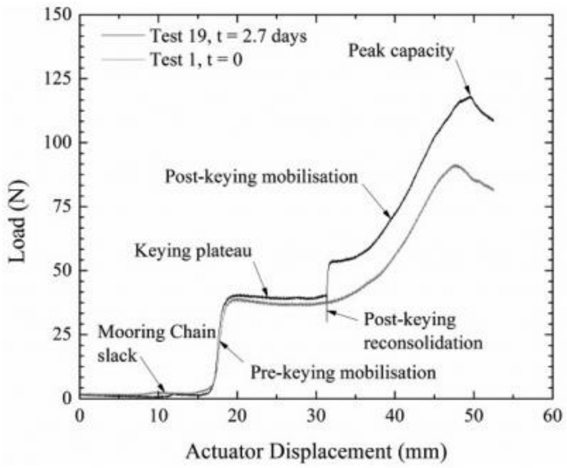

Figure 2.28 – Effect of consolidation on the force-displacement response of a square plate anchor in clay (Blake et al., 2011).

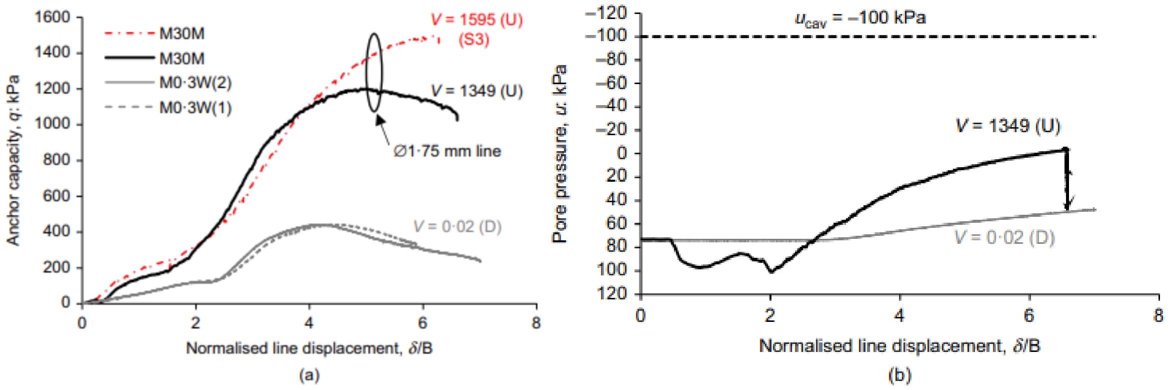

Figure 2.29 – Monotonic results for centrifuge tests: (a) load– displacement; (b) pore pressure profiles; (Chow et al., 2020). – Notation: δ in the figure refers to the chain displacement d in the list of symbols of this thesis.

Further tests with the same anchor geometry and experimental set-up, but with methocel instead of water (to increase the viscosity of the pore fluid and to control the consolidation conditions), confirmed the much higher capacities for higher non-dimensional velocities induced by different degrees of consolidation (Figure 2.30).

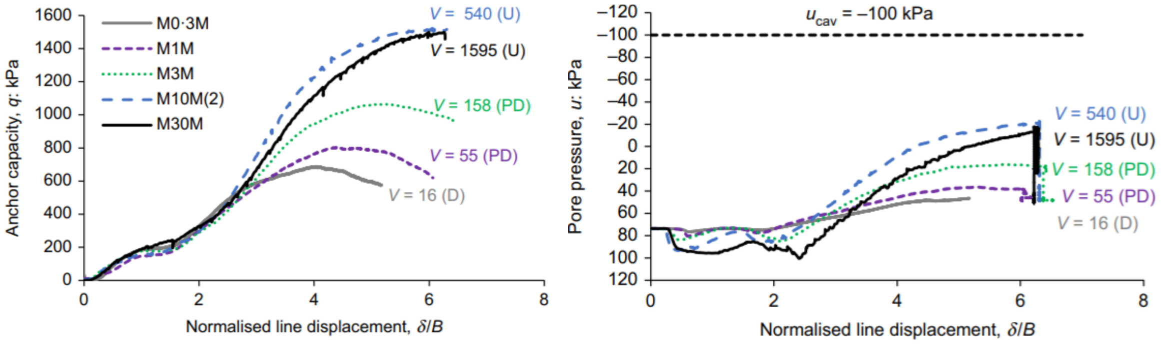

(a) (b)

Figure 2.30 – Monotonic results for centrifuge tests: (a) load–displacement; (b) pore pressure profiles (Chow et al., 2020). – Notation: δ in the figure refers to the chain displacement d in the list of symbols of this thesis.

The same study by Chow et al. (2020) investigated the effect of soil drainage on the cyclic behaviour of plate anchors. Both drained (in black/grey) and undrained (in blue) tests showed similar increase in capacity of 33% and 27%, respectively (Figure 2.31a). In the tentatively drained test, a small excess pore pressure generation was observed during cyclic loading, but this was dissipated before the final monotonic loading stage after cyclic loading (Figure 2.31b). The post-cyclic pore pressure profile was similar for both monotonic and cyclic drained tests. For the undrained tests, significant excess pore pressure was generated during cyclic loading, and during the post-cyclic monotonic stage, the negative excess pore pressure exceeded the monotonic pore pressure. This led to the higher post-cyclic capacity in the undrained cyclic test in comparison with the undrained monotonic test.

Further studies on the effect of cyclic loading and consolidation were also conducted by Zhou et al. (2020) with vertical plate anchors in calcareous silt subjected to horizontal load. Four centrifuge tests involving one or more episodes of cyclic and/or maintained loading were performed, as shown in Figure 2.32. All tests started with undrained monotonic loading up to a steady anchor resistance. During Test 1, maintained load was applied for 3 hours after the initial monotonic load, allowing at least 95% of the excess pore pressure to dissipate, followed by a final monotonic stage. A gain in anchor capacity of 51% was observed for the final monotonic stage in comparison with the initial pull-out. Test 2 involved the application of 1080 cycles of load varying between 25 and 75% of the initial steady resistance, followed by a final monotonic load. The gain in capacity was 50% compared to the initial resistance previous to the cyclic loading. Tests 3 and 4 applied one and five episodes, respectively, of maintained load and cyclic load, followed by a final stage of monotonic load. Gains in capacity of 90 and 150% were observed, respectively.

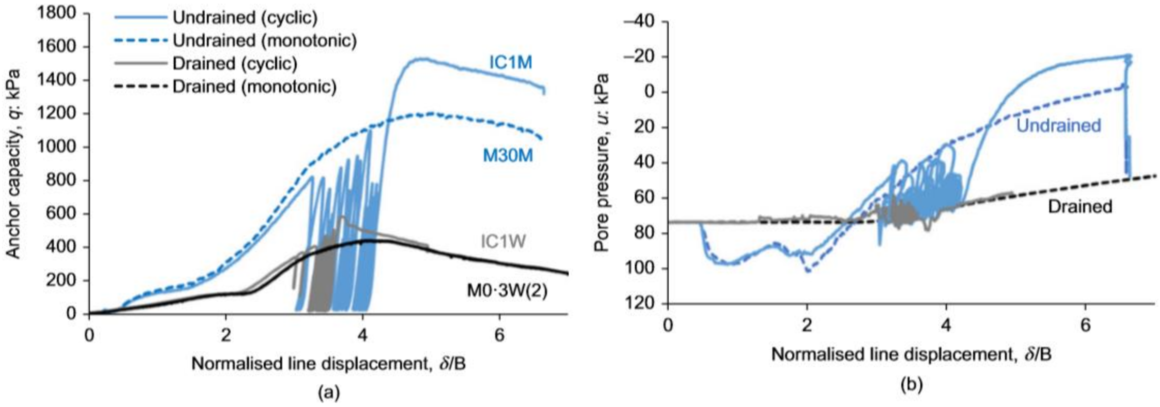

Figure 2.31 – Effect of consolidation on plate anchor cyclic behaviour: (a) force-displacement; (b) pore water pressure (Chow et al. 2019). – Notation: δ in the figure refers to the chain displacement d in the list of symbols of this thesis.

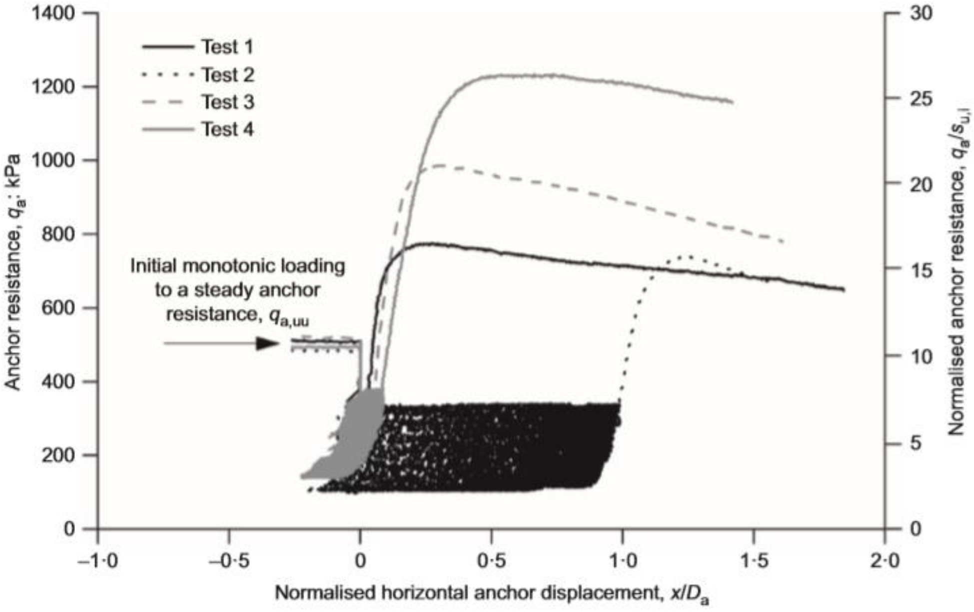

Figure 2.32 – Anchor capacity for centrifuge tests involving cyclic and maintained loading (Zhou et al., 2020).

The tests carried out by Zhou et al. (2020) demonstrated that, although the effective stress initially reduced due to positive excess pore pressure generation, after 35 cycles the effective stress increased due to excess pore pressure dissipation outweighing pore pressure generation. Therefore, the gain in capacity was attributed solely to the increase in soil effective stress due to excess pore pressure dissipation (i.e. soil consolidation). A theoretical framework proposed in the same study will be presented in section 2.6.3.

The effect of the rate of loading on the anchor capacity can be visualised in the 'backbone curve' framework, with has been reported for several applications, such as shallow foundations (Finnie & Randolph, 1994), pipeline upheaval buckling (Bransby & Ireland, 2009) and cone penetration (Suzuki & Lehane, 2015). The backbone curve framework can capture the evolution of soil strength (and consequently of anchor capacity) as the soil behaviour transitions from drained to undrained with increasing non-dimensional velocity. For dilatant soils, anchor capacity increases with increasing velocity due to negative excess pore pressure generation, while in contractive soils anchor capacity decreases with increasing velocity as positive excess pore pressure is generated (Chow et al., 2020) up to a point before viscous effects under undrained conditions take place. The backbone curve applied for plate anchor capacity in sand is shown in Figure 2.33.

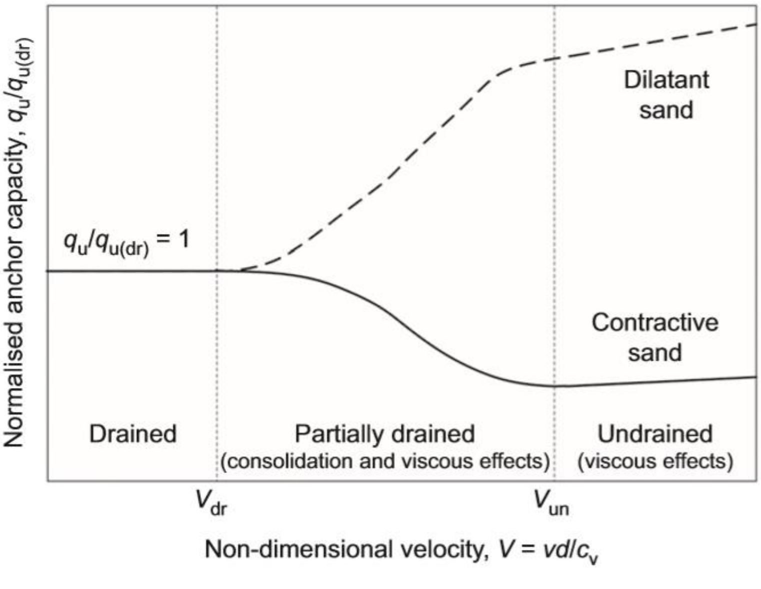

Figure 2.33 – Back-bone curve – interpretation framework for loading rate effects (Chow et al., 2020) – Notation: *V* in the figure refers to the normalised velocity *V** in the list of symbols of this thesis; *d* in the figure is the diameter of an equivalent circle with the same projected area of the anchor.

The backbone framework may also include viscous effects, as in Figure 2.34, which shows the effect of strain rate in triaxial tests in kaolin clay. The right-hand-side part of the curve shows an increase in deviatoric stress (*q* in the notation of the original publication) with increasing normalised velocity (*V* in the notation of the original publication) due to viscous effects, where the soil strength increases with strain rate in undrained conditions. It should be emphasised that viscous effects, where strength changes with velocity under undrained conditions, should be differentiated from drainage effects, where the change in strength occurs due to partially drained conditions (Robinson, 2019).

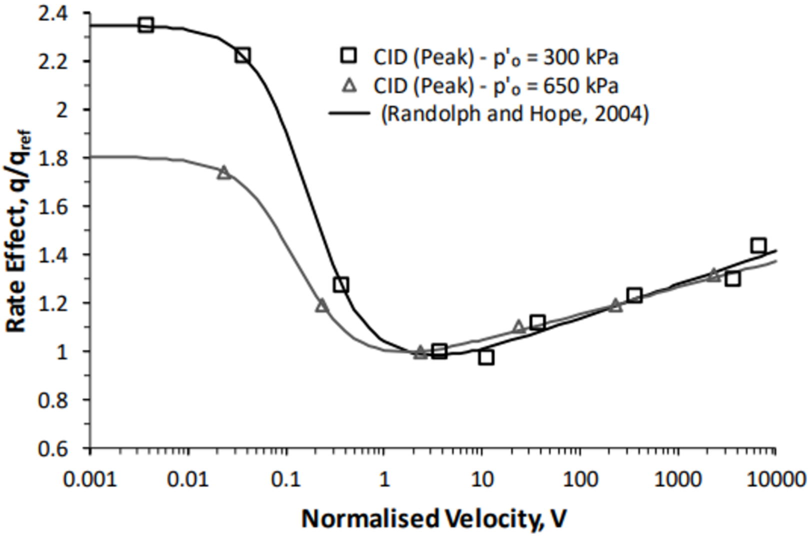

Figure 2.34 – Back-bone curve – interpretation framework for loading rate effects in triaxial tests in kaolin clay, including viscous effects (adapted from Robinson, 2019) – Notation: *q* in the figure is the deviatoric stress in the triaxial test; and *V* in the figure refers to the normalised velocity V^* in the list of symbols of this thesis.

Even though the studies in this subsection provided relevant insights on the consolidation-dependent behaviour of plate anchors, most of them were based on experimental results, with only one modelling proposed (Zhou et al., 2020) to account for such effects, as shown in 2.6.3. In Chapters 4 to 6, a new framework accounting for changes in pore water pressure during long-term operations will be proposed and compared with experimental results.

2.5.5.2. Consolidation-dependent behaviour of other embedded structures

Significant work on loading rate effects has also been done on cable and pipeline ploughing. Lauder et al. (2012), for example, analysed the variation of tow force with velocity in sands with different relative densities (from very loose to dense). The results were presented in a format similar to the backbone curve, but including an additional term to the normalised velocity [Δ*e*/(1+*e*)] (where *e* is the in situ void ratio and Δ*e* is the change in void ratio from the in situ value to that of the critical state) to account for volume changes due to dilation, as shown in Figure 2.35. The different format allowed results for different relative densities, plough depths and soil types to be grouped together in one curve. Previously, Palmer (1999) had also shown that the rate effects in sands and silts during ploughing could be described through a relationship between force *F* and normalised velocity including changes in volume $vD^3[\Delta e/(1+e)]/k$, where (in the notation of the original publication) *D* is the plough's depth, *k* is the soil permeability and *v* is the plough's velocity.

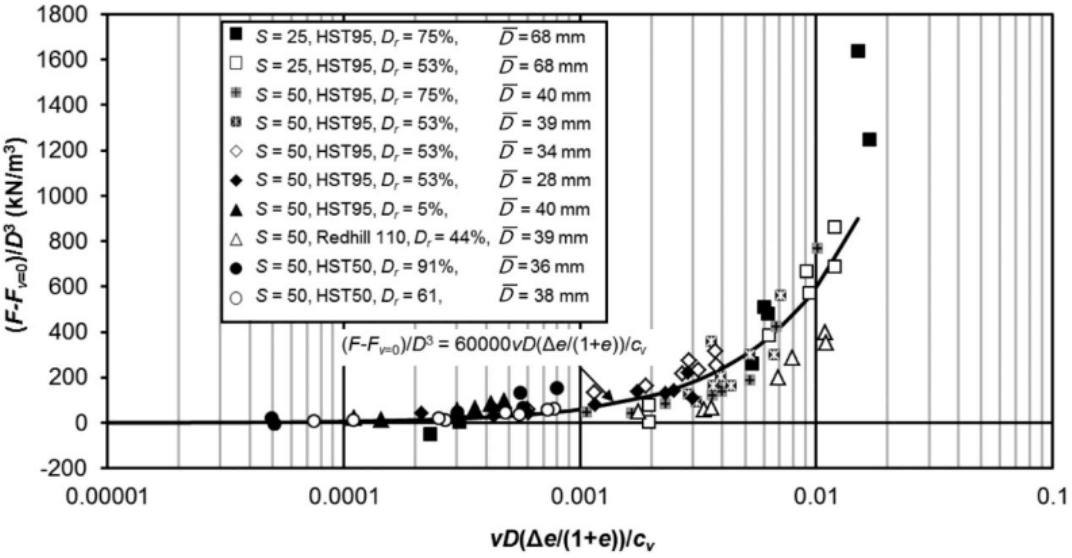

Figure 2.35 – Interpretation framework for tow force variation with velocity accounting for dilation effects (Lauder et al., 2012) – Notation: *F* and $F_{v=0}$ in the figure are the tow forces for a given velocity and for $v = 0$, respectively; and *D* in the figure refers to the embedment depth *Y* in the list of symbols of this thesis.

Another form of accounting for rate effects is through a factor that quantifies the variation of strength per log cycle due to (strain or displacement) rate effects. In Robinson (2019), for example, the effect of several clay parameter, such as liquid limit, plasticity index, slope of critical state line and percentage of certain minerals, on the increase in shear strength per log cycle was analysed for different clay types. The results of the dependency of the rate effect factor ($\lambda_{\varepsilon q=1\%}$) on the liquidity index (LI) of three clays, for example, is shown in Figure 2.36. A rate effect factor $\lambda_{\varepsilon q=1\%}$ of 0.12 represents an increase of 12% in shear strength per log cycle for a deviatoric strain of 1%.

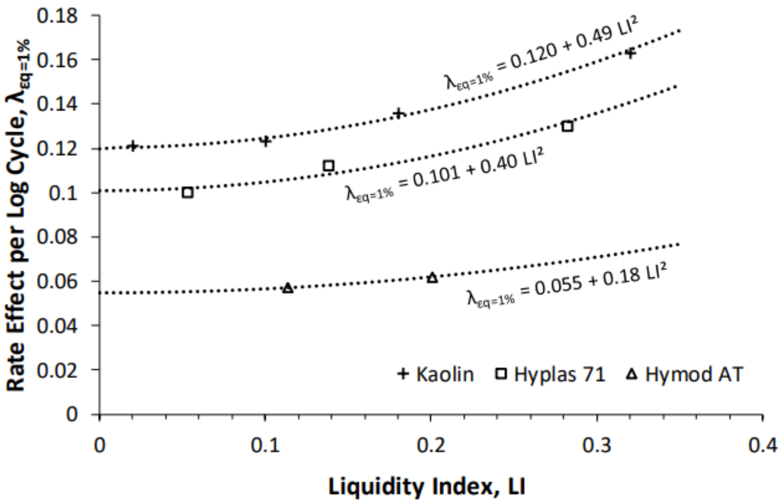

Figure 2.36 – Interpretation framework for increase in shear strength per log cycle for triaxial tests in clay (Robinson, 2019).

The studies of Lauder et al. (2012) and Robinson (2019), although not developed for plate anchors, can provide insights on how to determine representative values of normalised velocities for drained, undrained and partially drained behaviour from element or 1**g** tests (which is out of the scope of this thesis). As will be shown in Chapter 6 (section 6.4.3.6), these values can vary significantly among studies and depending on the application.

In this thesis, the effects of loading rate on anchor capacity are presented within the backbone curve framework, as in Chapter 6 the results from the proposed model are compared with experimental results presented in a similar way to that in Figure 2.33.

2.6. Modelling of anchors

Although experimental investigations in geotechnical engineering are very valuable and usually effective in giving insights into soil and structure behaviour, extended assessments of embedded plate anchors with different geometries and under different soil conditions can be time consuming. Furthermore, challenges with respect to sample preparation and consistency between experiments are often encountered. In that context, modelling techniques have been employed to assess plate anchor behaviour, notably finite-element (FE) modelling and, more recently, macro-element modelling.

This section will present a summary of the main studies involving FE and macro-element modelling on plate anchors, including the main findings and challenges with both approaches.

2.6.1. Finite-element (FE) modelling

2.6.1.1. *Unidirectional capacities in clay*

Several FE studies on plate anchors were conducted over the last decades, mainly since the 1980s, though not all of them were focused on offshore applications. Most FE studies presented charts for the normal capacity of plate anchors for different embedment ratios and soil properties. The first rigorous numerical studies on plate anchors in clay were carried out by Rowe and Davis (1982a), which also presented experimental results (see section 2.5.2), mainly for strip but also for axisymmetric conditions. The analyses employed an elastoplastic FE analysis incorporating either immediate breakaway or no breakaway (fully-bonded model) between the soil and the structure. The effects of anchor roughness and thickness were also considered.

More recently, Merifield et al. (2001) employed a numerical limit analysis to provide upper and lower bound solutions the undrained stability of vertical and horizontal strip anchors in clay. The model used a rigid perfectly plastic clay model with a Tresca yield criterion. Diagrams in the form of a break-out factor N_{c0} (Equation (2.2) versus embedment ratio were presented and compared with previous experimental results for horizontal and vertical anchors subjected to vertical pull, as presented in Figure 2.37. In the same study, Merifield et al. (2001) analysed the effect of overburden pressure and the transition from shallow to deep anchor behaviour.

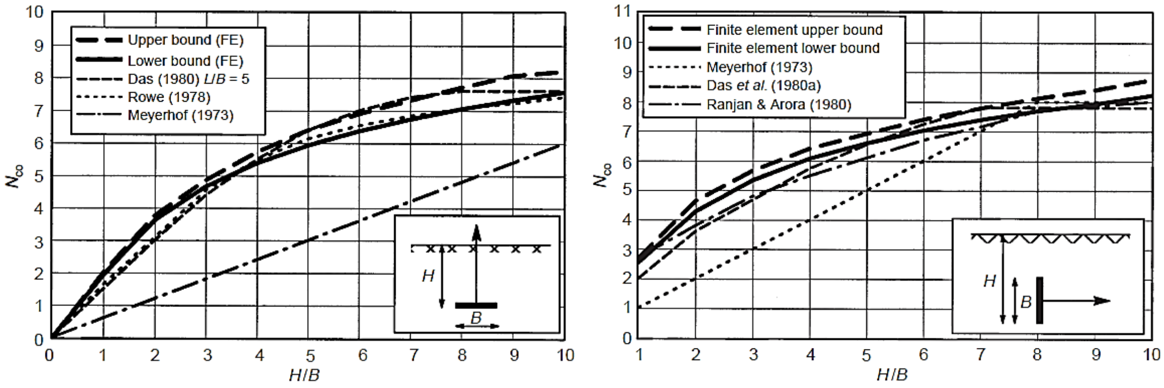

(a) (b)

Figure 2.37 – Comparison of breakout factors for (a) horizontal and (b) vertical plate anchors in homogeneous clay with: existing experimental results (Merifield et al., 2001). – Notation: *H* in the figure refers to the embedment depth *Y* in the list of symbols of this thesis.

$$N_{co} = \frac{q_u - \gamma' Y}{s_u} \tag{2.2}$$

Further studies by Merifield et al. (2003) used three-dimensional numerical limit analysis to assess the effect of anchor shape (circular, square, and rectangular) on the pull-out capacity of horizontal anchors. The effect of anchor roughness was found to be negligible for all anchor shapes, as opposed to Rowe and Davis (1982a) who showed that anchor roughness can increase the capacity of vertical anchor plates up to a certain embedment ratio. A procedure for calculation of uplift capacity was suggested and an example of application was presented. It was found that the break-out factors were higher for square, circular, and rectangular anchors were higher than those for strip anchors, but rectangular plates with embedment ratios $L/B > 10$ can be considered as strip anchors.

Aghazadeh Ardebili et al. (2012) conducted PLAXIS analysis in saturated clay to compare different soil models: Mohr-Coulomb, Modified Cam Clay and Soft Soil (Brinkgreve, 2021). The numerical analyses involved the vertical pull of horizontal plates under plane-strain and axisymmetric conditions. The type of analysis was undrained effective stress analysis using effective stress parameters. The results were compared to the lower-bound solutions by Merifield et al. (2003) and with existing experimental results. It was found that the Modified Cam Clay and Soft Soil models were in good agreement with each other and in better agreement with experimental results in comparison with Mohr-Coulomb, especially for the axisymmetric case.

Aubeny (2018) used a virtual work analysis to derive an upper-bound analytical solution for the case of a strip plate anchor of length L and thickness t_a deeply embedded in cohesive soils.

$$N_{nmax} = \frac{F_{nmax}}{s_u L} = 3\pi + 2 + \frac{2t_a}{L}\left(\alpha_a + \frac{(1+\alpha_a)}{\sqrt{2}}\right) \tag{2.3}$$

where the adhesion factor α_a is the ratio of adhesion at the soil-plate interface.

The sliding resistance factor N_{smax} proposed by Bransby & O'Neill (1999) for a strip anchor subjected to pure tangential loading follows the same upper bound approach as Equation

(2.3). The simplified solution following the assumption of an end bearing factor $N_e \approx 7.5$ (Murff et al., 2005) takes the form of Equation (2.4).

$$N_{smax} = \frac{F_{smax}}{s_u L} = 2\alpha_a + 2\,N_e \frac{t_a}{L} \approx 2\alpha_a + 15\frac{t_a}{L} \tag{2.4}$$

The slip mechanism for purely rotational loading on a strip plate anchor (Figure 2.38) can be given by the upper bound bearing factor N_{mmax} in Equation (2.5).

$$N_{mmax} = \frac{M_{max}}{s_u L^2} = \frac{\pi}{2}\left[1 + \left(\frac{t_a}{L}\right)^2\right] \tag{2.5}$$

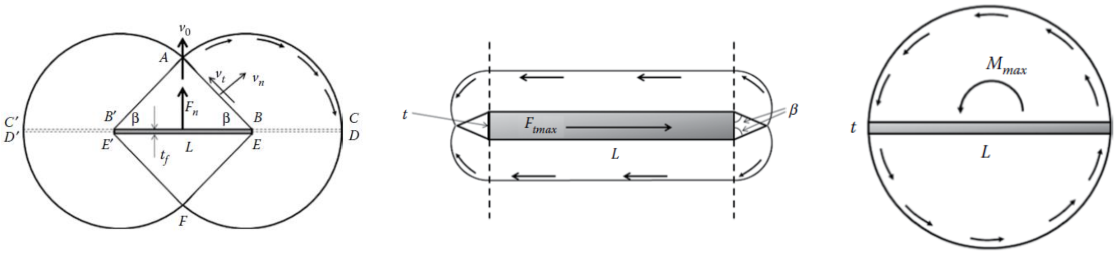

(a) (b) (c)

Figure 2.38 – Capacities for strip plate anchors in clay: (a) normal, (b) sliding and (c) rotational (Aubeny, 2018).

2.6.1.2. *Unidirectional capacities in sand*

Similarly to the studies on plate anchors in clay, Rowe and Davis (1982b) conducted numerical analyses on plate anchors in sand for a wide range of anchor geometries. The modified capacity factor $F_\gamma' = F_\gamma\, R_\psi\, R_R\, R_K$ incorporated correction factors for the effect of soil dilatancy (R_ψ), roughness (R_R) and initial stress state (R_K) to the basic capacity factor $F_\gamma = q_u/(\gamma' Y)$.

Furthermore, numerical analyses of strip (Merifield & Sloan, 2006) and circular, square, and rectangular (Merifield et al., 2006) anchors were also conducted in sands. The results are presented in the form of Terzaghi's break-out factor N_γ in Equation (2.6) for a wide range of embedment ratios Y/B and friction angles φ' and for both vertical and horizontal plates.

$$N_\gamma = \frac{q_u}{\gamma' Y} \tag{2.6}$$

The effect of anchor-soil roughness was found to be minimal on the calculated capacity for horizontal anchors but was found to significantly affect the results for vertical anchors. Changing from the interface from rough to smooth was shown to lead to a reduction of up to 67% in anchor capacity. Soil dilation was found to be significantly important to the anchor pull-out capacity, especially for vertical anchors.

From the three-dimensional analyses, Merifield et al. (2006) found that the capacities of both circular and square anchors are significantly higher than that of strip anchors, especially for medium to dense sands with friction angles greater than 30°, which is in agreement with Rowe and Davis (1982b). The effect of anchor shape was expressed in terms of the shape factor $S_f = N_{\gamma,circle}/\ N_{\gamma,square}$ (Figure 2.39)

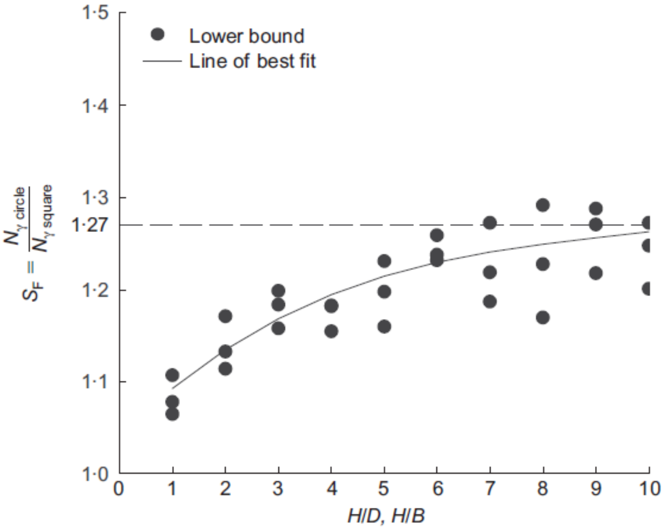

Figure 2.39 – Shape factors for square and circular plate anchors in sand (Merifield et al., 2006). – Notation: H in the figure refers to the embedment depth Y in the list of symbols of this thesis.

A transition in the trend of capacity factor with depth can be observed from shallow to deep anchors at around $Y/B = 4$ (Merifield et al., 2006). The difference is due to the different failure mechanism between shallow and deep anchors. For shallow anchors, the failure surface extends to the soil surface, as shown in Figure 2.40. In all studies to be conducted in Chapters 5 and 6, the mechanism is assumed to be that of a deep foundation, as the initial embedment of the anchors is large in all cases.

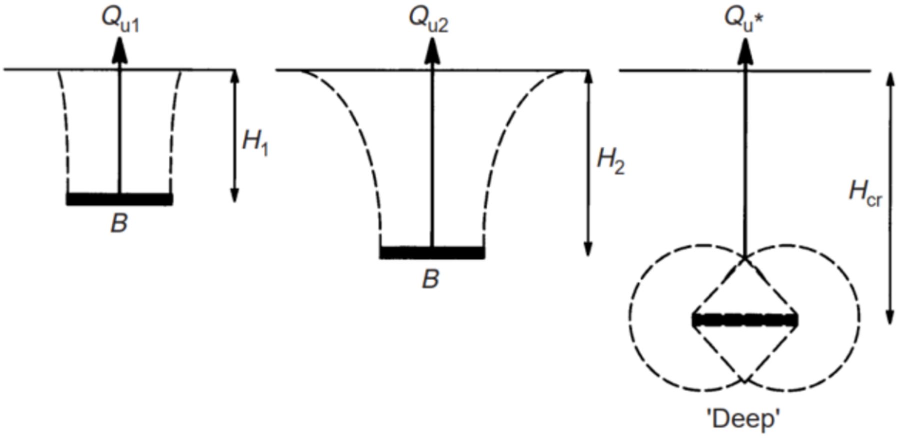

Figure 2.40 – Shallow and deep failure mechanisms (Merifield et al., 2001). – Notation: *H* in the figure refers to the embedment depth *Y* in the list of symbols of this thesis.

Recently, Cerfontaine et al. (2019) compared analytical solutions for anchor capacity with axisymmetric FE analyses using PLAXIS. The numerical simulations used a non-linear elasto-plastic constitutive model (hardening soil with small strain stiffness, also known as HS Small) to obtain the vertical capacity of circular plate anchors in Congleton sand. The results were similar for low embedment depths, but significant difference was observed for higher embedment ratios, as shown in Figure 2.41.

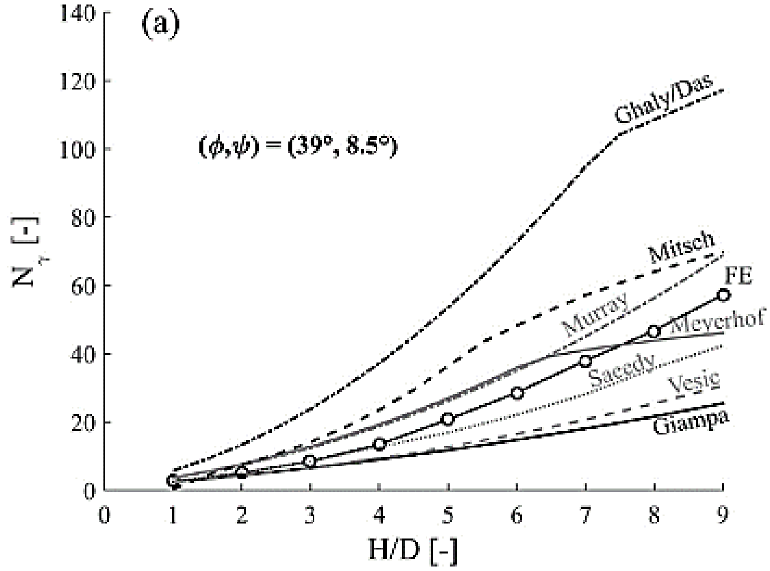

Figure 2.41 – Comparison of analytical criteria with numerical FE simulations in Congleton sand with relative density Dr = 50%. (Cerfontaine et al., 2019). – Notation: *H* in the figure refers to the embedment depth *Y* in the list of symbols of this thesis.

Whereas extensive data on the normal capacity of plates in sand can be found in the literature, little has been studied about the pure shear and rotational capacities in granular soils. Sarkar et al. (2018) conducted two-dimensional FE analyses in ABAQUS on horizontal strip anchors in sand subjected to pure vertical, horizontal and moment loads. Normal capacity factors ranged between 2 and 7 for embedment ratios of 1 and 8, respectively, and a friction angle of 35. For the same friction angle, the moment capacity was reported to be in the range of 1.5 to 4.5, therefore much lower than the vertical capacity, especially for high embedment ratios and high friction angles. The shear capacity was shown to be higher than the normal capacity for friction angles higher than 30.

2.6.1.3. Three-dimensional capacity of plate anchors

The response of plate anchors subjected to rotation, as reported previously in section 2.5.3, has also been assessed through FE modelling. The results from the FE analyses focused mainly on force-displacement, rotation and trajectory of the anchors. Due to the large deformations experience by these problems, the Remeshing and Interpolation Technique with Small Strains (RITSS) approach, originally proposed by Hu & Randolph (1998), was implemented by several researchers for the keying behaviour of plate anchors.

Song et al. (2009) used the RITSS technique to analyse plate anchor keying in normally consolidated clay and compared the numerical result with the previous centrifuge test by O'Loughlin et al. (2006). While the FE results for $e_n/B = 0.5$ and $e_n/B = 1.0$ agree well with the centrifuge test data, the final plate orientation in the tests only reached 20° rather than 0° in the FE simulation. This difference was attributed to the frictional resistance between the side walls of the container and the anchor (Song et al., 2009). The significant difference between FE and centrifuge data for $e_n/B = 0.17$ was attributed to the much higher effect of friction between the anchor end and Perspex panel. A similar difference in the final orientation between FE and centrifuge analysis was observed by Wang et al. (2011), who compared the numerical results with centrifuge data by Song et al. (2006). The difference of 10° in the final plate orientation was attributed to a misalignment between anchor padeye and pulley caused by the horizontal movement of the anchor during rotation.

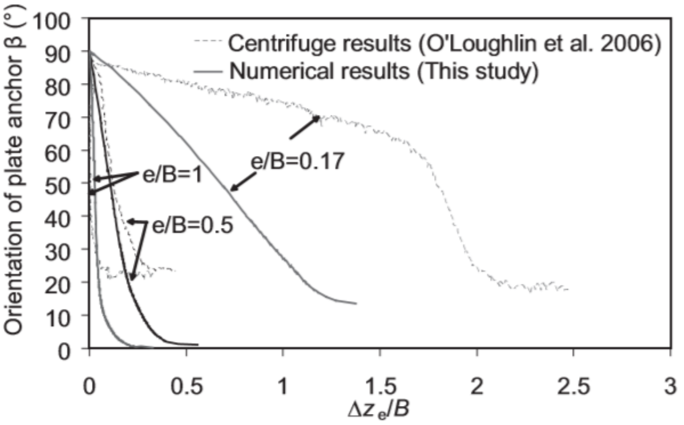

Figure 2.42 – Comparison between FE and centrifuge test results (Song et al., 2009).

The study by Song et al. (2009) also included centrifuge tests in transparent soil, aiming to avoid frictional effects. The results from the centrifuge tests with an anchor subjected to inclined load ($\theta_a = 60°$) were compared with FE analysis with and without the anchor shank. The FE result with the anchor shank agreed much better with the centrifuge tests result, which underlines the effect of differences in anchor geometry between numerical and experimental analyses.

The effect of the padeye offset e_p/B and padeye eccentricity e_n/B was analysed by Tian et al. (2015). The analyses identified two counteracting effects: the detrimental effect of change in anchor orientation (as the bearing area is reduced) and the beneficial effect of reduction in loss of embedment (as the anchor mobilises stronger soil). Higher peak capacities were observed for the cases with a higher eccentricity e_n and for higher offsets e_p. However, higher capacities came at cost of more loss of embedment. An optimised ratio between offset and eccentricity was found to be in the range of 0 to 0.2, but this varies according to the strength gradient with depth.

The effect of a full-length hinged flap attached to the rectangular anchor flukes was investigated by through centrifuge (e.g. Gaudin et al., 2010) and FE modelling (e.g. Wang et al., 2013; Tian et al., 2014). It was shown that the flap is only activated after the keying process has been completed, meaning it only rotates once the anchor motion is predominantly normal to the plate. The effect of a conventional keying flap in which the flap is allowed to rotate outward (Figure 2.43a) was shown to have no effect on the loss of embedment and resulted in a reduction of the anchor capacity, but a new design proposed by Tian et al. (2014), which allows the anchor to rotate inward (Figure 2.43b), was shown to reduce the loss of embedment and to increase the post-keying capacity of the anchor.


(a) (b)

Figure 2.43 – Keying flap designs: (a) flap rotates outward; (b) flap rotates inward (Tian et al., 2014).

2.6.2. Macro-element modelling of plate anchors

There are currently only two macro-element models to predict full three-dimensional behaviour of plate anchors under monotonic loading. The first one, named CASPA – Chain and SEPLA Plasticity Analysis (Cassidy et al., 2012) was originally developed for plate anchors in clays and is capable of predicting anchor behaviour during keying up to peak load. The second was developed by Yang et al. (2012) and, although similar to CASPA, accounts for the presence of a hinged flap on the plate anchor.

The CASPA model will be used as a starting point for the development of an improved macro-element model in Chapter 3. For this reason, the CASPA model will be presented here in detail.

The CASPA model has three basic features as follows:

1) A capacity surface (F) that represents the capacity of the anchor for different loading combinations (V – vertical loads, H – horizontal loads, M – moment loads);
2) A loading state – given by the current combination of loads – located always on the strength surface F;
3) The displacements w, u and β on a specific point depend on a vector that is normal to the strength surface (i.e. associated flow rule).

A simplified sketch presenting the geometric approach within which CASPA works is depicted in Figure 2.44. The sketch is presented in a two-dimensional space (*V*-*H*) to facilitate the understanding, whereas the actual model works in a three-dimensional space (*V*-*H*-*M*).

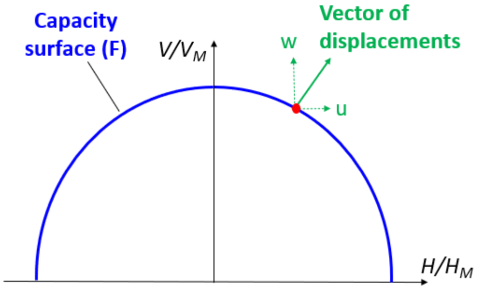

Figure 2.44 – Two-dimensional sketch representing the three basic features of CASPA.

CASPA is a purely plastic model with an associated plastic potential, meaning that the capacity surface controls the displacements through the aforementioned normal vector. Another important characteristic of CASPA is that it includes a chain solution (Neubecker & Randolph, 1995) that relates the angles θ_a (direction of chain load at the anchor padeye) to θ_0 (direction of chain load at the mudline) and provides the force T_a acting on the anchor, as shown in Figure 2.45.

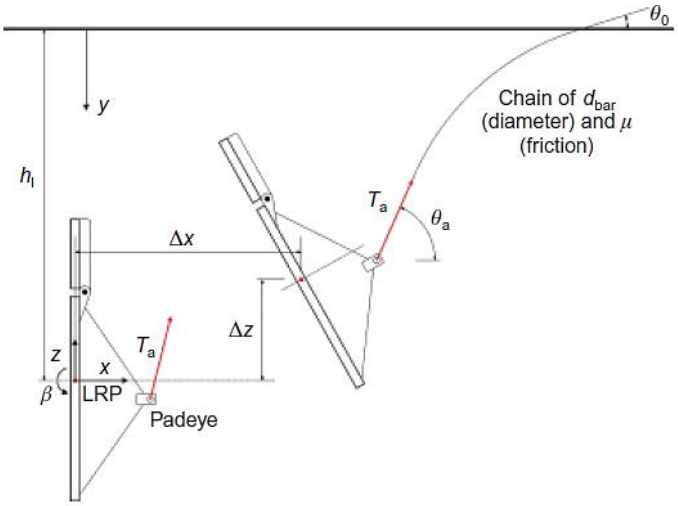

Figure 2.45 – Illustration of the angles θ_a and θ_0 related through the chain solution (Cassidy, et al., 2012).

The forces acting on the anchor are given by Equations (2.7) to (2.9) and depend on the force T_a acting on the anchor as well as the anchor orientations, weight and load eccentricities.

$$V = T_a \sin(\beta + \pi/2 - \theta_a) - W_a \sin\beta \tag{2.7}$$

$$H = T_a \cos(\beta + \pi/2 - \theta_a) - W_a \cos\beta \tag{2.8}$$

$$M = T_a[e_n \cos(\beta + \pi/2 - \theta_a) + e_p \sin(\beta + \pi/2 - \theta_a)] \tag{2.9}$$

where: e_n is the load eccentricity normal to fluke; e_p is the load eccentricity parallel to fluke; V is the force normal to the plate; H is the force parallel to the plate; M is the moment load; T_a is the chain load acting on the anchor; W_a is the submerged weight of the anchor; and β is the rotation of the anchor from the initial position.

The sign conventions and nomenclature used can be seen in Figure 2.46.

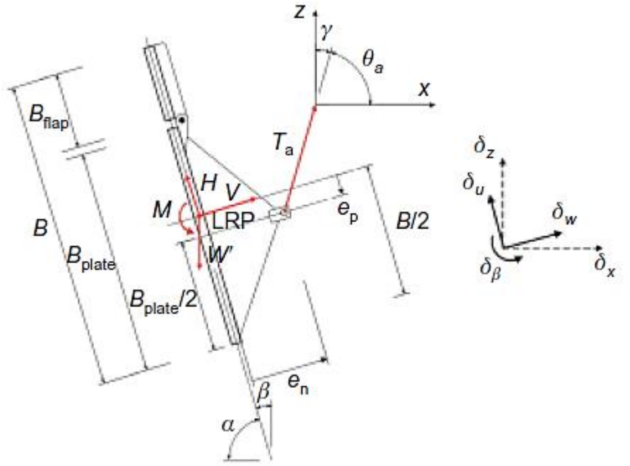

Figure 2.46 – Nomenclature and sign convention (Cassidy et al., 2012).

The capacity surface is represented by the function F, whose form is given by Equation (2.10).

$$F = \left(\frac{V}{V_M}\right)^q - 1 + \left[\left(\frac{|M|}{M_M}\right)^m + \left(\frac{|H|}{H_M}\right)^n\right]^{\frac{1}{p}} = 0 \tag{2.10}$$

where V_M, M_M and H_M are the normal, rotational and sliding capacity of the anchor when acting independently; and the exponents m, n, p and q define the shape of the three-dimensional surface.

The displacements w, u and β are given by Equation (2.11) and depend of a vector normal to the strength surface, which is given by the derivatives of the function F.

$$\begin{pmatrix} \delta w \\ \delta u \\ B\delta\beta \end{pmatrix} = \mu \begin{pmatrix} \partial F/\partial V \\ \partial F/\partial H \\ \partial F/\partial(M/B) \end{pmatrix} \tag{2.11}$$

where μ is the plastic multiplier given by Equation (2.12).

$$\mu = \frac{d_a}{\sqrt{\left[\frac{\partial F}{\partial V} + \frac{e_p}{B}\ sign(M)\frac{\partial F}{\partial(M/B)}\right]^2 + \left[sign(H)\frac{\partial F}{\partial H} + \frac{e_n}{B}\ sign(M)\frac{\partial F}{\partial(M/B)}\right]^2}} \tag{2.12}$$

where d_a represents the net displacement of the anchor padeye.

The chain solution proposed by Neubecker & Randolph (1995) is given by Equation (2.13).

$$\begin{aligned} & e^{\mu_c(\theta_a-\theta_0)}(\cos\theta_0 + \pi\sin\theta_a) - \cos\theta_a - \pi\sin\theta_a \\ & \qquad = E_n d_{bar} N_c\left(s_{u0}z_p + \frac{k_{su}{z_p}^2}{2}\right)\left(\frac{1+{\mu_c}^2}{T_a}\right) \end{aligned} \tag{2.13}$$

where d_{bar} is the diameter of the chain; E_n is a multiplier giving the effective chain width in the normal direction to the chain; N_c is the bearing capacity factor for the chain; z_p is the current vertical depth of the padeye; s_{u0} and k_{su} are the soil shear strength at the mudline and the rate of increase with depth; and μ_c is the friction of the chain.

Typical results from CASPA model include the anchor trajectory (vertical and horizontal displacements), anchor inclination and loads (vertical, horizontal, moment and chain load), as shown in Figure 2.47.

It can be observed that, for certain padeye offsets, CASPA predicted a re-embedment of the anchor at large displacements. Particularly for e_p = -0.492 m, CASPA results (Figure 2.47) showed a downwards vertical displacement, contrary to the centrifuge tests (Figure 2.23) that showed that the anchor moved upwards in the direction of pull. Cassidy et al. (2012) stated that the difference can be attributed to "quite subtle aspects of the yield envelope shape, resulting in a greater tendency for the anchor to fail in a sliding mode in the plasticity analysis" (p. 832) and that "the principle of a yield envelope and anchor motion dictated by an associated flow rule is one that has been validated in many different applications, such as shallow foundations and suction caissons, though all still for relatively small deformations" (p. 832-833). Furthermore, the authors affirm that the difference might also be due to inaccurate values of H_M obtained from LDFE analyses, as interface elements around the plate anchor were not incorporated. This also led to excessive backwards movements at the early stages of keying.

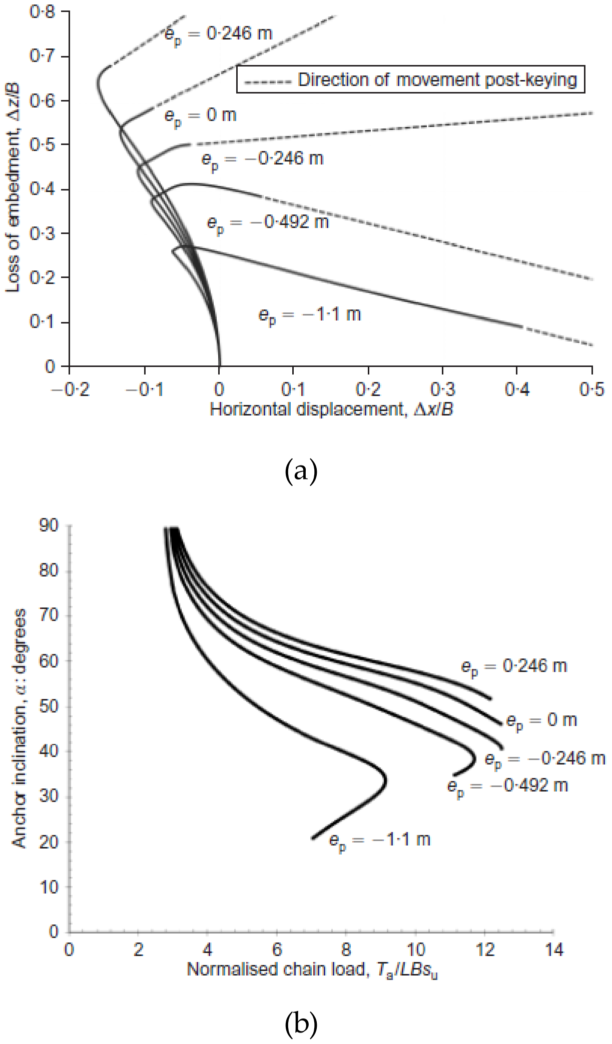

Figure 2.47 – (a) Anchor trajectory and (b) rotations for distinct load eccentricities and pull-out angle θ_o = 40° (Cassidy et al., 2012).

Similarly to CASPA, the macro-element model by Yang et al. (2012) employed a rigid plasticity approach with an associated plastic potential and a chain solution to predict load capacity and anchor trajectory, but accounting for the presence of a hinged flap. The presence of the flap resulted in reduced backward movement, slightly more embedment loss and higher ultimate capacity. The CASPA model will be further explored in Chapter 3, as the proposed model will start CASPA as a starting point for further developments.

2.6.3. Consolidation-dependent behaviour of anchors

Following the centrifuge tests previously presented in section 2.5.5 (Figure 2.32), Zhou et al. (2020) developed the first modelling framework for plate anchors that accounts for the evolution of soil strength dependent on pore water pressure generation and dissipation (i.e. consolidation). Based on critical state concepts and originally proposed by Zhou et al. (2019) for T-bar penetration tests and spudcan footing installation, the framework was employed to explain the changes in soil strength during the application of maintained and cyclic loads in the centrifuge tests. The changes in anchor capacity were assumed to occur solely due to changes in soil strength, as the failure mechanism had been previously shown to be minimally affected by it (Stanier & White, 2019). Through the new framework, it was shown that the excess pore pressure dissipation outweighs the pore pressure generation after a high number of cycles, leading to gains in normal effective stress and consequently in anchor capacity.

For one of the tests involving long-term cyclic loading, for example, the framework showed that, after 340 cycles, the effective stress path starts moving to the right, as the vertical effective stress increases due to pore pressure dissipation outweighing pore pressure generation.

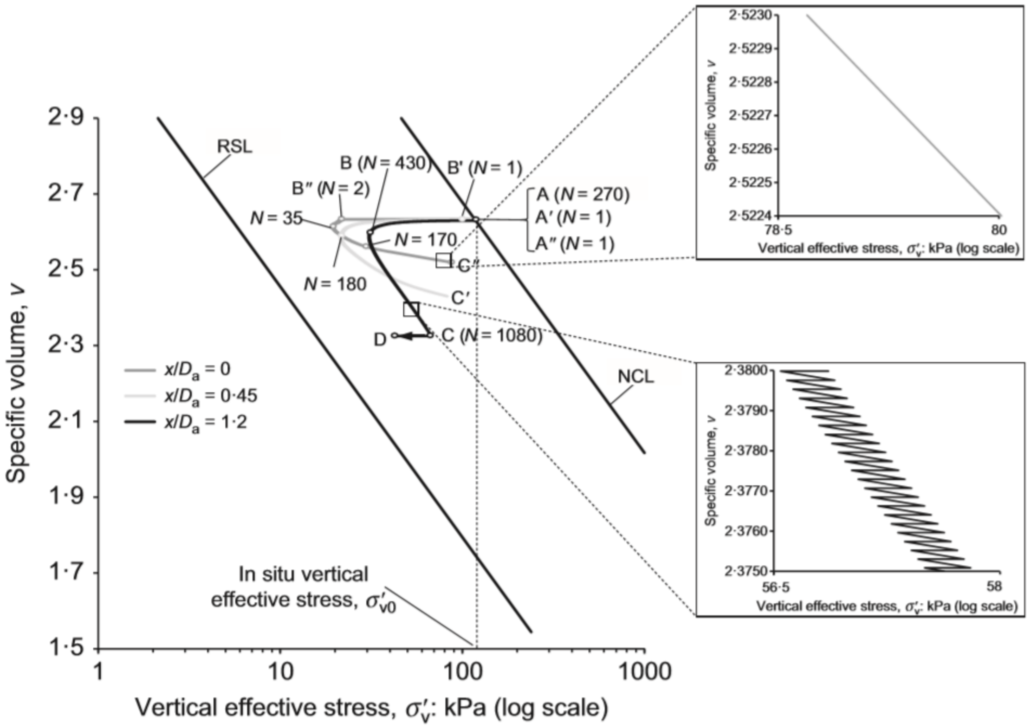

Figure 2.48 – Effective stress paths for the critical state framework proposed by Zhou et al. (2020).

Although the model proposed by Zhou et al. (2020) provided valuable insight on how pore pressure generation and dissipation control the evolution of soil strength during long-term cyclic loading, the model was developed for a testing scenario in which the anchor is subjected to loading whose direction perpendicular to the anchor plane. In this scenario, anchor rotation does not occur, and the anchor moves solely in one direction.

In that sense, a model that is able to consider both the evolution of soil strength and the kinematics of the anchor in loading scenarios that induce anchor rotation and displacements in different directions has not yet been developed.

2.7. Macro-element models for other geotechnical applications

The concept of macro-element model consists in condensing the response of a foundation and the surrounding soil to a force-displacement relation at seabed (Correia, 2011; Page et al., 2018). The macro-element method was originally based on the superelement concept employed by aerospace engineers in the 1960s. A superelement consisted of different structural members of an airplane which may have various shapes, material properties and boundary conditions (Wang et al., 2015). Within a geotechnical context, the macro-element concept originated from the work of Roscoe & Schofield (1957)[1] applied to the stability of free and tied peers subjected to overturning moments, but the development of macro-elements dedicated for integrated structural analysis further advanced mainly in the 1990s (Page et al., 2018).

The first macro-element developments focused on flat footings subjected to combined vertical, horizontal and moment loading or with load eccentricity (Figure 2.49), but further applications also included models for spudcans and, more recently, bucket foundations and monopiles.

---

[1] The statement attributed to Roscoe & Schofield (1957) is based on Page et al. (2018).

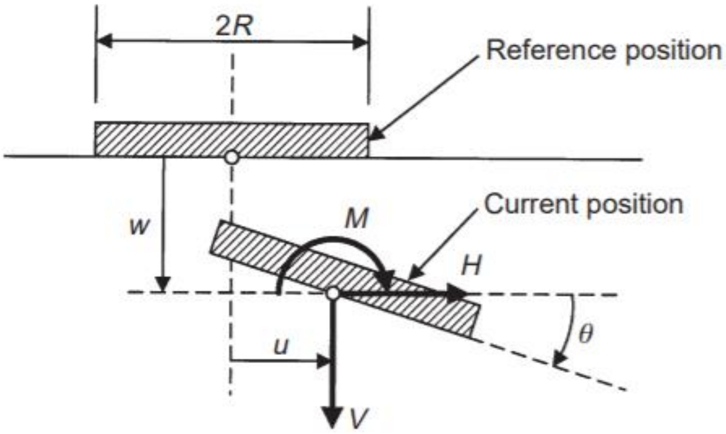

Figure 2.49 – Flat footing subjected to combined loading (Gottardi et al., 1999).

The main advantage of macro-element models over typical finite-element analyses is the time efficiency. While finite-element and finite-difference simulations are usually able to provide an accurate estimate of non-linear soil-structure interaction problems, its application may be heavy-handed and time consuming (Cremer et al., 2001; Muir Wood, 2004; Wang et al., 2015). For instance, each of the 14 large-deformation finite-element (LDFE) analyses for monotonic pull-out of anchors carried out by Tian et al. (2015) using ABAQUS took approximately 40 hours to complete. In that sense, macro-element modelling may be a practical and time-effective approach for non-linear geotechnical problems (Cremer et al., 2001; Muir Wood, 2004).

On the other hand, the simplicity of macro-element models may come at cost of poorer accuracy (Wang et al., 2015; Skau et al., 2018). For that reason, macro-element's use in design may be used either as a rapid 'order-of-magnitude' estimate or in combination with some finite-element and/or physical modelling (Muir Wood, 2004; Skau et al., 2018).

Most plasticity-based macro-element models have four basic components (Muir Wood, 2004; Martin & Houlsby, 2000):

- the elastic properties;
- a yield surface in the load space (usually *V-H-M*);
- a flow rule or plastic potential providing the magnitudes of the incremental plastic displacements;

- a plastic hardening rule defining the relationship between plastic displacements and the size of the yield surface.

2.7.1. Macro-element models for shallow foundations

Nova & Montrasio (1991) developed one of the first macro-element models for geotechnical application. The model was developed within a rigid plasticity framework and aimed to calculate settlements and rotations in rigid shallow foundations in loose sand. In this model, soil and foundation are assumed as a macro-element and their behaviour is evaluated under the combined action of vertical, horizontal and eccentric loads.

It included a strain-hardening function with a non-associated flow rule. The presence of a non-associated flow rule means that the displacements are given by a vector normal to a surface g (the plastic potential) rather than to the strength surface f as typical of models with associative flow rule.

The capacity surface accounted for the combination of vertical, horizontal and moment loads, as shown in Equation (2.14).

$$F = \left(\frac{H}{f_1\, V_{max}}\right)^2 + \left(\frac{M}{f_2\, B\, V_{max}}\right)^2 - \left(\frac{V}{V_{max}}\right)^2 \left[1 - \frac{V}{V_{max}}\right]^{2\beta} = 0 \qquad (2.14)$$

where f_1 is the soil-foundation friction coefficient, f_2 is a non-dimensional constitutive parameter and β is a shape factor of the capacity surface F.

An additional loading surface f depending on the displacement-hardening term ρ_c is introduced. The function ρ_c varies from 0 to 1 and increases with the displacement components w, u and β.

$$f = \left(\frac{H}{f_1\, V_{max}}\right)^2 + \left(\frac{M}{f_2\, B\, V_{max}}\right)^2 - \left(\frac{V}{V_{max}}\right)^2 \left[1 - \frac{{}^{V}\!/_{V_{max}}}{\rho_c}\right]^{2\beta} = 0 \qquad (2.15)$$

$$\rho_c = 1 - \exp\left\{-\frac{R_0}{V_M^2}\,[(w\, V_M)^2 + (a_1 u\, H_M)^2 + (a_1 B\, \beta\, M_M)^2]^{1/2}\right\} \qquad (2.16)$$

where a_1 and a_2 are non-dimensional constitutive parameters and R_0 is the initial stiffness of the load-displacement curve under centred vertical loading.

The plastic potential differs from the loading and capacity surfaces (non-associated plastic potential) and takes the form given by Equation (2.17).

$$g = \left(g_1 \frac{H}{f_1\, V_{max}}\right)^2 + \left(g_2 \frac{M}{f_2\, B\, V_{max}}\right)^2 - \left(\frac{V}{V_{max}}\right)^2 \left[1 - \frac{\frac{V}{V_{max}}}{\rho_g}\right]^{2\beta} = 0 \tag{2.17}$$

where g_1, g_2 and ρ_g are constitutive parameters. Basically, Equation (2.17) includes two more parameters (g_1 and g_2) that skews the size of the loading surface f in the H and M axes but maintains its original form. Since only the derivatives of g matter for obtaining the displacements, the numerical value of the parameter ρ_g is irrelevant.

The displacements are given by a vector normal to the plastic potential g and not to the loading surface f as in associative models. The vector $d\boldsymbol{q} = [dw, du, d\beta]^T$ of strain increments is defined in Equation (2.18). The terms w, u and β are the normal, tangential and rotational motion of the foundation, respectively.

$$d\boldsymbol{q} = \lambda \frac{\partial g}{\partial \boldsymbol{Q}} \tag{2.18}$$

where $\boldsymbol{Q}$ is a vector representing the loads (vertical – V, horizontal – H, and moment – M) and μ is the plastic multiplier.

Gottardi & Butterfield (1995) developed a similar model, based on load path experiments on surface footings in dense sand. The study improved the calibration of the shape of the yield surface and that of the plastic potential. Further studies by Gottardi et al. (1999) used displacement-paths to provide further insight into the shape of yield surfaces in macro-element models for planar footings. Even though experimental data from various sources suggested that a non-associated flow rule is required for the problem of planar footings (Gottardi & Butterfield, 1995), Gottardi et al. (1999) showed that an associated flow rule can be used in the H-M plane (i.e. for $V = 0$). Despite the different formulations for yield surfaces among models, all had a similar 'cigar-shaped' surface for combined loading (Figure 2.50).

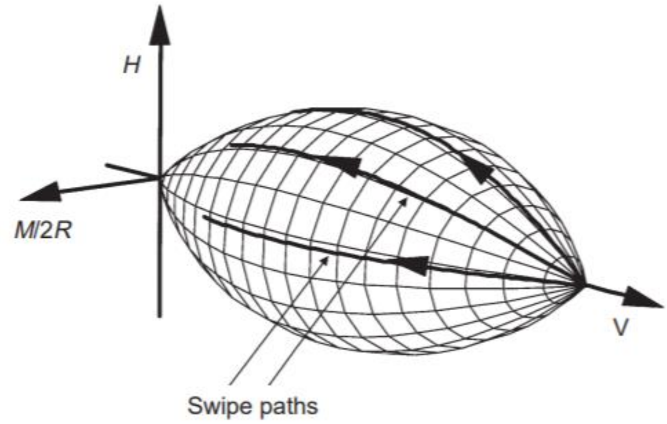

Figure 2.50 – 'Cigar-shaped' yield surface for combined loading (Gottardi et al., 1999).

The problem of shallow foundations subjected to vertical, horizontal and moment loads was also studied by Cremer et al. (2001). While all aforementioned models for sand were developed mainly for monotonic loading, Cremer et al. (2001) developed a macro-element model for foundations on cohesive soils and subjected to cyclic loading. The non-associative model also included consideration of the uplift of the foundation. Comparison with FE results showed good agreement in terms of overturning moment, uplift and rotation for different vertical loads.

Another macro-element model for shallow foundations on undrained clay was proposed by Martin & Houslby (2000). The footing shape chosen was a jack-up spudcan foundation (Figure 2.51).

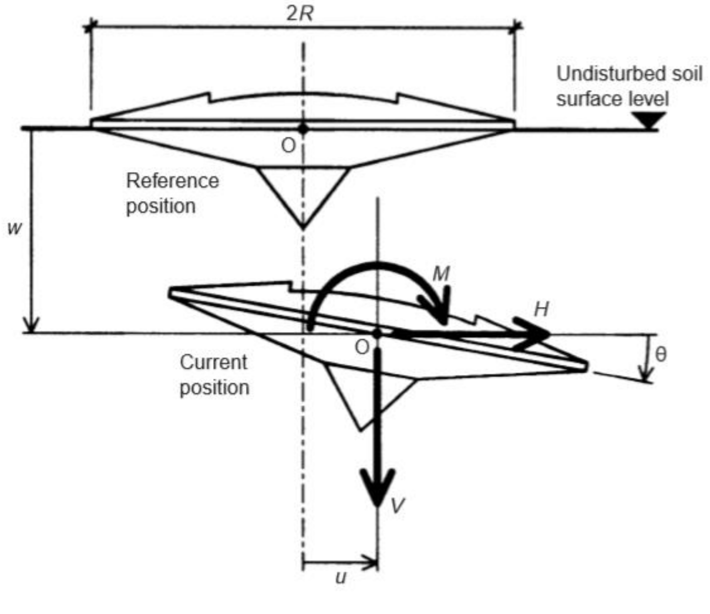

Figure 2.51 – Spudcan foundation subjected to combined loading (Martin & Houlsby, 2001).

A series of laboratory tests were carried out and used to calibrate and assess the macro-element model. A yield surface with a modified parabolic variation as proposed by Nova & Montrasio (1991) provided good fit with the experimental data:

$$f = \left(\frac{M}{M_{max}}\right)^2 + \left(\frac{H}{H_{max}}\right)^2 - 2\bar{e}\left(\frac{M}{M_{max}}\right)\left(\frac{H}{H_{max}}\right) - \bar{\beta}^2\left(\frac{V}{V_{max}}\right)^{2\beta_1}\left(1 - \frac{V}{V_{max}}\right)^{2\beta_2} = 0 \quad (2.19)$$

where β_1, β_2 and $\bar{e}$ are constitutive parameters.

It was found through the experiments that although the yield surface expanded significantly during vertical penetration, its shape remained nearly constant. The experiments also shown that the incremental rotational and horizontal displacements were accurately predicted by an associated flow rule. On the other hand, the vertical displacements were significantly overestimated, though the direction of these displacements was correctly predicted by the associated flow.

2.7.2. Macro-element model for pipelines

Tian & Cassidy (2008) proposed three macro-element models with different levels of complexity to simulate soil-pipe interaction. The models allowed the evaluation of the force-displacement response of pipelines under plane-strain conditions as well as long pipeline systems.

The first model was developed within a strain-hardening plasticity theory framework, hence a purely elastic domain was defined inside an expandable yield surface, as shown in Figure 2.52.

A non-associated flow rule was adopted, as a higher ratio of horizontal to vertical displacements was shown to be not perpendicular to the yield surface. A plastic potential with similar shape to the yield surface was assumed, as shown in Figure 2.53.

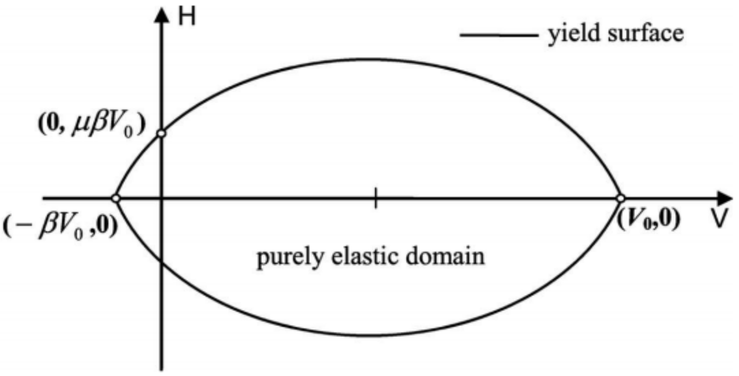

Figure 2.52 – Elastoplastic model for pipelines developed by Tian & Cassidy (2008).

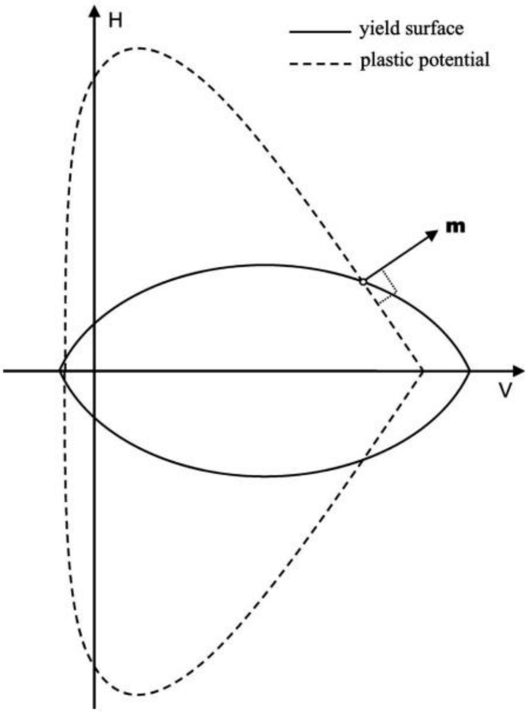

Figure 2.53 – Yield surface and plastic potential for elastoplastic model developed by Tian & Cassidy (2008).

The second model proposed by Tian & Cassidy (2008) includes the concept of bounding surface, as previously used by e.g. Dafalias (1986), Jardine (1992), and Russell & Khalili (2004). In the early studies of Jardine (1992), it was conceived that plastic strains became more significant as the stress path of a soil element approached the bounding surface, and that the path may not lie outside the bounding surface. The inclusion of a bounding surface reduces the purely elastic domain into a point in Tian & Cassidy (2008), which effectively means that there is no purely elastic behaviour. The region inside the bounding surface is defined as a transitional elastoplastic domain inside the bounding surface (Figure 2.54), and the current loading state lies always on a so-called "sub-loading surface", which can expand or contract. The sub-loading surface has the same shape as the bounding surface, but scaled up or down according to the loading level with respect to the bounding surface. When the loading state reaches the bounding surface, the sub-loading surface coincides with the bounding surface. The plastic modulus at a given load state is given by a radial mapping and depends on the ratio between the distances OA (point A on the sub-loading surface) and OB (point B on the bounding surface), as shown in Figure 2.55.

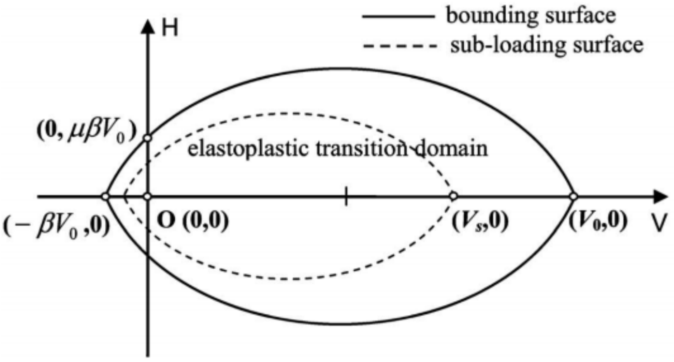

Figure 2.54 – Bounding surface model for pipelines developed by Tian & Cassidy (2008).

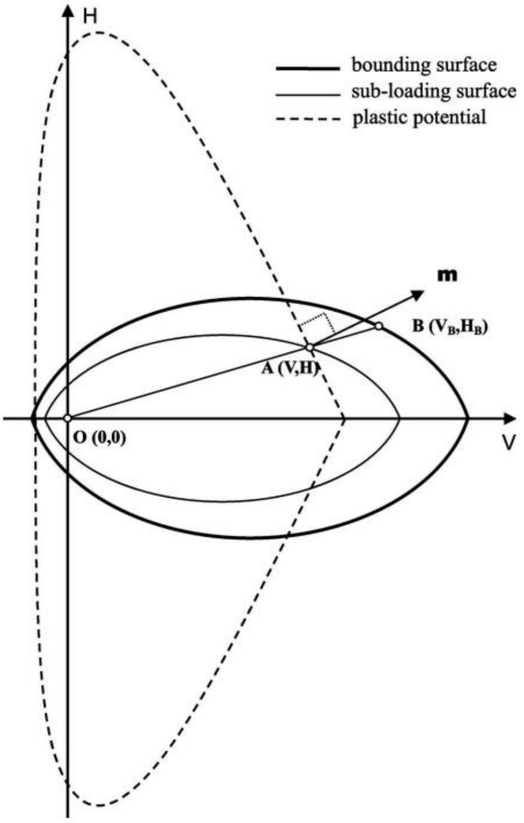

Figure 2.55 – Surfaces of bounding surface model developed by Tian & Cassidy (2008).

The third model proposed by Tian & Cassidy (2008) for pipelines included a purely elastic domain defined by a small surface (called "bubble surface") which floats freely inside the bounding surface, as shown in Figure 2.56. The areas inside the bounding surface that are not inside the bubble are part of the elastoplastic transition domain, similarly to the bounding surface model.

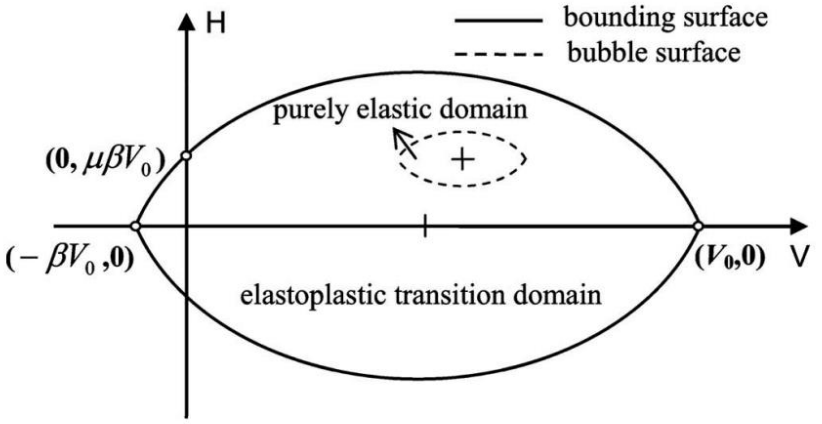

Figure 2.56 – Bubble model for pipelines developed by Tian & Cassidy (2008).

As pipelines are embedded structures, hence similar to anchors, many concepts defined in this section can be applied to the modelling of anchors. In particular, the bounding surface concept will be used for the model developments in Chapter 4.

2.7.3. Macro-element model for piles and bucket foundations

A macro-element model was developed by Li et al. (2015) for piles in sand subjected to three-dimensional conditions. The model was developed within the hypoplasticity framework. The general concept of the model included a failure surface *F* and a loading surface *f* with same shape but of smaller size (Figure 2.57), which coincides with the failure surface when the limit state is reached. The plastic flow direction was defined by an associative flow rule, i.e. the direction of plastic deformations is normal to the loading surface. An isotropic linear elastic constitutive model was used during loading, while the hypoplastic model was used to account for the stiffness degradation. The parameters were calibrated with three-dimensional FE simulations in ABAQUS.

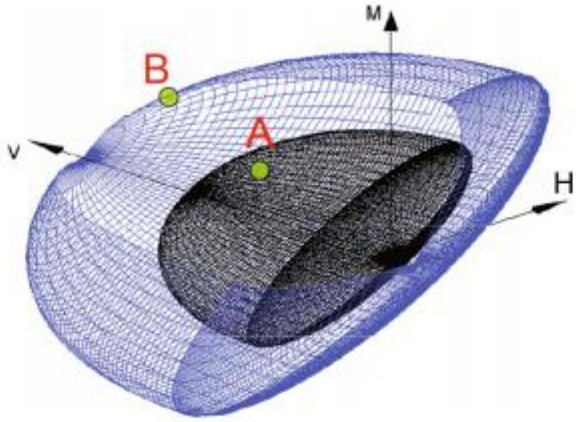

Figure 2.57 – Loading and failure surfaces in black and blue, respectively, of macro-element for piles (Li et al., 2015).

A macro-element was developed by Skau et al. (2017) to represent the load response of bucket foundations for offshore wind turbines subjected to irregular cyclic loading. The model was developed in a *V-H-M* space (vertical, horizontal and moment loads, respectively) and used a multi-surface approach, which had been previously employed by Lam & Houlsby (2005) for suction caisson foundations. The multi-surface approach consists of several surfaces that translate in the stress (or load) space (Skau et al., 2017). The region inside the smaller surface represents a purely elastic domain, while the bigger surface is a bounding surface that represents a limit load state. When the inner (elastic) surface translates, plastic displacement is generated, and kinematic hardening occurs. The approach is illustrated in Figure 2.58. The initial loading path A-B occurs within the elastic domain. When the loading point reaches the limit of the elastic domain in point B, the surface moves along the loading path B-C, during which the loading state always lies on the surface. During the loading stage B-C, plastic displacement occurs under kinematic hardening. If unloading occurs following a C-D path, the loading state goes back inside the smallest surface, hence elastic behaviour occurs. When the limit of the elastic domain is reached in D, the surface moves again, generating plastic displacement and kinematic hardening during unloading.

Similarly to Skau et al. (2017), a multi-surface approach was used by Page et al. (2018) for a macro-element model developed for the analysis of monopiles. The model was developed in the (*M*/*D*)-*H* space, as shown in Figure 2.59. An associated flow rule was adopted to provide the displacements $D\theta$ and u, where D is the pile diameter, θ is the pile rotation and u is the horizontal displacement.

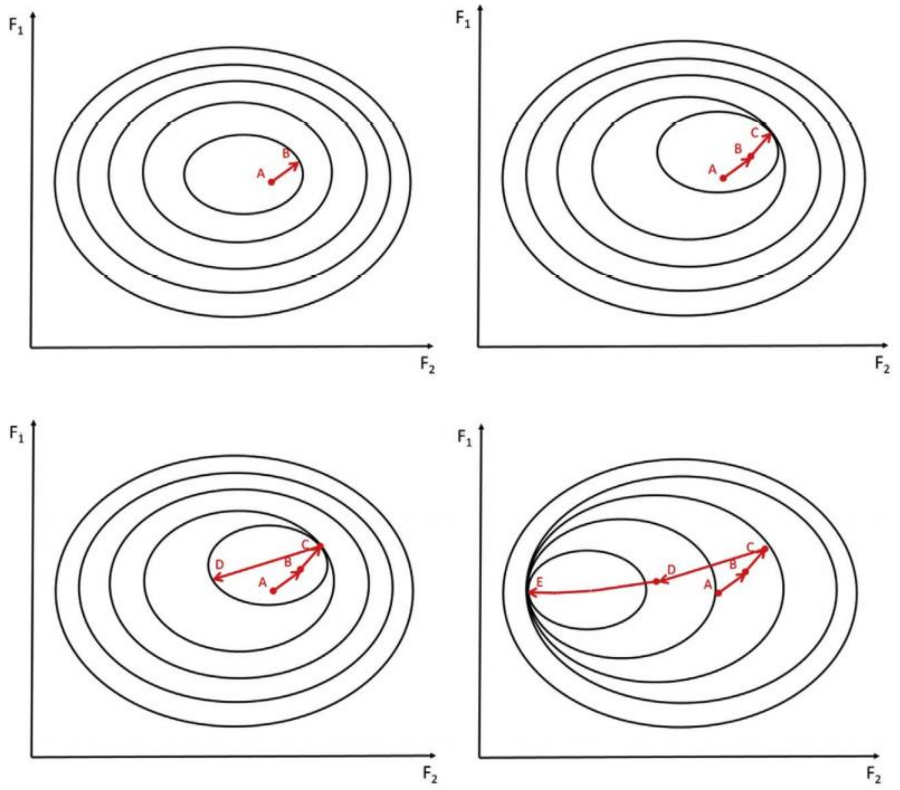

Figure 2.58 – Multi-surface plasticity approach, with translation of yield surfaces in the F_1-F_2 loading space (Skau et al., 2017).

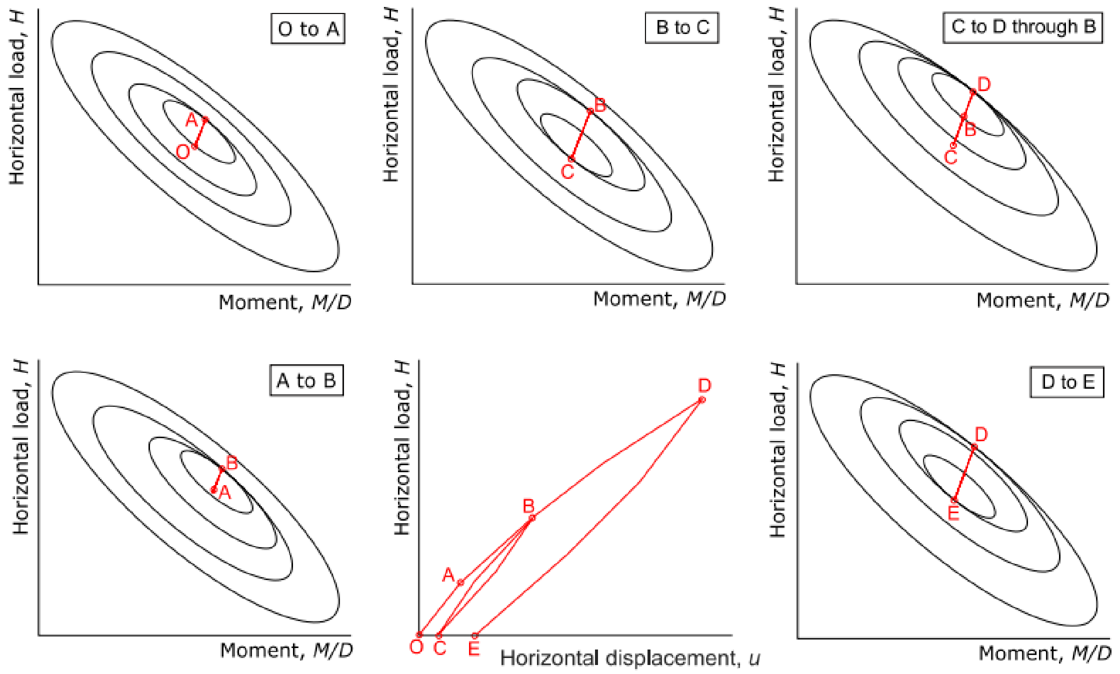

Figure 2.59 – Multi-surface plasticity approach applied to monopiles, with translation of yield surfaces in the (M/D)-H loading space (Page et al., 2018).

2.7.4. Hydro-mechanical effects in macro-element models

Few macro-element models have included the hydro-mechanical effects to account for partial drainage, but in the context of penetrometers and shallow foundations. To the author's knowledge, only two such models have been published. Houlsby & Cassidy (2011) used a mechanical analogy in which springs and sliders connected in series represent the elastic and plastic undrained deformations of the foundation, respectively. An additional spring represents the drained penetration, and it is connected in parallel to a dashpot that represents the drainage processes. The results from the model were compared to experimental data and it was shown to capture the effect of different loading rates applied to a spudcan. Similarly, Flessati et al. (2020) used a spring and a slider to represent the elastic and plastic deformations of a strip shallow foundation under undrained conditions. The partial drainage process was represented by a viscous damper (representing the drainage process) in parallel with a spring in series with a slider (to represent the elastic and plastic deformations during perfectly drained conditions).

2.8. Final remarks

As shown in this chapter, plate anchors have been widely studied, especially in the last three decades. These studies started with experimental studies on plates installed vertically and horizontally and subjected to normal loads. The experimental assessments evolved to the effect of shape and embedment depth, which was followed by finite-element calculations and other numerical models. More recently in the late 2000s up until the time of writing, experimental studies were carried out to investigate the keying behaviour of anchors installed vertically and loaded eccentrically under vertical or inclined orientations, such that the anchor exhibited rotation towards an orientation normal to the load direction. While the response of these anchors under operational conditions such as cyclic loading and different loading rates was analysed experimentally, modelling developments (finite-element analyses, theoretical/analytical models and macro-element models) were usually limited to fully drained or undrained monotonic loading. In addition, the large deformations experienced by anchors during keying required long computational times to complete the numerical analyses, such as the 14 LDFE analyses conducted by Tian et al. (2015), for which each simulation took 40 hours to complete.

In parallel to the FE modelling developments in anchors, macro-element modelling approach was developed as a time-effective alternative which could be used for several applications. While the first macro-elements for geotechnical applications were developed in the 1990s to analyse the force-displacement behaviour of shallow foundations under combined loading conditions (normal, sliding and rotational loadings), recent studies applied the macro-element framework to pipelines, monopiles and even anchors (Cassidy et al., 2012; Yang et al., 2012). However, their development typically considers either drained or undrained conditions, and the effects of the pore water pressure generation and consolidation processes, which affect the effective stress state and thus the soil strength, are not currently considered in available macro-element models. Few macro-element models have included the hydro-mechanical effects to account for partial drainage, yet all in the context of penetrometers (Houlsby & Cassidy, 2011) and shallow foundations (Flessati et al., 2020).

In that sense, there is a clear knowledge gap in understanding the effect of pore pressure generation and dissipation on anchor behaviour. The effective stress framework proposed by Zhou et al. (2020) accounted for such effects, but for anchors subjected to normal loading, hence the pore pressure effects were not integrated into a macro-element model. This thesis aims to fill this knowledge gap by proposing a macro-element model that accounts for consolidation effects as well the evolution of anchor kinematics due to eccentric loading conditions. Initially, an improved macro-element model for undrained conditions is presented in the next chapter.

CHAPTER 3. A macro-element model for plate anchors in clay under undrained monotonic loading

Objectives

- To propose a new macro-element model for undrained monotonic capacity of plate anchors in clay
- To present the new model ingredients and to compare the results of the new model with a previous model (CASPA model)
- To compare the results from the new model with previously published experimental and FE results
- To provide insight into anchor kinematics under cyclic loading in light of the new macro-element model

Statement

Sections 3.1 to 3.5 of this chapter are presented in the form of a journal article published online in the Canadian Geotechnical Journal on 12 January 2021 and entitled "A non-associative macro-element model for vertical plate anchors in clay". The article has been published with the co-authorship of Dr Andrea Diambra, Dr Dimitris Karamitros and Dr Shiao Huey Chow. Some extracts of the article have been previously mentioned in this thesis. The full article can be found in the link: https://doi.org/10.1139/cgj-2020-0314. Section 3.6 presents an extension of the macro-element accounting for the evolution of anchor kinematics during cyclic loading, which was published in the article "Macro-element modelling of plate anchor kinematics under cyclic loading in clay" in the Proceedings of the 4th International Symposium on Frontiers in Offshore Geotechnics (ISFOG), with the same authors as the aforementioned Canadian Geotechnical Journal paper. Section 3.7 summarises the conclusions from both studies.

3.1. Introduction

The offshore renewable energy sector is moving towards the installation of floating wind production plants in deeper water sites, as well as pioneering new floating wave energy converter devices. In this context, floating structures are fixed to the seabed through mooring lines connected to an anchoring system, which differs from fixed foundation solutions such as monopiles typically used in water depths of up to 60m. Among different anchoring solutions, plate anchors provide considerable vertical holding capacity through a large embedded plate, which is commonly referred as a fluke (Tian et al. 2015). Plate anchors can be installed by dragging into the seabed using drag-in vertically loaded plate anchors (VLAs) (e.g. Murff et al. 2005; Liu 2012; Aubeny and Chi 2014), or can be installed with the fluke in vertical position by an external mandrel, using suction (e.g. suction-embedded plate anchors – SEPLA, Dove et al. 1998; Wilde et al. 2001; Han et al. 2016) or free-fall gravity (e.g. dynamically embedded plate anchors – DEPLA, O'Loughlin et al. 2014). In plate anchors, the mooring line attached to the padeye is tensioned after the anchor is installed, making the anchor rotate from its initial position and become approximately normal to the load applied by the mooring line (Dove et al. 1998). This process of rotation is called keying, during which the anchor experiences vertical motion, resulting in loss of embedment (Gaudin et al. 2015). The major concern associated with offshore plate anchors is the anchor trajectory prediction during keying and the operational loading (Gaudin et al. 2006; Song et al. 2009; Yang et al. 2012), which enables accurate determination of current embedment and hence anchor's capacity.

Several researchers have carried out centrifuge tests and numerical analyses to assess the keying behaviour of plate anchors in clay (Song et al. 2006; Song et al. 2008; Hu & Song 2008; Song et al. 2009; Wang et al. 2011; Cassidy et al. 2012; Tian et al. 2015). Numerical modelling of anchor keying is a challenging and time-consuming 3-D problem which requires the careful handling of large mesh deformation associated with the considerable anchor displacements, as well as complex solutions for modelling the plate-soil-chain interactions. Centrifuge modelling, on the other hand, also faces considerable challenges in enabling extended assessments of plate-soil-chain behaviour due to the complexity of sample preparation and testing. In the interest of simplicity, macro-element modelling techniques can represent a valuable tool for exploring the mechanical response of soil-anchor interaction problems at very low computational costs while accounting for all the key problem variables (e.g. anchor geometry, embedment, soil properties, loading conditions). Macro-element models have already been successfully employed to predict the mechanical response of shallow foundation behaviour (e.g. Nova & Montrasio 1991; Cremer et al. 2001), spudcans (Martin & Houlsby 2001) and plate anchors (e.g. Cassidy et al. 2012), among others.

Two macro-element models for plate anchors are available in the literature (Cassidy et al. 2012; Yang et al. 2012). Chain and SEPLA Plasticity Analysis – CASPA (Cassidy et al. 2012) is based on a classical rigid plasticity theory developed to predict forces, rotation and displacements of the plate anchor during keying and up to the peak load. The model incorporates the chain solution by Neubecker & Randolph (1995). This model can predict the ultimate resistance of the anchor, the rotation and anchor displacement in the first stage of the keying process and the influence of different padeye offsets. However, the simplified nature of the employed macro-element model, especially in relation to rigid plasticity and the assumption of an associated flow rule governing the development and direction of plastic displacements, resulted in incorrect predictions of the anchor trajectory, including excessive initial backward and upward movements and downward trajectories (i.e. re-embedment of the anchor) in the medium-large displacement domain for many padeye offset values. Similarly, Yang et al. (2012) employed a rigid plasticity approach with an associated plastic potential and a chain solution to predict load capacity and anchor trajectory, but accounting for the presence of a hinged flap. The presence of the flap resulted in reduced backward movement, slightly more embedment loss and higher ultimate capacity.

Based on the above developments, an improved macro-element model for plate anchors is proposed in this Chapter. The new model is characterised by a non-associated plastic potential while a plastic hardening rule is also implemented. These two additional ingredients allow a controlled simulation of plastic displacements since the early stage of keying (through the inclusion of the plastic hardening rule) and enable a more accurate prediction of the anchor trajectory across the whole displacement domain and for a large range of padeye offsets (through the inclusion of the non-associated plastic potential). While these improvements come at the expense of four additional model parameters (three for the plastic potential and one for the hardening rule), the application of the model to different datasets of experimental and numerical studies for variable anchor geometries and initial conditions demonstrates that only one parameter related to the plastic potential needs to be calibrated in practice (alongside the parameter related to the hardening rule) and they may be used to capture the effect of the installation procedure. Still, this Chapter presents a set of parameters that produces satisfactory results for most analysed cases and therefore can be used as a starting point in the model calibration procedure.

The final section of the Chapter presents an expansion of the macro-element model to account for the effects of plate anchor kinematics during cyclic loading by modifying the hardening and plastic potential rules in order to account for repeated load reversals. Even though this first modelling development does not account for the variation of soil strength during cyclic loading, it offers valuable insight on how cyclic variation of the anchor's kinematics (e.g. progressive cyclic re-orientation) affects the overall anchor performance and capacity.

3.2. Geometry and definitions

The geometry of a generic plate anchor and the definition of the force and displacement components are represented in two-dimensions in Figure 3.1a, and a sketch is displayed in Figure 3.1b. The overall in-plane length of the anchor's fluke is denoted by B, while the position (eccentricity) of the padeye with respect to the centre of the fluke is defined by e_p and e_n in the direction parallel and perpendicular to the fluke, respectively. The chain is connected to the padeye of the anchor exerting a force T_a with an inclination θ_a, while the inclination of the chain at the mudline is denoted by θ_0. The pulling force of the chain results in a combination of loads to the anchor: normal (V), sliding (H) and rotational (M) forces which are considered to be applied at the centre of the fluke (i.e. $B/2$ from each end of the anchor). Imposing force equilibrium conditions on the anchor, the following relationships can be obtained:

$$V = T_a \sin(\beta + \pi/2 - \theta_a) - W' \sin\beta \tag{3.1}$$

$$H = T_a \cos(\beta + \pi/2 - \theta_a) - W' \cos\beta \tag{3.2}$$

$$M = T_a \, [e_n \cos(\beta + \pi/2 - \theta_a) + e_p \sin(\beta + \pi/2 - \theta_a) \tag{3.3}$$

where β is the current inclination of the anchor from the vertical direction and W' is the effective anchor weight. The incremental tangential and normal displacement (with respect to the fluke direction) and rotation of the anchor at the centre of the fluke are defined by δu, δw and $\delta\beta$. The horizontal and vertical displacement increments, defined by δx and δz, are linked to the incremental displacement by:

$$\delta x = \cos(\beta)\,\delta w - \sin(\beta)\,\delta u \tag{3.4}$$

$$\delta z = \sin(\beta)\,\delta w + \cos(\beta)\,\delta u \tag{3.5}$$

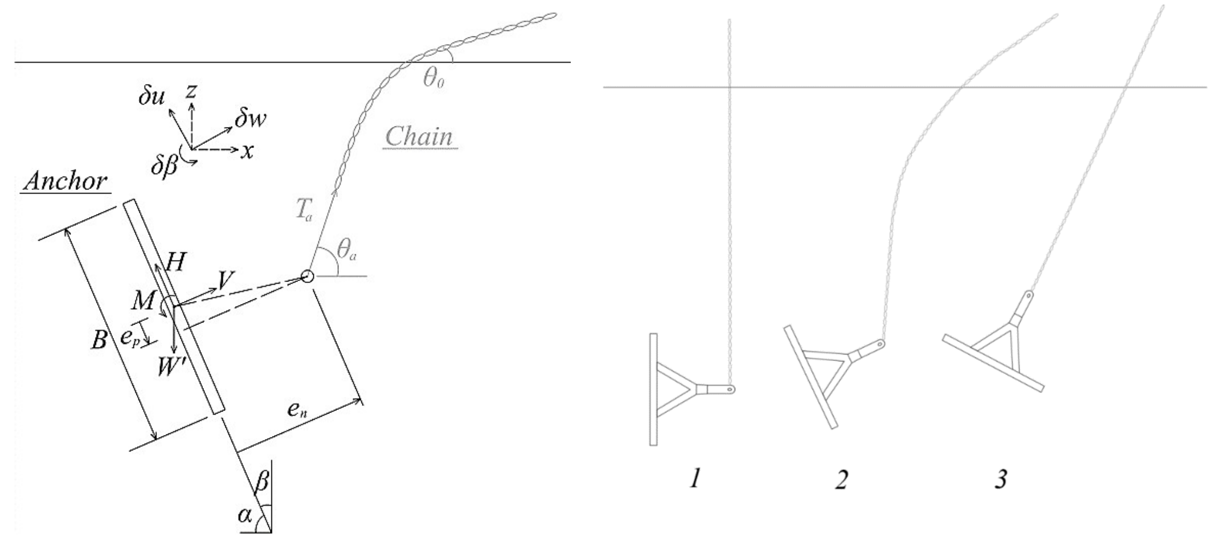

(a) (b)

Figure 3.1 – (a) Schematic 2-D representation of the anchor and chain geometry and definition of forces and displacements; (b) sketch of a plate anchor and chain configuration.

3.3. Modelling framework

3.3.1. General

Following previous developments (i.e. Cassidy et al. 2012), this model considers a macro-element model for the mechanical response of the anchor (shown in black in Figure 3.1a) interacting with the chain (shown in grey in Figure 3.1a) according to the solution proposed by Neubecker & Randolph (1995). The macro-element model for the anchor is based on the theory of incremental plasticity. A schematic 2-D illustration of the surfaces and modelling strategy for the mechanical response of the plate anchor is provided in Figure 2 in the normalised V/V_M

versus H/H_M force plane (imposing M/M_M =0). The terms V_M, H_M and M_M are the normal, sliding and rotational capacities when acting independently on the anchor. These capacities are commonly defined through the capacity factors N_v, N_h and N_m, with:

$$N_v = V_M/(L\ B\ s_u) \tag{3.6}$$

$$N_h = H_M/(L\ B\ s_u) \tag{3.7}$$

$$N_m = M_M/(L\ B^2\ s_u) \tag{3.8}$$

The current chain load state (*H*, *V*, *M*) lies on the loading surface (*f* in Figure 3.2) which can change in size during keying or operational loading. The strength surface (*F*) represents the maximum capacity of the anchors, and in turn the maximum size of the loading surface. The direction of the plastic deformation is defined by the normal to the plastic potential (*g*) passing through the current chain load state.

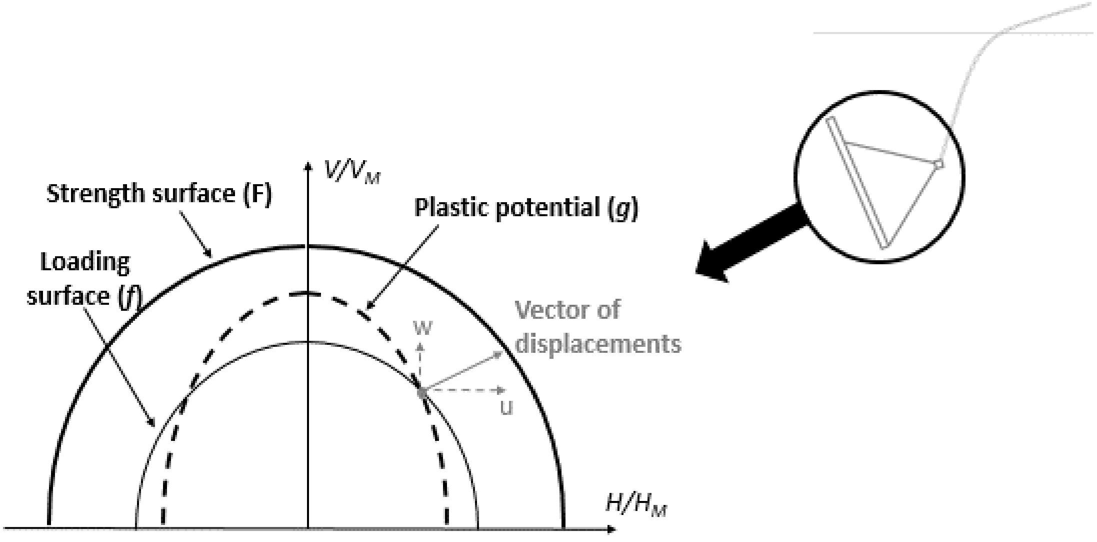

Figure 3.2 – Schematic 2-D representation (M/M_M=0) of the model surfaces, force state and plastic potential introduced in the proposed macro-element model for the plate anchor.

3.3.2. Macro-element modelling of plate anchor

Loading and strength surfaces. The loading surface (*f*), expressed in Equation (3.9), and the capacity surface (*F*) follow a similar format to that suggested by Bransby & O'Neill (1999) and applied to drag anchors (Elkhatib & Randolph 2005; Aubeny & Chi 2010) and to plate anchors (Murff et al. 2005; Cassidy et al. 2012; Yang et al. 2012). In its original form, Equation (3.9) included an exponent $1/p$ to the sum of the second and third terms (involving the moment and horizontal loads). However, the aforementioned references showed that p tends to values that are close to unity, thus it has been supressed in the present study:

$$f = \left(\frac{V}{V_M}\right)^q + \left(\frac{|M|}{M_M}\right)^m + \left(\frac{|H|}{H_M}\right)^n - \rho_c = 0 \tag{3.9}$$

where m, n and q are the terms defining the shape of the three-dimensional surface in the V/V_M-H/H_M-M/M_M space and ρ_c is the mobilisation of anchor capacity, which works as a hardening rule and varies between 0 and 1, defining the size of the loading surface. The strength surface (F) is obtained by imposing $\rho_c = 1$. The capacities V_M, H_M and M_M are dependent on the capacity factors N_v, N_h and N_m, as per Equations (3.6) through (3.8).

Hardening rule. As previously mentioned in this chapter, the inclusion of a hardening rule aims to provide a controlled simulation of the early stages of keying, especially in the force-displacement domain. According to the theory of incremental plasticity, changes in size of the loading surface are linked to plastic displacements experienced by the anchor. The relationship between the loading surface's hardening term ρ_c and the plastic displacements u, w and β follows the finite form proposed by Nova & Montrasio (1991), which was originally developed for shallow foundations subjected to eccentric and inclined loads:

$$\rho_c = 1 - e^{-R_0\,[w^2+u^2+(B\,\beta)^2]^{1/2}} \tag{3.10}$$

where R_0 is the non-dimensional hardening parameter. The hardening variable ρ_c is null at zero displacement and asymptotically approaches failure conditions ($\rho_c = 1$) for large value of displacements. It should be noted that, in its original form, Nova & Montrasio (1991) included two non-dimensional weighting parameters: a_1 multiplying the displacement u and a_2 multiplying the rotation β. However, a parametric analysis carried out in this study (shown in Figure 3.3 and Figure 3.4) has revealed that these additional parameters would have very little influence in the model predictions. Although the initial stiffness of the force-displacement curves is slightly affected by the values of a_1 and a_2, this can be controlled by the hardening parameter R_0, as shown later in Figure 3.6. It is worth noting that the values of a_1 and a_2 used in the parametric analyses of Figure 3.3 and Figure 3.4 represent the lower (in blue) and upper (in red) limits for which the model works – for values outside of this range, numerical errors occurred during the simulations.

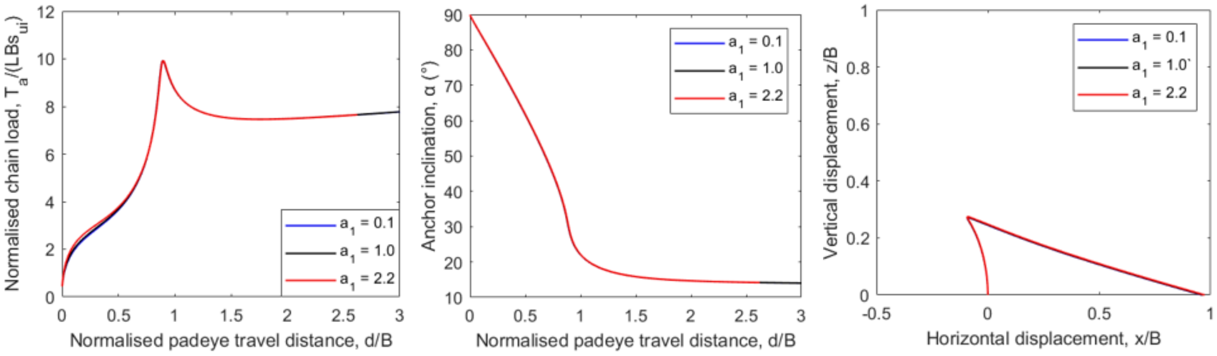

(a) (b) (c)

Figure 3.3 – Influence of weighing parameter a_1 in the behaviour of a plate anchor: (a) normalised load and padeye travel distance; (b) anchor inclination; (c) anchor trajectory. Plastic potential parameters: $\xi = \chi = \omega = 1$; hardening parameter $R_0 = 1$.

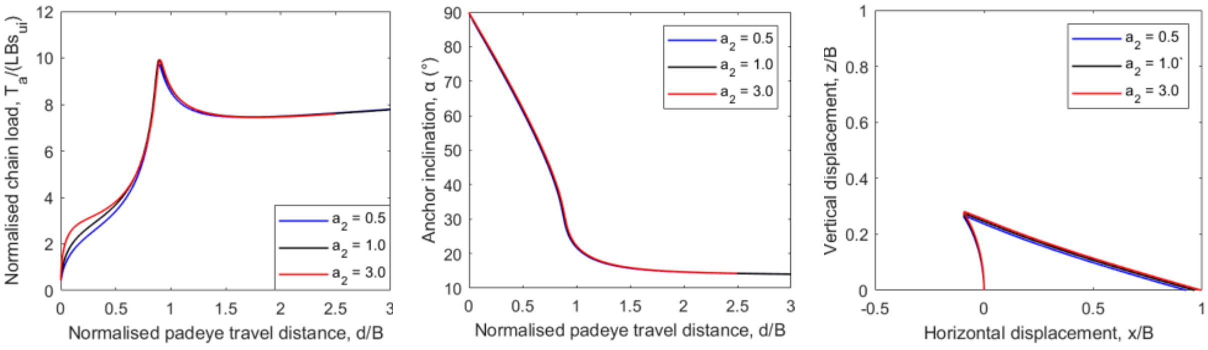

(a) (b) (c)

Figure 3.4 – Influence of weighing parameter a_2 in the behaviour of a plate anchor: (a) normalised load and padeye travel distance; (b) anchor inclination; (c) anchor trajectory. Plastic potential parameters: $\xi = \chi = \omega = 1$; hardening parameter $R_0 = 1$.

Plastic potential and flow rule. It is assumed that the plastic potential is characterised by an expression similar to the loading and failure surfaces, but its shape is modified through the introduction of scaling factors ξ, χ and ω for the normal, sliding and rotational capacities (V_M, H_M and M_M, respectively). An expression similar to the proposed by Nova & Montrasio (1991) has been selected as it provides an independent modification of the skewing on the V/V_M, H/H_M and M/M_M axis, which allows an independent calibration, as shown later in this manuscript. A slight modification to the power of the horizontal loads, if compared to the loading and strength surfaces in Equation (3.9), has been introduced following the authors' experience in using the model and the better agreement achieved for all simulations carried out in the following of this thesis.

$$g = \left(\frac{V}{V_M/\xi}\right)^q + \left(\frac{|M|}{M_M/\omega}\right)^m + \left(\frac{|H|}{H_M/\chi}\right)^m - \rho_g = 0 \tag{3.11}$$

where the parameter ρ_g defines the current size of the plastic potential but its numerical value has no practical relevance since only the derivatives of g are of interest for the determination of the vector of anchor incremental displacements $\delta\boldsymbol{q}$ (δw, δu and $\delta\beta$):

$$\delta\boldsymbol{q} = \begin{pmatrix} \delta w \\ \delta u \\ B\delta\beta \end{pmatrix} = \mu \begin{pmatrix} \partial g/\partial V \\ \partial g/\partial H \\ \partial g/\partial(M/B) \end{pmatrix} \tag{3.12}$$

where μ is the plastic multiplier. Satisfaction of the consistency condition expressed in equation (13) ensures that the current load state ($\boldsymbol{Q}$ = $[V, H, M]^{\mathrm{T}}$) lies always on the loading surface:

$$df(\boldsymbol{Q}, \rho_c) = \frac{\partial f}{\partial \boldsymbol{Q}} d\boldsymbol{Q} + \frac{\partial f}{\partial \rho_c} d\rho_c = 0 \tag{3.13}$$

By substituting the derivatives of Equation (3.10) into Equation (3.13) and then introducing Equation (3.12), the following expression for the plastic multiplier can be obtained:

$$\mu = \frac{-\left(\frac{\partial f}{\partial V}\dot{V} + \frac{\partial f}{\partial H}\dot{H} + \frac{\partial f}{\partial(M/B)}\dot{M}\right)}{\frac{\partial f}{\partial \rho_c}\left(\frac{\partial \rho_c}{\partial w}\frac{\partial g}{\partial V} + \frac{\partial \rho_c}{\partial u}\frac{\partial g}{\partial H} + \frac{\partial \rho_c}{\partial(B\beta)}\frac{\partial g}{\partial(M/B)}\right)} \tag{3.14}$$

3.3.3. Chain solution

The chain solution proposed by Neubecker & Randolph (1995) is included to relate the angle of pull at the mudline (θ_0) to the chain angle at the padeye (θ_a):

$$\begin{aligned} &e^{\mu_c(\theta_a - \theta_0)}(\cos\theta_0 + \mu\sin\theta_a) - \cos\theta_a - \mu\sin\theta_a \\ &\qquad = E_n d_{bar} N_c \left(s_{u0} z_p + \frac{k_{su} {z_p}^2}{2}\right)\left(\frac{1 + {\mu_c}^2}{T_a}\right) \end{aligned} \tag{3.15}$$

where d_{bar} is the diameter of the chain; E_n is a multiplier giving the effective chain width in the normal direction to the chain; N_c is the bearing capacity factor for the chain; z_p is the current vertical depth of the padeye; s_{u0} and k_{su} are the soil shear strength at the mudline and the rate of increase with depth; and μ_c is the friction between the soil and the chain.

3.3.4. Model parameters and calculation procedure

The proposed macro-element model requires the definition of (i) the geometry and properties of the anchor and the chain, (ii) the soil conditions and (iii) the calibration of the parameters for the anchor models. All these quantities are summarised in Table 1, which also provides the values adopted in the following parametric analysis and in the simulation exercises against different sets of experimental or numerical data, which considered uniform seabed profiles characterised by an undrained shear strength either constant or increasing linearly with depth ($s_u = s_{u0} + k_{su} z$, where s_{u0} is the undrained shear strength at mudline level, k_{su} is the strength gradient and z is the depth of the anchor centroid). The section in which the simulation exercises were carried out are indicated in square brackets. While 10 macro-element parameters are introduced, the following calibration procedure and model validation will show that most of them can be either determined from the literature or lie within a very narrow range, leaving just one of the plastic potential parameters (ω) to be calibrated.

The calculation procedure involves the following stages:

i) DEFINITION OF INITIAL CONDITIONS: The initial conditions of the simulation procedure consider a vertical orientation of the chain at the padeye after installation, by imposing an initial value of $\theta_a = 90°$. The chain inclination at seabed level θ_0 is set to comply with the desired boundary conditions of the analysed problem. The chain solution in Equation 3.15 is then employed to determine the initial value of the chain force T_a. Using the force-equilibrium Equations (3.1) to (3.3), the initial value of the load components H, V and M on the plate anchors are determined and in turn the initial value of the hardening parameters ρ_c can be defined through Equation (3.9). The initial values of the displacements u and w are also updated using Equation (3.10) where it is simplistically imposed no rotation of the plate (β=0^0) and that the ratio u/w=H/V is valid for the initial conditions. This is a rudimentary estimation with insignificant influence on the model simulations as the displacements under these initial conditions are negligible.

ii) SIMULATION OF KEYING AND LOADING. The simulations are carried out imposing dynamic step increments to the monotonically-increasing hardening parameter ρ_c from the initial value determined in stage 1 above to the asymptotic value of 1. Imposing increments to ρ_c provides shorter computational time and more stability of the simulation than increments in force or displacement, for example. The problem is then solved by using a 4th order Runge-Kutta method to simultaneously solve the incremental form of force-equilibrium (Equation 3. 1 to 3.3), the consistency condition (Equation 3.13), the three expressions for the plastic potential defined by Equation (3.12), the chain solution in Equation (3.15) and the displacement relationships in Equations (3.4) and (3.5) to find the values of the problem variables: load components (H, V, M); the displacements with respect to the fluke directions (u, w, β); the absolute displacement of the anchor (x and z); and the inclination and force at the padeye (θ_a and T_a, respectively).

3.4. Effect of new modelling features

The CASPA model, proposed by Cassidy et al. (2012), can be considered the predecessor of this model with the limitation of being formulated within a rigid plasticity framework and associated flow rule. Compared to CASPA, the proposed model introduces four new model parameters (ξ, χ, ω related to the shape of the plastic potential, and R_0 governing the hardening rule) whose influence will be analysed in this section. For this exercise, the same anchor and soil properties as in Cassidy et al. (2012) are assumed (Table 3.1). The initial orientation of the anchor is vertical (β=0^0) while the imposed chain angle – and therefore the direction of the monotonic load – at the mudline is constant with $\theta_0 = 45°$.

3.4.1. Plastic potential parameters

The variation of the value of the three plastic potential related parameters permits skew of the shape of the plastic potential (g) and modifies the direction of the normal vectors to the plastic potential surfaces. The inclusion of these model parameters provides an additional degree of freedom to control the incremental displacements and the overall plate anchor trajectory during loading. Figure 3.5 presents the independent influence of each of the three model parameters on the normalised total chain load (T_a/LBs_{ui}, with s_{ui} being the soil undrained shear strength at the initial anchor depth) and anchor rotation ($\alpha = 90^0 - \beta$) versus the normalised padeye travel distance (d/B), and on the overall anchor trajectory. The anchor trajectory is represented in the normalised vertical displacement (z/B) versus the normalised horizontal displacement (x/B) plot. The padeye travel distance is defined by:

$$d = \int \sqrt{{\delta x_P}^2 + {\delta z_P}^2} \qquad (3.16)$$

where δx_p and δz_p are the incremental horizontal and vertical displacements of the padeye, respectively.

Four values were adopted in the sensitivity analysis of the parameter ξ (0.5, 1.0, 1.5 and 2.0, with 0.5 and 2.0 being the lower and upper limit values for application in the model – if the model is used with values outside of this range, it does not resolve), which controls the intercept of the plastic potential on the V/V_M axis. This parameter seems to affect the load-displacement, rotation and trajectory of the anchor at large displacements only (Figure 3.5a, b, and c). The peak load (Figure 3.5a) slightly decreases when ξ increases from 0.5 to 2.0 whereas the post-peak drop is faster for lower values of ξ. Anchor rotation (Figure 3.5b) is not affected up to $d_a/B \approx 0.7$, beyond which lower values of ξ make the anchor rotate more rapidly up to its final orientation. The most important effect of ξ, though, is the capacity to modify the anchor trajectory (Figure 3.5c). For higher values of ξ, the anchor moves upwards and no longer embeds again after a certain point, as observed in the model with associated plastic potential ($\xi = 1$). This feature would not be possible without the inclusion of a non-associative plastic potential.

For the parameter χ controlling the skewing on the H/H_M direction of the plastic potential surface, the values adopted were 0.5, 1.0, 1.2 and 1.5 (values higher than 1.5 resulted in numerical errors, hence 1.5 is the upper limit of values of χ). As opposed to ξ, the parameter χ affects the anchor behaviour from the early stages of keying. Figure 3.5d shows that the peak load decreases by 10% and the padeye travel distance at the peak load increases by 75% when χ increases from 0.5 to 1.5. In terms of anchor rotation, it can be observed from Figure 3.5e that the anchor rotates more rapidly for lower values of χ. The increase in the padeye travel distance to peak load can be attributed to the increase in both vertical and horizontal displacements with increasing χ (see Figure 3.5f). Within the analysed range, the sole variation of the values of χ does not prevent the re-embedment of anchor into the seabed at large displacements, which does not seem realistic given that the anchor chain is pulled upwards at an angle of 45°.

The parameter ω, controlling the skewing of the plastic potential in the M/M_M direction has qualitatively similar but opposite effect to χ. The increase of ω from 0.65 to 2.0 increases the peak load by 11% (Figure 3.5g) and increases rotation significantly (Figure 3.5h), but decreases the anchor displacement (Figure 3.5i), including a 77% reduction to the displacement at peak load (Figure 3.5g). In terms of anchor trajectory (Figure 3.5i), ω is unable to modify the direction of travel of the anchor, which seems to be parallel irrespective of the value adopted for this parameter. Values of ω lower than 0.65 resulted in numerical errors of the model.

3.4.2. Hardening parameter R_0

Four values were selected (0.5, 1.0, 1.5 and 2.5) to show the influence of the hardening parameter R_0 on the response of a plate anchor. The main effect of the inclusion of R_0 can be observed in the normalised chain load versus padeye travel distance plot presented in Figure 3.6a. The increase of the hardening parameter R_0 provides larger initial stiffness but produces negligible effect on the peak loads. The influence of this parameter on the anchor rotation (Figure 3.6b) and trajectory is also negligible (Figure 3.6c). Values lower than 0.5 or higher than 2.5 can be used, and the trends followed are the same as presented in Figure 3.6c, i.e. initial softer behaviour for lower values and initial stiffer behaviour for higher values of R_0.

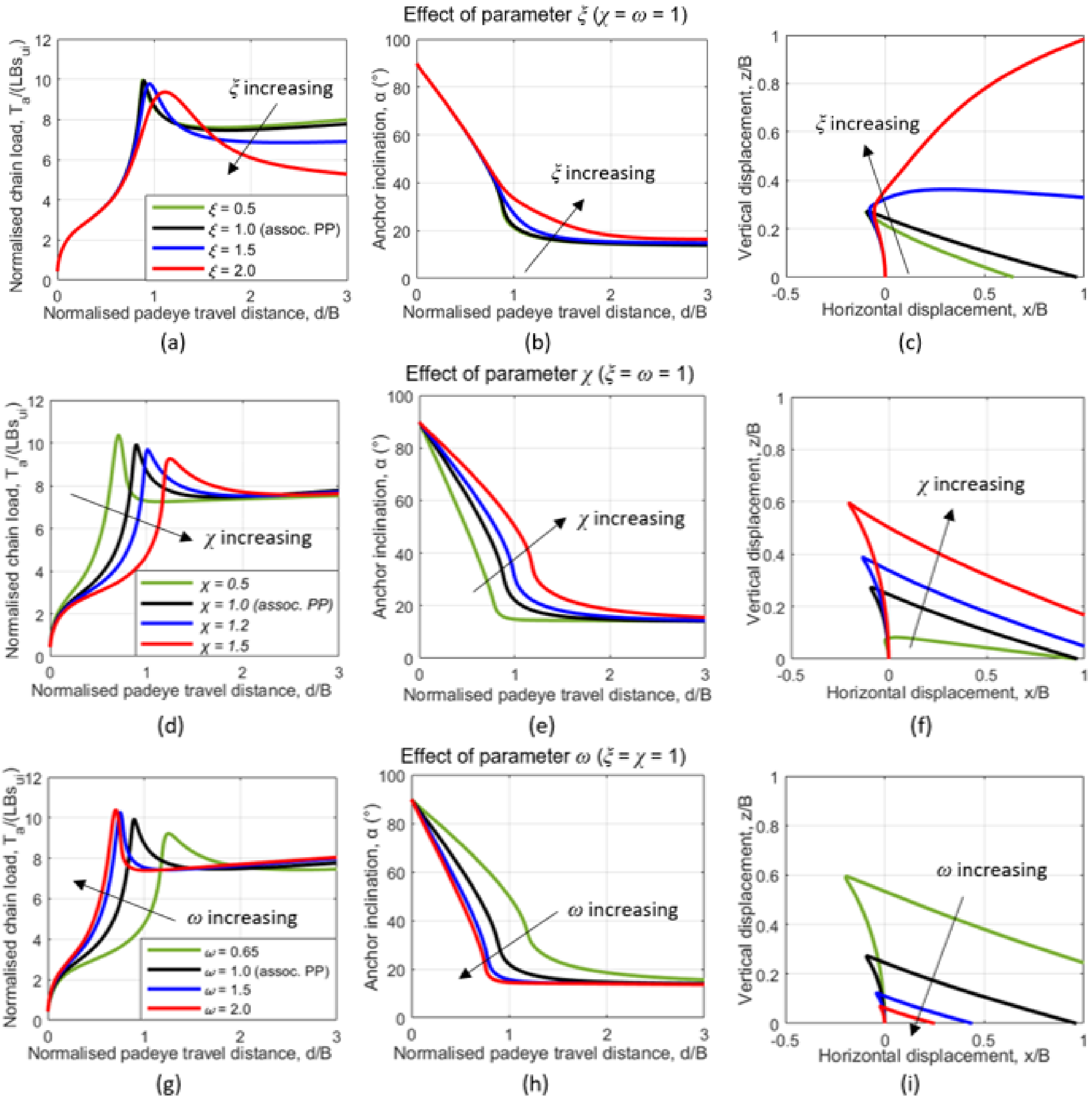

(a) (b) (c)

(d) (e) (f)

(g) (h) (i)

Figure 3.5 – Parametric analysis: influence of parameters ξ, χ and ω in the behaviour of a plate anchor; (a), (d), (g): normalised load and padeye travel distance; (b), (e), (h): anchor inclination; (c), (f), (i): anchor trajectory. A value of R_0 = 1.0 is assumed.

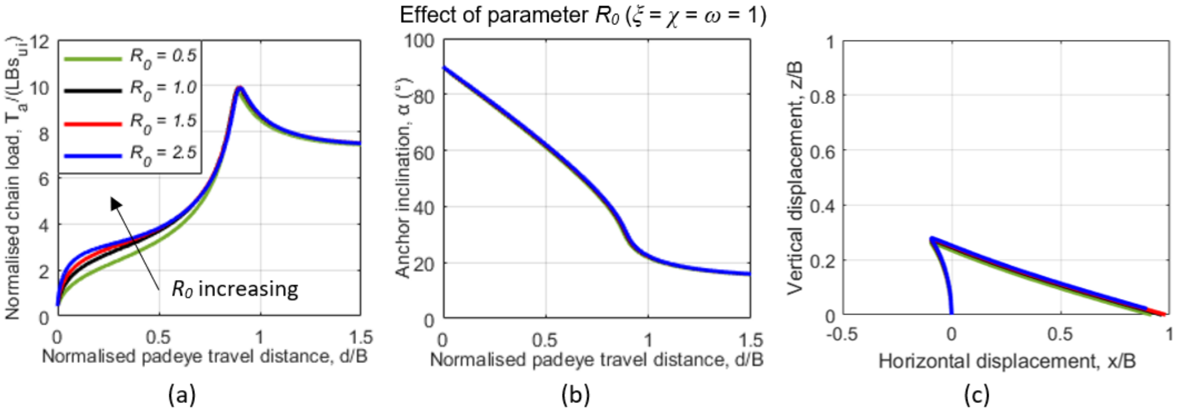

(a) (b) (c)

Figure 3.6 – Influence of hardening parameter R_0 in the behaviour of a plate anchor: (a) normalised load and padeye travel distance; (b) anchor inclination; (c) anchor trajectory. Plastic potential parameters: $\xi = \chi = \omega = 1$.

3.4.3. Discussion on chain load path and incremental displacement

While the introduced modelling features provide additional capability and versatility to the macro-element model, they do not seem to considerably influence the load path experienced by the anchor as shown in Figure 3.7, where comparison for a CASPA type model and the new displacement hardening, non-associated flow model is presented. Beyond the fact that for the latter model the load path originates inside the strength surface, the main difference between the cases lies in the direction of the plastic incremental displacement vectors. It is the control of such directions, not limited to be normal to the strength surface, that provides the additional model capabilities for predicting the anchor trajectory, evolution of its rotation, peak response and post-peak drops.

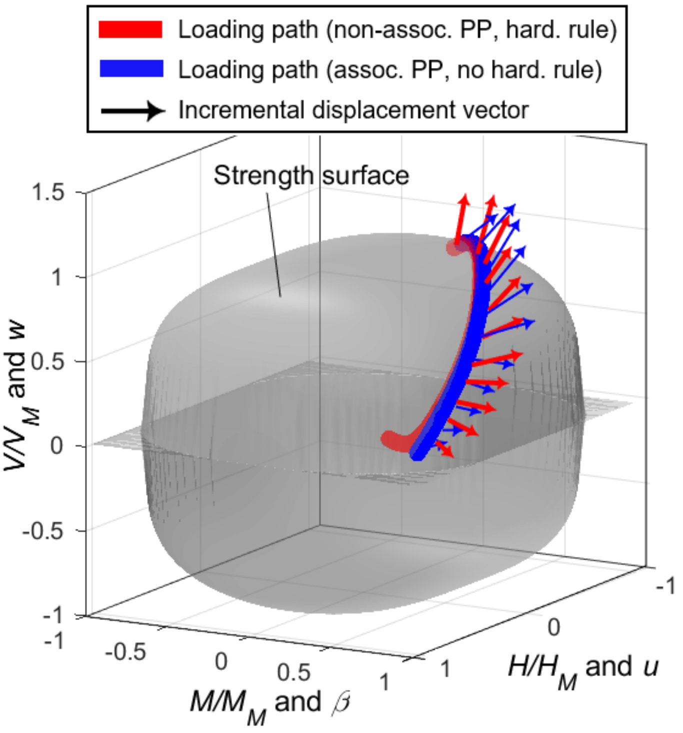

Figure 3.7 – Comparison of typical load paths and incremental displacement vectors for macro-element model without and without the new modelling features (non-associative flow rule and displacement hardening).

3.5. Model predictions

3.5.1. Introduction

For validation purposes, it is desirable that the model is calibrated and challenged against an extensive set of data covering wide a range of loading and geometrical conditions (e.g. padeye eccentricities, anchor geometry or initial embedment). While extensive field or centrifuge testing programme of this type are not available, results from numerical analyses, such as the three dimensional large-deformation finite-element (LDFE) analyses by Tian et al. (2015), offer a comprehensive set of data. In the numerical studies by Tian et al. (2015) the soil was modelled as elastic-perfectly plastic Tresca material with undrained shear strength s_u increasing with depth. The elastic behaviour of the soil was modelled by a Young's modulus $E = 500s_u$ and a Poisson's ratio $\nu = 0.49$ (to model near undrained conditions). Seven padeye offsets e_p varying from 0 to $0.5B$ for two conditions of padeye eccentricities $e_n = 2.5$ and 5m ($e_n/B = 0.5$ and 1.0) will be first employed to calibrate and challenge the macro-element model. In this process, further comparison with an associated flow rule hypothesis will be carried out to demonstrate the importance of the proposed model addition. The newly proposed model will be subsequently challenged against a wider set of LDFE analyses and centrifuge data from the literature, as listed in Table 3.1.

3.5.2. Calibration

Calibration of the 10 model parameters is required: 3 normalised capacities (N_v, N_h and N_m) governing the size of the failure surface, 3 shape parameters of the loading and failure surfaces (m, n, q), 3 parameters defining the plastic potential surface (ξ, χ and ω) and 1 hardening parameter (R_0), as listed in Table 3.1.

The normalised capacities (N_v, N_h and N_m) defined in Equations (3.6), (3.7) and (3.8) have been subject of previous literature studies. From an extensive set of finite-element analyses, Wang et al. (2011) suggested a value of 14 for N_v which was also applied by Cassidy et al. (2012) for rectangular anchors. Similarly, Elkhatib (2006) has numerically derived a value of 1.73 for the moment capacity N_m. However, these simulations did not take into account the effect of the shank, therefore a value of 2 has been adopted, as suggested by Cassidy et al. (2012). The value of parameter N_h is influenced by both anchor geometry and the roughness of the anchor material. Cassidy et al. (2012) reported a range of values varying between 2.78 and 3.41 and adopted a value of 3, which is also adopted in the present study.

Table 3.1 – Geometrical and modelling parameters of the proposed macro-element model and values adopted in parametric analyses and model simulations.

	Sym-bol	Description	Values adopted for the following simulation exercises:					
			Parametric analysis [s. 4]	Tian *et al.* 2015 [s. 5.3]	Song *et al* 2006,2009 [s.5.4.1]	Wang *et al.* 2011 [s. 5.4.1]	Cassidy *et al.* 2012 [s. 5.4.2]	Gaudin *et al.* 2006 [s. 5.4.3]
Anchor geometry and properties	B	Anchor height (m)	4.64	5.0	4.0	4.0	4.64	5.075
	L	Anchor width (m)	7.92	5.0	4.0	4.0	7.92	5.075
	e_n	Padeye normal eccentricity (m)	2.59	2.5-5.0	2.5	2.5	2.59	3.35
	e_p	Padeye offset (m)	0.492	0.0-2.5	0.0	0.0	0.492	0.0
	W_a	Submerged anchor weight (kN)	416.25	331.25	396.90	396.90	416.25	199.80
Chain geometry and	d_{bar}	Bar diameter (m)	0.41	-	-	-	0.41	0.319
	E_n	Effective width multiplier	1.0	-	-	-	1.0	1.0
	μ	Friction of chain	0.1	-	-	-	0.1	0.1
	N_c	Bearing capacity of chain	7.6	-	-	-	7.6	7.6
Soil conditions	s_{u0}	Undrained shear strength at mudline (kPa)	1.0	1.5	13.0	18.0	1.0	0.1
	k_{su}	Strength gradient (kPa/m)	1.25	1.5	0.0	0.0	1.25	1.1
Parameters of anchor Macro-element model	m	Exponent (moment)	2	2	2	2	2	2
	n	Exponent (horizontal)	4	4	4	4	4	4
	q	Exponent (vertical)	4	4	4	4	4	4
	N_v	Normalised normal capacity factor	14	14	14	14	14	14
	N_h	Normalised sliding capacity factor	3	3	3	3	3	3
	N_m	Normalised rotational capacity factor	2	2	2	2	2	2
	ξ	Plastic potential parameter (vertical)	0.5-2.0	1.6	1.6	1.6	1.6	1.6
	χ	Plastic potential parameter (horizontal)	0.5-1.5	1.1	1.1	1.1	1.1	1.1
	ω	Plastic potential parameter (moment)	0.65-2.0	1.5	1.5	1.5	1.75	0.95-1.5
	R_0	Hardening parameter	0.5 – 2.5	2.5	2.5	2.5	2.5	0.3

The shape parameters for the loading and failure surfaces have also been selected according to the recommendation of the literature. Elkhatib (2006) found a value of $q = 4.0$ for square and rectangular anchors. The parameter n was found to vary between 3.72 (square anchors, Elkhatib 2006) and 5.31 (strip anchors, Elkhatib & Randolph 2005; Bransby & O'Neill 1999). For rectangular anchors, a value of 4.2 was used by Cassidy et al. (2012). For the sake of simplicity, an integer value was selected herein ($n = 4$) with minimal influence on the model predictions. Finally, the parameter m was found to vary between 1.07 and 2.58 (Elkhatib 2006 & Elkhatib and Randolph 2005, respectively) therefore an integer value of $m = 2$ is selected here.

It follows that only the parameters for the plastic potential (ξ, χ, ω) and the hardening parameter (R_0) need to be directly calibrated when using this model. The numerical results for the intermediate padeye offset value of $e_p/B = 0.3$ and $e_n/B = 0.5$ have been chosen for the calibration process, while the other available data will be used for independent challenging of the model. The calibration is carried out by comparing and fitting the three experimental plots: anchor inclination (α) vs vertical displacement (z/B) (Figure 3.8a), normalised chain load ($T_a/(LBs_u)$) vs vertical displacement (z/B) (Figure 3.8b), and vertical (z/B) vs horizontal displacement (x/B) (Figure 3.8c). Each parameter is calibrated to capture the respective behavioural feature as discussed in sections 4.1 and 4.2 above: ξ is adjusted to fit the anchor trajectory in the horizontal versus horizontal displacement plot (Figure 3.8c); χ and ω are adjusted to match the length of the plateau in the force displacement plot (Figure 3.8a) and the evolution of anchor rotation (Figure 3.8b); R_0 is adjusted to match the initial part of the force displacement curve (Figure 3.8a).The parameters' values of $\xi = 1.6$, $\chi = 1.1$, $\omega = 1.5$ and $R_0 = 2.5$ provide an overall good fit of the LDFE results as shown in Figure 3.8. These values can be used as an initial attempt for other sets of numerical and experimental data, as will be shown later in this study.

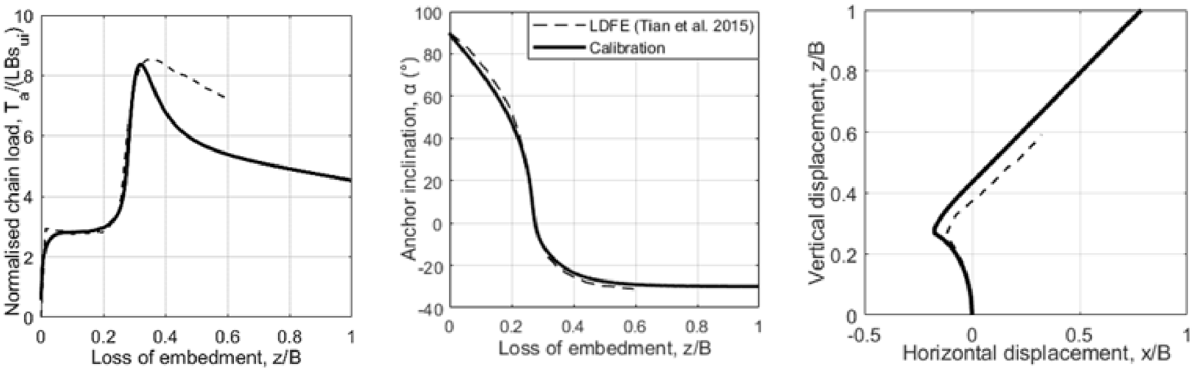

(a) (b) (c)

Figure 3.8 – Calibration of the new macro-element model (ξ = 1.6, χ = 1.1, ω = 1.5 and R_0 = 2.5): (a) force-displacement, (b) anchor inclination and (c) anchor trajectory.

3.5.3. Model simulations

3.5.3.1. *Effect of padeye eccentricity and offset*

The model performance is initially evaluated against the results from three-dimensional LDFE analyses carried out by Tian et al. (2015) for a padeye eccentricity of e_n/B=0.5 and seven distinct padeye offsets (e_p/B = 0, 0.05, 0.1, 0.2, 0.3, 0.4 and 0.5), all subjected to monotonic vertical load. Comparison of LDFE results (Figure 3.9a, d, g) with model simulations are presented for macro-element model with (Figure 3.9b, e, h) and without (Figure 3.9c, f, i) the new features (non-associated flow rule and displacement hardening). To ensure fairness of such comparison, an independent calibration of the associated plastic potential model has been carried out in order to obtain the best fit with the FE results: values of m = 4, n = 3 and q = 4.5 have been imposed to the strength surface formulation.

Figure 3.9c shows the rotational behaviour predicted by the macro-element model with associated plastic potential and no hardening rule. The model shows significantly higher vertical displacement than predicted by LDFE simulations (Figure 3.9a). Furthermore, an underestimation of the final anchor inclination can be observed. On the other hand, with the inclusion of a non-associated plastic potential and a strain-hardening rule (Figure 3.9b), the macro-element model simulations exhibit good agreement for all seven padeye offsets e_p/B. Both initial rotation and final orientation of the anchor are well captured.

Analysis of the anchor trajectories demonstrates also the superior capabilities of the new model (Figure 3.9e), in comparison with the non-associative model (Figure 3.9f), to predict the overall anchor trajectory given by the LDFE analyses (Figure 3.9d). Although the initial backward movement of the anchor is slightly overpredicted by the new model for high eccentricities (i.e. $e_p/B>0.1$) both horizontal and vertical movements seem reproduced quite well. The absence of displacement hardening and non-associated flow rule results in much larger displacements than the LDFE simulations (Figure 3.9f).

Analysing the predicted force-displacement trends, both versions of the macro-element model successfully predict the peak load. However, the new model (Figure 3.9h) offers an improved agreement with the LDFE results (Figure 3.9g) in terms of vertical displacement at the peak conditions when compared with the non-associative rigid model (Figure 3.9i). This modelling capability may be important for field applications when an assessment of the anchor movement at its full load capacity is required. While some discrepancies can be observed between the LDFE and new macro-element predicted post-peak behaviours, this is a post-failure behavioural feature which would be less relevant for field applications.

The simulations were also conducted for a higher padeye eccentricity ($e_n/B=1.0$) and showed good agreement with LDFE analyses of Tian et al. (2015). Whereas the anchor inclination (Figure 3.10a, b) is well reproduced by the new macro-element model simulations, tendency to slightly underestimate the peak load between 0.7% and 12.4%, depending on the padeye offset (Figure 3.10d, e), and overestimate the movement in both horizontal and vertical directions (Figure 3.10c, d) is also observed – and accentuated for $e_n/B=1.0$ in comparison with $e_n/B=0.5$.

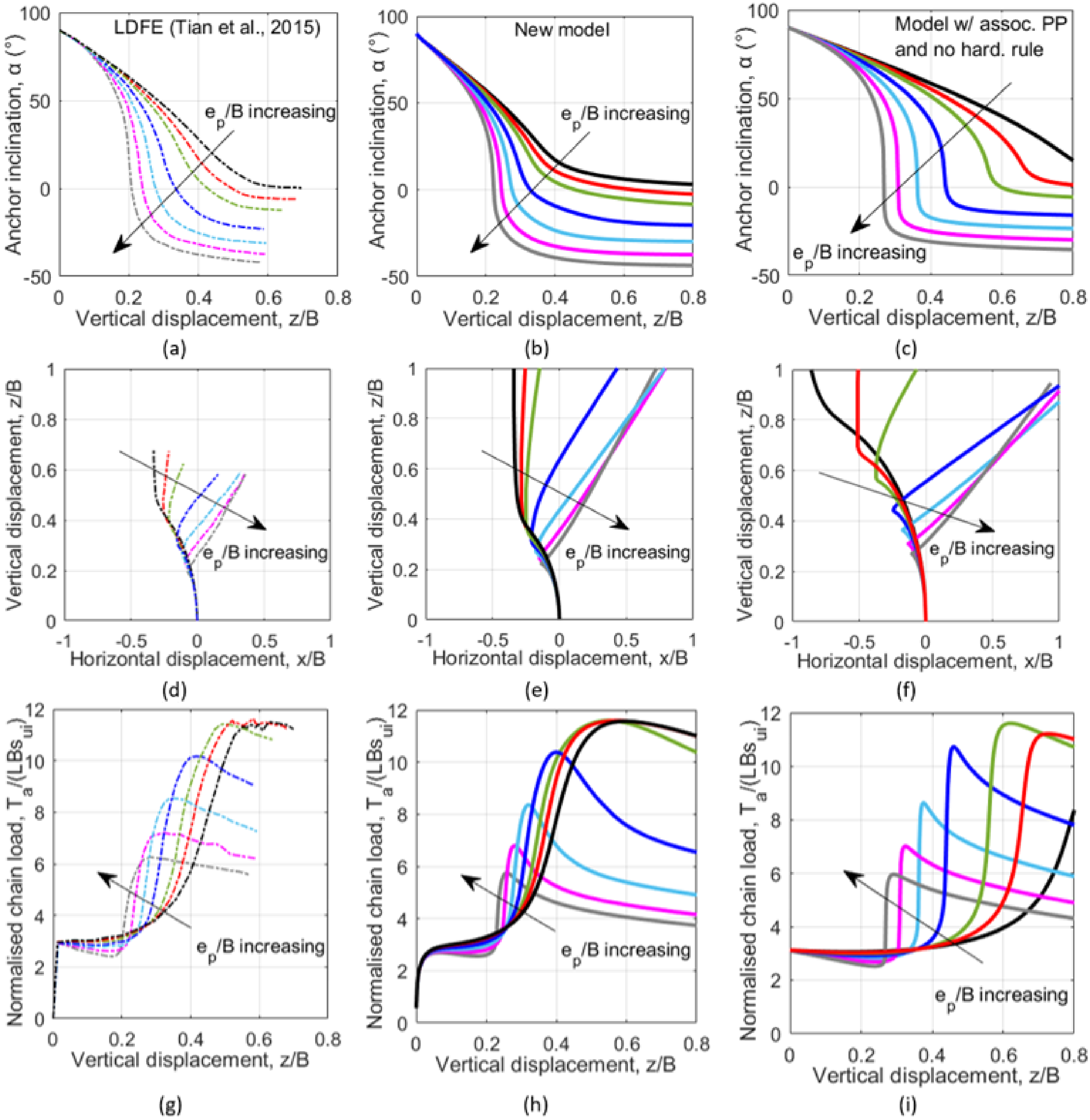

Figure 3.9 – Comparison of the rotational behaviour of macro-element models with LDFE simulations by Tian et al. (2015) for e_n/B=0.5 and e_p/B=0, 0.05, 0.1, 0.2, 0.3, 0.4 and 0.5: (a), (c), (e) model with associated plastic potential and no hardening rule (m = 4, n = 3 and q = 4.5); (b), (d), (f) model with non-associated plastic potential (ξ = 1.6, χ = 1.1, ω = 1.5) and strain-hardening rule (R_0 = 2.5).

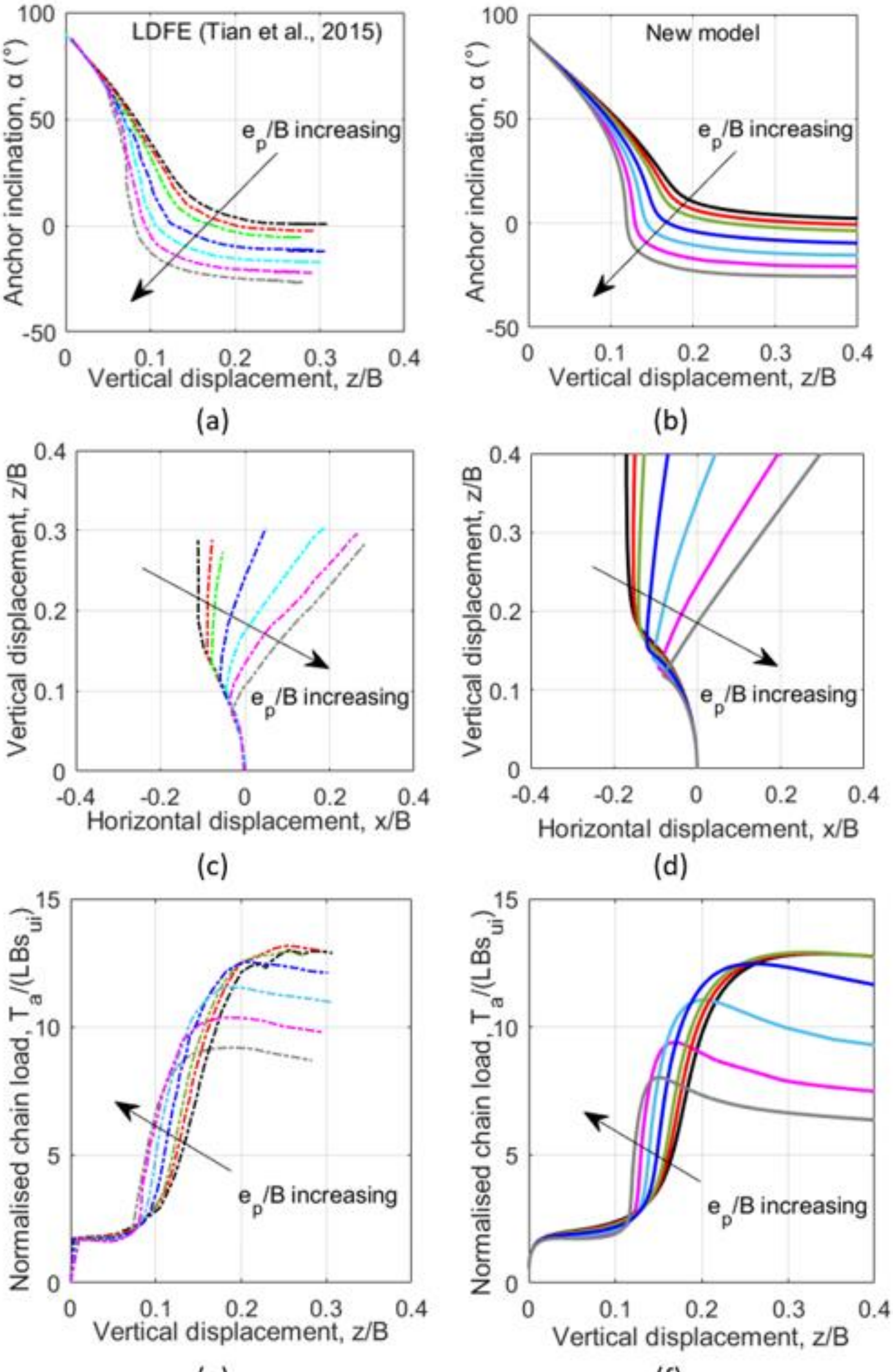

(a) (b)

(c) (d)

(e) (f)

Figure 3.10 – Comparison of the rotational behaviour of macro-element models with LDFE simulations by Tian *et al.* (2015) for e_n/B=1.0 and e_p/B=0, 0.05, 0.1, 0.2, 0.3, 0.4 and 0.5: (a) force-displacement, (b) anchor inclination and (c) anchor trajectory results of the model with non-associated plastic potential (ξ = 1.6, χ = 1.1, ω = 1.5) and strain-hardening rule (R_0 = 2.5).

3.5.4. Further validation

In this section, the proposed macro-element model is further challenged against other sets of numerical and experimental data from the literature to show the model capabilities for different loading and geometrical conditions. The same model parameters as previously calibrated in the section 'Calibration' are assumed here, with the exception of the parameter ω, which will be adjusted to reproduce the observed pre-failure behaviour (i.e. padeye travel distance to peak load) of the plate anchors. In cases where the macro-element model is compared with LDFE, the anchor is 'wished-in-place'. For cases where it is compared with centrifuge tests, remoulding is not accounted for due to the lack of post-installation characterisation of the soil.

3.5.4.1. Comparison with LDFE and centrifuge test under vertical pull-out

Model capabilities are assessed here against numerical (Wang et al. 2011) and centrifuge results in transparent soil (Song et al. 2006, 2009) on vertically installed plate anchors subjected to vertical monotonic ($\theta_0 = \theta_a = 90°$) pull-out at the mudline. It is worth noting that transparent soils are artificial soils and might not behave as a real soil. The representativeness of the transparent soil with respect to a real soil has not been investigated in this thesis, and it has been assumed that the undrained shear strength parameters provided in the original publication are representative for real soils as well as for transparent soils.

Anchor geometry and soil properties are presented in Table 3.1 and the results are presented in Figure 3.11. It can be observed that LDFE and centrifuge test data exhibit different anchor capacities. Wang et al. (2011) suggest that remoulding of the soil during anchor installation and degradation of the undrained shear strength s_u is the reason for the lower experimental capacity in comparison with the LDFE result. The same study reports that T-bar tests showed a 25% reduction in resistance during extraction compared with during penetration. Therefore, the macro-element model simulations are carried out with the original undrained shear strength (s_u=18 kPa) to match the final capacity for LDFE data and with a degraded undrained shear strength reduced by 25% (s_u=13 kPa) to match the final capacity for the centrifuge test as shown in Figure 3.11b. The model parameters remain unchanged and assume the same value as in the previous challenging exercise (ξ = 1.6, χ = 1.1, ω = 1.5 and R_0 = 2.5). There is a clear practical advantage in assuming fixed values for these parameters and this thesis shows that the adopted values can provide satisfactory simulations for several cases.

The comparisons of the rotational behaviour in Figure 3.11a shows that the model simulation lies between centrifuge and LDFE results. Whereas reducing the undrained shear strength from 18 kPa to 13 kPa is not sufficient to match the experimental curve, the difference can be explained by the experimental set-up. The macro-element model simulation assumes that the anchor padeye is pulled at a constant angle θ_a of 90^0, which makes the anchor progressively rotate until becoming horizontal (perpendicular to the direction of pulling) at large displacements. In the centrifuge test, instead, the pulley was initially located just above the padeye but, as the anchor is being pulled, a misalignment between the padeye and pulley is created due to the horizontal displacement of the anchor padeye. This misalignment can explain the difference between centrifuge and macro-element (and LFDE) results as well as the residual final orientation of 10^0 observed in the centrifuge test (Song et al. 2009; Wang et al. 2011). The results obtained from the model with associated flow rule and without hardening show that, for this model, the vertical displacement of the anchor is significantly overestimated (Figure 3.11b) when compared to the centrifuge and LDFE data.

Comparison among force-displacement trends in Figure 3.11c shows that the model-predicted anchor peak capacities agree well with centrifuge and LDFE data. However, the model predicts a lower displacement at mobilisation of the peak resistance. This slight difference may be explained by the assumption made for the calculation of chain displacement which, in the macro-element, is considered to be equal to the variation of the linear distance between the padeye and pulley neglecting any curvature of the chain after anchor installation. Conversely, the force-displacement curve for the associative model without a hardening rule (Figure 3.11d) does not capture the non-linear response at the early stages of keying, while the peak resistance is mobilised after a slightly higher displacement if compared to the non-associative plastic potential case.

3.5.4.2. *Comparison with LDFE and centrifuge testing under inclined pull-out*

The performance of the new macro-element model was also verified through comparison with the results published by Cassidy et al. (2012) for monotonic inclined pull-out ($\theta_0 = 40°$), as shown in Figure 3.12. The parameter ω was calibrated against the rotation (Figure 3.12a) and trajectory (Figure 3.12b) plots from the LDFE analysis, and a value of 1.75 was found to be the best fit. The anchor rotation (Figure 3.12a) predicted by the new model shows good agreement with LDFE results and reasonable agreement with centrifuge PIV. The vertical displacement at $\alpha \approx 60°$, for example, is z/B = 0.104 for the LDFE, z/B = 0.096 for the new macro-element model (i.e. 7.7% lower) whereas for the associative model, z/B = 0.244 (i.e. 135% higher than the LDFE). The new model's result shows that the anchor continues to rise vertically, as opposed to the model with associated plastic potential, which shows an anchor re-embedment beyond a certain point ($\alpha \approx 40°$). This can be explained by the change in the shape of the surface that governs the direction of displacements and rotations, as previously shown in Figure 3.7. The deviation between the centrifuge PIV and LDFE results can be attributed to the experimental set-up (Cassidy et al. 2012), where the anchor is continuously pulled (with θ_0 increasing progressively) and not dragged with θ_0 remaining constant, as implied by LDFE models and by the proposed model.

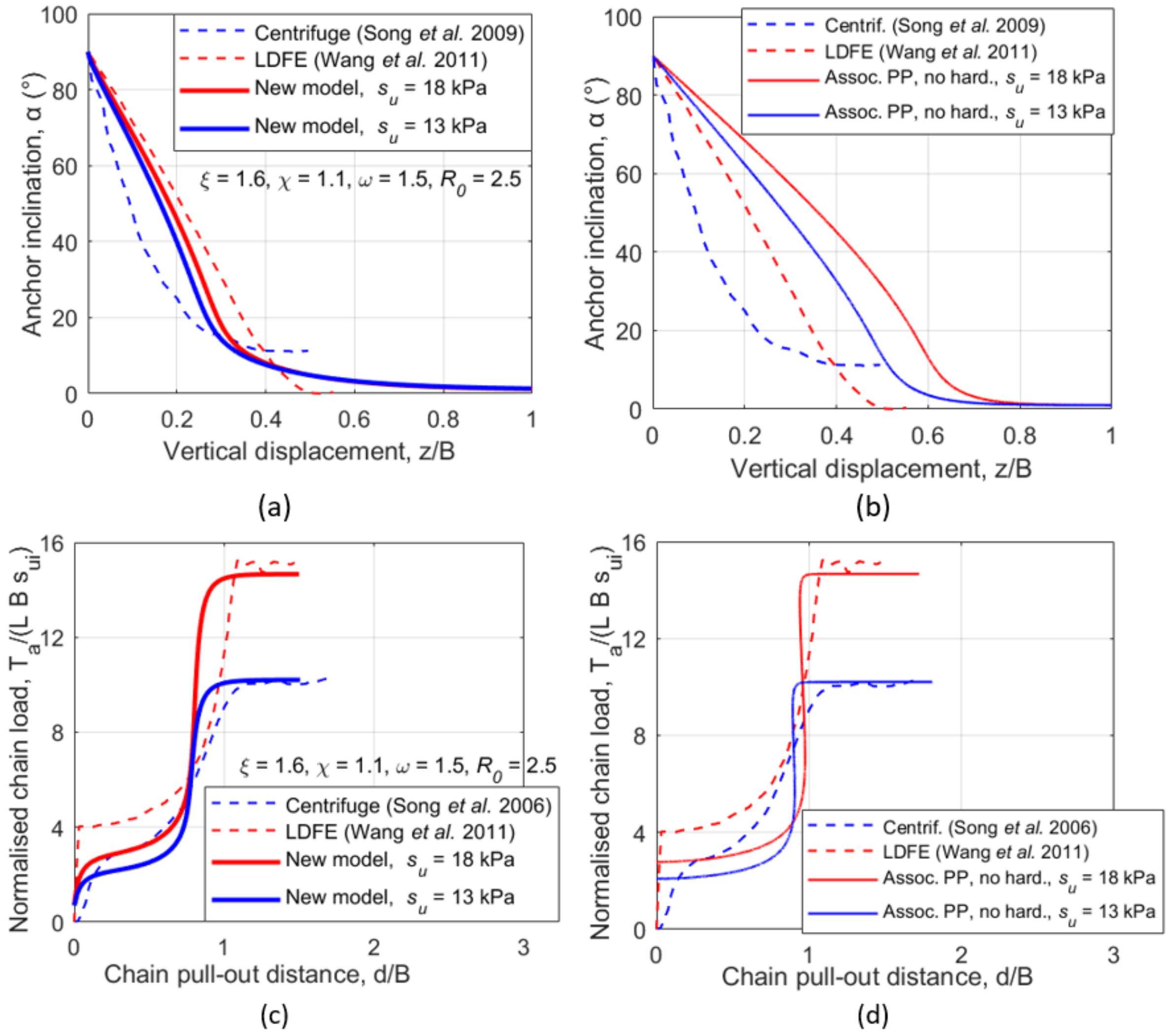

Figure 3.11 – Comparison between results from centrifuge tests (Song *et al.* 2006, 2009), LDFE analyses (Wang *et al.* 2011) and macro-element model: Rotation under vertical pull-out ($\theta_0 = \theta_a = 90°$) (a) for the new model and (b) for the associative model; normalised force-displacement (c) for the new model and (d) for the associative model.

In terms of anchor trajectory (Figure 3.12b), the results from the new model also show good agreement with LDFE and centrifuge PIV. The initial vertical and backward motion is reduced in comparison with the model with associated plastic potential. The maximum backwards displacement from the new model is x/B = -0.021, which is only 5% larger than the displacement from the LDFE analysis (x/B = -0.020), whereas for the non-associative model the backwards displacement is almost 3 times as large (x/B = -0.058). Furthermore, the new non-associative model, the re-embedment at large displacements is avoided.

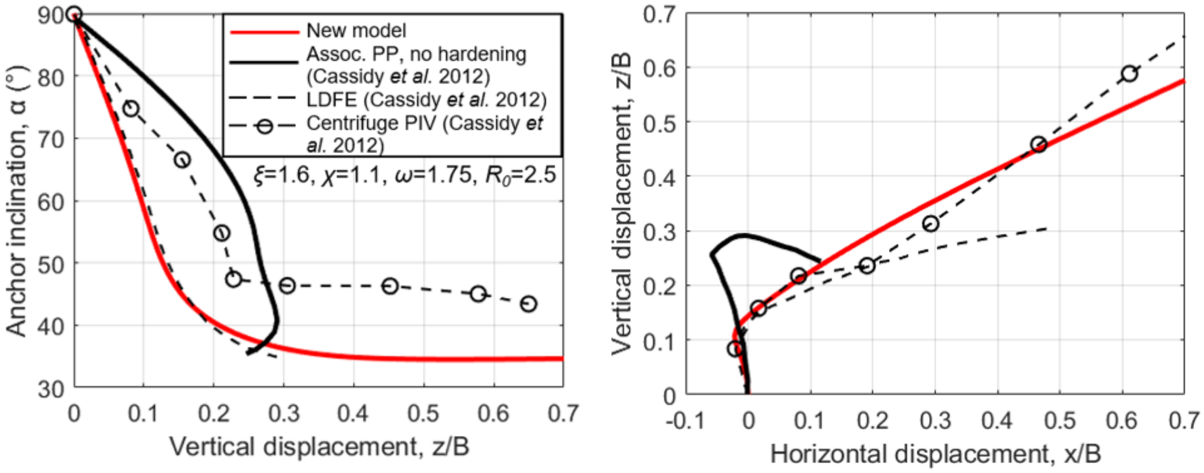

(a) (b)

Figure 3.12 – Comparison of (a) anchor rotation and vertical displacement; and (b) trajectory, for centrifuge test, LDFE analysis and macro-element models under inclined pull-out (θ0 = 40°).

3.5.4.3. *Effect of caisson extraction method in SEPLA's*

Gaudin et al. (2006) carried out several centrifuge modelling tests on a square SEPLA in kaolin clay subjected to monotonic inclined pull-out (θ_0 = 45°) (see Table 3.1 for details), with various caisson extraction processes after suction installation of the anchor: reverse pumping versus vented pull-out extraction; short term versus long term pull-out (time allowed between end of installation and anchor pull-out). Three cases are presented in Figure 3.13: PE-LT (reverse pumping extraction, long-term pull-out), VE-LT (vented extraction, long-term pull-out) and VE-ST (vented extraction, short-term pull-out).

The results presented in Figure 3.13 (where s_{up} is the undrained shear strength at the estimated anchor embedment depth at the peak load) show that it is possible to fit the force-displacement curves for distinct retrieval methods by varying the parameter ω, while keeping the other plastic potential parameters unchanged with respect to the initial calibration. For comparison, the curve predicted using a model with associated plastic potential and without hardening rule is also shown in Figure 3.13 and lies between the VE-LT and VE-ST experimental load-displacement curves.

For the proposed non-associative hardening model, good agreement is observed for all the three curves, and the prediction of the initial part of the curve is much improved due to the addition of the hardening rule when compared with the model without such ingredient. Furthermore, the peak load is well captured and so is the vertical displacement at which the peak load is reached. However, it is worth noting that a hardening parameter R_0 = 0.3 was adopted in all three simulations, as opposed to R_0 = 2.5 in all other simulations carried out in this chapter. This may be related to the soil disturbance caused during installation and extraction of the caisson, but also to some simplifying assumptions in the experimental determination of the initial loss of embedment as discussed in the original paper (Gaudin et al., 2006). The influence of installation and extraction processes is of interest for further research, as the relationship between such aspects and the parameters ω and R_0 could be further explored and rationalised.

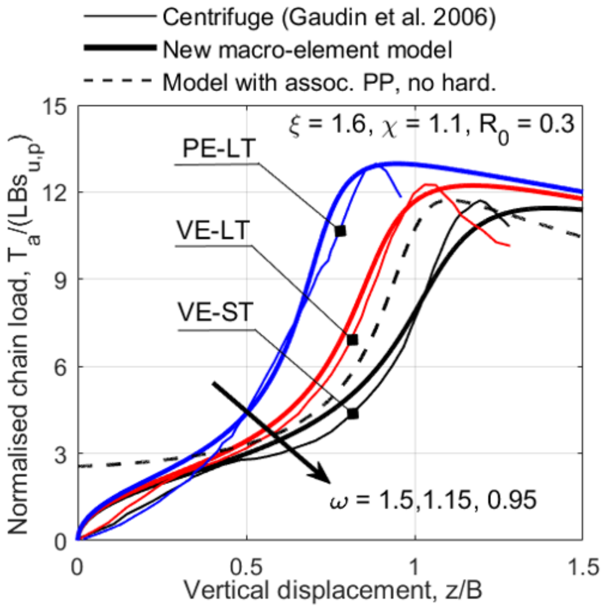

Figure 3.13 – Inclined pull-out (θ0 = 45°) of SEPLA for distinct caisson retrieval methods: reverse pumping (PE), vented pumping (VE), with short-term (ST) and long-term (LT) anchor pull-out – comparison of centrifuge tests (Gaudin et al. 2006) with macro-element models.

3.6. Plate anchors kinematics under cyclic loading

The model presented in this chapter was initially developed for undrained monotonic loading. This model can be expanded to account for the effects of plate anchor kinematics by modifying the hardening and plastic potential rules in order to account for repeated load reversals. These improvements presented are only the first stage of a larger modelling development task and, in this chapter, material's effects such as soil's strength changes due to pore pressure generation or de-structuration are neglected. Despite this simplification (which will be addressed in the next Chapters), the model offers valuable insight on how cyclic variation of anchor's kinematics (e.g. progressive cyclic re-orientation) affects the overall anchor performance and capacity.

In Equation (3.10) presented previously, the exponential form of the expression made ρ_c increase quickly for small displacements and slowly for higher displacements, as it is expected for the force-displacement behaviour of structures embedded in or supported by the soil.

During unloading-reloading cycles, however, the mathematical form of the hardening rule must change since the final target of the term ρ_c depends on the loading conditions: 1 for loading and -1 for unloading. Indicating with $\rho_{c,i}$ the form of evolution for ρ_c during the loading portion i, with i being the consecutive number of loading or unloading cycles applied, the hardening rule assumes the following form:

$$\rho_{c,i} = \pm 1 - \left(\pm 1 - \rho_{cR,i-1}\right) \mathrm{e}^{-R_0\sqrt{(w-w_{R,i-1})^2+(u-u_{R,i-1})^2+\left(B\,(\beta-\beta_{R,i-1}\right)^2}} \qquad (3.17)$$

where the sign '+' holds for loading conditions and the sign '-' for unloading. The quantities $\rho_{cR,i-1}$, $w_{R,i-1}$, $u_{R,i-1}$ and $\beta_{R,i-1}$ are the values of ρ_c, w, u and β at the end of the previous loading packet (LP), i.e. the point of load reversal. Figure 3.14 schematically shows the evolution of the term ρ_c and the values of the quantities $\rho_{cR,i-1}$, $w_{R,i-1}$, $u_{R,i-1}$ and $\beta_{R,i-1}$ for four loading/unloading cyclic packages.

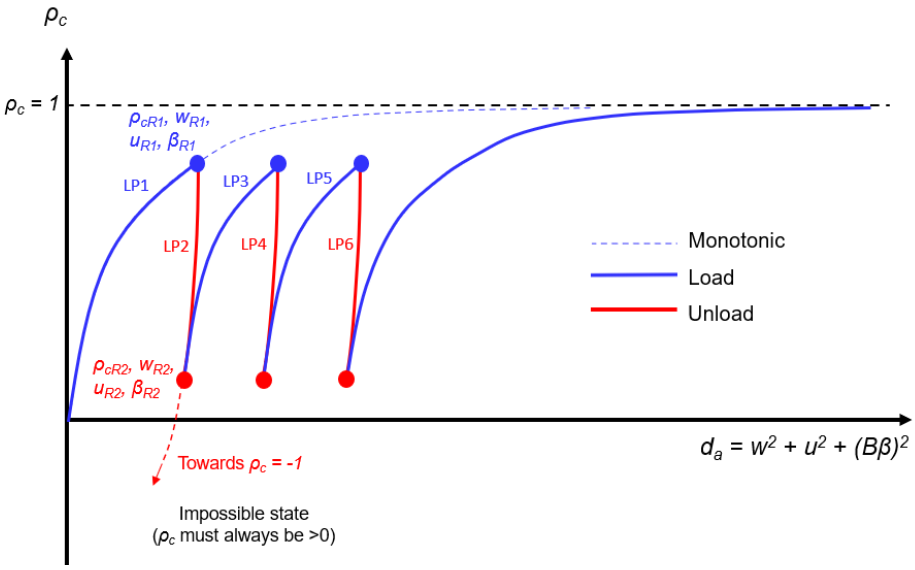

Figure 3.14 – Representation of the hardening term ϱc under unloading-reloading behaviour.

Extension to cyclic loading of the incremental displacement definition could consider a procedure involving the mapping of the flow direction on the opposite side of the load reversal point. However, taking advantage of an assumed symmetry for the model surfaces, this can be accounted by simply changing the sign of the incremental displacement definition previously presented in Equation (3.12), depending on whether the anchor is being loaded or unloaded. It assumes the form shown in Equation (3.18).

$$\begin{pmatrix} \delta w \\ \delta u \\ B\delta\beta \end{pmatrix} = \lambda \begin{pmatrix} t\,\partial g/\partial V \\ t\,\partial g/\partial H \\ t\,\partial g/\partial(M/B) \end{pmatrix} \tag{3.18}$$

where the t assumes the value of 1 for loading and -1 for unloading conditions, respectively. A more rigorous approach, in which the sign of the flow rule comes by mapping the flow direction to the plastic potential surface on the opposite side of the return point will be employed in the next chapter.

The effect of number of cycles and cyclic load ratio level (CLRL = Q_c/Q_u, where Q_c is the cyclic load amplitude and Q_u is the monotonic pull-out capacity of the anchor) on the post-peak pull-out resistance and cyclic displacement accumulation is assessed for a vertical SEPLA anchor (initially $\beta = 0°$) subjected to vertical loading ($\theta_a = \theta_0 = 90°$). Anchor and soil properties used in the analyses are the same as for Cassidy et al. (2012) ($B = 4.64$ m, $L = 7.92$ m, $e_n = 2.59$ m, $e_p = 0.492$ m, initial embedment 20.25 m, s_{u0} = 1.0 kPa, k_{su} = 1.25 kPa/m) whereas the model parameters assume the value previously calibrated for this anchor ($m = 2$, $n = 4$, $p = 1$, $q = 4$, $\xi = 1.6$, $\chi = 1.1$, $\omega = 1.75$ and $R_0 = 2.5$), as previously shown in Figure 3.12.

3.6.1. Effect of number of cycles

The effect of number of cycles (N_{cyc}) in the post-cyclic resistance can be visualised in Figure 3.15. Figure 3.15a shows the force-displacement behaviour of the anchor subjected to post-cyclic pull-out after different number of cycles (CLRL = 0.60). The peak post-cyclic resistance decreases with increasing number of cycles (Figure 3.15a). This can be attributed to the fact that as cyclic loads are applied, the anchor re-orientates to find the path of least resistance towards the peak capacity, modifying the forces V, H and M through the equilibrium equations. As a consequence of that, the loading path moves further away from the strength surface F, reducing the loads V, H and M and hence reducing the anchor load T_a. This can be visualised clearly in Figure 3.15b, where the loading paths for 5 and 10 cycles approach the centre of the strength surface and follow a path of less resistance towards its peak load. It can be observed that the cyclic loading paths only reach the strength surface at the end of the keying process, whereas for monotonic load this is achieved at an earlier stage.

Another aspect that can be analysed is the effect of number of cycles on the anchor rotation and trajectory. The circled area in Figure 3.16a reveals that the rotation increases during cyclic loading, which causes a reduction in the loss of embedment but an increase in the horizontal displacement, as shown in Figure 3.16b. The re-orientation starts at an approximate angle of 20°, which governs the redistribution of forces V, H and M as explained previously. Whereas the cyclic loading does not seem to affect the final orientation of the anchor when subjected to post-peak pull-out, the trajectory is slightly affected.

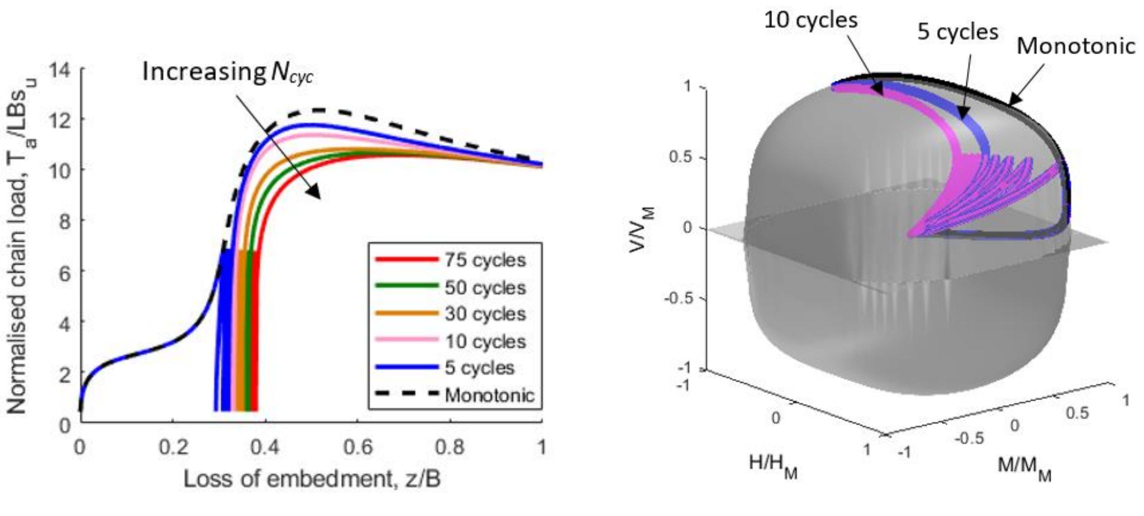

(a) (b)

Figure 3.15 – Model results for post-cyclic vertical pull-out (CLRL = 0.60) and different numbers of cycles: (a) force-displacement and (b) loading paths.

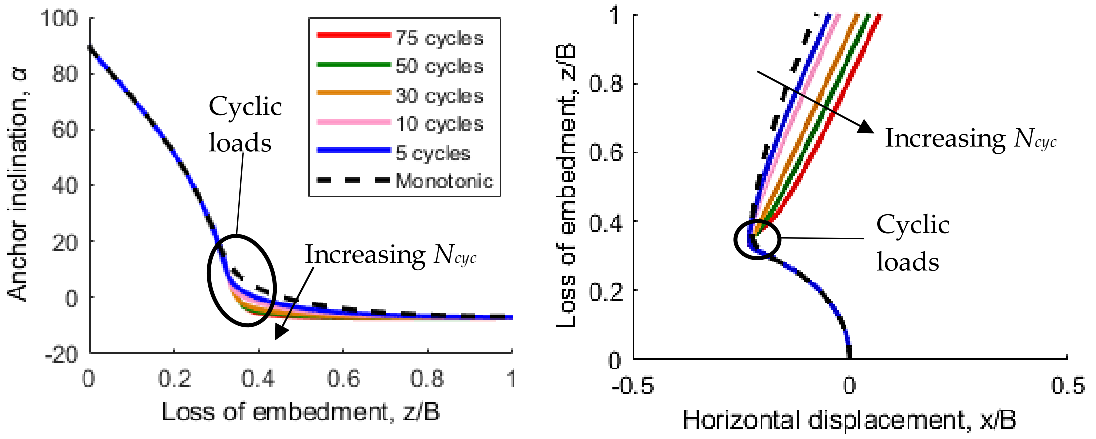

(a) (b)

Figure 3.16 – Model results for post-cyclic vertical pull-out (CLRL = 0.60) and different numbers of cycles: (a) anchor rotation and (b) trajectory.

3.6.2. Effect of cyclic amplitude

Figure 3.17 presents the effect of cyclic amplitude (CLRL) in the post-peak pull-out resistance of the anchor after being subjected to 50 cycles of vertical load. As expected, the post-cyclic pull-out behaviour is affected by the load amplitude. A reduction of the peak resistance is observed for higher CLRLs in Figure 3.17a, which was previously reported by Singh (1998) for circular plate anchors subjected to cyclic loads. Furthermore, a rigid behaviour can be observed during unloading, as a consequence of the current load state ρ_c moving towards the asymptotic value of -1 during unloading (Equation (3.17)). From Figure 3.17b, it can be observed that load paths for cycles with higher amplitudes move faster towards the centre of the strength surface, reducing the loads V, H, M and T_a and hence decreasing the post-peak pull-out resistance. This behaviour is similar to the one observed in Figure 3.15b.

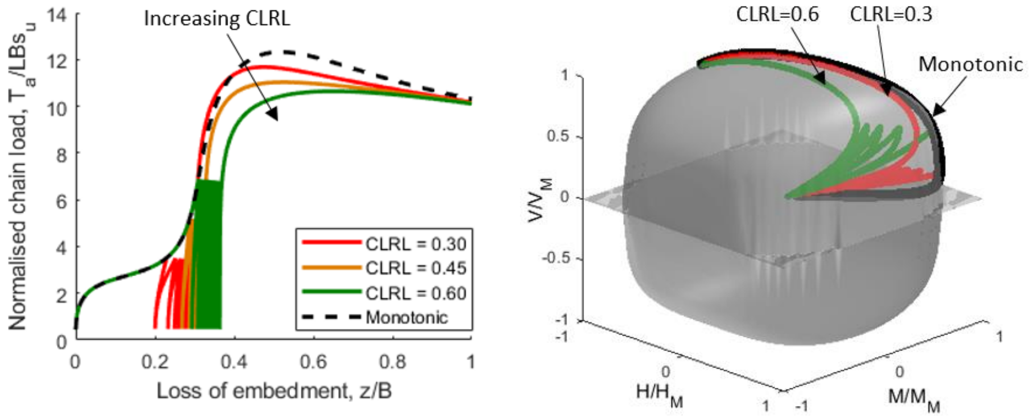

(a) (b)

Figure 3.17 – Model results for cyclic vertical pull-out for different CLRL's: (a) force-displacement and (b) loading paths.

3.6.3. Analysis of results

The post-cyclic peak capacity was shown to decrease with increasing number of cycles and with increasing cyclic amplitude. Furthermore, anchor rotation increases with the number of cycles, whereas loss of embedment seems to increase. Although the results presented in this section are difficult to validate – as the variations in soil strength cannot be prevented in real experiments – the results suggest that the anchor's capacity decrease occurs not only due to changes in soil's conditions, but also to the particular evolution of anchor's kinematics caused by anchor re-orientation to find the path of least resistance towards the strength surface F.

However, changes in soil strength should be considered in combination with the evolution of anchor kinematics. The centrifuge tests carried out by Zhou et al. (2020) on an anchor subjected to purely normal load (i.e. without anchor rotation) showed that the variation in soil strength can lead to significant changes in anchor capacity.

In the next Chapter, a new macro-element modelling approach that includes the effects of changes in soil strength will be presented. This approach will combine the effect of anchor kinematics with the evolution of soil strength due to not only cyclic loading, but also long periods of maintained loading.

3.7. Conclusions

An improved macro-element model for vertically installed plate anchors was proposed in this chapter and compared to a previously published model. The proposed model includes (i) a non-associated plastic potential and (ii) a strain-hardening rule into the plasticity theory framework. Four new parameters (three for the plastic potential and one for the hardening rule) were included and calibrated with an LDFE analysis from Tian et al. (2015). The results of model simulations were compared with four other studies, including results from LDFE simulations and centrifuge tests with PIV measurement technique. The following conclusions can be drawn:

- The proposed macro-element model was shown to be an effective tool to predict the force-displacement, rotation and trajectory of plate anchors covering distinct anchor geometries, soil properties and loading conditions.
- The addition of a non-associated plastic potential is fundamental to predict the expected trajectory of the anchor during keying avoiding large initial backwards and upwards movements and allowing the control of the direction of anchor motion. It is also essential to predict the anchor vertical displacement at peak load.
- Validation of the model against four different sets of numerical and centrifuge data suggests that fixed values of the newly introduced parameters ξ = 1.6, χ = 1.1 can be assumed while only the parameter ω should be calibrated for practical use. Variation of the parameter ω was also found to be effective in capturing the influence of different anchors' installation methods.
- It is desirable to calibrate the model's parameters against a limited set of centrifuge experimental data, numerical simulations or field tests (one or more) in order to apply the proposed macro-element model for design purposes. The calibration procedure could use the strategy identified in the model calibration section of this chapter. Since the values of parameters adopted (ξ = 1.6, χ = 1.1, ω = 1.5 and R_0 = 2.5) seem to produce satisfactory simulations for most analysed cases, these may be used as starting point in

the calibration process. Alternatively, it may be also conceivable that such values may be used for initial/outline assessment of expected anchor behaviour in the field, for example to assess the effect of different anchor geometries, padeye eccentricities, load inclination and/or soil properties. Nevertheless, validation and challenging of the proposed model against real field data would be beneficial and boost the potential use of macro-element modelling in anchor design.

- An extension of the macro-element model to provide insights into the effect of anchor kinematics due to cyclic loading was presented. Macro-element analyses with the extended approach suggested that anchor's capacity decrease occurs not only due to changes in soil conditions, but also due to the evolution of anchor's kinematics due to anchor re-orientation to find the path of least resistance towards the strength surface F. The effect of changes in soil strength on anchor response will be addressed in the next chapter.

CHAPTER 4. A new macro-element modelling approach considering the evolution of soil strength

Objectives

- To propose a new macro-element modelling framework that accounts for changes in soil strength
- To present the assumptions, theoretical framework and modelling strategy
- To present the mathematical formulation of the model

Statement

Some extracts of this chapter have been published in a journal article in the Journal of Marine Science and Engineering (JMSE) on 13 February 2021, entitled 'A Cyclic Macro-Element Framework for Consolidation-Dependent Three-Dimensional Capacity of Plate Anchors'. The article has been published with the co-authorship of Dr Andrea Diambra, Dr Dimitris Karamitros and Dr Shiao Huey Chow. The full article can be found in the link: https://doi.org/10.3390/jmse9020199.

4.1. Introduction

The macro-element model presented in Chapter 3 was shown to be effective in predicting the response of vertically-installed plate anchors under undrained monotonic pull-out in clay. The evolution of pore water pressure and soil strength during long-term operation was, therefore, not accounted for directly. However, the evolution of soil strength and stiffness during operation has been recognised by several studies in offshore applications, most of them in shallow foundations (e.g. Lehanne & Jardine, 2003; Gourvenec & Randolph, 2010; Gourvenec et al., 2014). Changes in soil strength and stiffness due to set-up effects and cyclic loading have also been acknowledged in pile foundations (e.g. Jardine & Standing, 2012; Tsuha et al., 2012; Ciavaglia et al., 2017), and for a number of other geotechnical applications during 'whole-life' operations (Gourvenec, 2018). In particular for plate anchors, to date only a few studies that quantify the evolution of soil strength with time have been carried out (Wong et al., 2012; Han, 2016; Han et al., 2016; Zhou et al., 2020), though this has not been incorporated into macro-element models.

In that context, this chapter presents a new macro-element modelling framework to account for changes in pore water pressures and effective stresses of the soil within a macro-element modelling approach. The incorporation of such features into the macro-element model aims to reproduce typical features of whole-life anchor operation such as consolidation, pore water pressure build-up during cyclic loading, and rate effects, which will be analysed in Chapters 5 and 6. The modelling framework expands the macro-element model presented in Chapter 3 and combines it with a simple one-dimensional model of shearing and consolidation for a representative soil element around the anchor. The addition of the representative soil element into the macro-element model aims at incorporating these features by tracking the effects of pore pressure generation and changes in effective stress on the soil strength, which in turn governs the anchor capacity in the macro-element model.

4.2. Modelling strategy

A visual representation of the adopted modelling strategy is shown in Figure 4.1. The approach combines a macro-element for the anchors with a simple one-dimensional undrained shearing and consolidation model for a soil element representative of the whole soil mass. The macro-element model governs the force–displacement behaviour and kinematics of the anchor, while the one-dimensional undrained shearing and consolidation model for the soil tracks the evolution of pore water pressure generation, effective stress and soil density, which govern the current strength of the soil (τ_c) on which the capacity of the anchor depends. This implies that the capacity factors of the anchor, N_v, N_h and N_m, previously defined in Equations (3.6) through (3.8) and dependent on a constant undrained shear strength (s_u) for a certain depth in Chapter 3, are now given by Equations (4.1) through (4.3), in which the capacities depend on the current soil strength τ_c (defined later in this Chapter), which varies according to the response of the representative soil element.

$$N_v = V_M/(L\,B\,\tau_c) \tag{4.1}$$

$$N_h = H_M/(L\,B\,\tau_c) \tag{4.2}$$

$$N_m = M_M/(L\,B^2\,\tau_c) \tag{4.3}$$

Since the loading and failure of an anchor are closely related to shear stress mobilisation and shear failure in the soil around the anchor, a simple one-dimensional shearing condition was selected as the stress path for the representative soil element. This soil element allows for estimation of the amount of shear stress mobilised in the soil, which governs the shear-induced excess pore water pressure generation, as a function of the anchor loading. The constitutive model for the representative soil element will be discussed in sections 4.4 and 4.4.2, whereas the macro-element model of the anchor was described in Chapter 3. The two models are linked by some compatibility conditions which, among others, impose that the mobilised capacity in the anchor is equal to the mobilised strength in the soil. This will be further discussed in section 4.5.

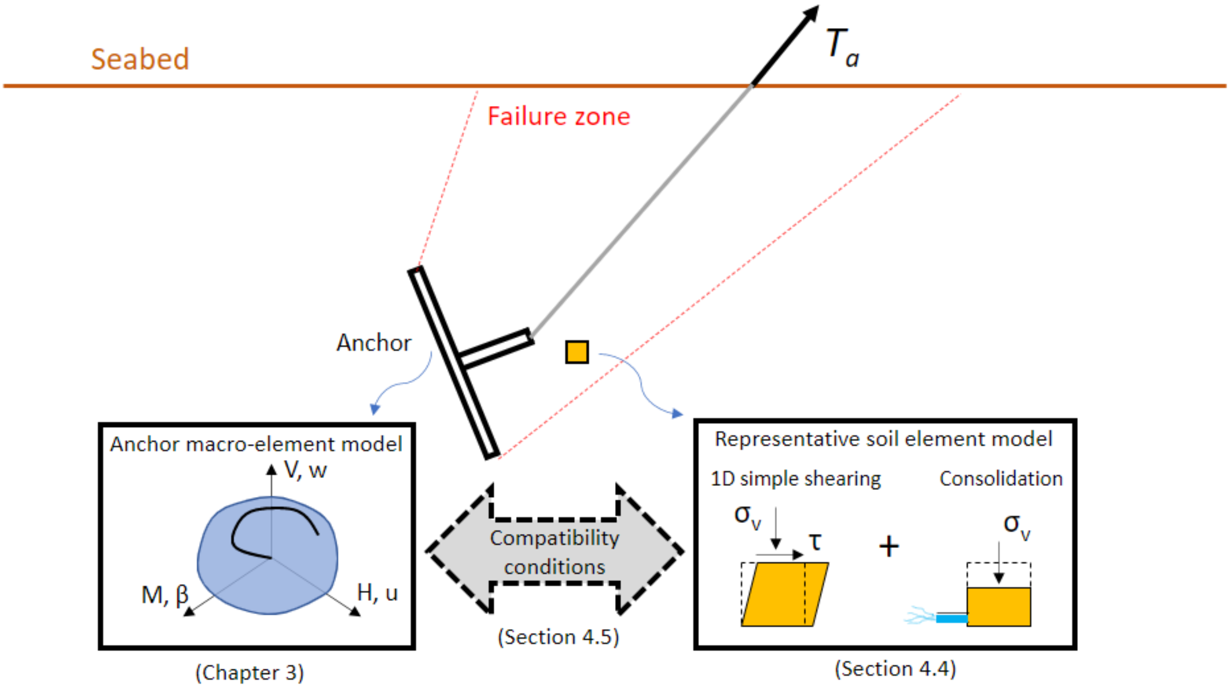

Figure 4.1 – Relationship between the macro-element model for the anchor and the soil constitutive model.

It should be clarified that the representative soil element is an idealised concept and its location with respect to the anchor is unknown. However, since the anchor's capacity is typically related to the undrained shear strength at the depth of the anchor mid-point, it is initially assumed that the representative soil element lies at such depth. Nevertheless, this condition can be easily altered if required in future developments of the model. The effect of assuming a constant or variable depth of the representative soil element will be further discussed in Chapter 6.

The new macro-element framework requires a number of modelling ingredients, which may acquire different formulations as the ones used in this thesis. The modelling framework follows the structure described below:

- Macro-element model for the kinematics of the anchor under monotonic load
- One-dimensional consolidation model for the representative soil element:
    a. normal consolidation line (NCL)
    b. rule for pore water pressure dissipation
- One-dimensional undrained shearing model for the representative soil element:
    a. critical state line (CSL)
    b. state parameter ψ
    c. elastic properties
    d. bounding surface (current strength)
    e. stress-dilatancy rule (flow rule)
    f. hardening rule
    g. stress-strain relationships
- Soil-anchor compatibility conditions
    a. mobilised anchor capacity and mobilised soil strength
    b. current soil strength governing the capacity surface of the anchor

Detailed description of the modelling ingredients is provided in the following sections.

4.3. Expansion of anchor macro-element model to cyclic loading

The extension of the macro-element model presented in Chapter 3 to cyclic loading involves two modifications: (i) on the plastic potential mapping rule; and (ii) on the hardening rule previously presented in Equation (3.10).

The plastic potential is now calculated on the image point on the capacity surface (point **Q_i**), defined through a radial mapping rule passing through the current load (point **Q**) from the origin (point **O**), as shown in Figure 4.2. Although by imposing the change of the sign in Equation (3.18) would not affect the results since all quadrants in the *V-H-M* space are identical, that would imply a concave potential surface and a flow inwards into the capacity surface, which is theoretically incorrect in light of Drucker's stability postulation (Drucker, 1958).

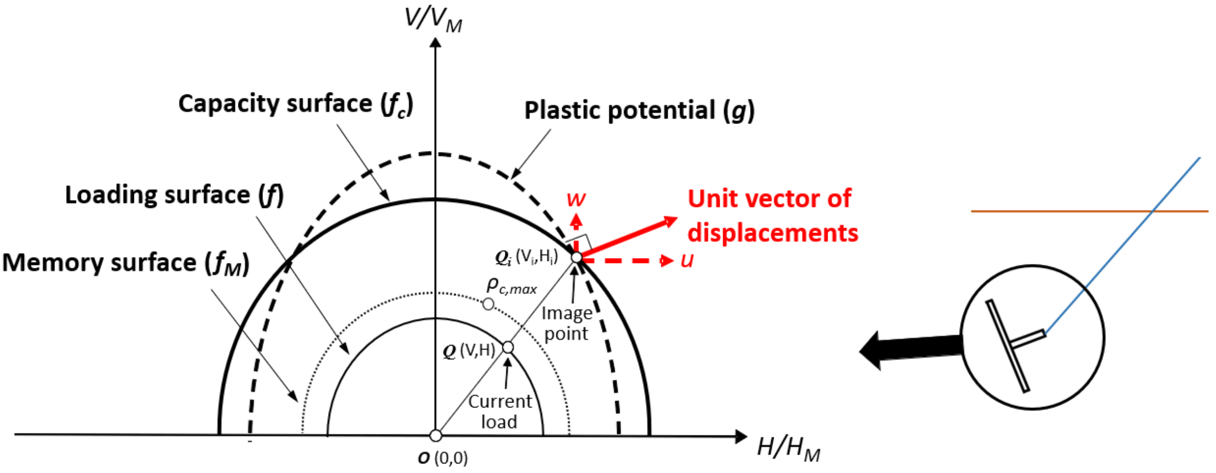

Figure 4.2 – Schematic two-dimensional representation ($M/M_M=0$) of the model surfaces, force state and plastic potential introduced in the proposed macro-element model for the plate anchor.

The modification of the hardening rule, similarly to the modification presented in Equation (3.17) in Chapter 3, considers a modified origin which takes into account the load reversal point and a different target value at large displacements, depending on the loading condition: 1 for loading and -1 for unloading. Whereas in Chapter 3 the hardening rule for cyclic loading was presented in a finite form, an incremental form is used throughout this chapter for a more generalised account of the non-monotonic variation of ρ_c. Both finite and incremental forms present similar results and can easily be interchanged. In an incremental form, the hardening rule, analogous to that proposed by Nova & Montrasio (1991), takes the form:

$$\delta\rho_c = R_0 \delta d_a \tag{4.4}$$

where the travel distance δd_a is defined as:

$$\delta d_a = \sqrt{(\delta w)^2 + (\delta u)^2 + (B\delta\beta)^2} \tag{4.5}$$

and the total distance travelled by the anchor is $d_a = \Sigma(\delta d_a)$.

When expanded to cyclic loading, the expression of the hardening term $\rho_{c,i}$ for a generic loading stage i (where i tracks the cumulative number of applied loading and unloading stages) follows an incremental form of Equation (4.4) but modified to account for an offset related to the point of load reversal:

$$\delta\rho_{c,i} = \left(\pm 1 - \rho_{cR,i-1}\right) R_0 \, \mathrm{e}^{-R_0\left(d_a - d_{a,R,i-1}\right)} \, \delta d_a \tag{4.6}$$

where the sign (+) holds for loading conditions and the sign (−) for unloading. The quantities $\rho_{cR,i-1}$ and $d_{a,R,i-1}$ are the values of ρ_c and d_a at the end of the previous loading packet (LP), i.e., the point of load reversal.

Figure 4.3 schematically illustrates the evolution of the term ρ_c and the values of the quantities $\rho_{cR,i-1}$ and $d_{a,R,i-1}$ for six loading/unloading cyclic packages followed by monotonic loading to failure. It is worth noting that negative values of ρ_c are not physically possible as and the curve is drawn in Figure 4.3 only to show the rationale and methodology for the extension from monotonic to cyclic loading.

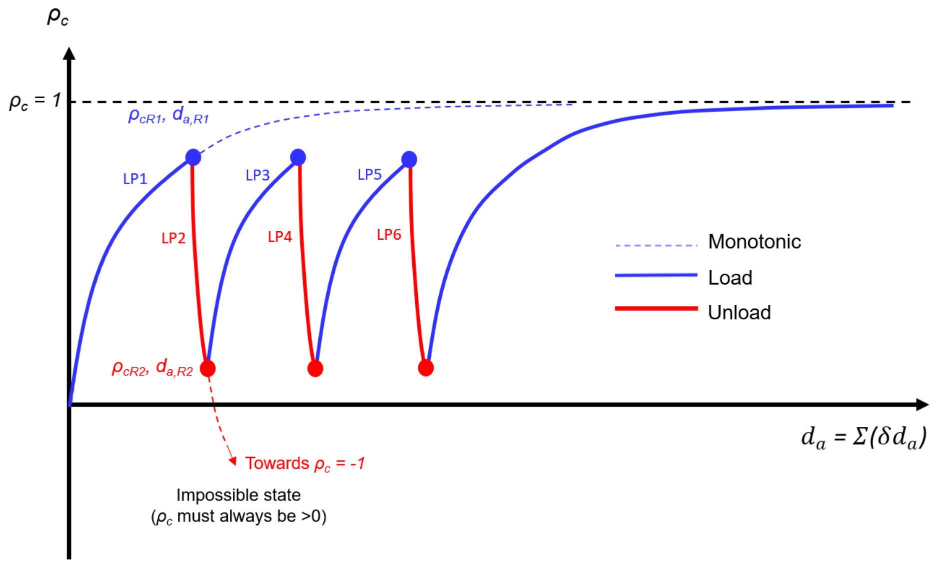

Figure 4.3 – Representation of the hardening term ρ_c under unloading–reloading behaviour.

Extension to cyclic loading of the incremental displacement definition is automatically captured by the flow rule for the anchor model defined in Equation (3.12), since the radial mapping rule (Figure 4.2) automatically considers the flow direction on the opposite side of the load reversal point. An additional surface, analogous to the memory surface framework proposed by Corti et al. (2016), is included in the model. The original memory surface framework tracked the load state already experienced by the soil and ensured the soil exhibited higher stiffness within this region. The memory surface employed in this thesis tracks the maximum value of the mobilised anchor capacity (ρ_{cM}). When in a virgin load state, the memory surface expands following the current value of ρ_c such that $\rho_{cM} = \rho_c$. When unloading occurs and the current load state has been experienced before, the memory surface retains its size and the current load state lies inside the memory surface. The stiffness of the anchor response depends on whether the current load state is inside or on the memory surface, as further explained in section 4.5.

4.4. One-dimensional model for representative soil element

In order to simplify the modelling of the soil behaviour, the processes of shearing and consolidation are decoupled. It is assumed that undrained shearing of the soil is triggered by the loading of the anchor, while consolidation is triggered by the process of pore water pressure dissipation with time during stages of maintained anchor loading or load application over a period of time. Partial drainage is therefore simulated through the application of fully undrained shear induced by the load followed by pure consolidation during a period of time equal to the duration of the load. This follows a similar approach to that employed in other studies, where partial drainage was simulated through a series of undrained loading phases followed by consolidation phases during which the load was kept constant (e.g. Gourvenec et al., 2014; Andersen, 2015; Flessati, et al., 2020). Fundamental model parameters are shared between the consolidation and shearing mechanisms as detailed in the following sub-sections. It is worth noting that it is assumed herein that partial drainage can be represented by uncoupled phases of undrained loading followed by consolidation. The potential effects of this assumption on the stiffness of the system was not investigated in the aforementioned studies.

4.4.1. One-dimensional consolidation model

The one-dimensional consolidation model for the soil follows the conventional yielding assumed for clays under one-dimensional compression (Muir Wood, 2004). As shown in Figure 4.4, the model considers the existence of a normal compression line (NCL) and an unloading–reloading line (URL) which are both linear in the specific volume (υ) versus ln σ' plane. The equation of the NCL can be expressed as

$$\upsilon_{NCL} = \Gamma_{NCL} - \lambda \, ln \, \sigma_v{}' \qquad (4.7)$$

where Γ_{NCL} is the intercept on the υ axis for σ' = 1 kPa and λ is its slope. The slope of the URL in the υ–ln σ' plane is defined by κ.

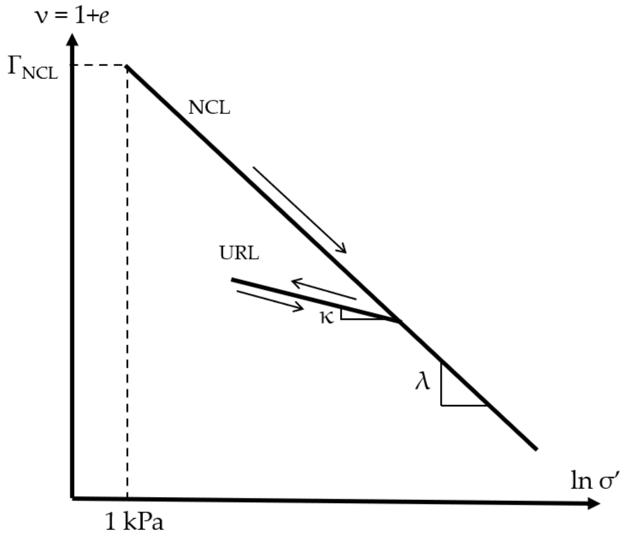

Figure 4.4 – Normal compression line (NCL) and unloading–reloading line (URL) represented in the specific volume versus vertical effective stress plane.

The process of consolidation is governed by the dissipation of the pore water pressure previously generated by the undrained shearing. Several expressions can be employed to model the pore water pressure dissipation. In this work, the hyperbolic relationship suggested by Singh & Chatterjee (2018) for plate anchors is adopted:

$$\frac{\Delta u_w}{u_{w,initial}} = \frac{1}{1 + \left(\frac{T}{T_{50}}\right)^a} \tag{4.8}$$

where $\Delta u_w / u_{w,initial}$ is the normalised excess pore pressure (Δu_w is the variation of excess pore pressure and $u_{w,initial}$ is the excess pore pressure available at the start of consolidation), a is a curve fitting parameter and T_{50} is the dimensionless time factor T for 50% dissipation of the initial excess pore pressure. The factor T is given by Equation (4.9), where c_v is the coefficient of consolidation and t_c is the time of consolidation.

$$T = c_v t_c / B^2 \tag{4.9}$$

The consolidation time t_c is reset to zero for each stage of consolidation. For instance, let us imagine that an initial stage of shearing of the soil generated an excess pore pressure $u_{w,initial} = 100$ kPa, after which a consolidation stage took place for a period of 1 hour with a variation of excess pore pressure $\Delta u_w = -10$ kPa (i.e. the excess pore pressure available is now 90 kPa). If a second shearing stage occurs, during which a further excess pore pressure of 30 kPa is generated, the available excess pore pressure for a subsequent consolidation stage is now $u_{w,initial} = 120$ kPa. During this consolidation stage, t_c is re-set to zero, and the variation of pore pressure Δu_w is calculated for each incremental step in time t_c.

4.4.2. One-dimensional undrained shearing model

The one-dimensional undrained shearing model builds upon a critical state theory and bounding surface plasticity framework to allow flexibility in model capabilities and the application to a large range of soils from clays to sand. However, the model application to undrained shearing conditions only combined with the unnecessity to track the evolution of soil strains considerably simplifies the required modelling equations as shown later in this section.

A schematic view of the model behaviour is shown in the shear stress (τ) versus effective stress (σ') plane (Figure 4.5) and in the specific volume (v) versus ln σ' plane (Figure 4.6). As is typical of direct simple shear tests, the total vertical stress σ is assumed to be constant during undrained shearing; therefore, any changes in the vertical effective stress σ' are assumed to be due to the variation in the pore pressure u_w.

4.4.2.1. *Critical state line*

The critical state line (CSL) is linear in the υ versus ln σ' plane and parallel to the NCL defined in the one-dimensional consolidation model. The equation for the CSL is

$$\upsilon_{CSL} = \Gamma_{CSL} - \lambda \, ln \, \sigma_v' \tag{4.10}$$

where Γ_{CSL} is the intercept on the υ axis for $\sigma' = 1$ kPa of the CSL. In the τ–σ' plane, the CSL is also linear and defined by the equation

$$f_{CSL}\,(\sigma') = \tau_{\mathrm{CSL}} - t\,\sigma_v' \tan \varphi_{cs} \tag{4.11}$$

where φ_{cs} is the critical state friction angle and t assumes the value of 1 for loading and -1 for unloading conditions.

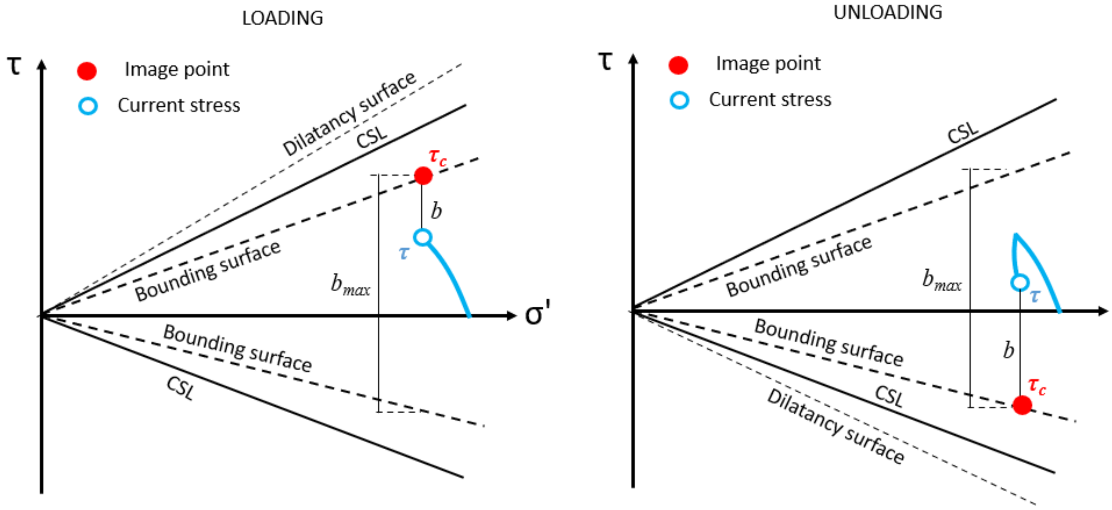

Figure 4.5 – Model for undrained shearing of the representative soil element.

4.4.2.2. *State parameter*

In its original form defined by Been & Jefferies (1985), the state parameter, represented in this thesis by ψ, was defined as a parameter that combines the influence of void ratio and stress against a reference condition. The reference condition as defined by Been & Jefferies (1985) was referred to as "steady state line", and whether the critical state and the steady state are the same does not affect the critical state concept (Been & Jefferies, 1985). The state parameter was originally defined as the difference between the initial void ratio e and the critical state void ratio at the same mean effective stress, as defined in Equation (4.12).

$$\psi = e - e_{CS} \tag{4.12}$$

With this approach, the state parameter ψ is positive for soils on the loose side of the CSL and negative for soils on the dense side of the CSL, and equals zero for sands on the CSL.

This concept was proven to be effective through experimental research on clays and sands and it is suggested that the behaviour of soils with same state parameter will have similar behaviour irrespective of their stress-strain history (Yu, 1998). Although the critical state parameter concept was proven to work for sands and clays, in some cases it might be of interest to use an alternative definition of the state parameter. Particularly in clays, the overconsolidation ratio (OCR) is usually employed to describe the response of clays under loading conditions. The OCR for clays is expected to play a similar role to the state parameter for sands (Yu, 1998).

In that sense, the new state parameter may be defined in terms of stress rather than soil density, therefore the distance to the critical state line (CSL) should be measured horizontally rather than vertically, and as a ratio rather than a difference. A suitable form is presented in Equation (4.13), where σ' is the initial effective stress and σ_{cs}' is the corresponding effective stress on the critical state at the same specific volume v (i.e. at the same void ratio e). Figure 4.6 illustrates the difference between the two state parameter concepts.

$$\psi = \frac{\sigma'}{\sigma'_{CS}} = \frac{\sigma'}{e^{\frac{\Gamma - v}{\lambda}}} \tag{4.13}$$

This formulation for the state parameter is similar to the one proposed by Bobei et al. (2009), which involved the ratio between the current mean effective stress p' and the respective effective stress on the CSL p'_{CSL} for the same void ratio.

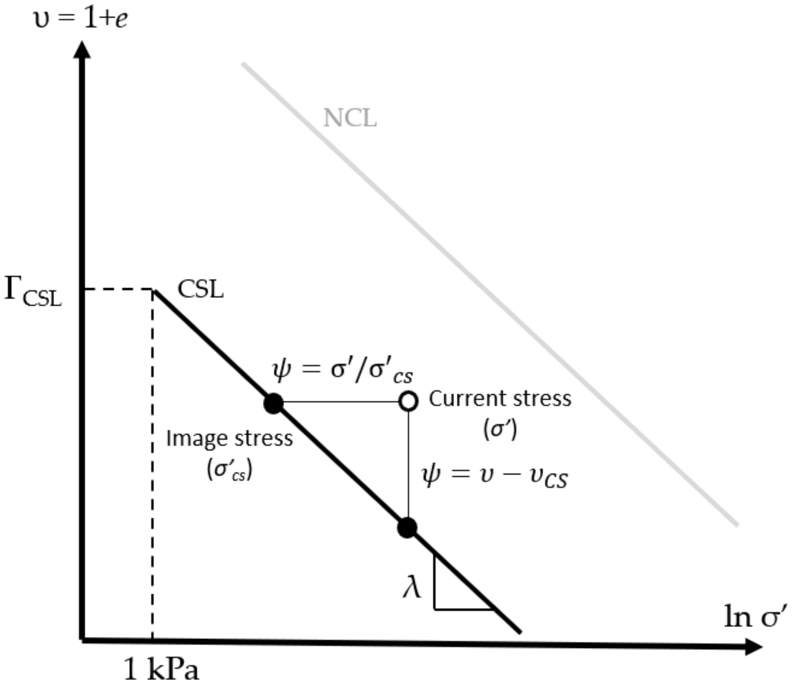

Figure 4.6 – State parameter definitions

It is worth noting that whereas in its original definition (Been & Jefferies, 1985) the state parameter was equal to zero ($\psi = 0$) for soil states on the critical state, for the new definition the state parameter is equal to unity ($\psi = 1$) on the critical state, $\psi > 1$ for loose states and $\psi < 1$ for dense states.

4.4.2.3. Elastic properties

Following the one-dimensional rule for isotropic elasticity (Muir Wood, 2009), the bulk modulus K_e is assumed to be proportional to the effective normal stress σ'.

$$K_e = \frac{\upsilon\sigma'}{\kappa} \tag{4.14}$$

By assuming a constant Poisson's ratio ν, the shear modulus G can be calculated:

$$G = \frac{3(1-2\nu)}{2(1+\nu)}K_e \tag{4.15}$$

4.4.2.4. Bounding surface

The size of the bounding surface F_s is related to the state parameter as follows:

$$F_s(\sigma') = \tau_c - t\,\sigma' \tan\varphi_{cs}\,\psi^{k_r} \tag{4.16}$$

where k_r is a model parameter defining the link between the current state parameter and the soil strength.

4.4.2.5. Flow rule

The stress–dilatancy rule discriminates between soil compression and dilation state and governs the plastic volumetric behaviour during shearing. The form adopted here is similar to that of Cam Clay and to that used by Gajo & Muir Wood (1999) in which the dilatancy rule plays the role of the flow rule. This form accounts for the effect of the state parameter as proposed by Manzari & Dafalias (1997) in order to better capture the effect of picnotropy (or void ratio dependency):

$$d_s = \frac{\dot{\varepsilon}}{\dot{\gamma}} = A[t \tan\varphi_{cs}\,\psi^{k_d} - \tau/\sigma'] \tag{4.17}$$

where d_s is the dilatancy, A and k_d are model parameters, $\dot{\varepsilon}$ and $\dot{\gamma}$ are the incremental volumetric and shear strain, respectively.

4.4.2.6. Hardening rule

The hardening rule is based on deviatoric mapping where the image stress (or current soil strength, τ_c) is the vertical projection of the current stress state on the bounding surface, as shown in Figure 4.5 and defined below:

$$\tau_c = t\,\sigma' \tan\varphi_{cs}\,\psi^{k_r} \tag{4.18}$$

The hardening modulus H_m is defined in the customary way for bounding surface plasticity models (Russell & Khalili, 2004), accounting for a hardening term of the image stress on the bounding surface (H_b) and an arbitrary modulus (H_f) depending on the distance b (see Figure 4.5) between the current stress state τ and its image τ_c on the bounding surface:

$$H_m = H_b + H_f \tag{4.19}$$

The term H_b is defined from the observation that isotropic hardening occurs with changes in plastic volumetric strains and by imposing that the image stress always lies on the bounding surface (Russell & Khalili, 2004). The critical state parameter ψ controls the size of the bounding surface and therefore acts as a hardening parameter.

$$H_b = -\frac{\partial F_s}{\partial \psi}\frac{\partial \psi}{\partial \varepsilon^p}\frac{m_\sigma}{\left\|\frac{\partial F_s}{\partial \boldsymbol{S}}\right\|} \tag{4.20}$$

where the vector of stresses $\boldsymbol{S}$ is defined as $\boldsymbol{S} = [\tau, \sigma]^{\mathrm{T}}$. The first component on the right-hand side of the equation is obtained from Equation (4.16). The second is obtained from Equation (4.13) and by applying the substitutions $\dot{v} = -v\dot{\varepsilon}$ and $\dot{\varepsilon} = \dot{\varepsilon}^p + \dot{\varepsilon}^e = \dot{\varepsilon}^p + \dot{\sigma}/E$, where $\dot{\varepsilon}^p$ and $\dot{\varepsilon}^e$ are the plastic and elastic components of the incremental volumetric strain $\dot{\varepsilon}$ and E is Young's modulus (linked to the bulk modulus K_e by the Poisson's ratio ν through classic elastic relationships).

The vectors $\boldsymbol{m}$ and $\boldsymbol{n}$ determine the unit direction of the plastic flow and the direction of loading (normal to the bounding surface F_s), according to the plasticity theory.

$$\boldsymbol{m} = \frac{\frac{\partial g}{\partial \boldsymbol{S}}}{\left\|\frac{\partial g}{\partial \boldsymbol{S}}\right\|} = [m_\tau, m_\sigma]^T \tag{4.21}$$

$$\boldsymbol{n} = \frac{\frac{\partial F_s}{\partial \boldsymbol{S}}}{\left\|\frac{\partial F_s}{\partial \boldsymbol{S}}\right\|}[n_\tau, n_\sigma]^{\boldsymbol{T}} \tag{4.22}$$

Even though the plastic potential function g is not defined explicitly in Equation (4.17), the components m_τ and m_σ can be calculated:

$$m_\tau = \frac{t}{\sqrt{1 + {d_s}^2}} \tag{4.23}$$

$$m_\sigma = \frac{t\, d_s}{\sqrt{1 + {d_s}^2}} \tag{4.24}$$

The full derivation of the hardening term H_b in Equation (4.30) is omitted for the sake of brevity.

$$H_b = \frac{-t\left(\frac{\tan(\varphi_{cs})\,\sigma'\psi^{k_r}}{k_r}\right)\left(\frac{\sigma' v}{\lambda \exp\left(\frac{\Gamma - v}{\lambda}\right)}\right) m_\sigma}{\sqrt{1 + \left\{-t\,\tan(\varphi')\,\psi^{k_r}\left[1 + \frac{\sigma' k_r}{\psi \exp\left(\frac{\Gamma - v}{\lambda}\right)}\left(1 - \frac{\sigma' v}{\lambda E}\right)\right]\right\}^2}} \tag{4.25}$$

where m_σ is the component parallel to the σ-axis of the unit vector normal to the plastic potential (defined in Equation (4.24)) and

$$H_f = \frac{b^2}{C b_{max}} \tag{4.26}$$

where C is a model parameter and b_{max} is the maximum value that the distance b between the current stress state and the respective image stress on the bounding surface can assume, as shown in Figure 4.5.

$$b_{max} = 2\sigma' \tan\varphi_{cs}\,\psi^{k_r} \tag{4.27}$$

4.4.2.7. Stress-strain relationships

The stress-strain relationship is given by the elasto-plastic constitutive relationship following Gajo & Muir Wood (1999), but in the σ-ε and τ-γ spaces.

$$\dot{\gamma} = \frac{m_\tau n_\sigma}{H_m}\dot{\sigma}' + \left(\frac{1}{3G} + \frac{m_q n_\tau}{H_m}\right)\dot{\tau} \tag{4.28}$$

$$\dot{\varepsilon} = \frac{m_\sigma n_\tau}{H_m}\dot{\tau} + \left(\frac{1}{K_e} + \frac{m_\sigma n_\sigma}{H_m}\right)\dot{\sigma}' \tag{4.29}$$

The application of the model to undrained shear conditions imposes that $\dot{v} = 0$, which implies the following constraint on the volumetric strains–strain relationship:

$$\dot{\varepsilon} = \frac{m_\sigma n_\tau}{H_m}\dot{\tau} + \left(\frac{1}{K_e}\right)\dot{\sigma}' = 0 \tag{4.30}$$

where K_e is the elastic bulk modulus of the soil and n_τ is the component parallel to the τ-axis of the unit vector normal to the loading surface:

$$n_\tau = \frac{1}{\sqrt{1 + \left\{-t\ \tan(\varphi_{cs})\,\psi^{k_r}\left[1 + \frac{\sigma' k_r}{\psi \exp\left(\frac{\Gamma - \upsilon}{\lambda}\right)}\left(1 - \frac{\sigma'\upsilon}{\lambda E}\right)\right]\right\}^2}} \tag{4.31}$$

Rearrangement of Equation (4.30) provides a direct relationship for the evolution of effective stress during undrained shearing ($\dot{\varepsilon} = 0$).

$$\dot{\sigma}' = -K_e \frac{m_\sigma n_\tau}{H_m}\dot{\tau} \tag{4.32}$$

This expression controls the effective stress path followed by the representative soil element, as will be shown in Chapter 5.

The generation of the pore water pressure can be determined using $\dot{\sigma}' = \dot{\sigma} - \dot{u}_w$, while the currently available soil strength at any moment of loading can be determined using Equation (4.18).

4.5. Soil-anchor compatibility conditions

Careful compatibility conditions must be imposed between the macro-element model for the anchor and soil model to ensure that the two models are closely linked. As discussed above, the current soil strength τ_c governs the capacity surface of the macro-element model through the terms V_M, H_M and M_M. The further condition is the assumption that the mobilised capacity of the anchor ρ_c corresponds to the mobilised soil strength during undrained shearing:

$$\rho_c = \tau/\tau_c \tag{4.33}$$

This ensures that both models reach the failure conditions at the same point, such that the anchor capacity is fully governed by the capacity of the soil. Since the function of the representative soil element is to track the changes in excess pore water pressure and the related changes in soil effective stress and available strength, no relationship between the displacements of the anchor and strain in the representative soil element is required in these modelling developments.

The hardening term ρ_c varies between 0 and 1 and is controlled by the anchor displacements. The term ρ_c can be seen as a mobilisation of anchor capacity, i.e. the closer ρ_c is to 1, the closer the anchor is to reach its ultimate capacity.

In terms of soil strength, it is well known that the shear strength of the soil is dependent on the acting effective normal stress. The distance from the current stress state to failure (i.e. the bounding surface) can also be seen as a mobilisation of soil strength, as it measures how far the soil sample is from reaching failure. Therefore, the compatibility condition presented in Equation (4.33) is a simple way to measure this distance in such a way that the mobilisation of soil strength also varies between 0 and 1.

This approach is somewhat similar to the analogy between the lateral loading of a pile element with the shearing of a DSS soil element presented in several studies (e.g. Zhang et al., 2016; Zhang et al., 2019; Zhang et al., 2020). The analogy employed in those studies proposes that the mobilisation of shear stress (τ/s_u) in a soil element is equivalent to the level of mobilisation in terms of lateral bearing capacity pressure (p/p_u). Furthermore, it was shown that the normalised lateral displacement of the pile can be scaled from the shear strain on the DSS stress-strain curve.

The Mobilizable Strength Design (MSD) method proposed by Osman & Bolton (2004) for retaining walls in clay also relates the behaviour of a soil mass to a representative soil element. In that approach, a representative soil sample at the mid-height of the retaining wall prior to excavation is used to deduce the average shear strength that can be mobilised at a certain shear strength. The stress path of the representative soil element informs how far the shear strength τ is from the undrained shear strength s_u, and the displacements of the wall are related to the strains of the soil sample. The MSD concept was further applied to other structures, such as to braced walls supporting excavation (Osman & Bolton, 2006), to bored piles in London clay (Vardanega et al., 2012) and to unproped cantilever walls (Zhang et al., 2015).

The MSD concept basically assumes failure of the whole soil-structure system rather than failure either of the structure or of the soil (Vardanega & Bolton, 2016), which is in line with the framework proposed in this thesis, in which both anchor and surrounding soil reach their maximum mobilizable capacity or strength simultaneously. In this thesis, the mobilisation of anchor capacity (ρ_c) is assumed to reach failure at the same time as the soil, which is given by the mobilisation of soil strength (τ/τ_c), in such a way that the whole soil-anchor system reaches failure rather than soil or structure failure. The main difference between the newly proposed framework and the MSD studies is that anchor displacements are not linked to the strains of the representative soil element, whereas in MSD the displacements of the structure (e.g. cantilever wall) is related to the shear strains of a soil element.

But similarly to those studies, the mobilisation of anchor capacity (ρ_c) is linked to the mobilisation of soil strength (τ/τ_c) through Equation (4.33), hence the theoretical principles behind are somewhat similar.

4.6. Optional relationship between hardening parameter R_0 and soil strength τ_c

Besides the mobilisation of anchor capacity given by the term ρ_c, the hardening parameter for the anchor's macro-element model R_0 may also linked to the representative soil element. It is proposed that the current stiffness of the anchor behaviour is related to the mobilisation of soil strength ($\tau_c/\tau_{c,ref}$). The dependency of stiffness on soil strength has been previously reported in the literature. For cohesive soils, the stiffness can be related to the effective stress (Atkinson, 2000) or to a normalised undrained shear strength ratio ($s_u/s_{u,ref}$) as proposed by Zhou et al. (2019). In the context of the macro-element model presented in this thesis, the hardening parameter R_0 controls the stiffness of the force-displacement curves. The dependency of R_0 on $(\tau_c/\tau_{c,ref})^M$ was chosen due to observations that the values of R_0 that provided better agreement with experimental results varied largely according to the strength of the soil, as will be shown in Chapter 5.

It is worth noting that the dependency of R_0 on current soil strength τ_c is only needed when a significant variation of soil strength occurs during testing, i.e. mainly in situations that involve episodes of long-term cyclic loading. For cases in which the strength of the soil τ_c does not vary significantly, it is convenient to assume constant values of R_0 without affecting the results, as will be shown in section 5.3.2.2.

The stiffness is also dependent on the load history. Following a similar approach to the Memory Surface Hardening Model (Corti et al., 2016), in which the soil behaviour is stiffer during repeated loading compared with virgin loading and where the original hardening modulus is re-established once the soil reaches a virgin state, the hardening parameter R_0 is expressed in the form presented in Equation (4.34), which combines the dependency of R_0 both on the current strength τ_c and on the distance to the maximum mobilised capacity of the anchor, ρ_{cM}.

$$R_0 = M^* \left(\frac{\tau_c}{\tau_{c,ref}} \right)^{N^*} \tag{4.34}$$

where

$$M^* = \exp\left[R_1 \left(\frac{\rho_{cM} - \rho_c}{\rho_{cM}} \right) \right] \tag{4.35}$$

$$N^* = \exp\left[R_2 \left(\frac{\rho_{cM} - \rho_c}{\rho_{cM}} \right) \right] \tag{4.36}$$

where R_1 and R_2 are model parameters, $\tau_{c,ref}$ is a reference value taken as 100 kPa and ρ_{cM} is the value of ρ_c for the memory surface, i.e. the maximum mobilisation factor ρ_c experienced by the soil. The term $[(\rho_{cM} - \rho_c)/\rho_{cM}]$ is a measure of the normalised distance of the current state to the memory surface, while the exponential expressions of M and N ensure a smooth transition from load states inside the memory surface to (virgin) load states on the memory surface, as previously shown in Figure 4.2.

Figure 4.7 illustrates the memory surface approach. During the initial monotonic load in blue (Figure 4.7a), all load states and respective values of mobilisation of anchor capacity ρ_c are experienced for the first time (i.e. virgin states), therefore $\rho_c = \rho_{cM}$, $M^* = N^* = 1$ and R_0 depends solely on the variation of the current strength s_u. If, for example, during cyclic loading (grey curves) the values of ρ_c are lower than the maximum value ever experienced (ρ_{cM}), the normalised distance between the current ρ_c and ρ_{cM} plays a role and the hardening parameter R_0 increases with increasing distance between ρ_c and ρ_{cM}. If the load acting on the anchor increases again, ρ_c approaches ρ_{cM} and the difference $[(\rho_{cM} - \rho_c)/\rho_{cM}]$ approaches zero. If the load keeps increasing, eventually $\rho_c = \rho_{cM}$ from which moment the mobilisation of anchor capacity reaches a virgin state again (blue line on the right-hand side of Figure 4.7b) and smaller (i.e. less stiff) values of R_0 are re-established.

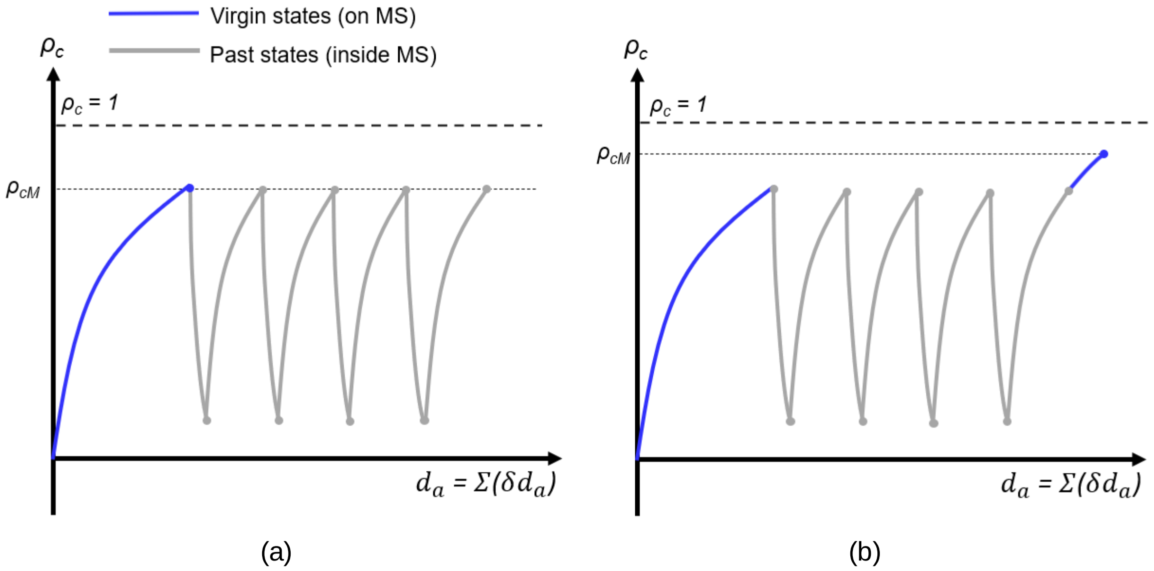

Figure 4.7 – Evolution of the mobilisation factor on the memory surface ρ_c for (a) initial monotonic loading and cyclic loading and (b) post-cyclic virgin loading.

4.7. Summary of the chapter

This Chapter proposed a new macro-element modelling framework aiming to capture the cyclic behaviour of plate anchors and the evolution of the cyclic capacity related to changes in soil strength, as triggered by processes of pore water pressure generation and/or consolidation during loading. The modelling framework combined the macro-element model for the anchor presented in Chapter 3 with a one-dimensional model of undrained shearing and consolidation for a soil element, representative of the whole soil mass around the anchor. The one-dimensional model of undrained shearing and consolidation for the soil element is based on the critical state and bounding surface concepts in order to accurately capture pore water pressure generation and dissipation during both consolidation and shearing mechanisms.

The model capabilities will be presented and compared with experimental results in cohesive and granular soils, as follows in Chapters 5 and 6, respectively. The following chapters will also provide an in-depth analysis of the representative soil element behaviour and how it affects the anchor capacity and its evolution with time.

CHAPTER 5. Application of the macro-element model to cohesive soils

Objectives

- To apply the macro-element modelling framework to plate anchors in clay subjected to long-term cyclic and maintained loading
- To analyse the effect of key parameters on anchor and soil response
- To identify which model parameters are most relevant and require special attention
- To provide guidance on parameter calibration
- To provide insights on the effect of changes in anchor kinematics and soil strength
- To discuss the difficulties of the modelling approach

Statement

Some parts of this chapter have been published in a journal article in the Journal of Marine Science and Engineering (JMSE) on 13 February 2021, entitled 'A Cyclic Macro-Element Framework for Consolidation-Dependent Three-Dimensional Capacity of Plate Anchors'. The article has been published with the co-authorship of Dr Andrea Diambra, Dr Dimitris Karamitros and Dr Shiao Huey Chow. The full article can be found in the link: https://doi.org/10.3390/jmse9020199.

5.1. Introduction

This chapter explores the application of the macro-element modelling framework presented in Chapter 4 to episodes of cyclic load and consolidation under maintained load in cohesive soils. The chapter aims at analysing the changes in two main features: soil strength and stiffness with time in cohesive soils, as previously shown in several studies involving modelling of offshore applications (e.g. Lehanne & Jardine, 2003; Gourvenec, 2018; Han, 2016; Zhou et al., 2019, 2020). The centrifuge tests carried out by Zhou et al. (2020) were selected for the assessment of the model under one-dimensional conditions (i.e. anchor displacements in one direction only), as the variation in soil strength is significant during the long-term cyclic and maintained loading conditions tested in the experiments. The centrifuge tests carried out by Blake et al. (2011) were used to assess the macro-element model in a different loading scenario which involved anchor rotation and tangential displacement, as well as normal displacements.

Section 5.2 applies the macro-element model to a one-dimensional case in which a vertical circular plate anchor is subjected to horizontal pull involving episodes of cyclic and maintained loading. The model parameters are calibrated with two centrifuge tests and challenged against two other centrifuge tests subjected to more complex loading.

Section 5.3 compares macro-element modelling predictions with centrifuge tests involving a vertically-installed anchor subjected to vertical loading. The consolidation-dependent behaviour of the anchor is assessed through the effect of different periods of maintained loading, which in turn lead to different capacities of the anchor.

Finally, section 5.4 discusses the main findings from this chapter as well as the capabilities and limitations of the macro-element model in terms of assessing anchor response under long-term operational conditions.

5.2. One-dimensional loading

The first scenario is the benchmarking against the loading conditions shown by Zhou et al. (2020). In the centrifuge tests presented in this section, a circular plate anchor embedded in a normally consolidated carbonate silt is subjected to varied episodes involving combinations of maintained and long-term cyclic loading, as well as undrained monotonic loading prior to and after the episodes of maintained and cyclic loading.

The circular plate with a diameter D = 5.25 m (prototype scale) was installed at an embedment depth (measured to the centre of the plate) of 4.3 D. The experimental set-up is shown in Figure 5.1. The carbonate silt used in the centrifuge tests had been previously characterised by Chow et al. (2020b) and its properties are presented in Table 5.1.

Table 5.1 – Experimental conditions – properties of the silt used in the centrifuge tests.

Symbol	Description	Value	Remarks
	SOIL PROPERTIES		
γ'	Effective unit weight (kN/m^3)	5.2	Chow et al. (2019)
λ	Slope of NCL and CSL	0.287	Chow et al. (2019)
κ	Slope of the swelling line	0.036	Chow et al. (2019)
Γ_{NCL}	Specific volume at $\sigma_v' = 1$ kPa on the NCL	4.0	Chow et al. (2019)
φ_{cs}	Critical state friction angle (°)	40	Chow et al. (2019)
Γ_{CSL}	Specific volume at $\sigma_v' = 1$ kPa on the CSL	3.8	Zhou et al. (2020)
c_{op}	Coefficient of consolidation (m^2/year)	4	Zhou et al. (2020)

The experiments involved three types of loading: monotonic loading, maintained loading and cyclic loading. The *monotonic loading* stages consisted of loading the anchor under displacement control at a velocity v = 1 mm/s (V^* = 276 using an operative coefficient of consolidation, c_{op} = 4 m^2/year) such that the response was undrained. In recent communication with the first author of Zhou et al. (2020), it was found that the increase in soil strength due to strain rate effects was less than 5% (Zhou, 2021, *personal communication*). The episodes of *maintained loading* involved keeping a constant load of 50% of the anchor steady resistance measured in the monotonic stage during 3 hours, such that consolidation could take place and that 95% of the excess pore water pressure was dissipated. The *cyclic loading* episodes involved 1080 cycles of regular load varying between 25% and 75% of the anchor resistance measured in the monotonic stage.

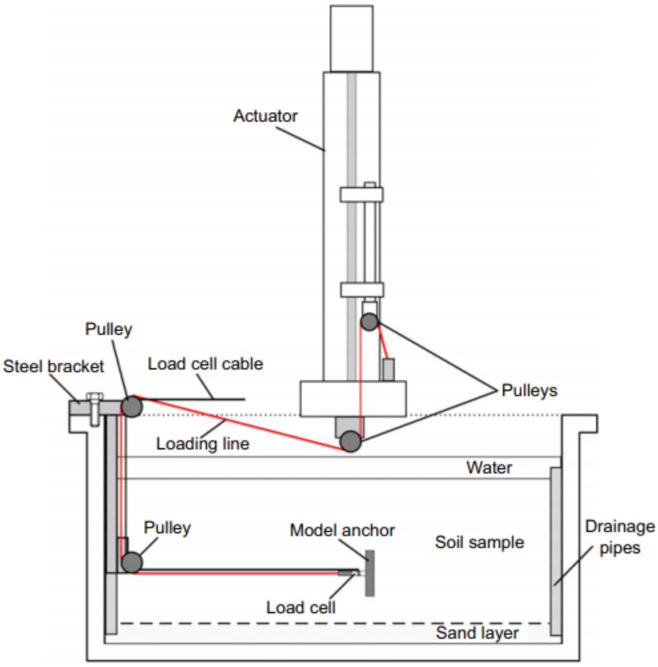

Figure 5.1 – Experimental set-up of the centrifuge tests (Zhou et al., 2020).

Four centrifuge tests were carried out. These are described below and shown in Figure 5.2. The figures are not to scale and are merely for visualisation purposes.

- Test 1: initial monotonic loading until the anchor capacity became steady, followed by unloading the anchor to 50% of the steady capacity. This load is kept constant for 3 h (maintained loading), after which a final monotonic stage is applied up to failure.
- Test 2: initial monotonic loading until the anchor capacity became steady, followed by 1080 cycles of loading, after which a final monotonic stage is applied up to failure.
- Test 3: initial monotonic loading until the anchor capacity became steady, followed by unloading the anchor to 50% of the steady capacity. This load is kept constant for 3 h (maintained loading), after which 1080 cycles of loading are applied. Another episode of 3 h of maintained loading is applied, followed by a final monotonic stage up to failure.
- Test 4: initial monotonic loading until the anchor capacity became steady, followed by unloading the anchor to 50% of the steady capacity. This load is kept constant for 3 h (maintained loading), after which 1080 cycles of loading are applied. This process of maintained and cyclic loading is repeated 4 more times, after which a final maintained loading and final monotonic stages are applied.

Points A, B, C, D1, D2, E and F in Figure 5.2 will be referred back to during the analysis of the representative soil element throughout the chapter.

As discussed in the previous chapter, the model used involves a macro-element model for the anchor and a model for the representative soil element. A simplification of the model presented previously is made due to the fact that the experiments carried out by Zhou et al. (2020) only involved forces that are normal to the anchor plane, where no rotation occurs ($V = T_a$ and $H = M = 0$). This turns the three-dimensional model into a one-dimensional model, which greatly reduces the number of necessary model parameters introduced in Chapter 3 for the anchor macro-element, as indicated in Table 5.2. If compared to a loading scenario that involves tangential (H) and moment (M) loads, for example, a one-dimensional loading requires seven parameters less: the sliding and rotational capacity factors (N_h and N_m, respectively), the plastic potential parameters (ξ, χ and ω introduced in Chapter 3) and the parameters m and n that control the shape of the loading surface. The reasons for such reduced number of parameters is explained below.

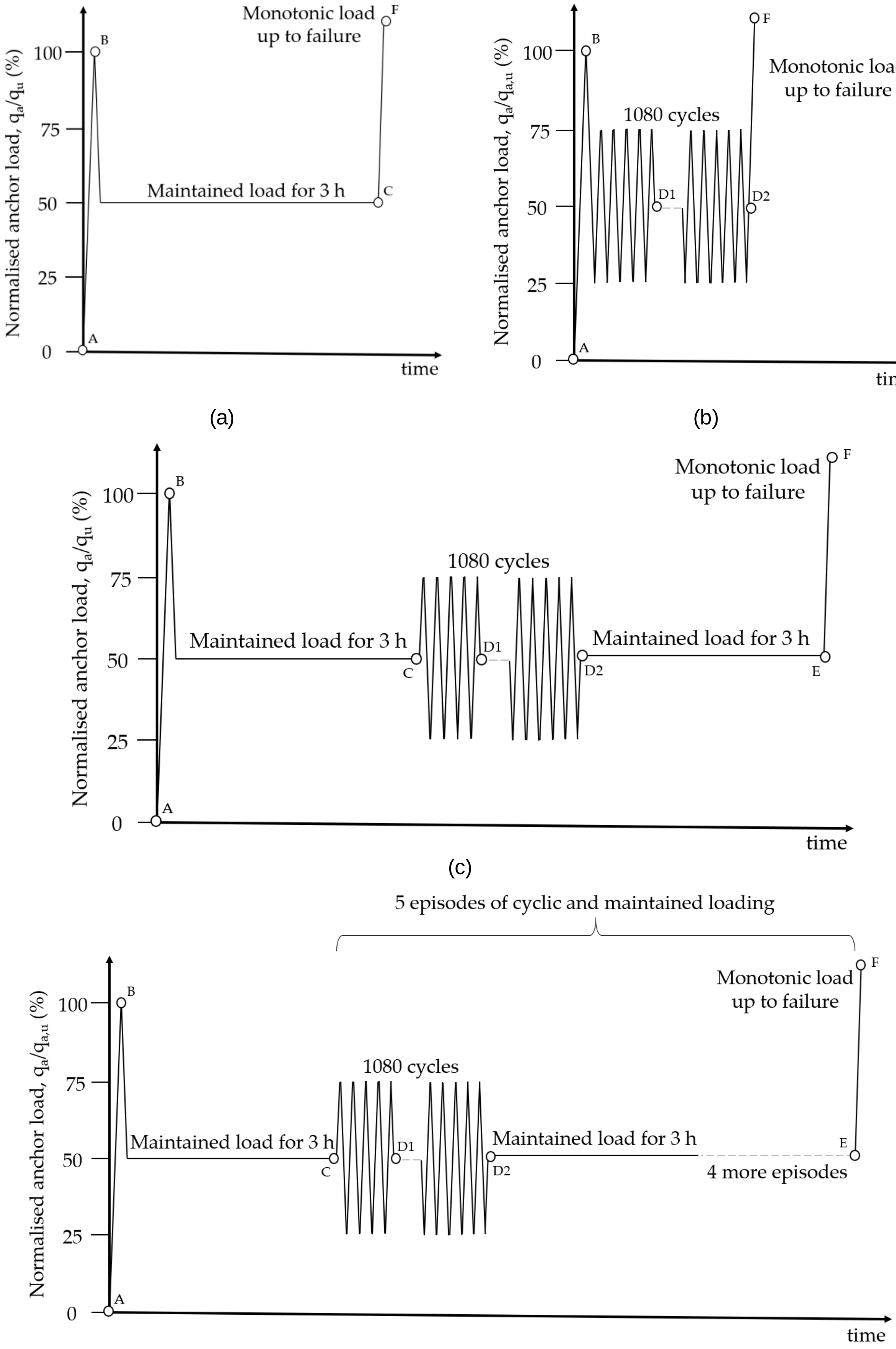

(a)

(b)

(c)

(d)

Figure 5.2 – Illustration of the loading sequence for centrifuge tests: (a) Test 1; (b) Test 2; (c) Test 3; (d) Test 4 (adapted from Zhou et al., 2020).

Table 5.2 – Soil and anchor parameters for one-dimensional loading.

Symbol	Description	Value	Remarks
	SOIL PARAMETERS		
T_{50}	Dimensionless time factor for 50% consolidation	0.01	Calibrated (Test 2)
a	Consolidation curve fitting	1.3	Calibrated (Test 2)
A	Flow rule multiplier	0.4	Calibrated (Test 2)
k_d	State parameter multiplier in flow rule	1.5	Diambra et al. (2013)
k_r	Link between state parameter and strength	-0.5	Diambra et al. (2013)[1]
C	Hyperbolic stiffness relationship parameter	0.00003	Calibrated (Monotonic tests)
	ANCHOR PARAMETERS		
I_σ	Boussinesq influence factor	0.46	Calibrated (Test 1)
m	Shape of loading surface (moment)	--	
n	Shape of loading surface (horizontal)	--	
q	Shape of loading surface (vertical)	1	
N_v	Normalised normal capacity factor	9.0	Singh & Ramaswamy (2008)
N_h	Normalised sliding capacity factor	--	
N_m	Normalised rotational capacity factor	--	
ξ	Plastic potential parameter (vertical)	--	
χ	Plastic potential parameter (horizontal)	--	
ω	Plastic potential parameter (moment)	--	
R_1	Memory surface parameter	8	
R_2	Memory surface parameter	0.8	

[1] The value actually used by Diambra et al. (2013) was $k_r = 1.5$, which gives the same results as the equivalent value of $k_r = -0.5$ with the new formulation of the state parameter in Equation (4.13).

As the only load involved in the test is normal to the anchor plane ($V = T_a$), the terms involving H and M in the loading surface equation [Equation (3.9)] become null, hence $\rho_c = (V/V_M)^q$. Since the mobilisation of the anchor capacity ρ_c depends solely on the ratio between the current load V and the normal capacity V_M, it is reasonable to assume that failure is reached when the load V reaches the maximum normal capacity V_M; therefore, $q = 1$. The normal capacity N_v was taken as 9.0, based on a previous study for circular plates in clay (Singh & Ramaswamy, 2008). The other parameters N_h and N_m are not necessary, since no tangential and moment loads are involved. Owing to the lack of displacements parallel to the anchor plane or any rotation ($u = 0$ and $\beta = 0$), the calibration of the plastic potential parameter is unnecessary in this case. This implies that loading and plastic potential surfaces are coincident (i.e. associated plastic potential) and that they are parallel to the loading axis.

It follows that, for the one-dimensional load case, the only anchor parameters that need to be calibrated are those related to the hardening parameter R_0, i.e. R_1 and R_2 (see Equation (4.34) through (4.36)), as well as the Boussinesq influence factor I_σ, which will be further explained in section 5.2.1. The parameters related to the constitutive model of the soil for shearing (A, C, k_d, k_r) and for consolidation (a and T_{50}) also require calibration. The soil parameters for shearing as well as the hardening parameters R_1, R_2 and k_1, are calibrated with both Tests 1 and 2. The effect of each of the soil parameters for shearing (A, C, k_d, k_r) on the behaviour of a soil element was analysed in detail by Gajo & Muir Wood (1999). The hardening parameters are calibrated such that anchor displacement during cyclic and post-cyclic loading agrees with those observed during the centrifuge tests. The influence factor I_σ is calibrated with Test 1, whereas the consolidation parameters a and T_{50} are calibrated with Test 2.

5.2.1. Model calibration – Tests 1 and 2

Tests 1 and 2 were selected for the model calibration as they involve maintained and cyclic loading separately, which allow independent calibration of parameters associated with both types of loading. As a starting point for the calibration process, the parameters associated with the representative soil element (Severn-Trent model parameters) initially assume equivalent values to those used by Diambra (2010) and Diambra et al. (2013) for Hostun sand (which are similar to values used in other studies, e.g. Gajo & Muir Wood, 1999, and Corti et al., 2016), and are varied individually to match the experimental results. The Severn-Trent model has not been previously employed for clays, therefore the range of suitable values for cohesive soil is unknown.

The influence factor I_σ, which depends on the position of the representative soil element, influences the soil strength during the application of maintained load, and is therefore calibrated through Test 1. The consolidation parameters a and T_{50} (see Equation (4.8)) control the pore water pressure generation and dissipation, which exhibit great variation during long-term cyclic loading. Hence, these parameters are calibrated with Test 2. The Severn-Trent parameters A, C, k_d and k_r either assume the same value reported in the literature, or are calibrated with Test 1 or 2, as shown as follows.

5.2.1.1. Parameter C – initial monotonic loading

The soil parameters C controlling the hyperbolic stiffness relationship in Equation (4.26) is calibrated with the initial monotonic stage of Test 1, as shown in Figure 5.3. Parameter C is calibrated to match the initial steady capacity of the anchor from Test 1 ($q_{u,ss}$ = 516 kPa). The value that provides the best fit is $C = 0.00003$.

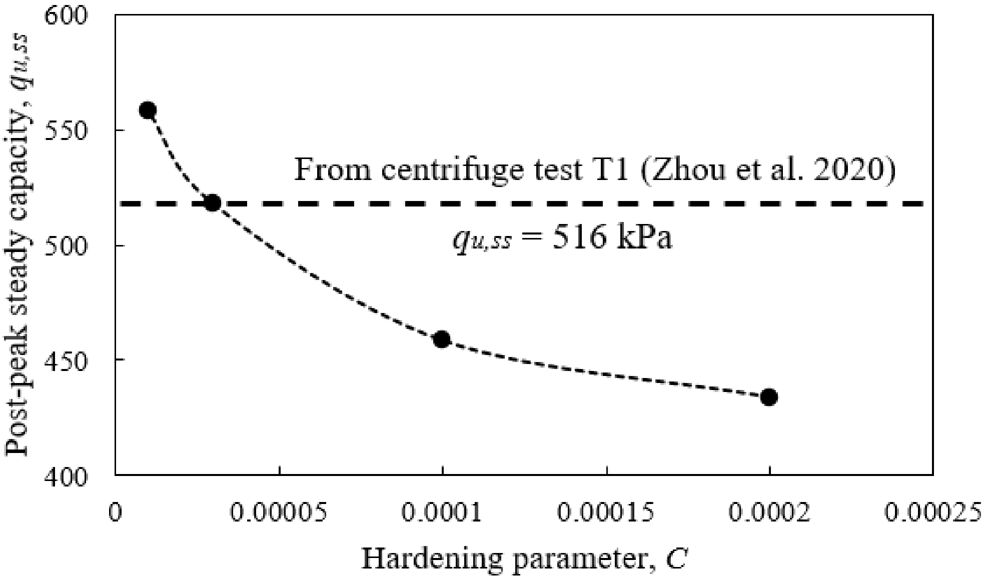

Figure 5.3 – Comparison between macro-element model and experimental results for monotonic load

5.2.1.2. *Test 1 (maintained loading) – Calibration of parameter I_σ*

Test 1 involved the application of a maintained load for 3 hours (after the initial monotonic loading) followed by a final monotonic stage up to anchor failure. For the maintained loading, the effect of the changes in the stress state on the representative soil element must be considered. Since the model for the representative soil element relates the soil strength to the vertical effective stress, any additional stresses added to the soil element must be converted to a vertical stress. In the particular case of a horizontal load, a horizontal stress is "felt" by the representative soil element. The horizontal stress is converted to an additional vertical stress on the representative soil element following a K_0 condition.

The horizontal stress "felt" by the representative soil element is a fraction of the horizontal stress "felt" by a point at null distance to the plate. This additional horizontal stress on the soil element decreases with increasing distance to the plate. The effect of distance on the stress transferred from a circular plate to the soil can be accounted for by means of the chart developed by Boussinesq (1885), as shown in Figure 5.4.

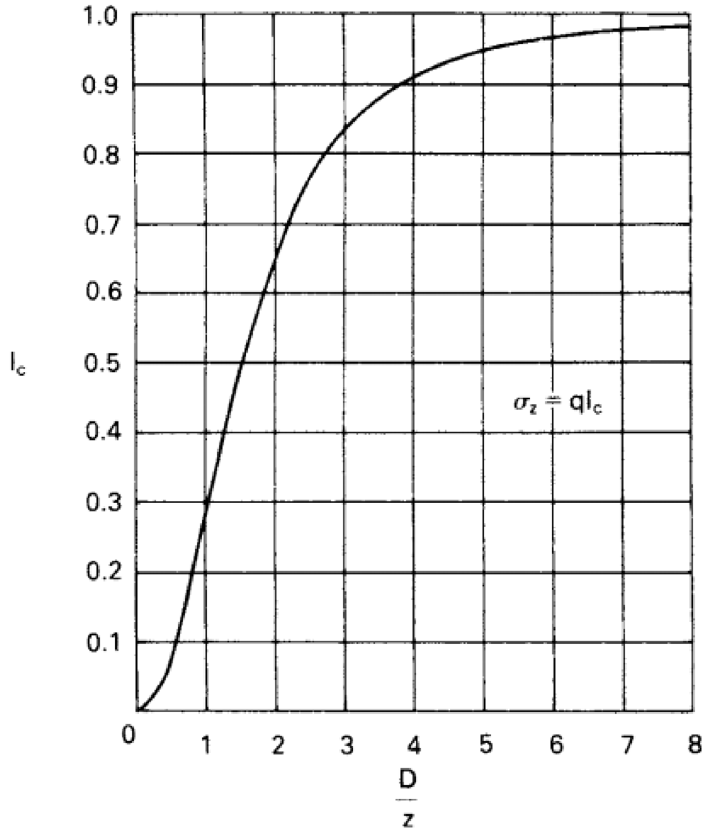

Figure 5.4 – Boussinesq solution for the stress on a point under the centre of a circular loaded area (Craig, 2004).

The additional horizontal stress on the representative soil element is $\sigma_h = I_\sigma q_a = I_\sigma (T_a / A_p)$, as illustrated in Figure 5.5. The conversion to an additional vertical loading is given by a K_0 condition, following Equation (5.1).

$$\sigma_v = K_0 \sigma_h = K_0 I_\sigma q_a \tag{5.1}$$

This solution was also adopted by Zhou et al. (2020, p. 740), according to whom "any maintained load on the anchor generates additional stress that is added to the vertical self-weight stress to enhance the equilibrium effective stress in the ground".

Although the lateral earth pressure K_0 is normally used to relate effective stresses, in the proposed macro-element model it relates horizontal and vertical total stresses. An additional vertical *total* stress on the anchor generated by the maintained load is added to the soil element. In undrained conditions, such additional total stress is taken by the pore water, leading to an equal increase in pore pressure and hence no changes in the *effective* stress. During the application of maintained loading, however, the pore pressure is gradually dissipated, and the additional *total* stress is gradually taken by the soil skeleton and converted into an additional *effective* stress. In practice, this means that the additional stress is only applied to the soil element when the pore-pressure dissipates and is converted into an effective stress.

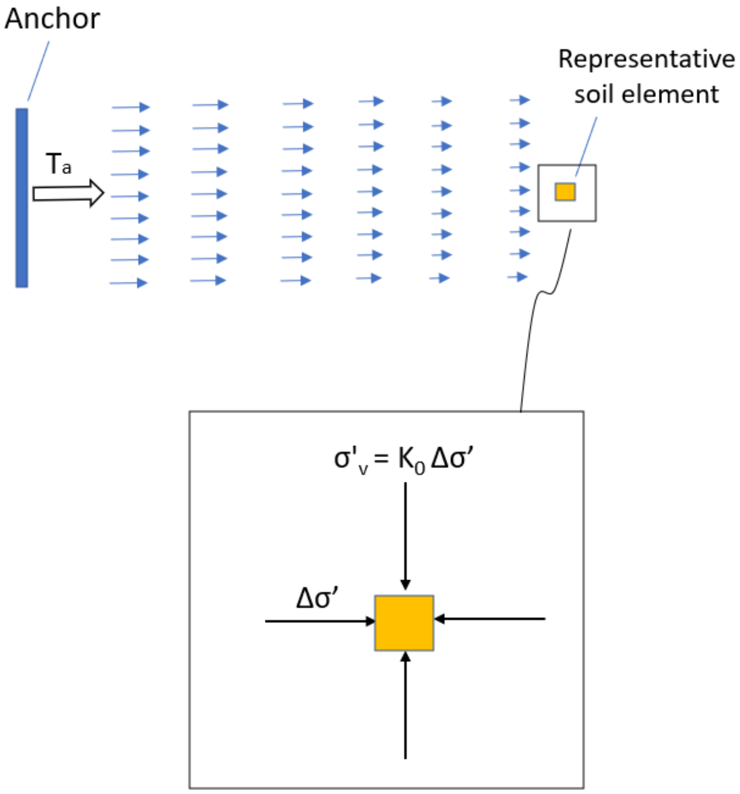

Figure 5.5 – Conversion from horizontal to vertical stress on the representative soil element.

Initially, the representative soil element was taken at a horizontal distance of 0.5 D from the centre of the anchor, which is the strength influence zone as reported by clay failure mechanisms (Yu et al., 2011). For a soil element at a distance 0.5 D of the centre of a circular plate, which gives an influence factor $I_\sigma = 0.65$, however, the macro-element model overestimates the peak capacity by 12% ($q_u = 873$ kPa against $q_u = 780$ kPa from the centrifuge test).

The influence factor I_σ for a soil element at a specific point (in this case, the representative soil element), depends on the distance to the loaded area (in this case, the plate anchor), according to Boussinesq (1885). As one expects, the influence factor decreases with increasing distance to the loaded area. Figure 5.6 below analyses the effect of the position of the representative soil element on the capacity of anchor subjected to Test 1. The results are summarised in Table 5.3.

Table 5.3 – Effect of representative soil element position on anchor capacity.

Distance to plate, x/D	Influence factor, I_σ	Anchor capacity (kPa)
0.25	0.91	1000
0.50	0.65	873
0.7	0.46	788
1.0	0.28	713
1.5	0.15	654
2.0	0.09	626

While the relationship between anchor capacity q_u and distance x/D of the representative soil element to the anchor centre is not linear (Figure 5.6a) due to the non-linear relationship between distance and influence factor shown in Figure 5.4, a linear relationship between influence factor and anchor capacity is observed, as presented in Figure 5.6b. The effect of the influence factor on anchor capacity is attributed to the change in vertical effective stress, which controls the current strength of the soil, as will be shown through the analysis of the representative soil element.

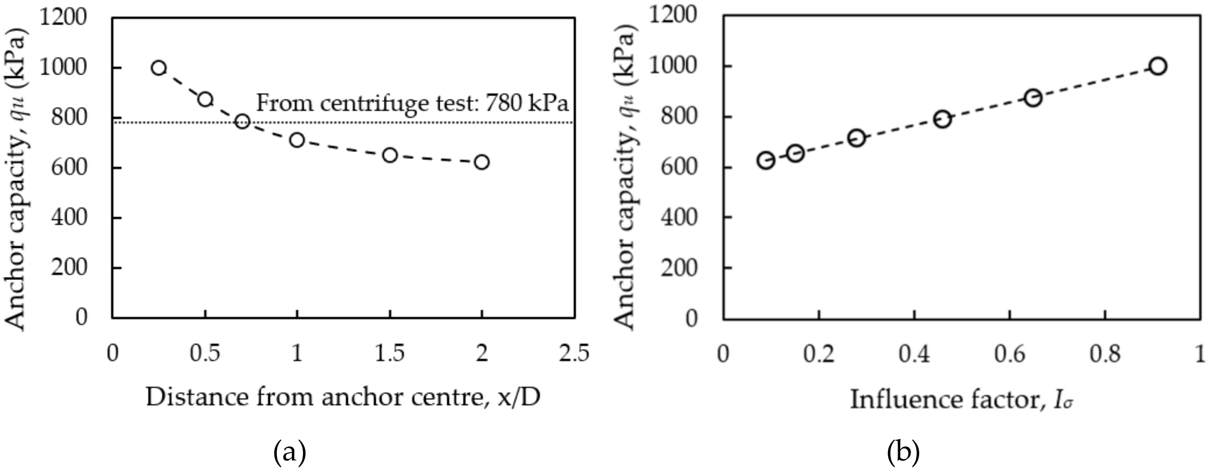

(a) (b)

Figure 5.6 – Anchor capacity as a function of: (a) position of the representative soil element and (b) Boussinesq's influence factor I_σ

It is clear that the selection of the influence factor I_σ plays an important role in the response of the anchor. For values of x/D varying between 0.25 and 2.0, the anchor capacity varies between 1000 kPa and 626 kPa, respectively, which is 28% higher and 20% lower than the capacity measured in the centrifuge test. A representative soil element distant 0.7 D from the circular plate, which gives an influence factor of approximately 0.46, provides an accurate prediction of the actual anchor capacity obtained through centrifuge test (788 kPa from the macro-element and 780 kPa from the centrifuge test). This value ($I_\sigma = 0.46$) is adopted for the modelling of Tests 2, 3 and 4.

Comparison between the force-displacement response of the macro-element model and that of the centrifuge tests result is presented in Figure 5.7. The force-displacement curves for $I_\sigma = 0.46$ and 0.65 are compared. For $I_\sigma = 0.46$, not only the peak and post-peak capacity of the anchor but also the displacement at which the peak capacity is reached is captured by the macro-element model.

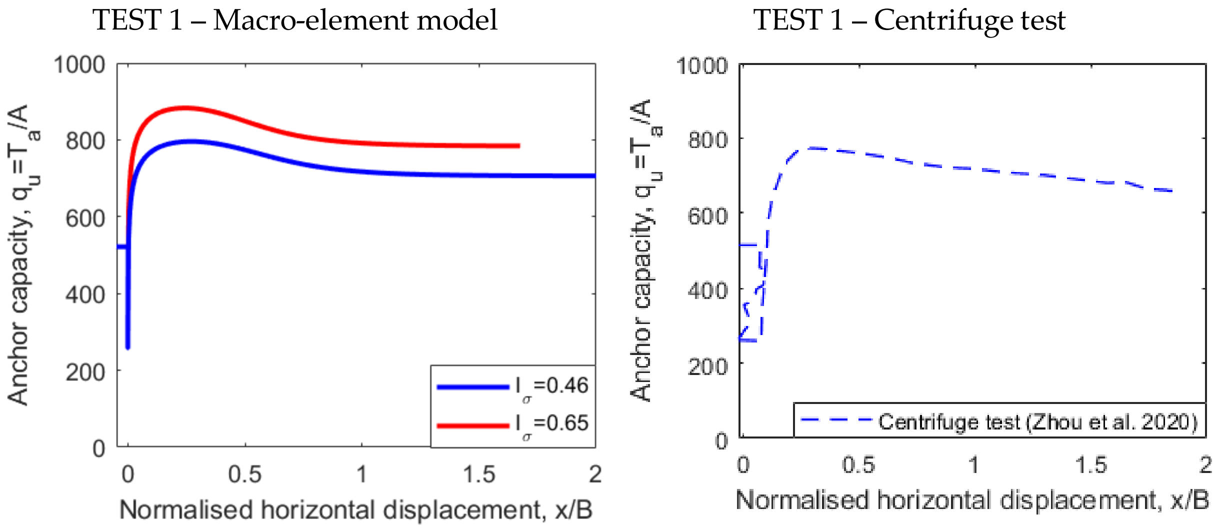

(a) (b)

Figure 5.7 – Comparison between macro-element model and experimental result with $I_\sigma = 0.46$ and 0.65 (Test 1).

The effect of the influence factor I_σ can be interpreted through the assessment of the soil element and the evolution of the soil strength, as introduced in Figure 5.8 (Figure 5.8a,b for $I_\sigma = 0.46$ and Figure 5.8c,d for $I_\sigma = 0.65$). During the initial monotonic stage (between points A and B), excess pore pressure is generated, causing a decrease in the vertical effective stress without changes in volume, as shown in Figure 5.8a. During this stage, the soil strength τ_c decreases from 69 to 66 kPa, as plotted in black in Figure 5.8b [calculated from Equation (4.16), $\tau_c = t\,\sigma' \tan\varphi'\,\psi^{k_r}$]. When the maintained load is applied during 3 hours (point B to C), the additional (total) stress induced by the anchor load gradually increases the effective stress – hence the soil strength – as the excess pore pressure dissipates. The effective stress increases from 106 to 160 kPa, which in turn increases the soil strength from 66 to 95 kPa. During the final monotonic stage, the pore pressure generation decreases the soil strength from 104 to 76 kPa, which is higher than the initial strength of 66 kPa.

For I_σ = 0.65, the effective stress during the maintained loading (B-C in Figure 5.8c,d) increases to 176 kPa, since more stress is transferred from the anchor to the representative soil element in comparison with the case for I_σ = 0.46. This, in turn, translates into a higher soil strength τ_c in point C (τ_c = 105 kPa as opposed to 95 kPa when I_σ = 0.46), which results in a higher anchor capacity, as show previously in Figure 5.7a.

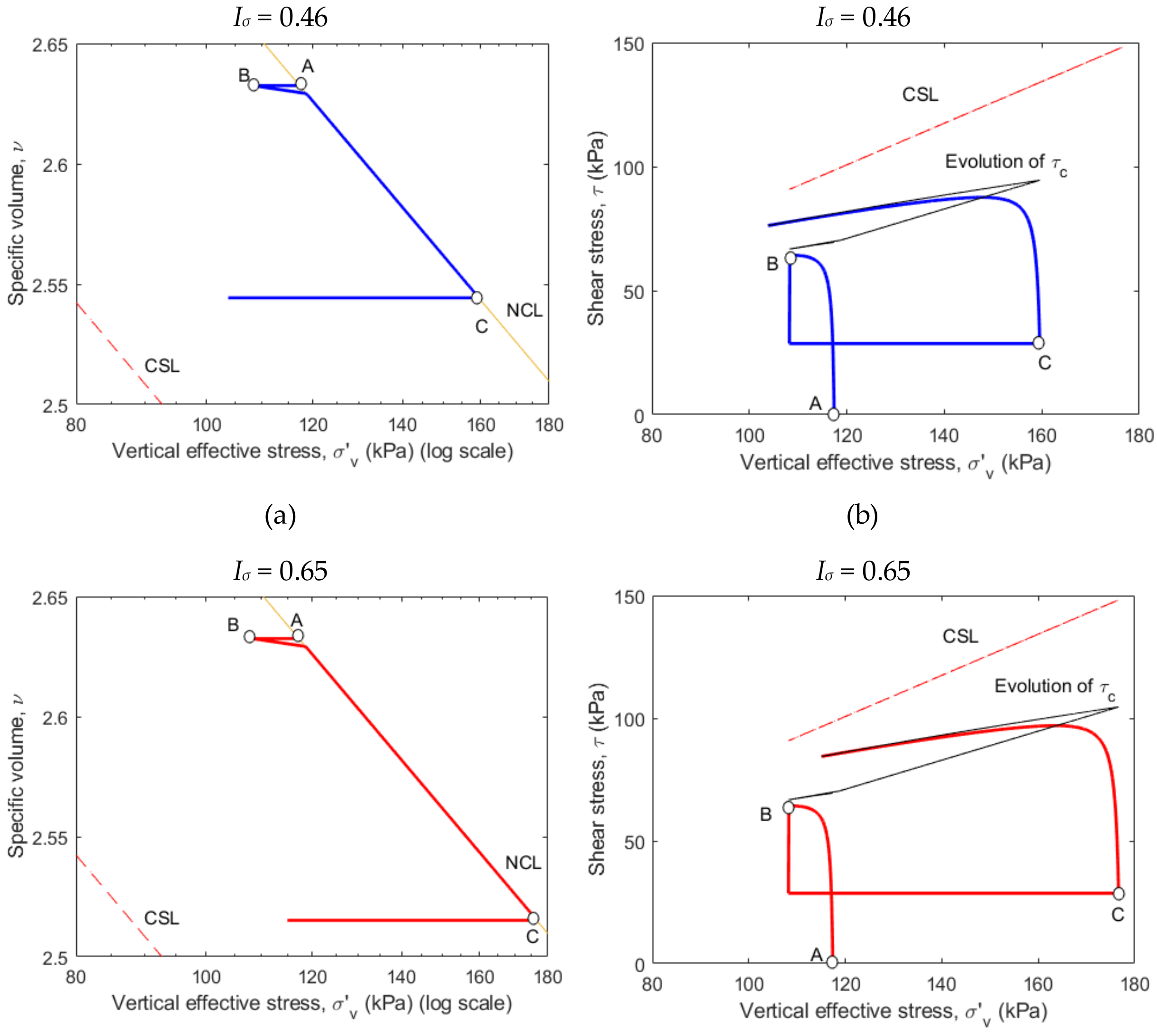
I_σ = 0.46

I_σ = 0.46

I_σ = 0.65

I_σ = 0.65

(a)

(b)

(c)

(d)

Figure 5.8 – Stress paths for Test 1 given by the macro-element model.

An interesting observation is that the centrifuge test shows a displacement of approximately $x/D = 0.1$ during the application of the maintained load. This displacement can be explained by analysing the behaviour of the representative soil element, which is used to explain how the evolution of soil strength affects the changes in anchor capacity. The anchor displacement observed during maintained loading can be attributed to the change in soil volume due to consolidation during the maintained load stage, as shown in the stress-volumetric path of the representative soil element in Figure 5.8a. The implementation of such a feature (translation of soil strain into anchor displacement) into a macro-element or theoretical model in an accurate way is rather complex, as the displacement of the anchor depends on the infinitesimal contribution of several soil elements to the overall volumetric soil deformation within the stress influence zone of the anchor. Moreover, the level of anchor displacement during maintained loading is highly dependent on the magnitude of the load, as shown through centrifuge tests and FE analyses by Han et al. (2016) on a horizontal strip anchor installed in normally consolidated kaolin clay and subjected to vertical sustained load. According to those studies, when the sustained load is lower than 60% of the monotonic (peak) capacity, the anchor displacement is very small throughout consolidation and an enhancement in anchor capacity is observed due to the increase in soil strength. For high levels of maintained load (over 88% of the monotonic capacity), the anchor exhibits significant displacement, which moves the anchor upwards into soil with lower strength and therefore causes anchor failure. For levels of maintained load between 60% and 88% of the monotonic capacity, breakaway at the base of the anchor is observed, though the decrease in anchor resistance caused by it is compensated by the gain in soil strength above the anchor due to soil consolidation (Han et al., 2016).

Even though the studies of Han et al. (2016) were conducted with different soil, anchor shape and orientation, it can be assumed that no significant displacement occurs during the application of maintained load, since the load applied is 50% of post-peak steady anchor capacity, which for all tests is lower than 70% of the peak capacity (i.e. the maintained load is less than 35% of the anchor peak capacity for all cases). Furthermore, the displacement observed during the maintained loading phase is small compared to the total anchor displacement. In that context, for the application of the proposed macro-element model to the cases reported by Zhou et al. (2020), it is assumed that no displacement occurs during this stage, i.e. no displacement associated with consolidation is considered. The relationship between anchor displacement and soil consolidation may be the subject of further research.

5.2.1.3. Test 2 (cyclic loading) – Calibration of parameters A, a and T_{50}

Test 2 involved (after the initial monotonic stage) the application of 1080 cycles with a loading frequency of 0.4 Hz (cyclic period of 2.5 seconds), which represents a dimensionless time factor $T = 0.00003$ in a single load cycle. The anchor was then horizontally loaded to failure after the cyclic loading. The load on the anchor T_a was assumed to be constant during consolidation, similar to a maintained load. Drainage within the cycle is modelled by imposing a consolidation stage after each packet of loading or unloading (e.g. Gourvenec et al., 2014; Andersen, 2015; Flessati, et al., 2020) and for the same duration of the packet. Hence, consolidation under maintained load was allowed during 1.25 seconds after loading and 1.25 seconds after unloading, which represents a consolidation time of 2.5 seconds per cycle.

The force-displacement curve obtained from the macro-element model is compared with the centrifuge test in Figure 5.9. The set of parameters selected for the macro-element analysis is $A = 0.4$, $C = 0.00002$, $k_d = 1.5$, $k_r = -0.5$, $a = 1.15$ and $T_{50} = 0.01$. The values of k_d and k_r are the same ones used by Diambra et al. (2013). The parameters that control the dependency of the hardening parameter R_0 on the current strength τ_c and that control the memory surface take the values of $R_1 = 8.0$ and $R_2 = 0.8$. The procedure that led to the selection of these values will be explained later in this section.

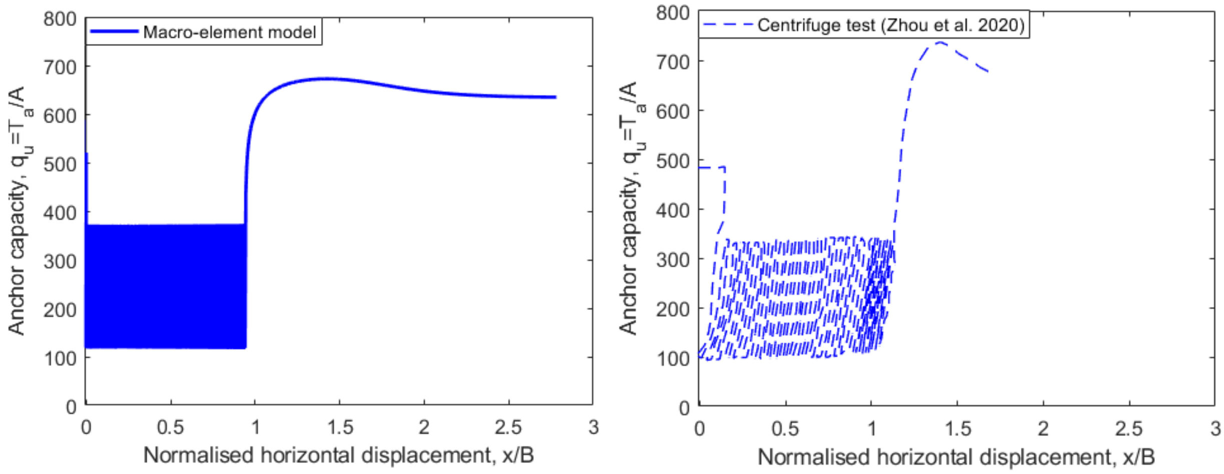

(a) (b)

Figure 5.9 – Comparison between macro-element model and experimental result (Test 2).

The displacement of the anchor during cyclic loading is accurately captured (x/D ≈ 1.0), as well as the post-peak capacity – approximately 670 kPa. The peak capacity is underestimated by 7.9% by the macro-element model (683 kPa from the macro-element model and 737 kPa from the centrifuge test). While the peak capacity could be better captured by modifying the parameter k_r, which links the critical state with the soil strength, keeping a constant value of $k_r = -0.5$ as reported in the literature reduces the number of parameters for which calibration is required.

The stiffness during cyclic loading, however, is not well captured, as a consequence of the parameter R_0 controlling both anchor displacement and stiffness within a cycle. Lower stiffness from the macro-element analysis could be obtained with smaller R_0, but that would also increase the displacement of the anchor during cyclic loading. An independent consideration of anchor displacement and stiffness would require the inclusion of additional parameters, which is not desirable from a practical point of view. Furthermore, the difference in stiffness during cyclic loading may be a result of simulating partial drainage using uncoupled stages of undrained load and consolidation. The equivalence of stiffness between the two approaches was not verified in previous studies that represented partially drained conditions by means of uncoupled stages of shear and consolidation (e.g. Gourvenec et al., 2014; Flessati et al., 2020). A comparison between two approaches is shown in Chapter 6 for granular soils, although the differences in stiffness were not directly investigated in this chapter.

The stress path of the representative soil element in Figure 5.10 reveals that, initially, the stress path moves to the left as the excess pore pressure increases and the vertical effective stress decreases during the initial monotonic stage (point A to B) and the first 153 cycles (B to D1). That is accompanied by a decrease in the available soil strength τ_c, as observed in Figure 5.10b. As the cyclic loading evolves, the pore pressure generation, which initially is greater than the pore pressure dissipation (point B to D.1) is outweighed by pore pressure dissipation (point D.1 to D.2), which results in a regain in effective stress and consequently in soil strength. At the same time, the specific volume υ decreases between points D.1 and D.2, which also contributes to the gain in soil strength. During the final undrained monotonic stage (point D.2 to F), the soil strength decreases again due to the decrease in effective stress induced by excess pore pressure generation. The soil strength at the end of cyclic loading (point D) is 78 kPa as opposed to 69 kPa before the initial monotonic stage (point A), which translates into a gain in anchor capacity with respect to the initial monotonic capacity.

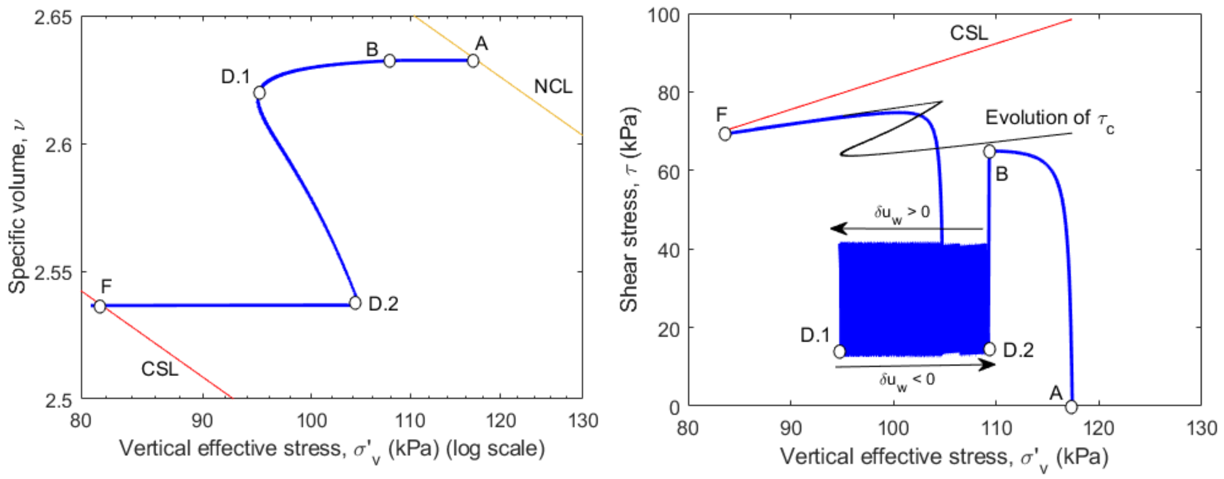

(a) (b)

Figure 5.10 – Stress paths for Test 2 given by the macro-element model.

The procedure that led to the results in Figure 5.9 and Figure 5.10 started by carrying out a macro-element analysis with values reported in the literature for the shear parameters of the representative soil element (i.e. the Severn-Trent model). As a starting point, the same set of values for the shear parameters adopted by Diambra et al. (2013) were used for the representative soil element ($A = 0.75$, $k_d = 1.5$, $k_r = -0.5$), except for parameter C, which had been calibrated from the monotonic tests ($C = 0.00003$). The parameters a and T_{50} initially assumed the values suggested by Singh & Chatterjee (2018) [$a = 1.86$ and $T_{50} = 0.083$], although that study involved a different experimental set-up with a horizontally-installed anchor subjected to vertical loading. The values of parameter A, which controls the pore pressure generation, as well as parameters a and T_{50}, which control the pore pressure dissipation, were then modified to match the post-peak capacity, whereas the hardening parameters R_1 and R_2 were adjusted to match the displacement of the anchor during cyclic loading and to ensure a smooth transition from cyclic to monotonic stage.

The effect of parameter A on the representative soil element is shown in Figure 5.11 while the effect on anchor capacity is shown in Figure 5.12.

From Figure 5.11b, it can be observed that although more excess pore pressure is generated for a higher value of A (0.75 in red), this also provides more excess pore pressure that is available for dissipation at the end of each cycle. After 1080 cycles, even though the stress-volumetric path in blue in Figure 5.11b ($A = 0.40$) is at a higher vertical effective stress (point 1) than for the red line (point 2), the stress-volumetric path in red ($A = 0.75$) dissipated more pore pressure at the end of each cycle, which brings the soil element to a denser state, i.e. to a state with lower specific volume. Hence, the state parameter ψ that controls soil strength through Equation (4.16) [$\tau_c = \tan(\varphi_{cs})\ \sigma_v'\ \psi^{kr}$] is lower for $A = 0.75$ (point 2) than for $A = 0.4$ (point 1), which in turn gives a higher soil strength at the end of cyclic loading for $A = 0.75$, as shown in Table 5.4. It is worth noting that, for undrained loading, the specific volume controls the soil strength, as the stress path moves horizontally in the υ-ln(σ_v') plane. On the other hand, for drained conditions, the vertical effective stress would control the soil strength, as the stress path would move vertically.

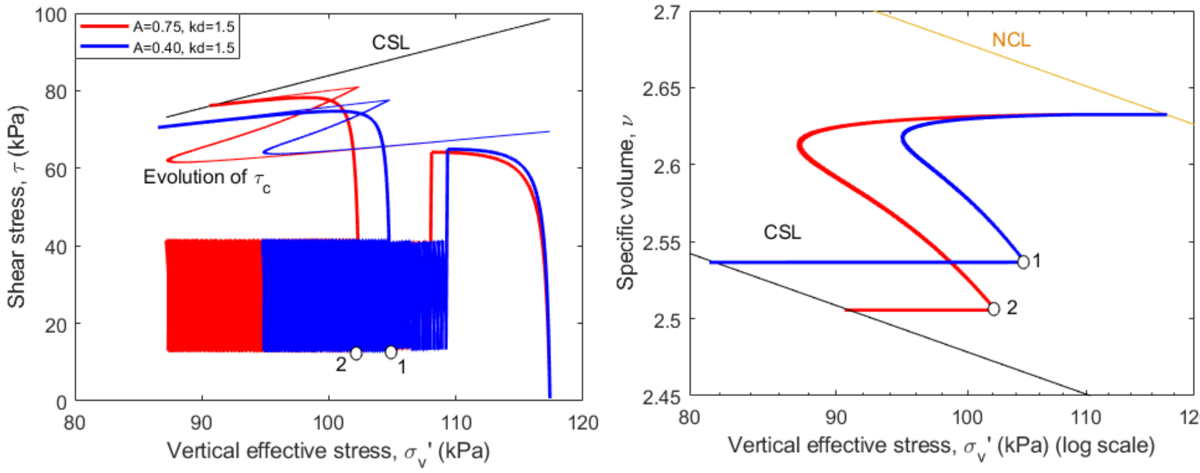

(a) (b)

Figure 5.11 – Effect of parameter A on the response of the representative soil element.

Table 5.4 – Effect of parameter A on soil strength.

Parameter A	Specific volume, υ	Effective stress, σ_v' (kPa)	Effective stress on CS, σ_{cs}' (kPa)	State parameter, ψ	Soil strength at the end of cyclic, τ_c (kPa)
0.4	2.537	104.8	81.5	1.28	77.6
0.75	2.506	102.4	90.8	1.13	80.9

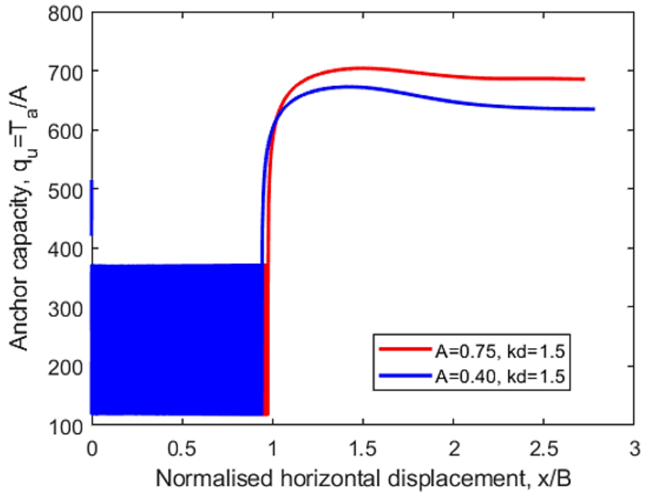

Figure 5.12 – Effect of parameter *A* on anchor capacity.

While parameter *A* controls the pore pressure generation in the macro-element model, the pore pressure dissipation during consolidation is controlled by the parameters a and T_{50} in Equation (4.8). These parameters were calibrated to ensure that the post-cyclic capacity agreed well with the value obtained from the centrifuge test, as previously shown in Figure 5.9. The effect of these parameters is displayed in Figure 5.13. For a higher value of a (= 1.86), the excess pore pressure dissipation is initially slower, but at $u_e/u_{e,i}$ = 0.5 the curves for a = 1.15 and 1.85 intercept each other, after which the excess pore pressure dissipation occurs quicker for a = 1.86. On the other hand, by increasing the value of T_{50}, the dissipation curve moves to the right, which means that the whole dissipation process is slower for a higher T_{50}.

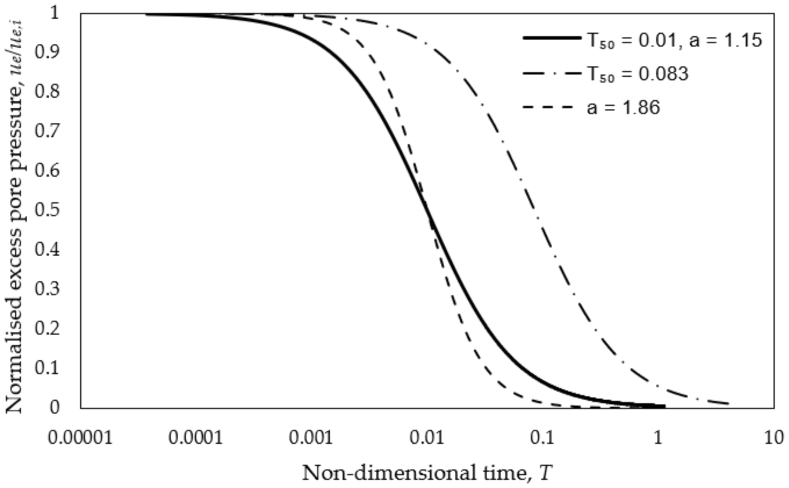

Figure 5.13 – Effect of parameters a and T_{50} on the pore pressure dissipation.

The effect of parameters a and T_{50} on the response of the representative soil element and on the anchor behaviour are presented in Figure 5.14 and in Figure 5.15, respectively. As expected, the macro-element analysis with higher values of a and T_{50} exhibits less pore pressure dissipation during cyclic loading. For a higher value of T_{50} or a, less consolidation occurs at the end of each loading packet, therefore a smaller fraction of the excess pore pressure generated in previous cycles is dissipated. This can be visualised in Figure 5.14, which shows higher effective stresses throughout the analysis for a = 1.15 and T_{50} = 0.01 (in blue). The occurrence of higher effective stresses in blue is attributed to less excess pore water pressure during cyclic loading, i.e. more dissipation of the excess pore water pressure generated during the initial monotonic and subsequent cyclic loading. Higher vertical effective stress results in higher soil strength τ_c (as shown in Figure 5.14a), which in turn results in higher anchor capacity, as displayed in Figure 5.15. The relationship between anchor capacity and shear stress is further explored later in this chapter.

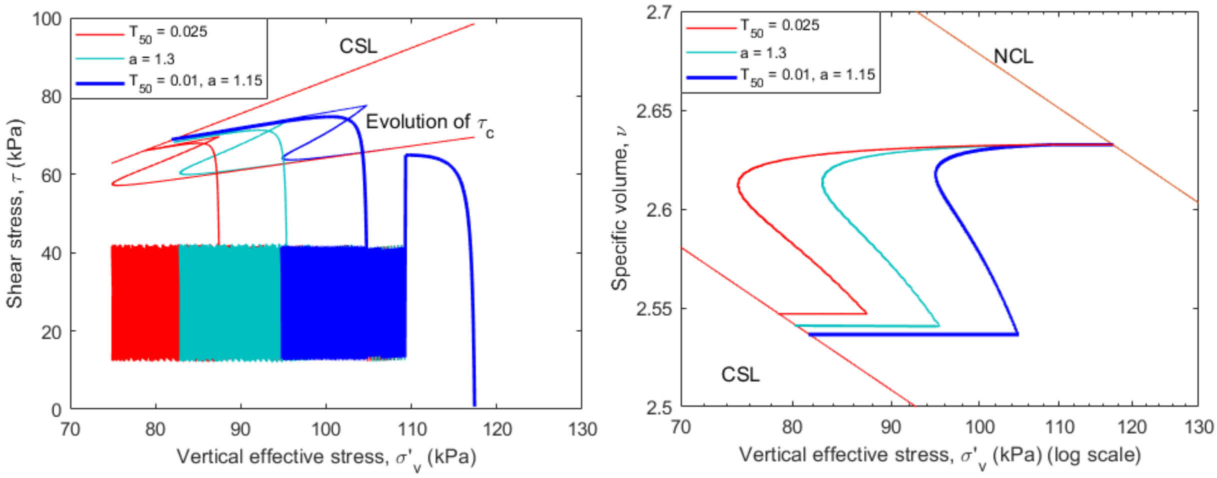

Figure 5.14 – Effect of parameters a and T_{50} on the representative soil element response.

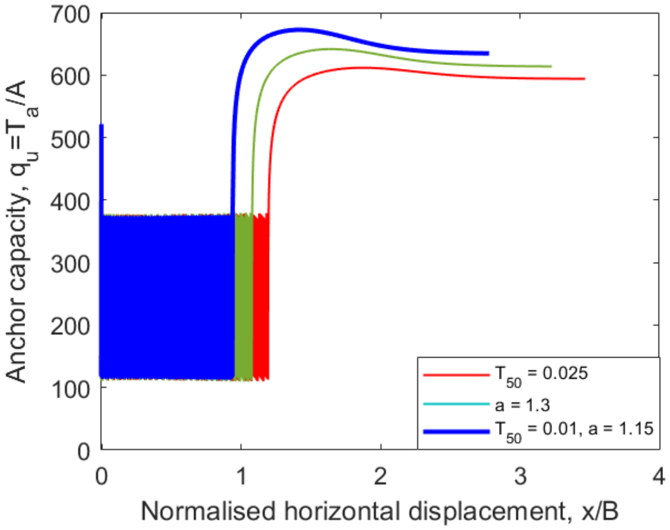

Figure 5.15 – Effect of parameters a and T_{50} on the anchor response.

Finally, the effect of assuming a constant value for the hardening parameter of the anchor (R_0) is analysed and compared with the case where R_0 is dependent on the current soil strength τ_c. As shown in Figure 5.16, by assuming a constant R_0, the displacement of the anchor during post-cyclic monotonic loading is significantly underestimated. While for the case of R_0 varying with τ_c the displacement between the end of cyclic loading and the point of peak load is $x/D = 0.484$, for the case with a constant value of R_0 (= 80) the displacement is of $x/D = 0.008$, i.e. 1.6% of the displacement obtained with a variable R_0. This is because the soil strength becomes much higher during long-term cyclic loading, as previously shown by the evolution of the representative soil element's strength in Figure 5.10b. As a consequence of that, the displacements within a cycle become very small as the number of cycles increases. In order to match the displacement during cyclic loading obtained from the macro-element model with that observed in the centrifuge test, a high value of R_0 is necessary (R_0 = 80). Consequently, the behaviour is also very stiff during the final monotonic stage, as shown in Figure 5.16.

When the dependency of R_0 on soil strength combined with a memory surface (as previously explained in section 4.6) is used, the behaviour is also very stiff during cyclic loading, but a less stiff response is re-established once a virgin state is reached (i.e. when the mobilisation of anchor capacity ρ_c reaches the maximum value experienced by the soil in the past, ρ_{cM}). It is worth noting the anchor capacity (peak load) for both cases is the same, as the choice for a constant or a variable R_0 does not affect anchor load.

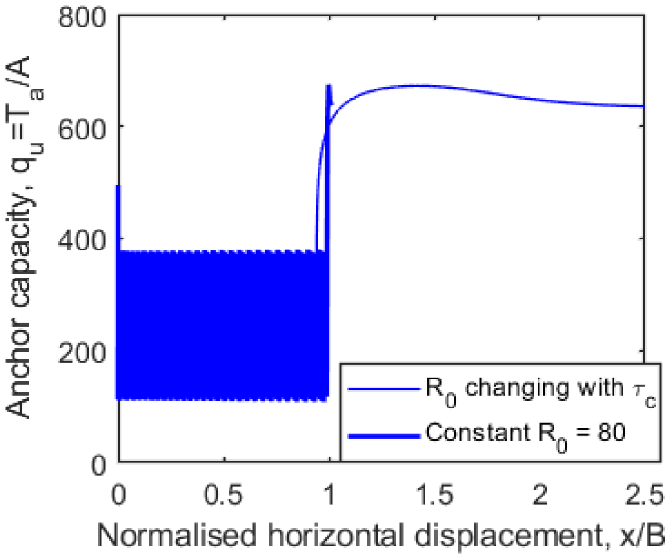

Figure 5.16 – Comparison between R_0 constant and dependent on soil strength τ_c.

The evolution of R_0 with anchor displacement is displayed in Figure 5.17. During the initial monotonic stage, the value of R_0 is approximately 0.7. During cyclic loading, the value varies between approximately 6 and 250 in the first cycles and 30 and 500 in the last cycles, which translates into very small anchor displacements within a cycle. As the mobilisation of anchor capacity ρ_c (and anchor load T_a) increases towards the highest mobilisation value experienced by the anchor (ρ_{cM}), ρ_c approaches ρ_{cM} and the difference $[(\rho_{cM} - \rho_c)/\rho_{cM}]$ approaches zero. Once $\rho_{cM} = \rho_c$, the hardening parameter R_0 depends solely on the ratio $\tau_c/\tau_{c,ref}$, according to Equation (4.34). The parameter R_0 then transitions from 30 at the end cyclic loading to 0.8 at the final monotonic loading.

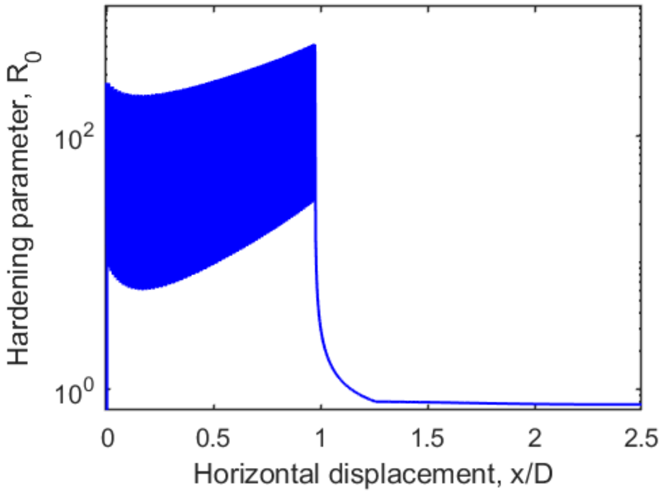

Figure 5.17 – Evolution of R_0 with anchor displacement.

Since the stiffness of the force-displacement curves and the prediction of anchor displacements by the macro-element model is much more in line with centrifuge tests when R_0 changes according to Equation (4.34), this approach will also be used for the model validation through comparison with Tests 3 and 4, as follows in the next section.

5.2.2. Model validation – Tests 3 and 4 – Maintained and cyclic loading

With all model parameters calibrated from Tests 1 and 2, further simulations can be carried out to verify the performance of the macro-element model with more complex conditions. While Test 1 involved an episode of maintained loading and Test 2 involved an episode of cyclic loading, Tests 3 and 4 involve one and five episodes of cyclic followed by maintained loading. The same parameters calibrated from Tests 1 and 2 are used in the analyses of Tests 3 and 4.

Test 3 consisted of the application of maintained loading during 3 hours (after the initial monotonic loading), followed by cyclic loading (1080 cycles) and then by another period of 3 hours of maintained loading, as detailed previously in Figure 5.2. A final monotonic stage was applied right after that.

Figure 5.18 depicts a comparison between macro-element model and centrifuge test results. The results show good agreement in terms of peak capacity of the anchor, which is slightly overestimated by 1.3% (q_u = 1003 kPa for the macro-element model and 990 kPa for the centrifuge test) as well as displacement during cyclic loading. As for Test 2 shown previously, the stiffness during cyclic loading is not well captured, as a consequence of the parameter R_0 controlling both anchor displacement and stiffness within a cycle. As mentioned previously, this difference in stiffness during cyclic loading may also be a result of simulating partial drainage using decoupled stages of shear and consolidation within the cycles.

Analysis of the representative soil element (Figure 5.19) shows that the initial decrease (point A to B) in soil strength during undrained monotonic loading is followed by an increase in soil strength during the period of maintained loading (point B to C initially following the URL line and then following the NCL line), similarly to the behaviour observed in Test 1 (Figure 5.8). The soil element then exhibits an initial decrease in soil strength from point C to point D1, followed by an increase from point D1 to D2 during cyclic loading, similarly to the behaviour observed in Test 2 (Figure 5.10). At the end of the cyclic loading, a final stage of maintained loading is applied (point D2 to E), which increases the soil strength due to the dissipation of the remaining excess pore pressure. The increase in effective stress due to the maintained and long-term cyclic load lead to a gain in soil strength: from 69 kPa at the start of the initial monotonic stage (point A) to 118 kPa after an episode of cyclic and maintained loading (point E), i.e. a gain of 71% in soil strength. The strength after the final monotonic stage (point F) is 95 kPa, which represents a gain of 44% in comparison with 66 kPa at the end of the first monotonic stage.

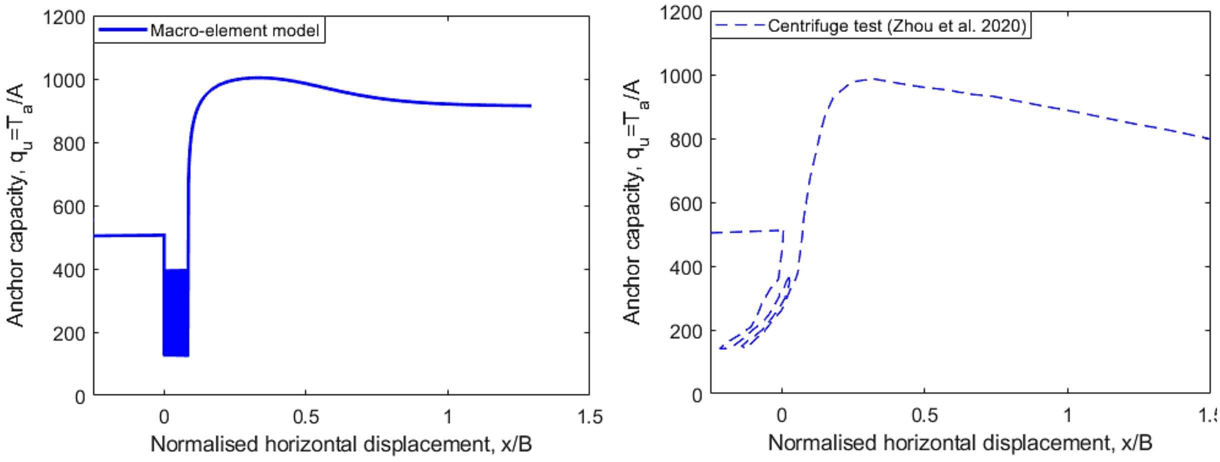

(a) (b)

Figure 5.18 – Comparison between macro-element model and experimental result for Test 3.

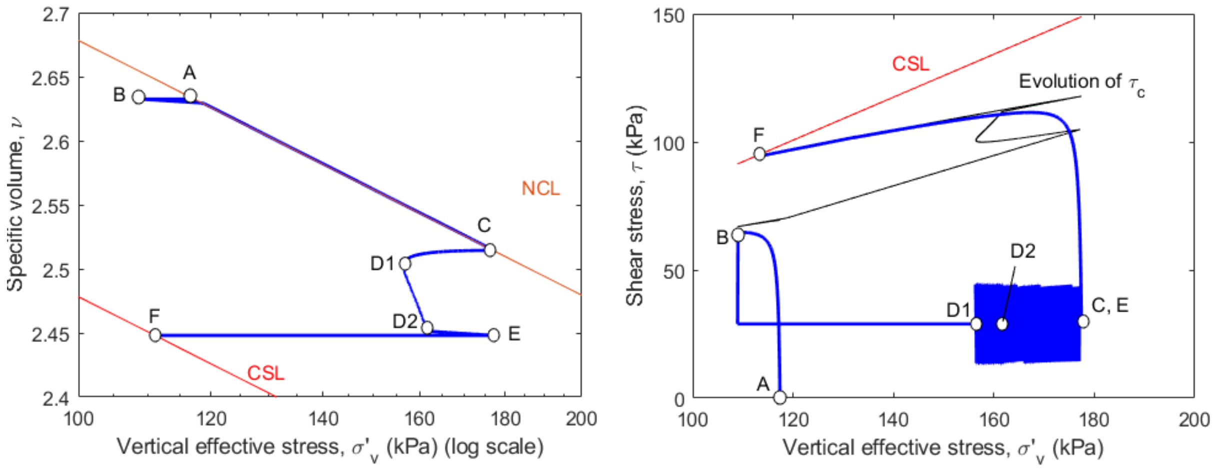

(a) (b)

Figure 5.19 – Stress paths for Test 3 given by the macro-element model.

Similarly to Test 3, Test 4 consisted of the application of an initial monotonic stage and a maintained loading stage followed by five episodes of 1080 cycles combined with 3 hours of maintained loading. A final monotonic stage was applied after the five episodes.

Good agreement is observed in terms of anchor capacity as well as of anchor displacement during failure (Figure 5.20). If compared with the monotonic capacity, a gain of 147% is achieved after the five episodes of cyclic and maintained loading (from 521 kPa to 1287 kPa). The anchor capacity is overestimated by only 4.6% by the macro-element model (1287 kPa from the macro-element model and 1230 kPa from the centrifuge test), whereas the anchor displacement during cyclic loading given by the macro-element model is approximately 0.14 *D* which is similar to the displacement of 0.10 *D* observed in the centrifuge test.

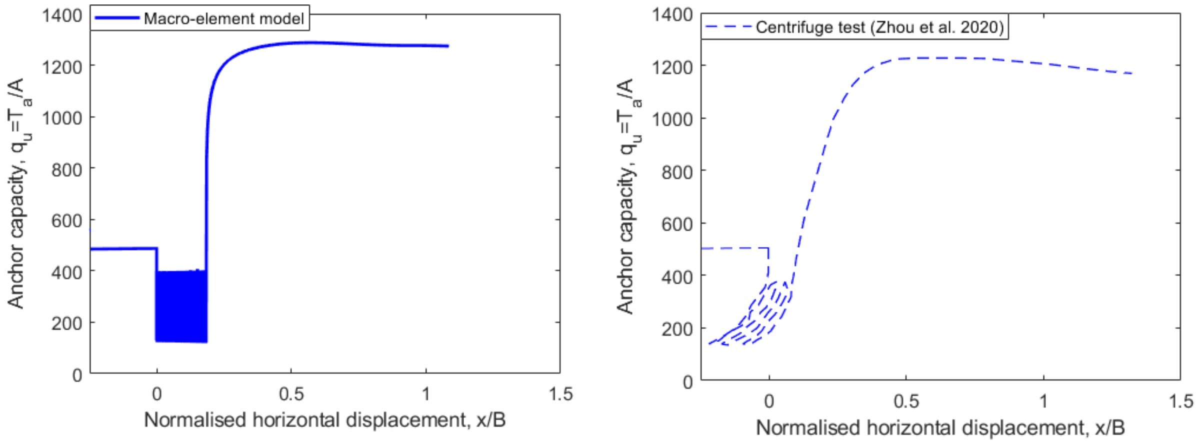

(a) (b)

Figure 5.20 – Comparison between macro-element model and experimental result (Test 4).

Analysis of the representative soil element (Figure 5.21) depicts a similar behaviour between the episodes of cyclic loading followed by maintained loading: initial loss in soil strength due to pore pressure generation (C-D1) followed by gain in soil strength due to pore pressure dissipation exceeding pore pressure generation (D1-D2), then followed by further gain in strength during the period of pure maintained load. It is worth noting, though, that although the soil strength continues to increase with the number of episodes, the gain decreases with increasing number of episodes. This is due to progressively less pore pressure being generated as the soil element is at a higher effective stress – and consequently a higher shear strength (as observed by Zhou et al., 2020). The peak shear stress during monotonic loading (point B in Figure 5.21b) is 57.4 kPa whereas, after the five episodes of cyclic combined with maintained loading, the maximum shear stress (near point F) was 143 kPa, which represents a gain of 149% – which is exactly the same gain in final shear stress observed in the soil element.

Table 5.5 shows that the final capacities obtained from the macro-element model agree well with those obtained from the centrifuge tests. The maximum percentage difference is observed in Test 2, for which the macro-element model predicts an anchor capacity about 7% less than the actual capacity observed in the centrifuge test.

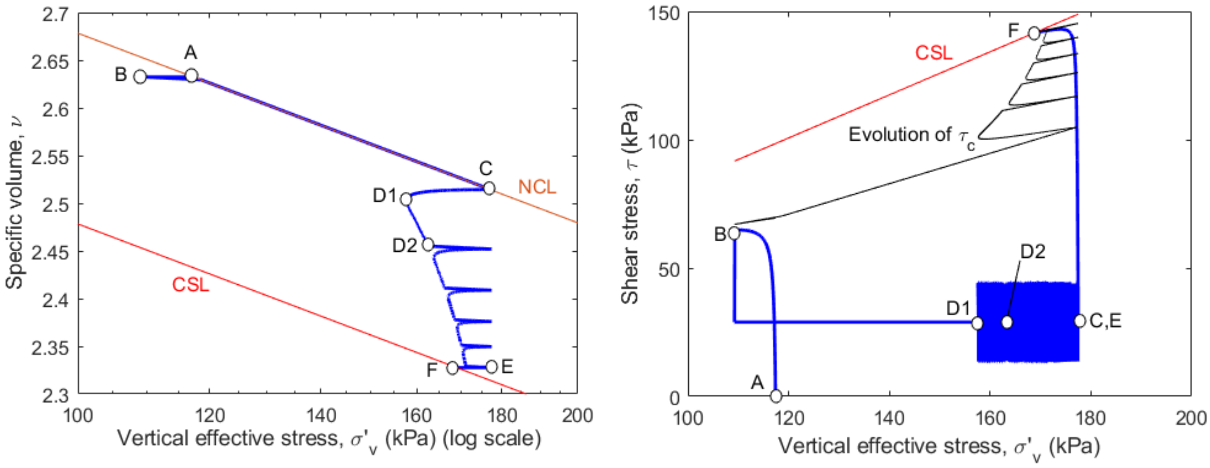

(a) (b)

Figure 5.21 – Stress paths for Test 4 given by the macro-element model.

Table 5.5 – Summary of anchor capacities – comparison between experimental and model results.

Test	Initial capacity (kPa)		Final capacity (kPa)		Gain in capacity (%)	
	Centrifuge (Zhou et al., 2020)	Macro-element model (% dif.)	Centrifuge (Zhou et al., 2020)	Macro-element model (% dif.)	Centrifuge (Zhou et al., 2020)	Macro-element model
1	516	516 (0%)	780	788 (+1.0%)	51%	53%
2	489	516 (+5.5%)	737	683 (-7.3%)	50%	32%
3	521	516 (-0.9%)	990	1003 (+1.3%)	90%	94%
4	492	516 (+4.9%)	1230	1287 (+4.6%)	150%	149%

It is worth noting that, from the macro-element simulations of Tests 1 to 4, there is a relationship between the shear stress on the representative soil element and the load (or pressure) on the plate anchor. A direct relationship between the maximum shear stress and the peak capacity of the anchor is observed, as shown in Table 5.6. The ratio between the peak capacity of the anchor ($q_{u,p}$) observed in the force-displacement curves and the peak shear stress of the representative soil element (τ_p) observed in the stress paths equals 9.0 for all four tests.

Table 5.6 – Relationship between anchor capacity and shear stress on the representative soil element

Test	Macro-element anchor peak capacity, $q_{u,p}$ (kPa)	Peak shear stress of representative soil element, τ_p (kPa)	Ratio $q_{u,p}/\tau_p$
1	788.2	87.6	9.0
2	683	75.9	9.0
3	1003	111.5	9.0
4	1287	143.0	9.0

This observation might be valuable for future studies, in the sense that in one-dimensional situations (i.e. where anchor displacements in only one direction are observed), the anchor capacity after long-term operations can be estimated by the evolution of a representative soil element tested in the laboratory. Furthermore, for three-dimensional loading scenarios, the contribution of changes in soil strength on the variation of anchor capacity could be estimated by laboratory tests and could be added to the effect of anchor kinematics to determine the overall changes in anchor capacity due to cyclic loading. The combined effect of changes in anchor kinematics and changes in soil strength should be supported by further studies.

5.2.3. Discussion, summary of procedures and difficulties

This section summarises the main procedures for the use of the macro-element model to account for episodes of cyclic and maintained loading in clay. A summary of strong points, uncertainties and difficulties is also presented.

Firstly, the experimental conditions, soil properties and anchor geometry have to be defined, as these are input quantities to the model:

- Soil properties: unit weight (γ'), friction angle at critical state (φ_{cs}), slope and intercept of the critical state line (λ and Γ, respectively), initial void ratio (υ_0);
- Anchor geometry: diameter (D) in the case of a circular anchor;
- Experimental conditions: initial embedment depth (Y), initial anchor orientation (β), load direction with the horizontal at the padeye (θ_a).

Secondly, several parameters that can be obtained from the literature are selected.

- Parameters for the shear model of the soil k_d and k_r: the suggested values $k_d = 1.5$ and $k_r = -0.5$ seem to be suitable for all cases analysed in this chapter. These values were reported by Diambra (2010) and Diambra et al. (2013), which are similar to those used by Gajo & Muir Wood (1999) and Corti et al. (2016).
- Model parameters of the anchor: for the one-dimensional case presented in this section, the only parameter related to the anchor that is required is the normalised capacity N_v, which was obtained from Singh & Ramaswamy (2008) for circular anchors in clay. The suggested value is $N_v = 9$.

Following the initial experimental conditions and parameters obtained from the literature, the parameter *C* which controls the hyperbolic stiffness relationship in the shear model of the soil, the parameter *A* controlling the pore pressure generation, and the parameters *a* and T_{50} controlling the pore pressure dissipation need to be calibrated by means of a few centrifuge tests.

- Monotonic test: parameter *C* can be calibrated by matching anchor capacity from an undrained monotonic centrifuge test.
- Test involving an episode of maintained loading: by carrying out a test in which the excess pore pressure generated during the initial monotonic loading is allowed to dissipate, the influence of an additional stress caused by the anchor on the soil can be measured, hence the influence factor of Boussinesq (I_σ) can be calibrated. The influence factor I_σ is calibrated to match post-consolidation anchor capacity, i.e. the capacity measured from an undrained monotonic stage after the episode of maintained loading. For easier calibration of this parameter, nearly full dissipation is suggested during the episode of maintained loading, such that the consolidation parameters *a* and T_{50} can be independently calibrated through another test.
- Test involving long-term cyclic loading: a centrifuge test involving long-term cyclic loading is required for the calibration of parameter *A*, which governs pore pressure generation, and parameters *a* and T_{50}, which govern pore pressure dissipation. The values of these parameters are selected to match anchor capacity after an episode of long-term cyclic loading, i.e. the capacity measured from an undrained monotonic stage after the episode of long-term cyclic loading. The post-cyclic capacity depends on the final shear strength of the soil, which is governed by the vertical effective stress on the representative soil element. Higher values of *a* and T_{50} result in less pore pressure dissipation, which translates into lower vertical effective stress and shear strength of the soil and smaller anchor capacity. Higher values of *A* also result in higher final soil strength, which translates into higher anchor capacity. It is worth noting that while higher values of *A* cause more pore pressure generation, more excess pore pressure is available for dissipation, which overall increases soil strength in the long term.
- Also from the test involving long-term cyclic loading, the value of the hardening parameter R_0 is selected to match the anchor displacement during cyclic loading. For a

smooth transition between cyclic and post-cyclic monotonic loading and for a better prediction of anchor displacement during the final monotonic stage, dependency of R_0 on the soil strength τ_c can be introduced, which requires the introduction of a memory surface calibration of parameters R_1 and R_2.

5.3. Three-dimensional loading

The proposed macro-element model can also be used to assess the effect of different consolidation periods on the capacity of plate anchors. This section aims to apply the macro-element model to the case of a plate anchor installed vertically but subjected to vertical load, which causes not only displacement normal to the plate but also in the direction parallel to the anchor, as well as rotation due to the eccentric load.

5.3.1. Experimental programme

The centrifuge tests carried out by Blake et al. (2011) are used to assess the model in a three-dimensional loading condition. The centrifuge tests, carried out at an acceleration level of 100g, involved a square plate anchor with length and breadth $L = B = 2.5$ m and thickness 0.1 m (prototype scale), as shown in Figure 5.22. The padeye eccentricity was $e_n/B = 0.6$ and the initial embedment depth was 4.5 B in normally consolidated kaolin clay. The anchor was initially installed at a vertical position, with the anchor padeye horizontally aligned with the actuator. The actuator pulls the chain up vertically, which translates into a nearly-vertical load applied on the padeye. The experimental set-up is illustrated in Figure 5.23.

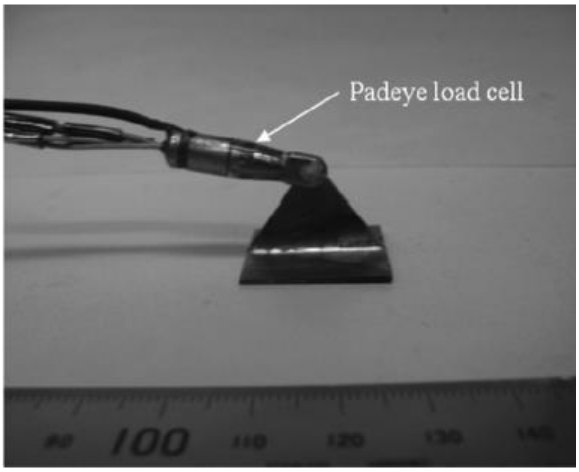

Figure 5.22 – Model square plate anchor used in centrifuge tests (Blake et al., 2011).

As previously mentioned in the literature review (Chapter 2), the centrifuge tests involved an initial monotonic load under undrained conditions, with a velocity of pull at the actuator of $v = 0.15$ mm/s, which corresponds to a normalised velocity $V^* = vB/c_v$ above 30. This normalised velocity is enough to ensure undrained conditions, according to House et al. (2001). The initial undrained load was applied up to the (assumed) end of the keying plateau in the force-displacement curve, after which "the actuator was stopped and the load allowed to relax" (Blake et al., 2011, p. 708), allowing for consolidation to occur. A further monotonic load up to the peak capacity was applied after the consolidation period (referred to herein as 'post-consolidation' stage). Different non-dimensional times of consolidation (T_{cons}) ranging from $T = 0$ to $T_{cons} = 474$ ($t_c \approx 66$ hours in model scale or 75 years in prototype scale) were analysed.

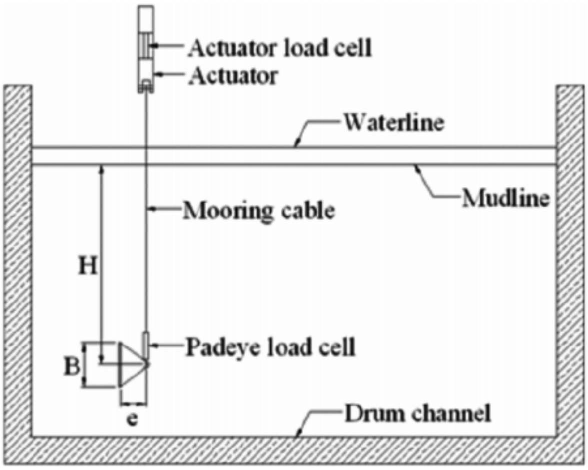

Figure 5.23 – Experimental set-up of centrifuge tests (Blake et al., 2011).

A summary of the properties of kaolin clay characterised by Stewart (1992) is presented in Table 5.7, while the relevant anchor dimensions are presented in Table 5.8.

Table 5.7 – Experimental conditions – anchor dimensions in prototype scale (Stewart, 1992).

Symbol	Parameter	Value
	SOIL PARAMETERS	
γ'	Effective unit weight (kN/m^3)	6.5 kN/m^3
G_s	Specific gravity of the solids	2.6
v	Initial specific volume	2.46
γ'	Effective unit weight (kN/m^3)	6.5
λ	Slope of NCL and CSL	0.205
κ	Slope of the swelling line	0.044
Γ_{NCL}	Specific volume at $\sigma_v' = 1$ kPa on the NCL	3.34
Γ_{CSL}	Specific volume at $\sigma_v' = 1$ kPa on the CSL	3.14
φ_{cs}	Critical state friction angle (°)	23
c_v	Coefficient of consolidation (m^2/year)	2.6

Table 5.8 – Experimental conditions – anchor dimensions in prototype scale (Blake et al., 2011).

ANCHOR PARAMETERS		
B	Anchor breadth (m) in prototype scale	2.5
L	Anchor length (m) in prototype scale	2.5
e_n	Padeye eccentricity (m) in prototype scale	1.5
e_p	Padeye offset (m) in prototype scale	0

The parameters used for the macro-element simulations are presented in Table 5.9. As for the previous modelling exercise under one-dimensional conditions, the values of the soil parameters used by Diambra et al. (2013) were adopted as a starting point. The selection of the most suitable parameters' values is described in section 5.3.2.2.

Table 5.9 – Soil and anchor parameters for three-dimensional loading.

Parameter	Description	Value	Remarks
	SOIL PARAMETERS		
T_{50}	Dimensionless time factor for 50% consolidation	10	Calibrated
a	Consolidation curve fitting	1.4	Calibrated
A	Flow rule multiplier	0.75	Diambra et al. (2013)
k_d	State parameter multiplier in flow rule	1.5	Diambra et al. (2013)
k_r	Link between state parameter and strength	-0.5	Diambra et al. (2013)
C	Hyperbolic relationship parameter	0.0005	Calibrated
	ANCHOR PARAMETERS		
I_σ	Boussinesq influence factor	0.5	Calibrated
m	Shape of loading surface (moment)	2	Chapter 3
n	Shape of loading surface (horizontal)	4	Chapter 3
q	Shape of loading surface (vertical)	4	Chapter 3
N_v	Normalised normal capacity factor	13	Elkhatib (2006)
N_h	Normalised sliding capacity factor	3	Elkhatib (2006)
N_m	Normalised rotational capacity factor	2	Elkhatib (2006)
ξ	Plastic potential parameter (vertical)	1.6	Chapter 3
χ	Plastic potential parameter (horizontal)	1.1	Chapter 3
ω	Plastic potential parameter (moment)	1.2	Calibrated
R_0	Hardening parameter of the anchor	1.5	Calibrated

The aim of this section is not to calibrate the model with one (or more) test and challenge against other tests, but rather verify whether the model is capable or reproducing certain aspects of anchor behaviour and also to provide insights in terms of which parameters and geotechnical properties are necessary for the application of the model.

5.3.2. Macro-element results

The results from the model analyses and centrifuge tests are compared in Figure 5.24. Two extreme cases, with $T_{cons} = 0$ (i.e. purely undrained conditions) and $T_{cons} = 474$ are presented. The procedure for parameter selection as well as the effect of the values selected for certain parameters will be explained in the next section.

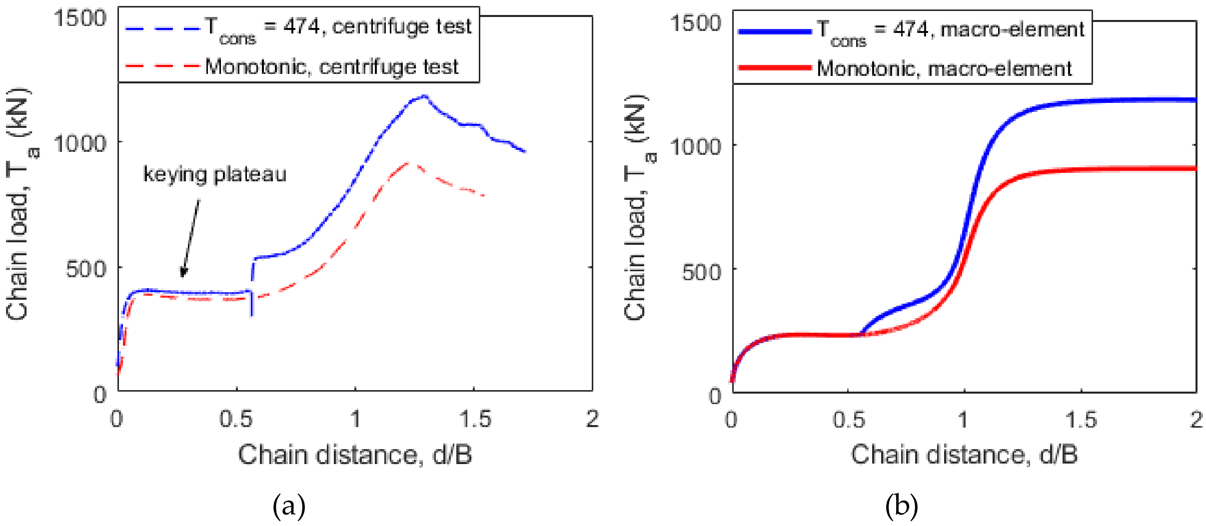

(a) (b)

Figure 5.24 – Comparison between macro-element model and centrifuge tests by Blake et al. (2011).

It can be observed that the curves for both cases agree well both in terms of anchor capacity and in chain distance at which the peak capacity is reached, though the 'keying plateau' is lower in the macro-element analyses. The peak capacities from the centrifuge test are 916 kN and 1183 kN for monotonic and long-term consolidation ($T_{cons} = 474$), respectively. The capacities obtained from the macro-element model are 903 kN and 1181 kN, which are 1.4% and 0.2% less than the capacities observed in the centrifuge test, respectively. However, the post-consolidation stiffness of the force-displacement curve is slightly different. For the centrifuge tests, an initial decrease in the chain load is observed during consolidation. The subsequent post-consolidation load shows very stiff initial behaviour with no changes in the chain distance, i.e. no anchor motion. For the macro-element analysis, on the other hand, the load was assumed to remain constant during consolidation, during which the soil regained strength which in turn resulted in increased post-consolidation stiffness combined with some anchor displacement.

The response of the representative soil element can be visualised in Figure 5.25. The behaviour is similar to the observed for the one-dimensional case in Figure 5.8. The initial undrained load up to the end of the keying plateau generates positive excess pore pressure, which decreases the vertical effective stress and moves the current stress state from A to B. The available soil strength decreases from 13.5 kPa (A) to 13 kPa (B) at the end of this stage. During consolidation, the stress path initially follows a κ-line in the υ-ln(σ_v') plane and then follows the NCL down to point C. At point C, the soil strength is 15.7 kPa. Finally, after the consolidation, the final undrained stage generates further excess pore pressure and decreases the vertical effective stress to 32.1 kPa at point F, at which the soil strength is 14.6 kPa. That is 31.5% than the available strength for a fully undrained monotonic load (point F_M), for which the available strength at the end of the simulation (i.e. at the critical state) is 11.1 kPa

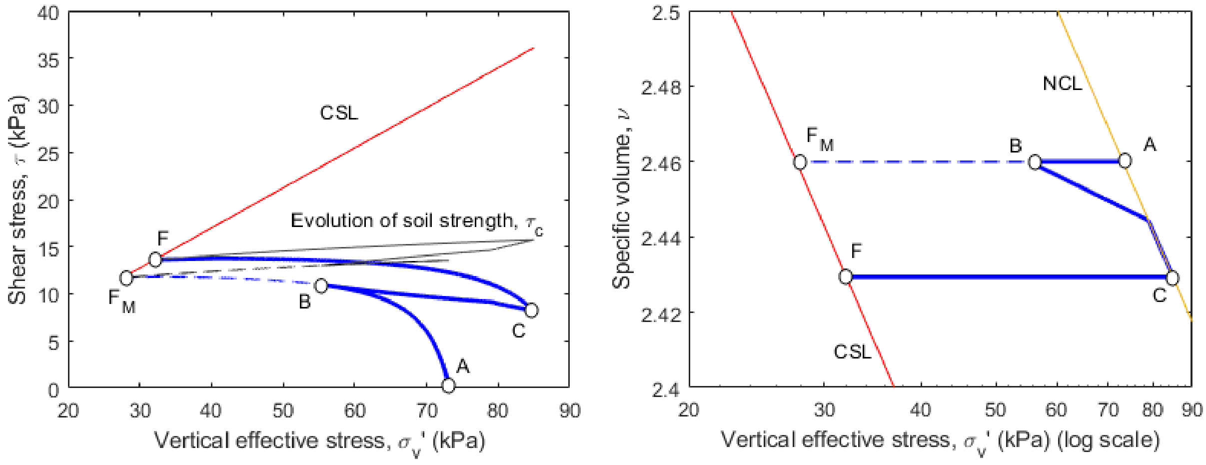

(a) (b)

Figure 5.25 – Representative soil element for T_{cons} = 474.

Several other macro-element simulations were carried out in order to compare the effect of different consolidation times with the behaviour observed by Blake et al. (2011) in the centrifuge tests. The consolidation periods used in the macro-element analyses were the same as for the centrifuge tests (see Table 5.10). Centrifuge tests with the same dimensionless consolidation time were simulated only once in the macro-element model.

The dependence of normalised anchor capacity on the non-dimensional consolidation time is shown in Figure 5.26. A curve fitting function is employed for the relationship between normalised capacities $T_p/T_{p,max}$ and the non-dimensional consolidation time, as proposed by Richardson et al. (2009) and used by Blake et al. (2011).

$$\frac{T_p}{T_{p,max}} = \frac{A_1 - A_2}{1 + \left(\frac{T}{T_{50}}\right)^p} + A_2 \tag{5.2}$$

Where T_p is the anchor's peak capacity, $T_{p,max}$ is the highest peak capacity in the drainage domain, A_1 is the initial value of the normalised capacity (i.e. the highest value of $T_p/T_{p,max}$ in the case of contractive soils), A_2 is the final value of the normalised capacity (i.e. the lowest value of $T_p/T_{p,max}$ in the case of contractive soils), T_{50} is the value of the non-dimensional consolidation time T at the mid-point between A_1 and A_2 and p is a fitting parameter governing the slope of the curve.

From Figure 5.26, it can be seen that the short-term or nearly-undrained capacity (for $T < 0.1$) is approximately 0.75 of the long-term or nearly-drained capacity (for $T > 100$) according to the centrifuge tests, whereas the ratio $T_p/T_{p,max}$ according to the macro-element model is about 0.76. The parameters used for the fitting curves were $A_1 = 0.75$, $A_2 = 1.0$, $T_{50} = 8.0$ and $p = 0.75$ for the centrifuge tests (Blake et al., 2011) and $A_1 = 0.76$, $A_2 = 1.0$, $T_{50} = 10.0$ and $p = 1.0$ for macro-element analyses. The slight difference in these parameters does not affect the fitting curve significantly, as will be further discussed in section 5.3.2.2.

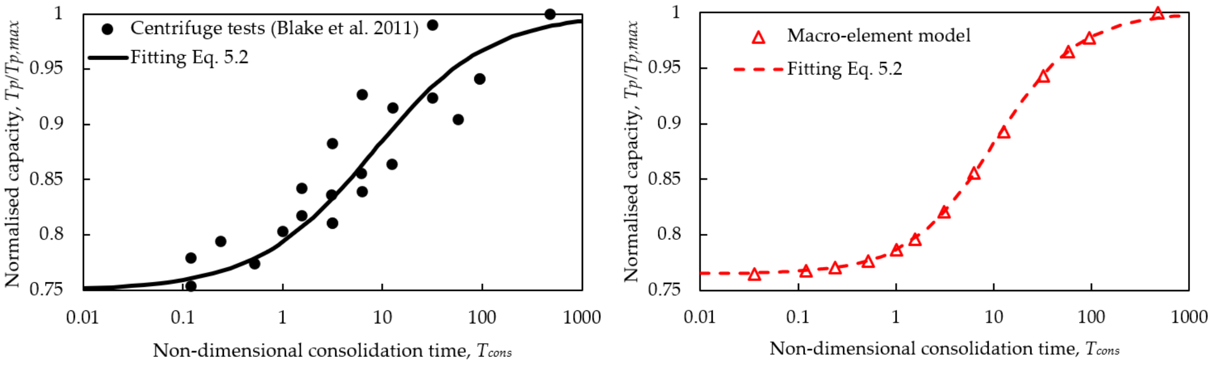

(a) (b)

Figure 5.26 – Normalised anchor capacities for (a) centrifuge tests (Blake et al., 2011); (b) macro-element model.

If the results are presented in terms of non-normalised capacities (T_p), good agreement between macro-element and centrifuge tests is also observed in Figure 5.27. From Table 5.10, it can be seen that the ratio of macro-element to centrifuge capacities are all within the range of 0.93-1.07, mainly due to the scatter observed in the experimental results. The average ratio of macro-element to centrifuge capacities is 0.99.

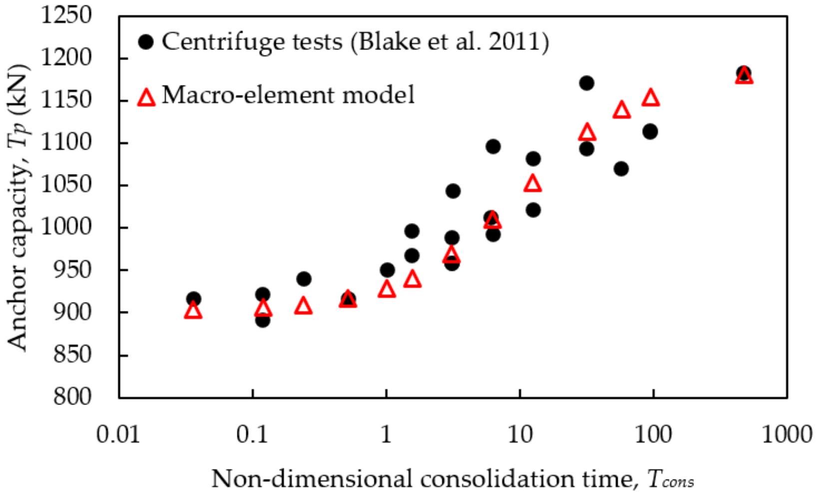

Figure 5.27 – Comparison in anchor capacities for centrifuge tests (Blake et al., 2011) and macro-element model.

Table 5.10 – Summary of centrifuge tests (Blake et al., 2011) and macro-element analyses.

Test	Time (h:m:s)	Dimensionless time, T_{cons}	Peak load, centrifuge test (kN)	Peak load, macro-element model (kN)	Ratio of macro-element to centrifuge capacity	Normalised capacity, $T_p/T_{p,max}$
1	00:00:00	0.00	916.4	903.3	0.99	0.76
2	00:25:55	3.10	989.1	968.9	0.98	0.82
3	00:52:34	6.28	992.8	1010.3	1.02	0.86
4	13:08:24	94.50	1113.6	1154.4	1.04	0.98
5	00:01:01	0.12	891.8	906.6	1.02	0.77
6	00:04:19	0.52	915.9	917.0	1.00	0.78
7	00:12:58	1.56	967.1	940.3	0.97	0.80
8	01:45:07	12.57	1022.0	1054.0	1.03	0.89
9	13:08:24	94.45	1113.9	1154.4	1.04	0.98
10	00:01:01	0.12	921.6	906.6	0.98	0.77
11	00:25:55	3.13	958.8	968.9	1.01	0.82
12	00:00:00	0.00	947.8	903.3	0.95	0.76
13	04:22:48	31.84	1171.1	1114.1	0.95	0.94
14	00:12:58	1.56	995.9	940.3	0.94	0.80
15	00:25:55	3.15	1044.0	968.9	0.93	0.82
16	04:22:48	31.57	1093.2	1114.1	1.02	0.94
17	00:52:34	6.31	1096.3	1010.3	0.92	0.86
18	01:45:07	12.61	1082.2	1054.0	0.97	0.89
19	65:42:00	474.05	1183.1	1181.0	1.00	1.00
20	00:02:01	0.24	939.4	909.8	0.97	0.77
21	00:08:38	1.01	950.4	928.5	0.98	0.79
22	00:52:34	6.11	1012.1	1010.3	1.00	0.86
23	08:13:54	57.44	1069.6	1139.6	1.07	0.96

The selection of the parameters that led to the results presented in Figure 5.24 through Figure 5.27 is explained as follows. The mechanism of stress transfer from the anchor to the soil element for three-dimensional loading is also explained.

5.3.2.1. Stress transfer from anchor to soil element

As previously mentioned in this chapter, the centrifuge tests carried out by Blake et al. (2011) involved an initial monotonic load under undrained conditions up to the assumed end of the keying plateau in the force-displacement curve, after which a relaxation of the load in the actuator took place, allowing for consolidation to occur. A further undrained monotonic load up to the peak capacity was applied after the consolidation period.

Although the experimental results showed that the anchor load decreases during the actuator relaxation, this is rather difficult to reproduce as the load was not controlled during the centrifuge test. Therefore, it is assumed in the macro-element simulations that the load on the anchor (T_a) is constant during the consolidation period. This assumption should not have significant influence on the main outcomes of the macro-element analyses.

As mentioned previously in section 5.2 for a one-dimensional case, an additional *total* stress is added to the representative soil element to account for the effect of the maintained load. In the one-dimensional case, the horizontal stress from the anchor acting on the representative soil element is multiplied by K_0 and hence accounted for in the vertical stress. In the case of unidirectional load, no rotations of the anchor occurred, therefore the direction of the involved stresses remained the same during the development of shear and consolidation processes.

For the case of a vertical anchor subjected to an eccentrically-applied vertical load, significant rotation of the plate is observed during the keying process before the rotation stabilises prior to reaching the peak load. The direction of the additional stress applied to the representative soil element due to the maintained load, therefore, depends on anchor orientation at the start of the consolidation process. If the anchor orientation is not vertical or horizontal, the rotation of stresses must be considered in order to obtain the additional vertical stress acting on the representative soil element.

For the particular case of the tests conducted by Blake et al. (2011), it was assumed in the original publication that the majority of anchor rotation occurred during the keying plateau (shown in Figure 5.24a) observed in the force-displacement curve. Therefore, minimal rotation was assumed to occur during and after the consolidation period. This assumption would imply that the anchor was at a nearly horizontal orientation and subjected to a vertical load at the start of the maintained load, as the orientation of plate anchors is nearly perpendicular to the direction of loading at the end of keying (e.g. Dove et al., 1998; Gaudin et al., 2014).

However, in recent communications with the first author of Blake et al. (2011) (Dr Anthony Blake), it was found that the anchor actually continued to rotate after the keying plateau, which is in line with the findings of Song et al. (2006) and O'Loughlin et al. (2014). The rotation of the anchor from its initial vertical position (β) at the end of the keying plateau was, therefore, verified through the macro-element analysis.

Since the additional stress $\Delta\sigma' = (T_a/B^2)\, I_\sigma$ is applied at an orientation perpendicular to the anchor plane, multiplying $\Delta\sigma'$ by the lateral earth pressure coefficient K_0 gives the additional stress perpendicular to the direction of the load, i.e. parallel to the anchor plane. The rotation of this additional stress by the angle β (rotation of the anchor relative to its initial vertical orientation) through Mohr's circle provides the vertical stress acting on the representative soil element, as shown in Figure 5.28.

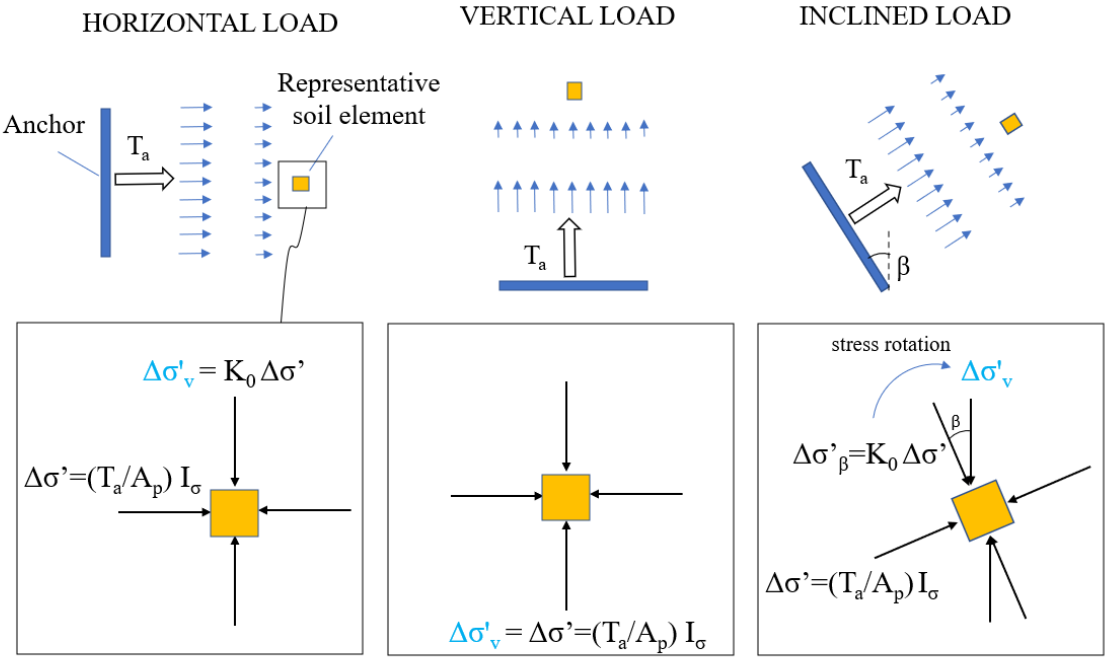

Figure 5.28 – Stress rotation due to anchor reorientation.

Therefore, the stress rotation through Mohr's circle depends on the orientation of the anchor with respect to the vertical, which in the case of a vertically installed anchor, is the same as the rotation β experienced by the anchor. Boussinesq's influence factor I_σ for a square or rectangular loaded area is given by the chart in Figure 5.29.

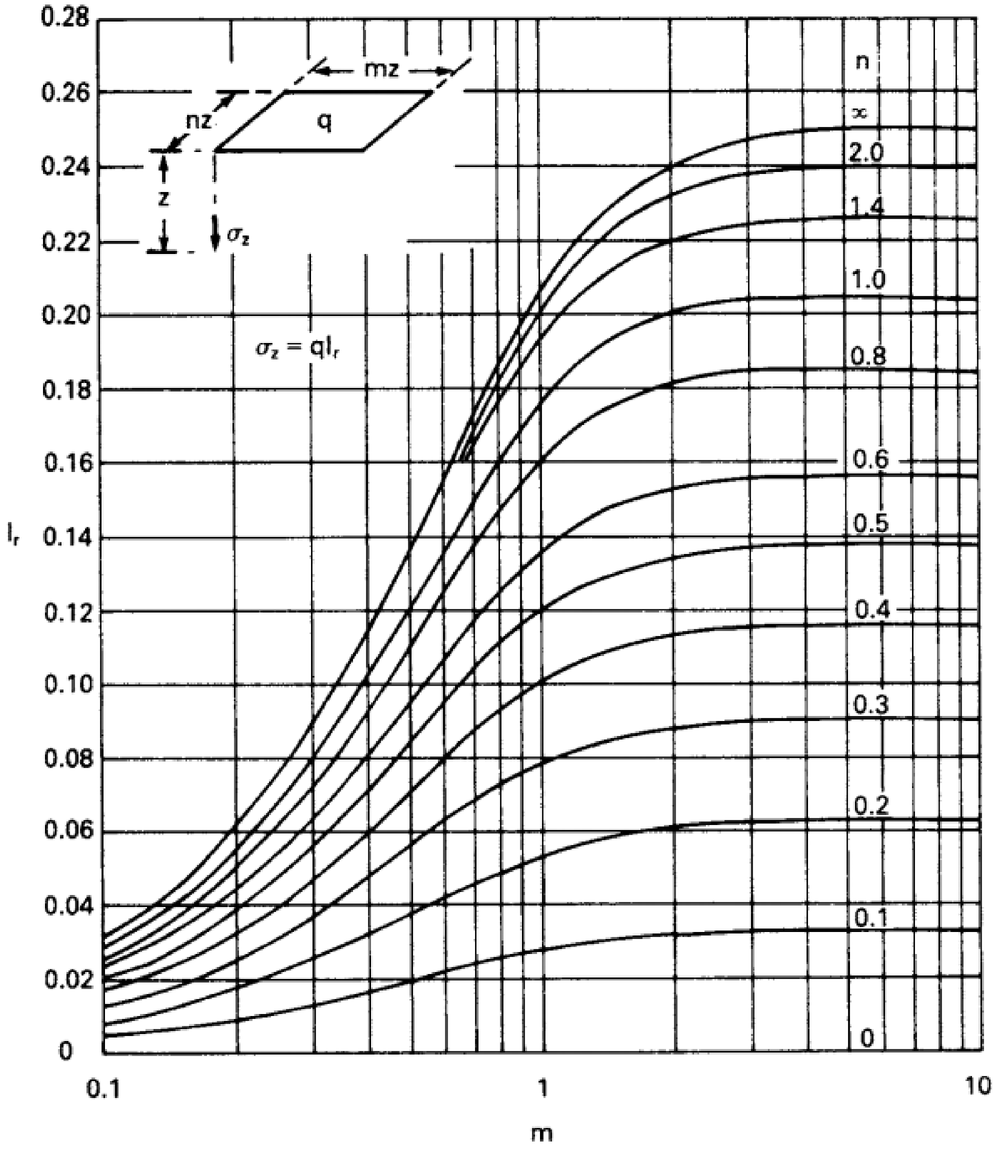

Figure 5.29 – Vertical stress under a corner of a rectangular area carrying a uniform pressure (Craig, 2004).

The stress transfer from the anchor to the representative soil element as well as the selection of Boussinesq's influence factor I_σ is further explained in the next section.

5.3.2.2. Parameter selection

Parameters for the shear model of the representative soil element

The slope of the CSL (λ) was assumed to be equal that of the NCL given by Stewart (1992). Since the clay is normally consolidated, the specific volume relative to the intercept of the normal consolidation line (NCL) with $\sigma_v' = 1$ kPa was taken as 3.34, such that the initial stress state ($v = 2.46$ and $\sigma_v' = 73.12$ kPa) lies on the NCL. Other geotechnical parameters such as slope of the swelling line κ, critical state friction angle φ_{cs}, specific volume of the critical state line at $\sigma_v' = 1$ kPa (Γ) and coefficient of consolidation (c_v) were also provided by Stewart (1992). As for the one-dimensional case, the parameters related to the shearing behaviour of the representative soil element (A, C, k_d and k_r) assumed the values reported by Diambra (2010) and Diambra et al. (2013) as a starting point and were modified in the same order, starting with parameter C which governs the hyperbolic stiffness relationship, which was calibrated to match anchor capacity for the undrained monotonic test (shown previously in Figure 5.24b in red). It follows that decreasing parameter C from its initial value (from 0.0025 to 0.0005) and keeping the values of the other parameters ($A = 0.75$, $k_d = 1.5$, $k_r = -0.5$) provides good agreement between the macro-element model and the centrifuge test.

Capacity factors of the anchor and shape factors of the loading surface

The capacity factors N_v, N_h and N_m were obtained from Elkhatib (2006) for square anchors, similarly to the values used in Chapter 3. The values selected were $N_v = 13$ (for square anchors, while in Chapter 4, $N_v = 14$ was used for rectangular anchors), $N_h = 3$ and $N_m = 2$. The parameters controlling the shape of the loading surface m, n and q used herein assume the same values used in Chapter 3 and in several other publications (e.g. Bransby and O'Neill 1999; Elkhatib and Randolph 2005; Cassidy et al. 2012).

Influence factor I_σ and plastic potential parameter ω

For the macro-element model simulations, an anchor rotation of $\beta = 37.26°$, was observed, whereas another 51.73° of rotation occur *after* the keying plateau. The precise orientation of the anchor after the keying plateau was not measured during the centrifuge tests carried out by Blake et al. (2011) and to date such information has not been found in the literature for other studies in clay. However, visual observations from a centrifuge test in transparent soil under undrained conditions (s_u = 18 kPa) published by Song et al. (2006, 2009) showed that, at the end of the keying plateau, the anchor had rotated approximately 35° (Figure 5.30), which is similar to the anchor rotation β = 37.26° observed in the macro-element analysis. The rotation of 37.26° was used for the calculation of the new stress states at the end of the keying plateau following stress rotations in the Mohr's circle, as previously shown in Figure 5.28 for an inclined load.

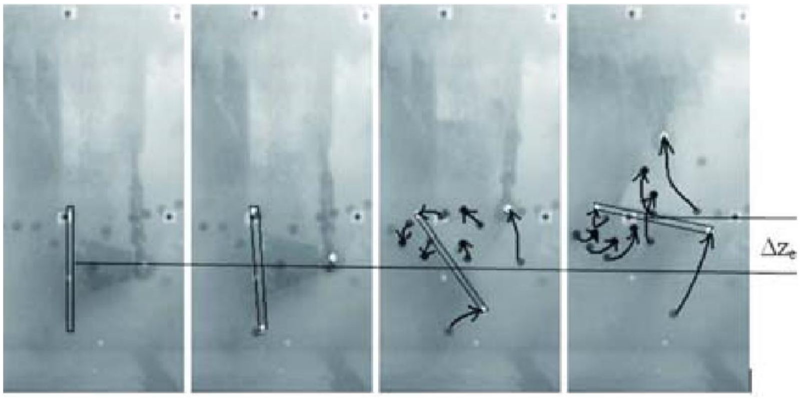

Figure 5.30 – Anchor orientation for a vertical pull-out in transparent soil (adapted from Song et al., 2006, 2009).

At the end of keying plateau, the chain load was T_a = 236 kN, which gives a stress of q_a = 37.76 kPa on a soil element at x/B = 0 from the plate. In order to obtain how much of this stress is transferred onto the representative soil element, the influence factor I_σ must be defined, since the stress at the soil element is given by $\Delta\sigma = I_\sigma\, q_a$. The influence factor I_σ is calibrated in combination with the plastic potential parameters, since both affect the anchor capacity.

The plastic potential parameters ξ and χ assume the constant values 1.6 and 1.1, respectively, and the parameter ω is the only plastic potential parameter that may vary from case to case, as shown in Chapter 3.

Figure 5.31 shows the effect of both plastic potential parameter ω and Boussinesq's influence factor I_σ on the force-displacement behaviour of the anchor subjected to a dimensionless time allowed for consolidation T_{cons} = 474. Although the macro-element analyses in Chapter 3 suggested that ω = 1.5 can be used as an initial attempt, a smaller value ω = 1.2 provides better agreement with the centrifuge test in terms of anchor displacement, particularly the displacement at peak load.

The influence factor I_σ does not seem to have a significant impact on the force-displacement response for this particular case, as the peak load for I_σ = 0.5 is only 5% smaller than that for

$I_\sigma = 0.9$ ($T_{a,p} = 1181$ kN and 1249 kN, respectively). An influence factor $I_\sigma = 0.5$ is adopted since this value provides good agreement with the peak capacity from the centrifuge test ($T_{a,p} = 1183$ kN). An influence factor of 0.5 is associated with a representative soil element at $x/B = 0.7$ from the anchor in a direction perpendicular to the plate plane, according to the chart in Figure 5.29.

The portion of the stress $q_a = 37.76$ kPa on a soil element immediately in front of the anchor that is transferred to the representative soil element is $\Delta\sigma = I_\sigma\, q_a = 18.88$ kPa. The stress in a direction parallel to the plate is given by $\Delta\sigma_\beta = K_0\, \Delta\sigma$ (with $K_0 = 1 - \sin \varphi_{cs}$) = 11.5 kPa. Rotation of stresses by of $\beta = 37.26°$ to a vertical stress gives an additional vertical stress $\sigma_a = 7.53$ kPa acting on the representative soil element. Hence, when consolidation occurs during $T_{cons} = 474$, not only the vertical effective stress returns to its initial state ($\sigma_v' = 73.12$ kPa), but also an additional $\sigma_a = 7.53$ kPa is transferred to the representative soil element, as depicted in Figure 5.25b.

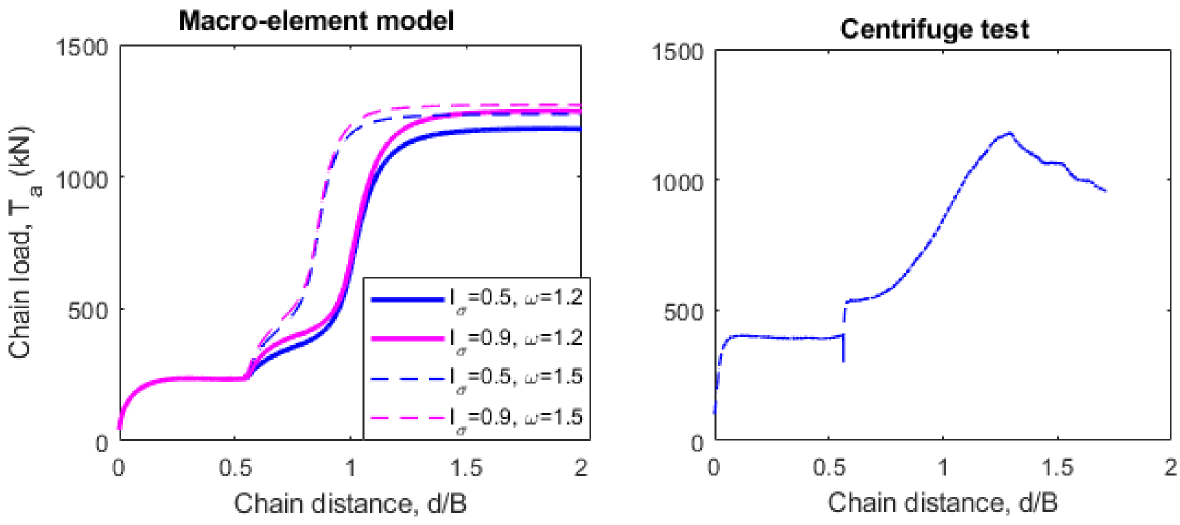

(a) (b)

Figure 5.31 – Effect of the plastic potential parameter ω and Boussinesq's influence factor I_σ on the force- displacement response of the anchor for a consolidation time $T_{cons} = 474$.

Hardening parameter of the anchor, R_0

The parameter R_0 was calibrated to match the initial part of the force-displacement curve. Since the variation of the shear strength of the soil τ_c does not vary significantly during the analysis, R_0 was assumed as constant, and not dependent on τ_c as in the one-dimensional case. The approach with R_0 dependent on the current soil strength and including a memory surface [following Equation (4.34)] was also simulated. It was found that force-displacement curve with a variable R_0 using $R_1 = 9$ and $R_2 = 1.4$ is coincident with the curve for a constant $R_0 = 1.5$.

Consolidation parameters, a and T_{50}

The consolidation parameters *a* and T_{50} were selected based on the results from the centrifuge tests carried out by Blake et al. (2011). T_{50} is the non-dimensional time at the mid-point between the maximum and minimum anchor capacity, while *a* controls the curvature of the pore pressure dissipation curve, as previously shown in Figure 5.13. Both parameters were selected such that macro-element simulations with a non-dimensional consolidation time $T > 100$ would cause nearly 100% of excess pore water pressure dissipation, i.e. nearly drained conditions, and such that nearly undrained conditions (i.e. pore pressure dissipation near zero) would occur for $T < 0.1$, as observed from the experiments of Blake et al. (2011) in Figure 5.32. It is worth noting that the parameter T_{50} used for the consolidation stage in the macro-element model is the same as the T_{50} value used in the fitting curve. The application of the selected value of T_{50} for the macro-element analyses ($T_{50} = 10$) that is different to the value used by Blake et al. (2011) for the fitting curve does not affect the results significantly, as also shown in Figure 5.32.

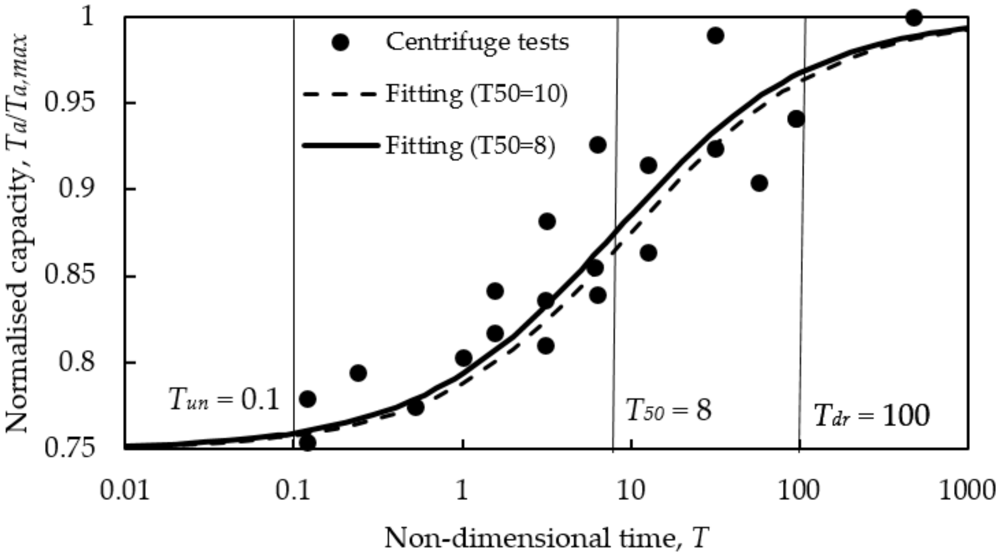

Figure 5.32 – Capacities and fitting curve for centrifuge tests (adapted from Blake et al., 2011).

5.3.2.3. *Discussion on parameters for three-dimensional loading*

The macro-element model seems to be able to capture the effect of different consolidation times on the capacity of the anchor. However, selection of appropriate model parameters has an important influence on the results.

- Consolidation parameters, a and T_{50}

In this modelling assessment, the consolidation parameters a and T_{50} were calibrated such that nearly-drained behaviour would occur for $T > 100$ and nearly-undrained behaviour would occur for $T < 0.1$. The calibration of a and T_{50} was only possible because the capacity values for different consolidation times was available from Blake et al. (2011). The values of these parameters differ significantly from values used by Singh & Chatterjee (2018), even though both studies were conducted with kaolin clay and similar soil parameters were used, as characterised by Stewart (1992). While $T_{50} = 10$ and $a = 1.4$ were calibrated with the centrifuge tests, Singh & Chatterjee (2018) suggested $T_{50} = 0.085$ and $a = 1.85$ for the consolidation of a point above an anchor subjected to vertical maintained load of 50% of the ultimate load and embedment ratio of 4.5, which is the approximate load level at which the anchor is during consolidation in Blake et al. (2011). However, several differences between the studies have to be accounted for. First of all, the point where consolidation was measured in Singh & Chatterjee (2018) was just a few centimetres from the anchor modelled in the finite-element software ABAQUS, while for the macro-element model the point considered was $0.7B$ (= 1.25 m) from the anchor. Secondly, in the study of Singh & Chatterjee (2018), the anchor is subjected to vertical load and no rotation of the plate occurs during the application of the load, i.e. the pulling force is always perpendicular to the anchor. In the centrifuge test by Blake et al. (2011) simulated by the macro-element model, the anchor experiences significant reorientation during the application of the load, and the magnitude as well as the orientation of the load acting on the representative soil element changes from case to case.

The selection of appropriate values for a and T_{50}, therefore, requires the results of a few centrifuge tests, such that the changes in anchor capacity due to pore pressure dissipation can be compared between at least two different consolidation times. The effect of experimental set-up and soil type on the values of these parameters needs to be further assessed by additional studies, as in the current study the calibration of these parameters was dependent on results from centrifuge tests.

- Boussinesq's influence factor I_σ

The influence factor $I_\sigma = 0.5$ was selected to match the anchor capacity for long-term consolidation given by Blake et al. (2011)'s centrifuge test. A noteworthy observation is that the distance associated with $I_\sigma = 0.5$ is x/B = 0.7, which is the same normalised distance (x/D = 0.7) observed for the one-dimensional case with a circular plate in section 5.2, even though anchor shape and stress transfer mechanism are different. It is worth noting that the influence factor I_σ only affects the capacity when consolidation occurs, i.e. when periods of maintained loading or long-term cyclic loading are imposed. For undrained monotonic loading, the additional stress caused by the loaded anchor results solely in an increase in pore water pressure and therefore does not affect the effective stress on the soil element, which in turn results in null effect on anchor capacity.

5.4. Further assessment of the model

Further assessment of the macro-element model under three-dimensional conditions is presented in this section. A hypothetical scenario involving an anchor subjected to eccentric loading (which induces rotation and both normal and tangential displacements) is simulated under cyclic loading. The analysis aims at investigating the conflicting effects of reduction in anchor capacity due to anchor kinematics, as previously shown in Chapter 3 (section 3.6) and the increase in anchor capacity due to gain in soil strength, as demonstrated in this chapter (sections 5.2 and 5.3). The configuration follows the study performed by Cassidy et al. (2012), but the assessment is extended here to the cyclic capacity of the anchor. The geometry considers a vertical plate anchor pulled vertically at its padeye, featuring both a horizontal and a vertical eccentricity with respect to the plate anchor mid-point. The anchor is subjected to vertical cyclic loading ($\theta_a = 90°$), as shown in Figure 5.33.

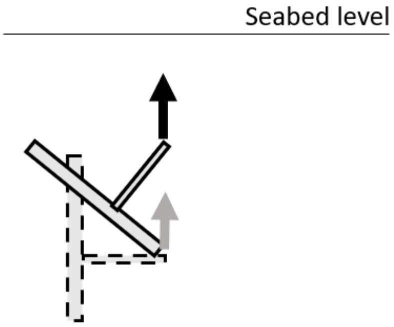

Figure 5.33 – Loading scenario for further assessment

The dimensions of the rectangular anchor are $B = 4.64$ m (breadth) and $L = 7.92$ m (length), and the anchor padeye is located at an eccentricity of $e_n = 2.59$m and an offset of $e_p = 0.492$ m. The initial embedment of the anchor is 20.25 m which corresponds to an embedment ratio of approximately 4.4. In this initial assessment, the selected model parameters related to the anchor are the same ones used in section 3.5.4 (see Figure 3.12). The parameters related to the representative soil element assume the values calibrated in the assessment with the centrifuge tests carried out by Zhou et al. (2020) and presented in Table 5.1 and Table 5.2.

The assessment of the cyclic capacity of the anchor explored the effect of both number of cycles and loading frequency. The applied amplitude of the cyclic loading was kept fixed in this assessment and forces T_a between 10% and 60% of the monotonic undrained anchor capacity were applied at the anchor's padeye.

In order to assess the relevance of the developments proposed in this chapter, but also to gain an insight on the cyclic behaviour, the cyclic simulations were performed with and without account for the behaviour of the representative soil element. To ensure that the simulations are comparable and that the variation of soil strength is the only aspect analysed, the hardening parameter R_0 was assumed constant, as the use of Equation (4.34) would change the value R_0 during the simulations with the representative soil element, but would not change it for the analyses with constant soil strength.

Figure 5.34 compares the simulations for monotonic undrained loading with those of 10 cyclic tests performed at a frequency of 0.4 Hz. When only the anchor kinematics are considered (i.e., neglecting the evolution of soil strength), the post-cyclic capacity of the anchor decreases by approximately 7% after 10 cycles in comparison with an undrained monotonic pull-out. On the other hand, when the changes in soil strength due to pore water pressure generation and dissipation are considered, the post-cyclic capacity is less than 2% smaller than the monotonic analysis, but the peak load is also reached for a higher loss of embedment. This increase in anchor capacity when changes in soil strength are considered is due to the pore pressure dissipation exceeding pore pressure generation after a certain number of cycles, making the soil regain part of the vertical effective stress that was lost during the first cycles.

The macro-element analyses previously presented in Chapter 4 suggest that anchor reorientation decreases the anchor post-cyclic capacity, and that the higher the number of cycles, the higher the loss in capacity. On the other hand, as shown in Zhou et al. (2020)'s centrifuge tests as well as in the macro-element simulations in this chapter, for long-term cyclic loading, high numbers of cycles cause a significant gain in soil strength. Model simulations for a range of number of cycles are provided in Figure 5.35. Figure 5.35a and Figure 5.35c display the force–displacement and rotational behaviour for the anchor when the changes in soil strength are considered, whereas Figure 5.35b and Figure 5.35d present results for when the soil strength is assumed as constant. The chain load in Figure 5.35c and Figure 5.35d was normalised by the current strength for each step during the model simulations.

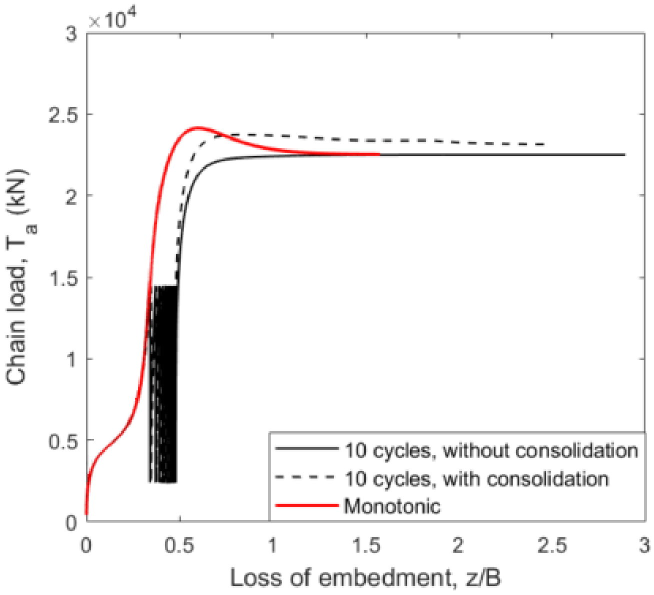

Figure 5.34 – Effect of the evolution of soil strength during 10 cycles of cyclic loading with a frequency of 0.4 Hz

The results in Figure 5.35b show that, if the soil strength is assumed constant and unaffected by the applied cyclic and consolidation stages, a decrease in post-cyclic peak capacity if compared to the monotonic capacity can be observed. The decrease is about 6% after 5 cycles and 7% after 10 cycles, after which the capacity loss seems to stabilise, as the same decrease (7%) is observed after 200 cycles. Conversely, Figure 5.35a shows that the slight decrease in the peak post-cyclic capacity observed after 5 and 10 cycles (both equal to approximately 2%) is followed by a considerable increase in the post-cyclic capacity equal to 23% after 200 cycles. This suggests that, while the anchor loses some capacity because of its reorientation during cyclic loading (see evolution of rotation in Figure 5.35b and Figure 5.35d), the gain in soil strength due to the consolidation process can initially counteract and then even largely outweigh the loss of capacity caused by the anchor kinematics in the cyclic loading process.

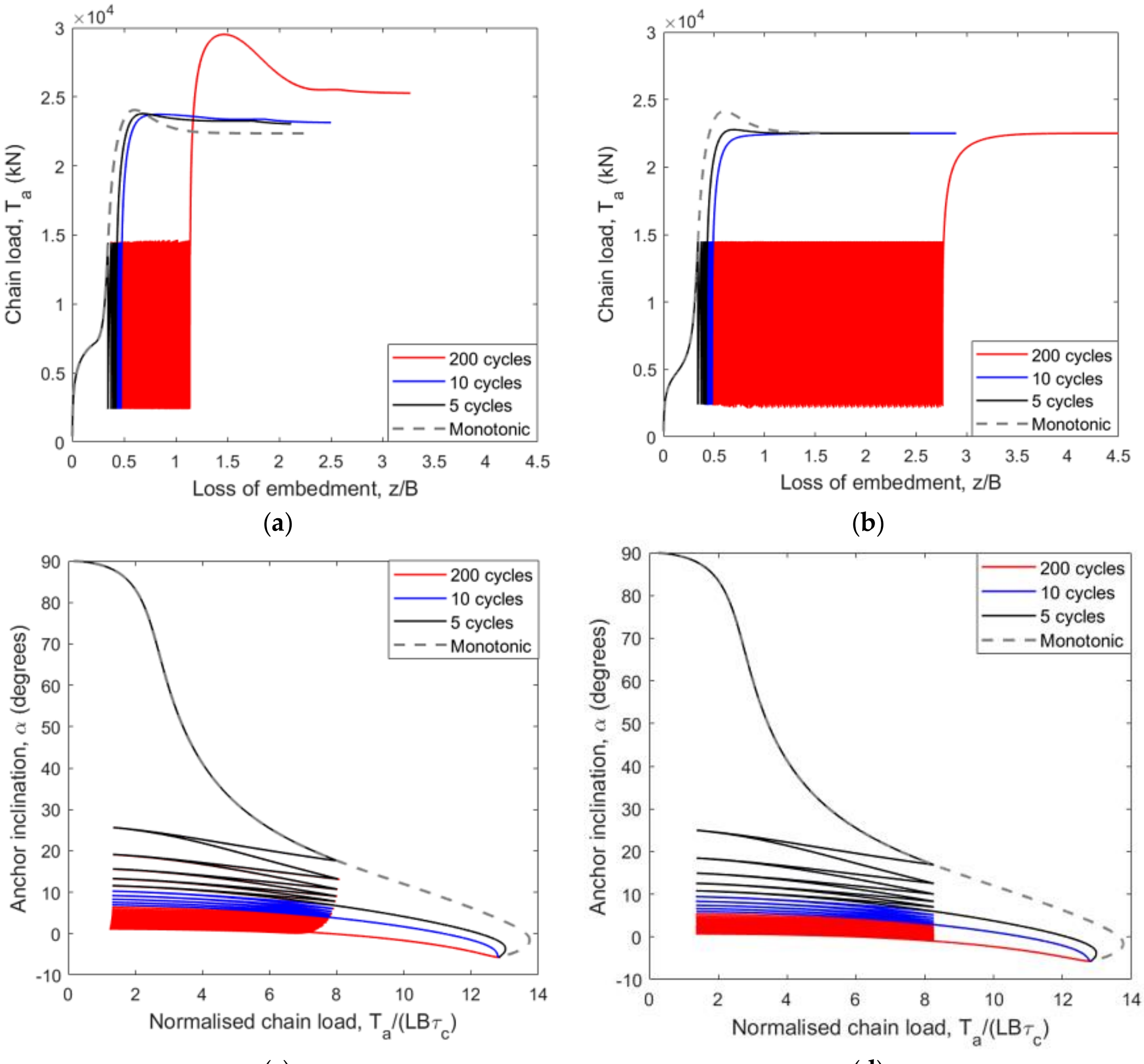

(a) (b)

(c) (d)

Figure 5.35 – Effect of the number of cycles on anchor capacity (**a**) with and (**b**) without consolidation and on anchor rotation (**c**) with and (**d**) without consolidation.

5.5. Final remarks

The macro-element model accounting for changes in soil strength due to pore pressure generation and dissipation was compared to two sets of centrifuge tests in cohesive soils. One set of tests involved long-term cyclic loading and maintained loading on circular plates installed vertically and subjected to horizontal loads, while the other set involved a square anchor installed vertically and loaded with an eccentric vertical load, for which different periods of consolidation were analysed. Based on the observations in this chapter, the following conclusions can be drawn:

- The macro-element model including a representative soil element is able to capture well the capacity of circular plate anchors subjected to one-dimensional loading. The model was calibrated with two centrifuge tests and challenged against two additional centrifuge tests.
- Two out of four parameters related to the shear model of the soil can assume the same values reported previously in the literature. The values of parameters k_d and k_r were obtained from Diambra et al. (2013). The parameter A controlling the pore pressure generation was calibrated with a long-term cyclic loading test, while the hyperbolic stiffness parameter C was calibrated with a monotonic test. The consolidation parameters a and T_{50} that govern consolidation were also calibrated with a centrifuge test involving long-term cyclic loading. The values represented an average contribution of the dissipation of all excess pore pressure generated in the previous episodes of cyclic loading.
- The influence factor I_σ was calibrated with a monotonic test involving a period of maintained loading. Several distances from the representative soil element to the centre of the plate were analysed, and an element distant 0.7 D from the anchor seems to provide the best result in comparison with the centrifuge test. Distances ranging from 0.25 D and 2.0 D provided anchor capacities 26% higher and 22% lower than the capacity measured in the centrifuge test, respectively.
- The simplified set-up of one-dimensional tests can be useful for the calibration of soil parameters, since the macro-element model of the anchor is significantly simplified, as no sliding and rotational forces are involved. The three plastic potential parameters (ξ,

χ and ω), the sliding and rotational capacities N_h and N_m, and the parameters m and n that control the shape of the loading and strength surfaces are eliminated from the model for a one-dimensional case.

- For a smooth transition between cyclic and post-cyclic monotonic loading and for a better prediction of anchor displacement during the final monotonic stage, dependency of R_0 on the soil strength τ_c can be introduced, which requires the introduction of a memory surface calibration of parameters R_1 and R_2. The dependency of the anchor's hardening parameter R_0 on soil strength τ_c is particularly important when significant variation of soil strength occurs during testing, i.e. mainly in situations that involve episodes of long-term cyclic loading. In cases where the variation of τ_c is not so significant, a constant value of R_0 can be assumed without affecting the results.
- For the three-dimensional case, the macro-element model captured well the effect of different times of consolidation on anchor capacity. The ratio of anchor capacities from macro-element to centrifuge tests ranged between 0.93 and 1.07, with an average value of 0.99.
- Using the values reported by Diambra (2010) and Diambra et al. (2013) as a starting point, only one out of four parameters related to the shear model of the soil had to be modified (parameter C, which governs the hyperbolic stiffness relationship).
- The influence parameter of Boussinesq I_σ was calibrated to match the anchor capacity after long-term consolidation. The value that provided the best agreement was $I_\sigma = 0.5$, which is representative of a soil element distant $0.7B$ from the anchor mid-point. Interestingly, the best agreement with centrifuge tests for the circular plate under one- dimensional loading was obtained when a representative soil element at $0.7D$ of the anchor mid-point was considered. It is worth noting that, while the influence factor I_σ affected significantly the capacity of the anchors in the one-dimensional case, this influence was less pronounced in the three-dimensional case.
- An initial assessment of the macro-element model under cyclic loading for three-dimensional loading conditions was carried out. It was shown that during cyclic loading, the anchor capacity may decrease for the kinematic effect of anchor reorientation and pore water pressure build up. However, gain in soil strength related to dissipation of pore water pressure generation may counteract both detrimental effects and increase the

overall cyclic capacity after a certain number of cycles. Despite being intuitively reasonable, the predictions of the model under three-dimensional cyclic anchor loading should be verified through appropriate experimental testing, which is not available to date. Therefore, it is hoped that the results of this initial assessment may provide inspiration for future testing but also provide some indication of the governing mechanism to be considered when assessing the cyclic three-dimensional behaviour of plate anchors.

CHAPTER 6. Application of the macro-element model to granular soils

Objectives

- To apply the macro-element modelling framework to plate anchors in sand subjected to different loading rates
- To provide a simplified approach which reduces the number of parameters and the computational time of simulation
- To analyse the effect of key parameters on anchor and soil response
- To provide guidance on parameter calibration
- To analyse chain effects on the prediction of anchor displacement
- To discuss the difficulties of the modelling approach

6.1. Introduction

The previous chapter showed the application of the macro-element model to cohesive soils and the effect of current strength variation on the capacity of plate anchors. This chapter aims to apply the same macro-element model to granular soils subjected to different loading rates.

The behaviour of anchors in sand is different to that in clays, as consolidation typically occurs within a very short time. While several studies on the behaviour of plate anchors have been carried out, as presented in Chapters 3 and 5, only limited work has been reported for the assessment of plate anchors in sand (O'Loughlin & Barron, 2012, Barron, 2014, Chow et al., 2018a, 2020). The behaviour of plate anchors (as well as other embedded structures) is usually assumed as drained. However, there is uncertainty around consolidation effects in sands, which adds further complexity to the problem (Chow et al., 2020). For instance, in a study by Heurlin et al. (2015), the capacity of plate anchors was underestimated by 40% in FE analyses that assumed fully-drained conditions, in comparison with field tests in drag anchors embedded in sand. The difference in results was attributed, among other aspects, to partly drained soil behaviour in the field tests. Furthermore, studies on other offshore structures that are somewhat similar to embedment anchors, have shown the effect of loading rates on the strength of sand-structure systems, e.g. Palmer (1999) and Lauder et al. (2012) for pipeline ploughs and Bransby & Ireland (2009) for pipeline upheaval, as previously explained in more detail in section 2.5.5.

Therefore, it appears relevant to study the influence of loading rates in sand, as different drainage regimes are induced.

This chapter consists of 6 sections. Section 6.1 simulates partial drainage through a decoupled approach, in which several episodes of load and consolidation are applied, inducing shear and consolidation in the representative soil element, respectively. Section 6.2 proposes a simplified approach in which the stress path in the specific volume υ – vertical effective stress σ_v' plane is approximated by a straight line. Section 6.3 validates the approach by comparison with centrifuge tests in sands subjected to different loading rates. Section 6.4 presents a further assessment without chain effects. Section 6.5 presents a discussion on the model's strong points, difficulties and a summary of procedures for the use of the model. Finally, section 6.6 presents the concluding remarks of the chapter.

6.2. General approach: Decoupled undrained load and consolidation analyses

In the previous chapters, the effect of consolidation during cyclic loading was assessed through the application of decoupled models for shearing and consolidation. It was assumed that consolidation occurred at the end of each half cycle. For the assessment of different loading rates, a similar approach may be employed for the macro-element analyses, i.e. a series of undrained loading phases followed by consolidation phases during which the load is kept constant (Flessati et al., 2020) can be applied.

As a modelling exercise, macro-element analyses are carried out in a generic anchor embedded in sand under four different loading rates. The anchor dimensions (width B = 4.64 m, length L = 7.92 m, parallel eccentricity e_p = 0.492 m and normal eccentricity e_n = 2.59 m) and the testing conditions (loading direction with the horizontal $\theta_0 = 40°$, initial embedment depth Y = 20.25 m) chosen for the modelling exercise is the same as the one used by Cassidy et al. (2012). This particular anchor and modelling set-up have been selected because the parameters associated with hardening and plastic potential parameters have been previously calibrated in Chapter 3. The soil selected for the macro-element simulations was Hostun RF sand, since it has been calibrated for a Severn-Trent model by Diambra (2010) and Diambra et al. (2013) and also by Corti et al. (2016), who used similar parameter values. The coefficient of consolidation c_v for Hostun RF sand is not known, therefore the value of c_v based on Equation (6.1) below was calculated based on an average value of permeability k = 1.7 x 10^{-4} m/s for fine marine sands (Terzaghi & Peck, 1967; Lambe & Whitman, 1969). It is worth noting that the actual permeability of Hostun RF sand can be significantly higher (e.g. Haigh et al., 2012), but in this hypothetical exercise a lower permeability was assumed such that partial drainage effects could be verified in the analyses.

$$c_v = \frac{k\, \upsilon\, \sigma_v'}{\lambda \gamma_w} \tag{6.1}$$

where k is the permeability, υ is the specific volume, σ_v' is the vertical effective stress, λ is the slope of the NCL and CSL and γ_w is the unit weight of the water, taken as 10 kN/m^3.

For the simulation of different loading rates, consolidation is assumed to take place after stages of a pre-defined displacement of the anchor. As mentioned previously in Chapter 3, stability and better performance of the model is achieved by imposing increments to the hardening term ρ_c. In order to relate the loading rate with a physically measurable quantity, such as the vertical displacement Δz, the rate of vertical displacement v_z is considered through the time allowed for consolidation after for each i steps of ρ_c:

$$t_c = \frac{(\Delta z)_i}{v_z} \tag{6.2}$$

where t_c is the time allowed for consolidation, $(\Delta z)_i$ is the vertical displacement after a stage of i incremental steps of ρ_c, and v_z is the loading rate (vertical displacement per unit of time). If, for instance, after a packet of $i = 30$ incremental steps of ρ_c the vertical displacement was 0.1 m and the target rate of vertical displacement is 0.02 m/s, then the time allowed for consolidation after $i = 30$ steps is $t_c = (0.1 \text{ m}) / (0.02 \text{ m/s}) = 5$ s.

A step size of $\delta\rho_c = 5 \times 10^{-6}$ is used, and for modelling purposes consolidation is assumed to occur after each loading packet of 30 steps of increment to ρ_c. Both the step size and the number of steps during a loading packet were selected after a sensitivity analysis, which is omitted here for the sake of brevity. It is assumed that anchor loading triggers shearing of the representative soil element, whereas during consolidation the shear stress τ on the element is constant, as explained in Chapter 4 and applied to clays in Chapter 5.

Figure 6.1 presents the results for the anchor and for the representative soil element under different loading rates in Hostun sand. The loading rates were selected to reproduce drained, undrained and partially drained response of the anchor (Figure 6.1), which can only be verified through analysis of the representative soil element (Figure 6.2). It can be seen that there is not a significant difference in the peak capacities of the anchor in Hostun sand. The drained peak capacity ($T_a = 3.82 \times 10^4$ kN) is only 21.3% higher than the undrained peak capacity ($T_a = 3.15 \times 10^4$ kN). This can be attributed to the values of the critical state parameters Γ and λ, which control the difference between drained and undrained shear strength of the soil element and, consequently, govern the anchor capacity. The vertical effective stress on the CSL for a nearly-drained vertical velocity $v = 0.1$ mm/s is about 118 kPa, whereas for a nearly-undrained velocity of $v = 30$ mm/s the vertical effective stress on the CSL is approximately 91 kPa. It is worth noting that, in Figure 6.2a, the stress-volumetric curve crosses the critical state line and then comes back towards it. This is more evident for partially-drained cases ($v_z = 0.1$ mm/s and $v_z = 1.0$ mm/s).

If slightly different values of Γ and λ are selected, both drained and undrained capacity are significantly affected, as shown in Table 6.1. If the parameter Γ is taken as 2.05 instead of 2.08, for example, the undrained capacity decreases by 61.9% (from $T_a = 3.15 \times 10^4$ kN to $T_a = 1.20 \times 10^4$ kN) and the drained capacity decreases by 48.2% (from $T_a = 3.82 \times 10^4$ kN to $T_a = 1.98 \times 10^4$ kN. In this case, the drained capacity is 65% higher than the undrained capacity. If the parameter λ increases from 0.031 to 0.036, the undrained capacity decreases by 46.7% (from $T_a = 3.15 \times 10^4$ kN to $T_a = 1.68 \times 10^4$ kN) whereas the drained capacity decreases by 38.0 %

(from $T_a = 3.82 \times 10^4$ kN to $T_a = 2.37 \times 10^4$ kN), and the drained capacity is then 41% higher than the undrained capacity.

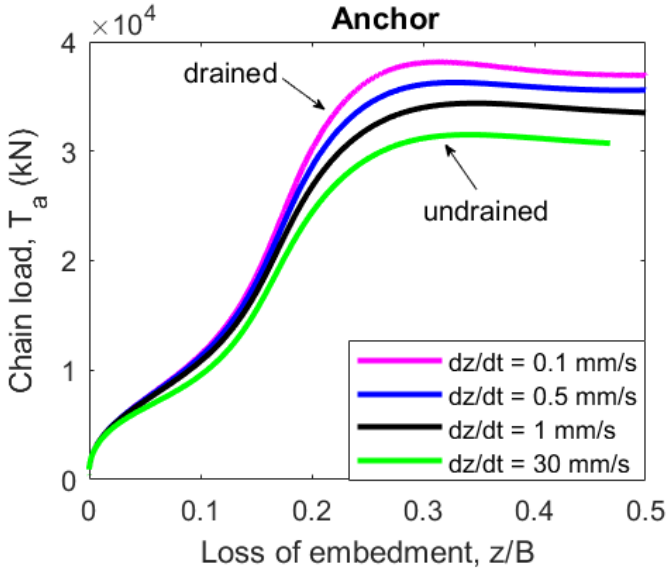

Figure 6.1 – Force-displacement curves for an anchor simulated with a decoupled model under different loading rates (Hostun sand, $\Gamma = 2.08$, $\lambda = 0.031$).

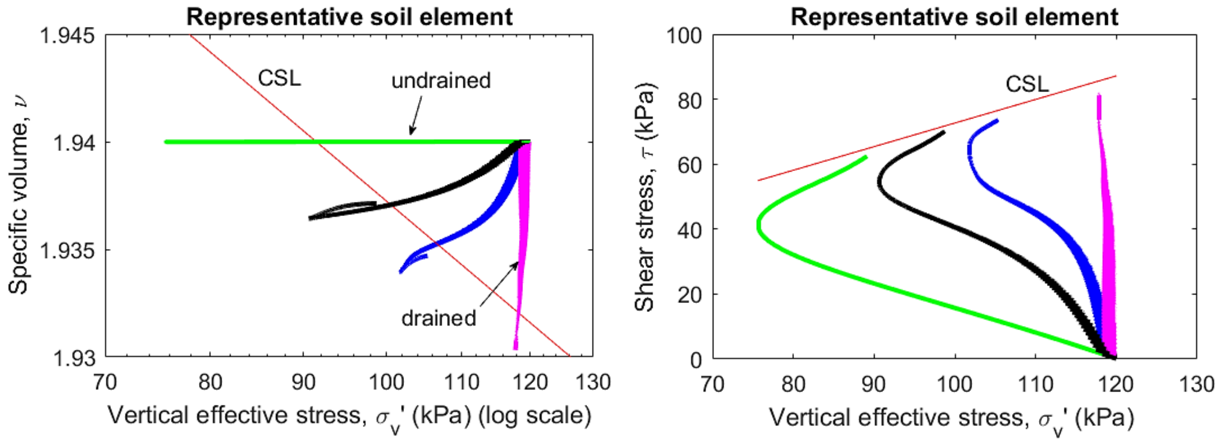

(a) (b)

Figure 6.2 – Stress paths of the representative soil element simulated with a decoupled model under different loading rates (Hostun sand, $\Gamma = 2.08$, $\lambda = 0.031$).

Table 6.1 – Sensitivity of drained and undrained capacities to parameters Γ and λ.

Γ	λ	Drained capacity (v=0.1 mm/s), $T_{a,dr}$ (kN)	Undrained capacity (v=30 mm/s), $T_{a,un}$	Ratio of drained to undrained capacity, $T_{a,dr}/T_{a,un}$
2.08	0.031	3.82×10^4	3.15×10^4	1.213
2.05	0.031	1.98×10^4	1.20×10^4	1.65
2.08	0.036	2.37×10^4	1.68×10^4	1.41

The results from the macro-element analyses for the anchor and for the representative soil element are presented in Figure 6.3 and Figure 6.4, respectively. Figure 6.3a shows the force-displacement behaviour of the anchor under undrained conditions (v = 30 mm/s). The peak capacity is significantly influenced by the selection of critical state parameters Γ and λ. The reason for such difference in anchor capacity can be attributed to the changes in soil strength (Figure 6.4), as the kinematics of the anchor (rotation and displacements) are just slightly affected by the rate of loading, as shown in Figure 6.3a and Figure 6.3b.

The strength of the soil, on the other hand, has a major influence on the capacity of the anchor. The critical state parameters Γ and λ affect the shear stress at critical state, which in turn controls the capacity of the anchor. As shown in Table 6.2, the ratio between the undrained capacity and the shear strength at CSL is approximately constant, since the influence of anchor kinematics is minimal.

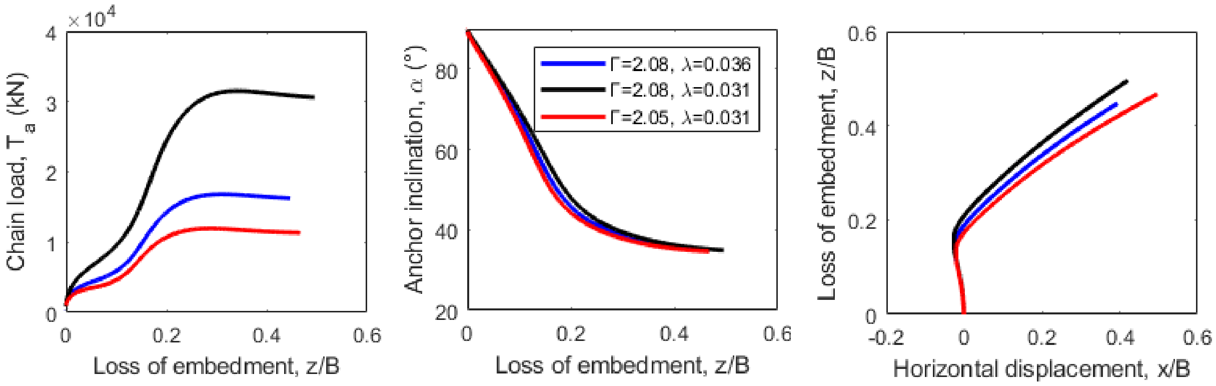

(a) (b) (c)

Figure 6.3 – Effect of critical state parameter on undrained anchor capacity.

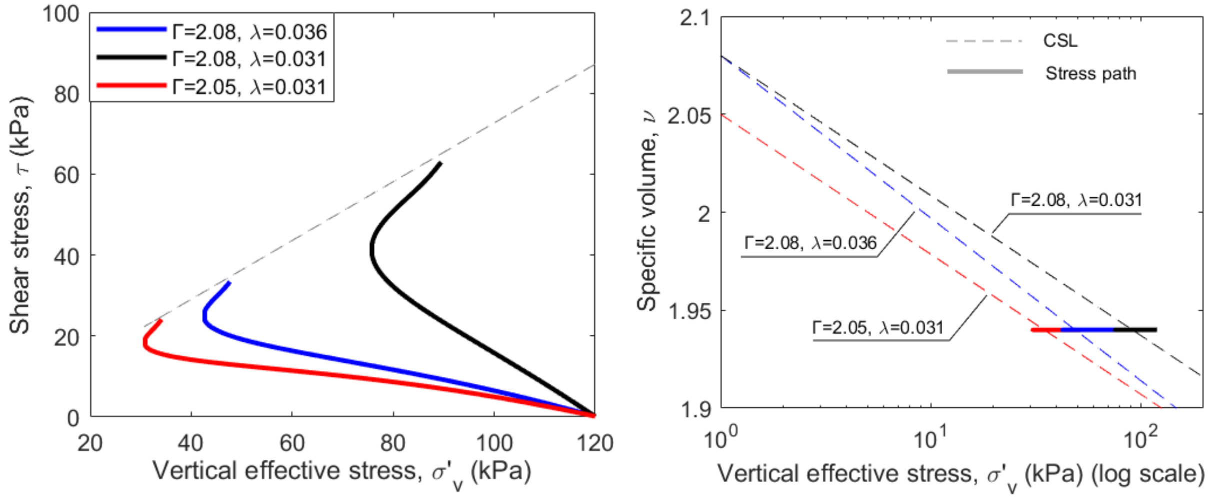

(a) (b)

Figure 6.4 – Effect of critical state parameter *Γ* and *λ* on stress paths the representative soil element for undrained conditions.

Table 6.2 – Sensitivity of drained and undrained capacities to parameters Γ and λ.

Γ	λ	Undrained capacity (v=30 mm/s), $T_{a,un}$	Shear strength at CSL, τ_{CSL} (kPa)	Ratio of undrained capacity to shear strength, $T_{a,un}/\tau_{CSL}$
2.08	0.031	3.15×10^4	66.3	4.75×10^2
2.05	0.031	1.20×10^4	25.3	4.74×10^2
2.08	0.036	1.68×10^4	35.3	4.76×10^2

Whereas for the parameters of Hostun sand the drained was only 21.3% higher than the undrained capacity, the difference can be much higher depending on the selected values of Γ and λ. As a modelling exercise, let us take a different generic sand with $\Gamma = 1.98$ and $\lambda = 0.01$, such that the difference between drained and undrained shear strength of the soil is higher.

It can be seen in Figure 6.5 that the difference in the peak capacities is much more pronounced than shown in Figure 6.1 when the Hostun sand critical state parameters are used. The nearly-drained capacity (v = 0.05 mm/s) is 3.91×10^4 kN, which is 103.6% higher than the nearly-undrained capacity (v = 20 mm/s) of 1.92×10^4 kN. From Figure 6.1 and Figure 6.5, it is clear that the anchor response to different loading rates is highly dependent on the critical state parameters Γ and λ, as these control the amount of pore pressure generated (and consequently the vertical effective stress variation) up to the critical state line. For the results in Figure 6.1, for example, the vertical effective stress at critical state for nearly-drained conditions (σ_v' = 118 kPa) is approximately 28.2% higher than the corresponding value for nearly-undrained conditions (σ_v' = 92 kPa). On the other hand, for different critical state parameters in Figure 6.5, the vertical effective stress for nearly-drained conditions is 103.4% higher than that for nearly-undrained conditions (σ_v' = 58 kPa).

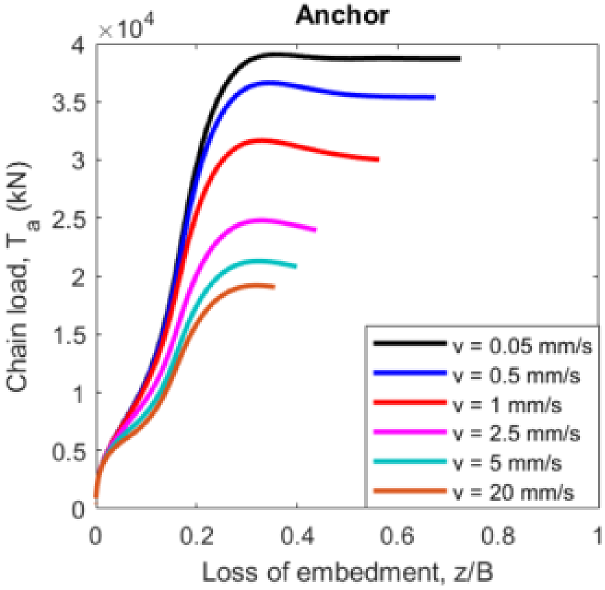

Figure 6.5 – Force-displacement curves for an anchor simulated with a decoupled model under different loading rates (generic sand, $\Gamma = 1.98$, $\lambda = 0.01$).

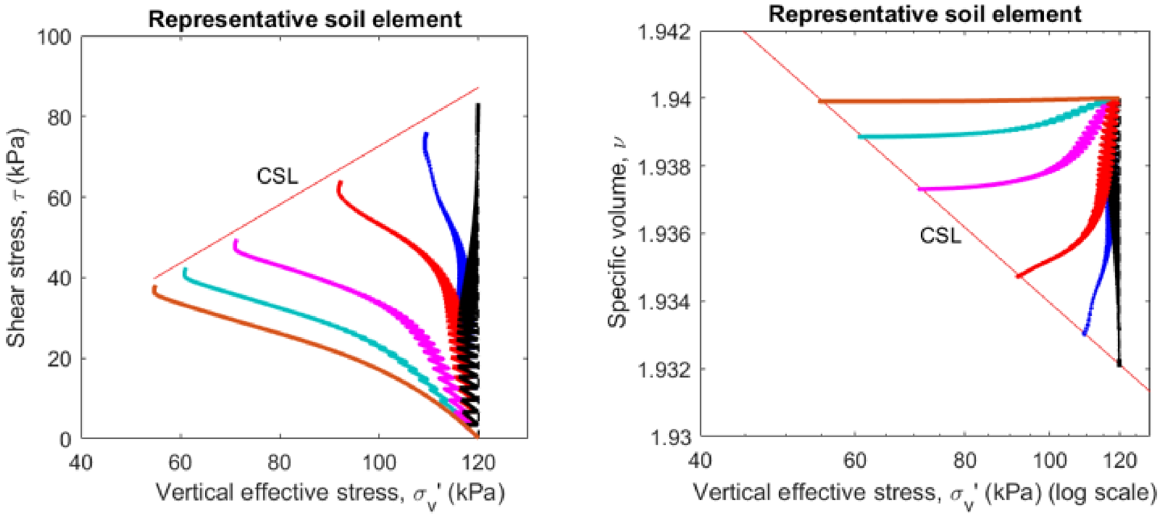

(a) (b)

Figure 6.6 – Stress paths of the representative soil element simulated with a decoupled model under different loading rates (generic sand, $\Gamma = 1.98$, $\lambda = 0.01$).

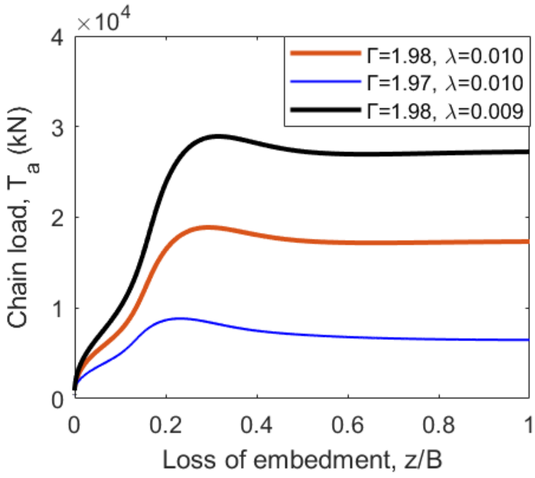

Figure 6.7 – Effect of critical state parameters *Γ* and *λ* on undrained anchor capacity.

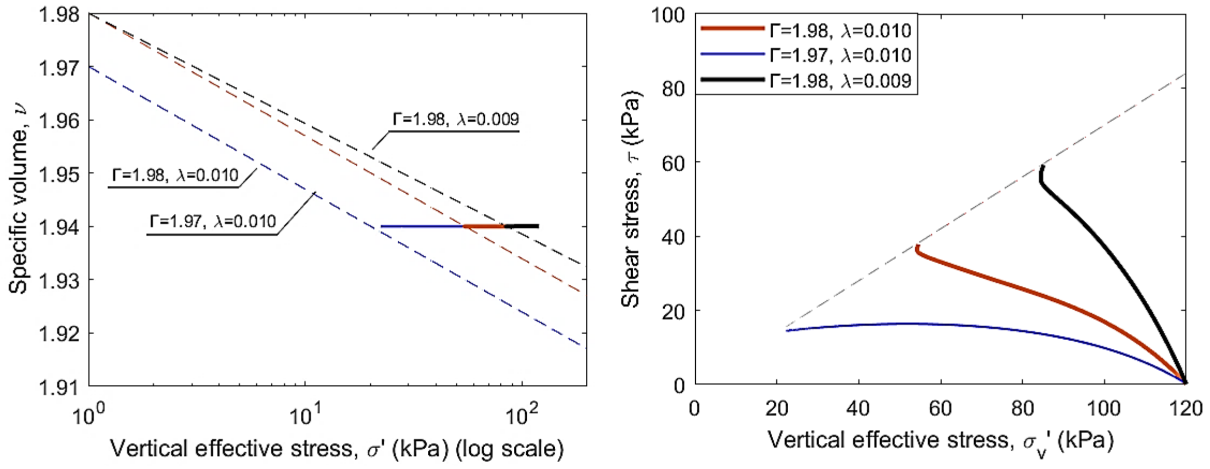

(a) (b)

Figure 6.8 – Effect of critical state parameters *Γ* and *λ* on anchor capacity.

Anchor capacity results are, also in this case, very sensitive to the values of critical state parameters *Γ* and *λ*, as shown in Figure 6.7 for undrained conditions. Such differences are attributed to the effect of the critical state parameters on the stress path of the soil element, as shown in Figure 6.8.

The fact that the model is highly sensitive to the values of these parameters raises questions about whether the values obtained from element testing are appropriate. Furthermore, critical state is difficult to reach in laboratory testing (e.g. Santamarina & Cho, 2001), and even when it is reached, high scatter can be observed in the critical state parameters (as per Chow et al., 2019, in which it is shown that the parameters *Γ* and *λ* for UWA silica sand are highly variable depending on equipment and testing procedure). It is also unknown whether the critical state of the soil-anchor system is reached when a specific soil element near the anchor reaches the critical state. Furthermore, not all elements around the anchor reach critical state conditions at the same time, as the phenomenon is highly non-linear. It is therefore introduced herein the concept of operational critical state line. The operational critical state is defined as the state at which soil element representative of the behaviour of soil around the anchor no longer experiences changes in volume and (shear and vertical effective) stresses. When the critical state is reached by the representative soil element, the anchor exhibits indefinite displacement with no changes in chain load. It is assumed that the operational critical state line has the same slope λ as the soil critical state line obtained from element tests, but they have different values of intercept Γ with $\sigma_v' = 1$ kPa.

In the next sections, it will be shown that using the critical state parameters of a soil element to demonstrate anchor behaviour does not produce reasonable results. A procedure for the calibration of the operational critical state line parameters Γ is then proposed and verified with a set of centrifuge test data.

6.3. Simplified approach: control of consolidation through element stress path

6.3.1. Comparison between approaches

An alternative approach for accounting for rate effects in anchor capacity is presented in this section. The approach consists of simplifying the shape of the stress path by assuming that it follows a straight line towards the CSL in the v-ln(σ_v') plane, i.e. the variation of specific volume ($\dot{v}$) with the excess pore pressure (and consequently the effective stress) follows a constant ratio K. If the vertical effective stress is assumed to change solely due to variations of the excess pore pressure, i.e. if the total vertical stress on the representative soil element is assumed to remain constant, Equation (6.3) also implies that $\dot{\sigma}_v' = K\,\dot{v}$.

$$\dot{u}_w = -K\,\dot{v} \tag{6.3}$$

The stress path in the υ-ln(σ') plane depicted in Figure 6.1 and Figure 6.5 shows that the stress path does not follow a straight line. Hence, in order to relate the slope of the straight line K in the υ-ln(σ_v') plane with the loading rate, an assessment of the effect of imposing the ratio presented in Equation (6.3) is carried out. For each loading rate in Figure 6.5, the values of the parameter K are selected such that the straight line in the υ-ln(σ_v') plane connects the initial stress-volumetric state with the point where the CSL is intercepted by the stress path, as illustrated in Figure 6.9.

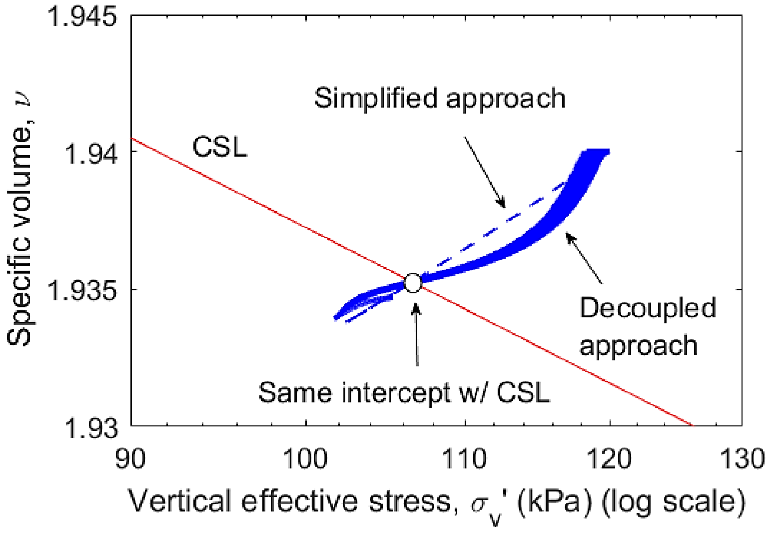

Figure 6.9 – Illustration of simplified approach connecting initial and final points of the stress path.

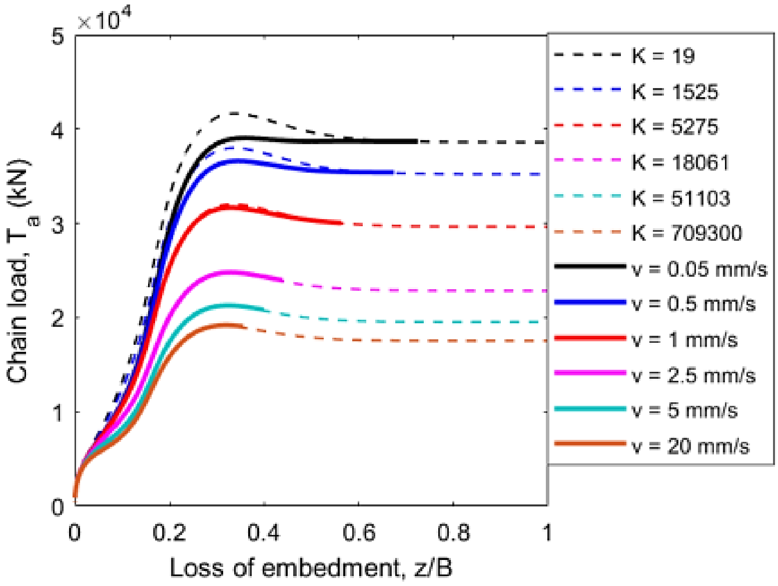

Figure 6.10 – Force-displacement of the anchor: comparison between K-model and decoupled model (generic sand, Γ =1.98, λ=0.01).

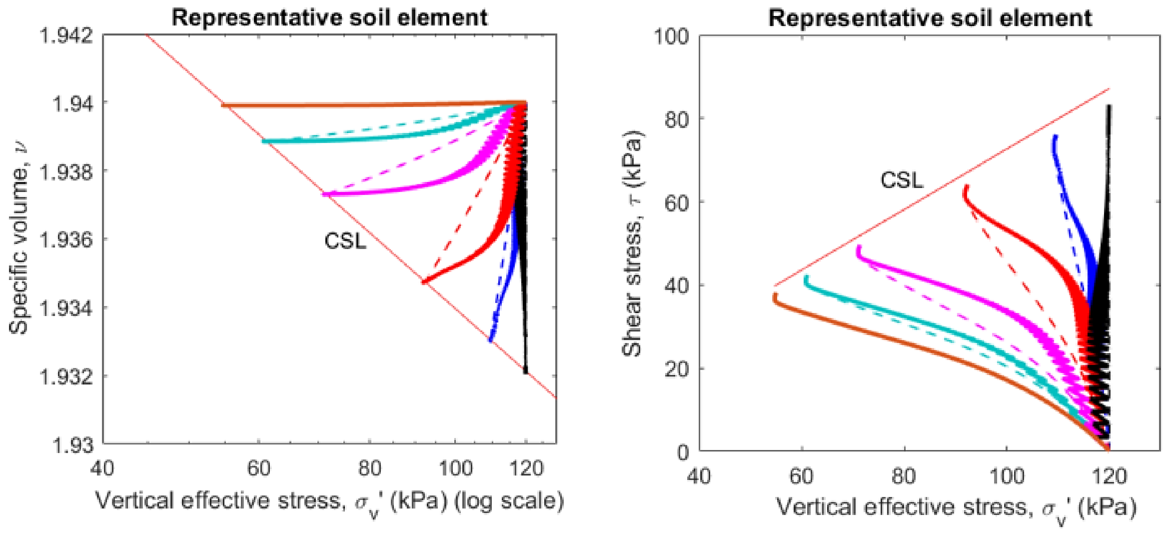

(a) (b)

Figure 6.11 – Stress paths of the representative soil element: comparison between *K*-model and decoupled model (generic sand, Γ =1.98, λ=0.01).

Figure 6.11 compares the results obtained from *K*-model approach with the decoupled model. The slopes *K* were calibrated such that the intercept of the stress paths with the CSL was coincident for both approaches. The force-displacement curves seem to match quite well, but the peak capacity is overestimated by 6.6% by the *K*-model approach (T_a = 41640 kN) in comparison with the decoupled model (T_a = 39060 kN) for the drained case (v = 0.05 mm/s and K = 19). Although the peak capacities for nearly-drained conditions are slightly overestimated by the *K*-model approach in comparison with the decoupled model, the former is much simpler and time-efficient than the latter which involves successive stages of shearing and consolidation. While each simulation of the decoupled model takes approximately 30 minutes to complete, for the *K*-model completion can be reached in less than 20 seconds, i.e. less than 1% of the time required for the decoupled model. The significant gain in computational time for the *K*-model approach occurs because the 1D consolidation model for the representative soil element is no longer necessary. Another advantage is that, since the 1D consolidation model is not used, three parameters associated with the consolidation stages and that previously required calibration are eliminated: a, T_{50} and I_σ.

6.3.2. Interpretation framework

The interpretation of the loading rate effect can be presented within the backbone curve framework (see Chapter 2). In this framework, the anchor capacities are presented as a function of the non-dimensional velocity, $V^* = vd/c_v$, where v is the loading rate, d is the nominal dimension of the anchor and c_v is the coefficient of consolidation (e.g. Finnie & Randolph, 1994; Bransby & Ireland, 2009; Suzuki & Lehane, 2014; Chow et al., 2018b). For a rectangular geometry, the representative dimension d is often taken (e.g. Chung et al., 2006; Colreavy et al., 2016) as the diameter of a circle with the same area (Chow et al., 2019). A curve fitting function can be employed for the relationship between the ratio $T_{a,p}/T_{a,p,max}$ and the normalised velocity, similarly to the expression used by Richardson et al. (2009) and Blake et al. (2011).

$$\frac{T_p}{T_{p,max}} = \frac{A_1 - A_2}{1 + \left(\frac{V^*}{V_{50}}\right)^p} + A_2 \tag{6.4}$$

where A_1 is the initial value of the normalised capacity (i.e. the highest value of $T_p/T_{p,max}$ in the case of contractive soils), A_2 is the final value of the normalised capacity (i.e. the lowest value of $T_p/T_{p,max}$ in the case of contractive soils), V_{50} is the value of the non-dimensional velocity V^* at the mid-point between A_1 and A_2 and p is a fitting parameter governing the slope of the curve.

Figure 6.12 presents the normalised peak capacities $T_p/T_{p,max}$ within the backbone curve framework and its respective fitting curve, with $A_1 = 2.05$, $A_2 = 1.0$, $V_{50} = 0.025$ and $p = 1.7$. The velocities were normalised with $c_v = 0.389$ m²/s, calculated from Equation (6.1). The normalised velocities that mark the transition from partially drained to drained (V_{dr}) and undrained (V_{un}) are $V_{dr} = 0.004$ and $V_{un} = 0.2$, respectively, while the mean velocity is $V_{50} = 0.025$.

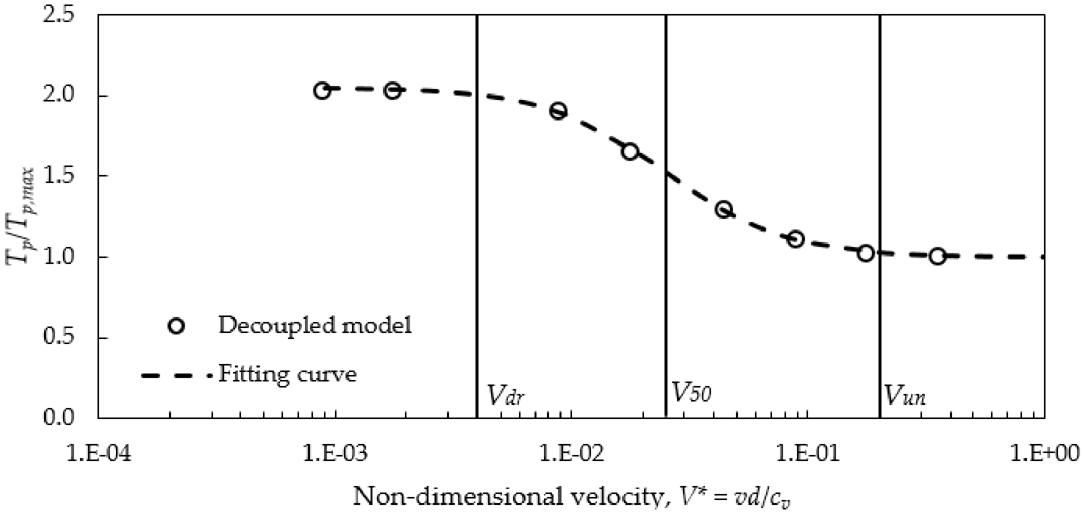

Figure 6.12 – Back-bone and fitting curves: normalised capacities as a function of non-dimensional velocity (V^*).

The normalised peak capacities $T_p/T_{p,max}$ may also be related to K within the backbone curve framework, and a fitting curve can be obtained by replacing the ratio V^*/V_{50} by K/K_{50} in Equation (6.4). The relationship with K is presented in Equation (6.5).

$$\frac{T_p}{T_{p,max}} = \frac{A_1 - A_2}{1 + \left(\frac{K}{K_{50}}\right)^p} + A_2 \tag{6.5}$$

By using the same values of A_1, A_2 and p, and $K_{50} = 8 \times 10^3$ at the mid-point between A_1 and A_2, good agreement is observed between the fitting curve and the K model results, with a maximum difference of 6% for the point on the far left of the graph, as shown in Figure 6.13.

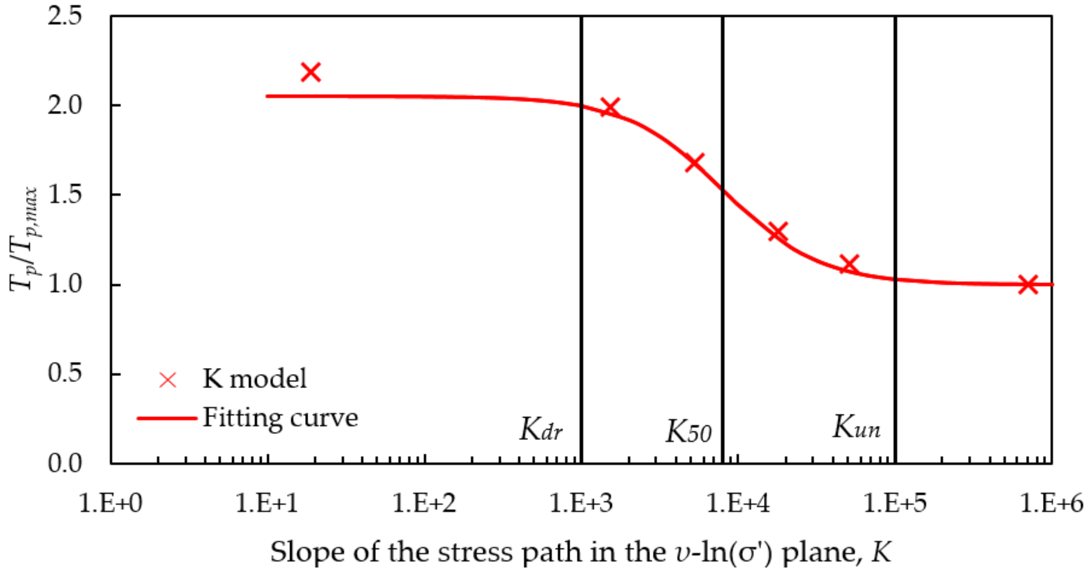

Figure 6.13 – Back-bone and fitting curves: normalised capacities as a function of K.

Based on the observation of the fitting curves in Figure 6.12 and Figure 6.13 and the fact that the same values for the parameters A_1, A_2 and p can be used, there seems to be a direct relationship between K_{50} and V_{50}.

The ratio K_{50}/V_{50}, in this particular case, is equal to 3×10^5. If all values of K are divided by 3×10^5, the results from the K model and the respective fitting curve are nearly coincident with those obtained from the decoupled model, as shown in Figure 6.14. The ratio can K_{50}/V_{50}, therefore, be treated as a conversion factor Ω from K to V.

$$\Omega = K_{50}/V_{50} \tag{6.6}$$

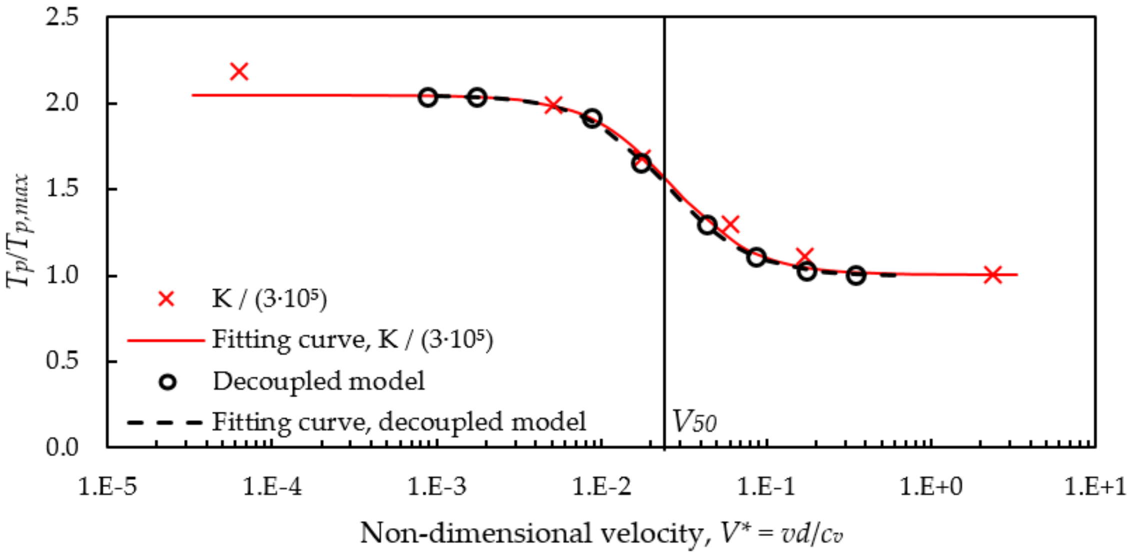

Figure 6.14 – Superimposed back-bone and fitting curves for vertical velocity: *K* and non-dimensional velocity *V*.

It is worth noting that a slightly higher value of A_1 ($A_1 = 2.2$) would provide an even better fit with the simulation points in Figure 6.13, but by using the same parameters A_1, A_2 and p, for both cases, the relationship between K and V^* can easily be drawn.

Another important remark is that the normalised velocity V^* depends on the non-normalised velocity v that was considered in the calculation. The results shown so far in this chapter used a constant vertical velocity of the anchor ($\Delta z/\Delta t$). If a different velocity is considered, that affects the normalised velocities of the back-bone curve. For instance, if the velocity of the anchor padeye relative to the actuator (d) (which is similar to the velocity of the actuator that pulls the mooring line) is used instead of the vertical velocity, the velocity v is then given by ($\Delta d/\Delta t$). A different backbone curve is then generated, as shown in Figure 6.15. For the set of data obtained from simulations with constant rate of d_a, the value of the mean velocity is $V_{50} = 9 \times 10^{-3}$, which is lower than $V_{50} = 2.5 \times 10^{-2}$ for the case of constant rate of Δz (i.e. constant vertical velocity). Therefore, for a constant velocity given by the rate of d_a, the conversion factor from K to V^* is also different and is given by $\Omega = K_{50}/V_{50} = 8 \times 10^3 / 9 \times 10^{-3} = 8.9 \times 10^5$. The results in Figure 6.15 also show the results of constant vertical velocity for comparison.

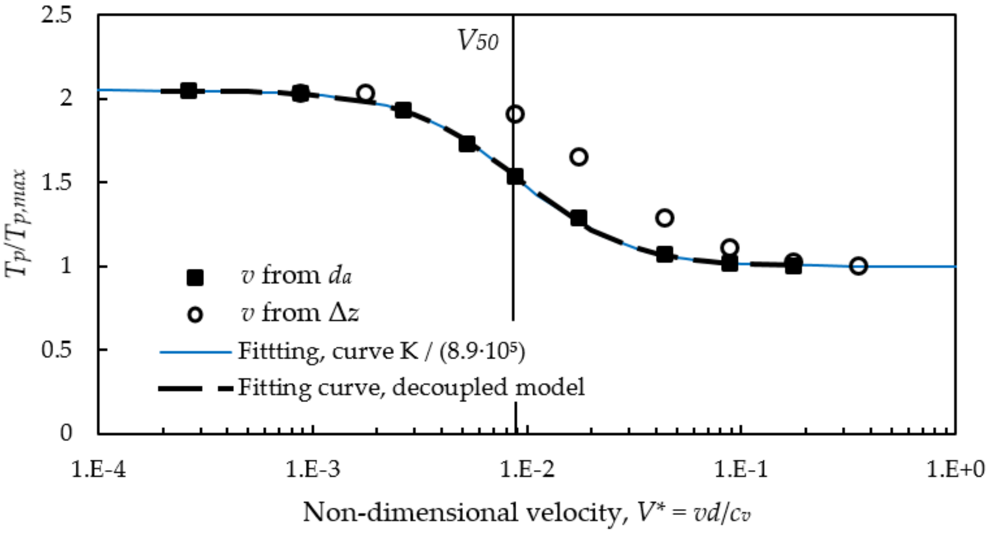

Figure 6.15 – Back-bone curves for velocity given by displacement of the anchor padeye.

It is shown through these results that the results *K*-model can be converted to results from different testing configurations, as long as an appropriate conversion is carried out. For the conversion to two different sets of analyses (with constant variation of d and with constant variation of Δz, for example), the same set of results from the *K*-model was used, only with a different conversion factor Ω. In the next section, the relationship between K and the normalised velocity V^* will be verified with results from centrifuge tests carried out with different loading rates in dense sand by Chow et al. (2020).

6.4. Validation of macro-element model for granular soils under different anchor pull-out rates

In this section, the proposed framework is validated by assessing the macro-element model in comparison with the experimental results from a set of centrifuge tests conducted by Chow et al. (2020). This set of centrifuge tests has been chosen because it is one of the few studies on the effect of loading rate in plate anchors – the only one in sand that involves anchor rotation. Furthermore, the set of experiments covered a wide range of velocities of pull for drained, partially drained and undrained conditions.

A calibration procedure is presented for the operational critical state parameters and the main parameters affecting the response of the model are discussed. Following an initial assessment using parameters reported in the literature for Hostun sand, which are used as a starting point, the effect of the parameters of the Severn-Trent model is analysed. The effect of the parameter R_0 in the relationship between anchor and representative soil element is also discussed. Some modelling considerations and how they affect the results are also presented and discussed.

6.4.1. Experimental programme

As previously presented in the literature review (Chapter 2), several centrifuge tests with different loading rates were carried out by Chow et al. (2020) with vertically installed plate anchors embedded in UWA (University of Western Australia) superfine silica sand, which had been previously characterised by Chow et al. (2019) as show in Table 6.3. The centrifuge tests were conducted in a 3.6 m dia. beam centrifuge at UWA. The tests were conducted at 50g acceleration with a rectangular anchor of breadth B = 20 mm, length L = 40 mm and thickness t_a = 4.35 mm, which gives B = 1 m, L = 2 m and t_a = 0.2175 m in prototype scale, as detailed in Table 6.4.

The anchor was initially installed vertically at depth 5 times the anchor breadth and then subjected to horizontal load inclination at the mudline. The set-up of the experiments is presented in Figure 6.16.

Table 6.3 – Experimental conditions – properties of UWA silica sand as characterised by Chow et al. (2019).

Symbol	Parameter	Value
	SOIL PROPERTIES	
γ'	Effective unit weight (kN/m^3)	10.23-10.53 kN/m^3
ρ_{min}	Minimum dry density	1497 kg/m^3
ρ_{max}	Maximum dry density	1774 kg/m^3
v	Initial specific volume	1.555
G_s	Specific gravity	2.67
λ	Slope of NCL and CSL	0.009
κ	Slope of the swelling line	0.036
φ_{cs}	Critical state friction angle (°)	31.9
Γ_{CSL}	Specific volume at σ_v' = 1 kPa on the CSL	3.8
c_v	Coefficient of consolidation (m^2/year)	0.00065 ln(σ_v') – 0.0015(m^2/s)

Table 6.4 – Experimental conditions – anchor dimensions in prototype scale (Chow et al., 2020).

	ANCHOR DIMENSIONS	
B	Anchor breadth (m) in prototype scale	2.0
L	Anchor length (m) in prototype scale	1.0
e_n	Padeye eccentricity (m) in prototype scale	1.0
e_p	Padeye offset (m) in prototype scale	0
t_a	Anchor thickness (m) in prototype scale	0.2175

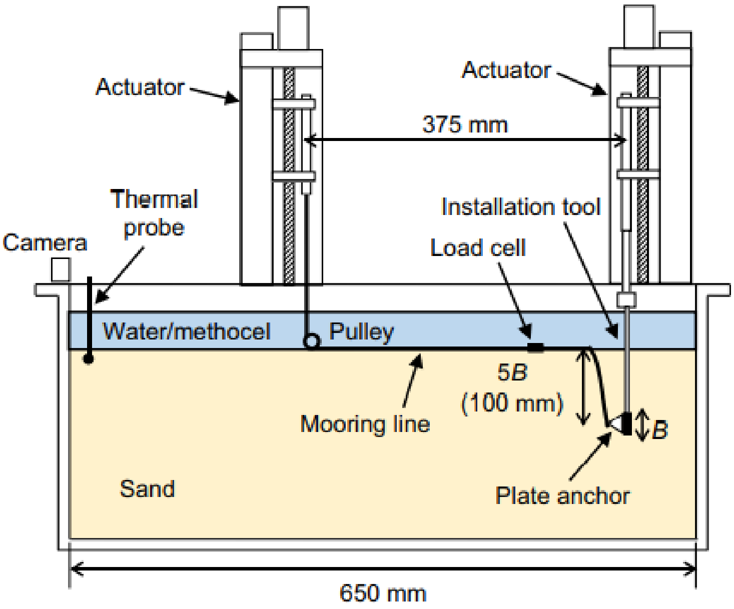

Figure 6.16 – Experimental set-up for the centrifuge tests (Chow et al., 2020).

The selected centrifuge tests were covered a range of loading rates (measured from the chain displacement on the actuator) from 0.3 to 30 mm/s. The soil was saturated with methocel instead of water, such that undrained conditions can be achieved at lower velocities than necessary for water as the pore fluid. The experimental programme is summarised in Table 6.5.

Table 6.5 – Experimental programme and results of centrifuge tests (Chow et al., 2020).

Test name	v **[mm/s]**	**Non-dimensional velocity,** V	q_u **[kPa] (**T_a **in prototype scale [kN])**
M0·3M	0.3	16	687.1 (1374.2)
M1M	1	55	802.9 (1605.8)
M3M	3	158	1067.0 (2134.0)
M10M(1)	10	533	1552.7 (3105.4)
M10M(2)	10	540	1522.8 (3045.6)
M30M	30	1595	1497.6 (2995.2)

6.4.2. Interpretation framework

In light of the backbone curve framework, the non-dimensional velocities which mark the drained and undrained boundaries (V_{dr} and V_{un}, respectively) can be defined, as previously shown in Figure 6.12. In the study carried out by Chow et al. (2020), these velocities were defined as $V_{dr} = 16$ and $V_{un} = 540$. The experimental data are fitted with an expression similar to Equation (6.4), which is much simpler than the expression used by Chow et al. (2020) as it does not account for viscosity effects caused by the use of methocel instead of water. The effect of viscosity does not have a significant influence on the results (Chow et al., 2020). The use of a simpler equation is advantageous to relate the normalised velocity V^* to the parameter K, as shown in the previous section.

$$\frac{T_p}{T_{p(dr)}} = \frac{A_1 - A_2}{1 + \left(\frac{V^*}{V_{50}}\right)^p} + A_2 \tag{6.7}$$

where A_1 is the lower value of the normalised capacity (i.e. $T_a/T_{a(dr)}$ for dilative soils), A_2 is the higher value of the normalised capacity (i.e. $T_{a(un)}/T_{a(dr)}$ for dilative soils), V_{50} is the value of the non-dimensional velocity V^* at the mid-point between A_1 and A_2 and p is a fitting parameter governing the slope of the curve. Figure 6.17 shows the fitting curve from Equation (6.7), with $A_1 = 1.0$, $A_2 = 2.5$, $V_{50} = 180$ and $p = 1.15$ as well as the fitting curve from Chow et al. (2020), in which a different formulation was used. The curves are nearly coincident, apart from the nearly undrained domain, for which the fitting curve used by Chow et al. (2020) continues to increase due to viscous effects, whereas the fitting curve from Equation (6.7) reaches a plateau.

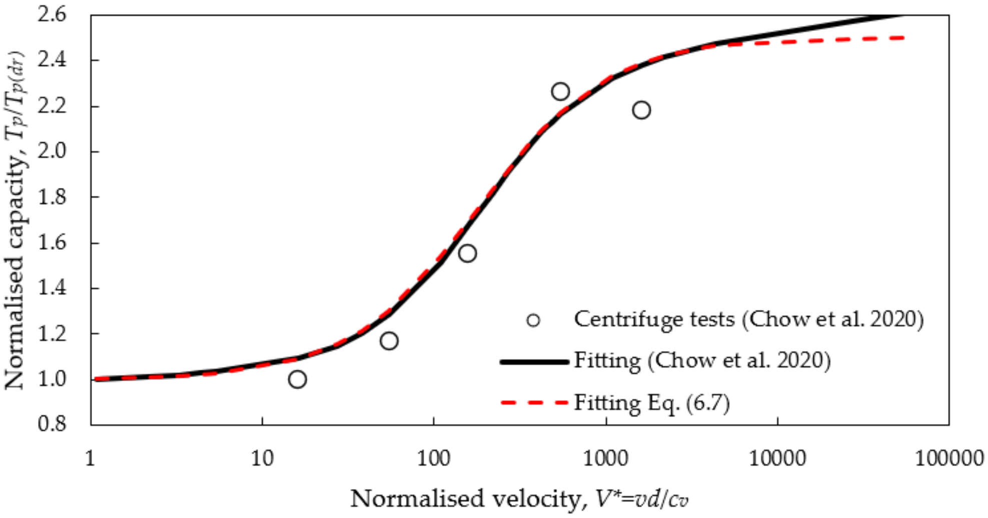

Figure 6.17 – Fitting curves for centrifuge data from Chow et al. (2020).

6.4.3. Macro-element analyses

This section presents the macro-element analyses carried out to reproduce the behaviour demonstrated in the centrifuge tests. The effect of certain parameters is analysed and discussed, as well as the limitations of the model.

The values of the parameters selected for the macro-element analyses are presented in Table 6.6. The calibration procedure and rationale that led to these values is explained throughout the chapter.

Table 6.6 – Model parameters and selected values for the analysis of different loading rates.

Symbol	Parameter	Value	Remarks
	SOIL PARAMETERS		
Γ	Specific volume at $\sigma_v' = 1$ kPa on the operative CSL	1.601	Calibrated
A	Flow rule multiplier	0.75	Calibrated
k_d	State parameter multiplier in flow rule	1.5	Diambra et al. (2013)
k_r	Link between state parameter and strength	-0.5	Diambra et al. (2013)
C	Hyperbolic relationship parameter	0.0002	Calibrated
	ANCHOR PARAMETERS		
m	Shape of loading surface (moment)	2	Chapter 3
n	Shape of loading surface (horizontal)	4	Chapter 3
q	Shape of loading surface (vertical)	4	Chapter 3
N_v	Normalised normal capacity factor	14	Chapter 3
N_h	Normalised sliding capacity factor	3	Chapter 3
N_m	Normalised rotational capacity factor	2	Chapter 3
ξ	Plastic potential parameter (vertical)	1.6	Chapter 3
χ	Plastic potential parameter (horizontal)	1.1	Chapter 3
ω	Plastic potential parameter (moment)	1.5	Chapter 3
R_0	Hardening parameter of the anchor	5.0	Calibrated

6.4.3.1. *Calibration of the critical state parameter*

As mentioned previously in section 6.2, calibration of the operational critical state parameters Γ and λ can be rather challenging, especially because the operational parameters can differ significantly from the actual critical state parameters of the soil. For Chow et al. (2019), for example, the CSL parameters for the UWA silica sand obtained from element testing (direct simple shear and both drained and undrained triaxial tests) were $\Gamma_{CSL} = 1.764$ and $\lambda = 0.009$. By using these parameters for the analysis of the macro-element model under undrained conditions (with $K = 5 \times 10^6$), the anchor capacity increases indefinitely at large displacements, as shown in Figure 6.18. This can be explained by the response of the representative soil element, whose initial state is very distant from the CSL of the soil (Figure 6.19b). The stress path followed by the representative soil element would only reach the CSL at extremely high stress levels ($\sigma_v' > 10^{10}$ kPa). This observation reinforces the need to select appropriate parameters for the operative critical state line that represents the behaviour of the whole soil mass around the anchor, rather than have the response of the soil bulk represented by parameters that were obtained by a specific loading condition (e.g. triaxial, ring shear) in element testing.

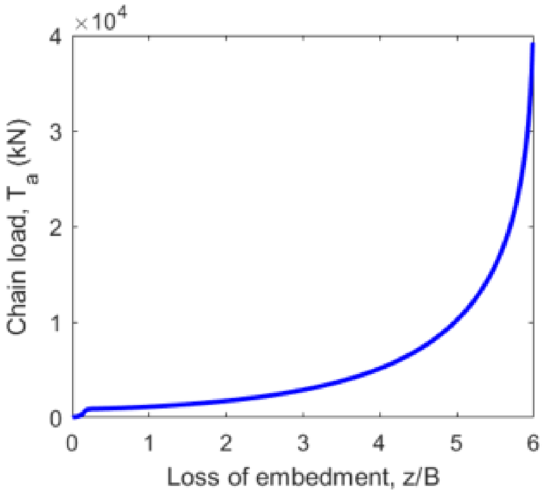

Figure 6.18 – Macro-element analysis with Γ_{CSL} = 1.764 and λ = 0.009 under undrained conditions: force-displacement behaviour of the anchor.

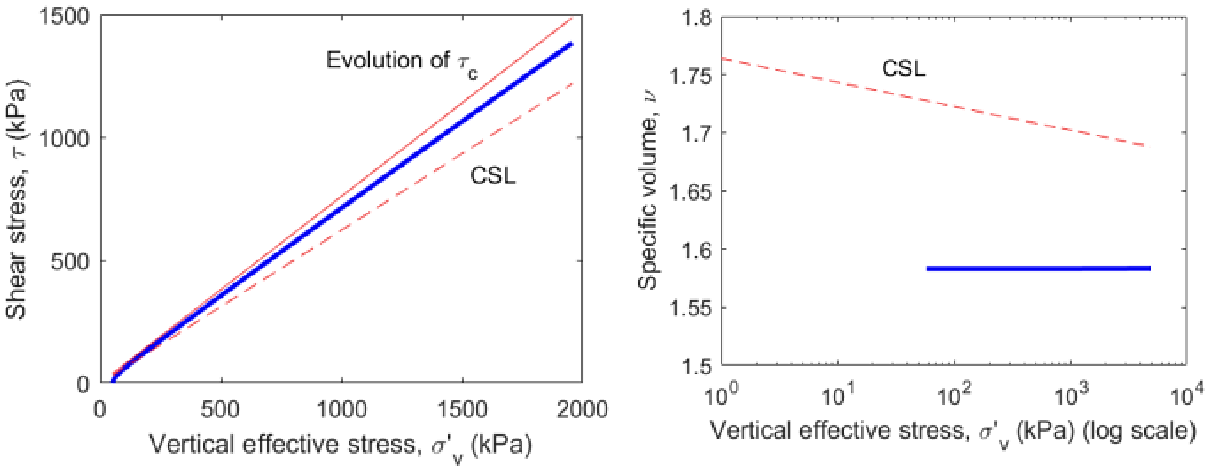

(a) (b)

Figure 6.19 – Macro-element analysis with Γ_{CSL} = 1.764 and λ = 0.009 under undrained conditions: force-displacement behaviour of the anchor.

In that sense, the operational critical state line ensures that the critical state is reached at reasonable stress levels, which in turn results in a reasonable force-displacement response of the anchor. A calibration procedure for the operational critical state line is proposed herein. Some assumptions have to be made for the sake of simplicity of the calibration procedure:

1) The slope of the operational critical state line is given by λ and is the same as that of the critical state line of the soil;
2) At peak load, the orientation of the anchor is perpendicular to the direction of the load at the padeye (θ_a), which implies that the rotation experienced by the anchor (β) is equal

to the orientation of the chain load with the horizontal (θ_a). It has been shown by several studies (e.g. Dove et al., 1998; Cassidy et al., 2012; Gaudin et al., 2014) and confirmed by the macro-element model (see Chapter 3) that at peak load the anchor orientation is nearly perpendicular to the direction of loading;

3) Since at peak conditions the anchor is being pulled at an angle nearly perpendicular to the anchor orientation, it is reasonable to assume that moment and horizontal loads are null ($M \approx 0$ and $H \approx 0$). In that way, the chain load T_a has no components M and H, therefore $V = T_a - W' \sin(\beta)$. At peak conditions, $T_a \gg W'$, hence $V \approx T_a$;
4) The hardening term ρ_c is approximately 1 when the peak load is reached.

For the calibration of the operational critical state parameter Γ, only the anchor capacity for undrained conditions ($T_{a(un)}$) is necessary. The initial specific volume (v) as well as the friction angle (φ_{cs}) and the slope of the critical state line (λ) of the representative soil element are also necessary, but these are experimental conditions and determined previously through element testing. The initial specific volume can be calculated from the specific volume of the soil, whereas the friction angle (φ_{cs}) and the slope of the critical state line (λ) can be obtained from element tests in the soil used in the experiments.

If the peak load T_a is known, from the force-equilibrium equations (Equation 3.1, 3.2 and 3.3) in combination with assumption 3 ($V \approx T_a$, $H \approx 0$ and $M \approx 0$), then from the loading surface equation (Equation 3.9) combined with assumption 4, $(V/V_M)^q = \rho_c \approx 1$. If both sides are taken to the power of $1/q$, the expression in Equation (6.8) is derived:

$$\frac{V}{V_M} = 1 \tag{6.8}$$

By substituting Equation (3.6) into Equation (6.8), the current strength of the soil (τ_c) at peak load can be obtained:

$$\tau_c = \frac{V}{N_v L B} \tag{6.9}$$

The vertical effective stress at the operational critical state line can then be obtained through Equation (4.11) ($\sigma'_{v,CSL} = \tau_c/\tan \varphi_{cs}$). Once the vertical effective stress on the critical state line is known, the intercept of the CSL on the υ axis for $\sigma' = 1$ kPa (parameter Γ) can be obtained through Equation (4.10) ($\upsilon = \Gamma - \lambda \ln \sigma_v'$), as illustrated in Figure 6.20.

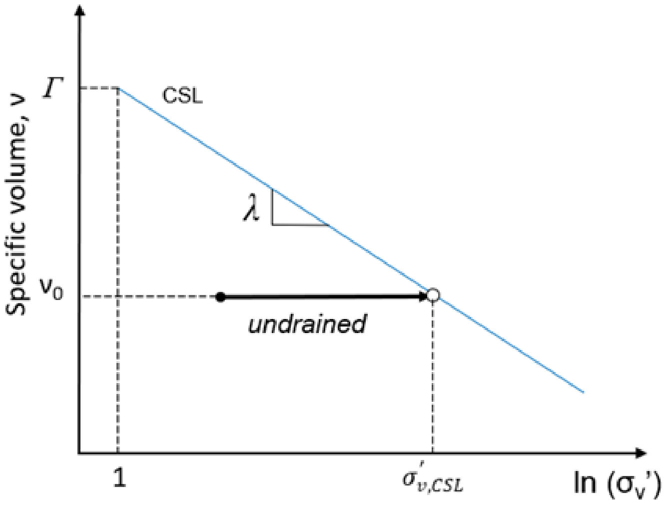

Figure 6.20 – Determination of operational critical state parameter Γ.

From the centrifuge tests carried out by Chow et al. (2020), the non-dimensional velocity that marks the transition from partially drained to undrained behaviour is $V_{un} = 540$, and the peak capacity for this velocity is $T_{a(un)} = 3045.6$ kN ($q_{u(un)} = 1522.8$ kPa and plate area at prototype scale $A_p = 2$ m^2). Following the procedure described above, the perpendicular component of the chain load (V) is equal to the chain load at peak conditions, hence $V = T_{a(un)} = 3045.6$ kN. The current strength of the soil τ_c can be calculated through Equation (6.9):

$$\tau_c = \frac{V}{N_v L B} = \frac{3045.6}{14 \times 2 \times 1} = 108.77\ kPa \tag{6.10}$$

From Equation (4.11), the vertical effective stress at which the critical state is reached can be calculated:

$$\sigma'_{v,CSL} = \frac{\tau_c}{\tan(\varphi)} = \frac{108.77}{\tan(31.9°)} = 174.75\ kPa \tag{6.11}$$

The intercept of the operational critical state can then be obtained:

$$\Gamma = \upsilon + \lambda \ln\left(\sigma'_{v,CSL}\right) = 1.555 + 0.009 \ln(164.75) = 1.601 \tag{6.12}$$

The operational critical state line can then be defined with Γ = 1.601 and λ = 0.009. The other parameters used in the analyses are presented in Table 6.6 and will be described in the following sections. The load orientation at the padeye θ_a was assumed as constant, hence no chain solution was used. The effect of load orientation on the results will be addressed later in this chapter.

6.4.3.2. Initial assessment

In the previous chapter, it was shown that, when using the same values for the soil parameters as in Diambra et al. (2013) as a starting point, only the parameters A and C had to be modified in order to provide good agreement with the experimental results. In this section, the parameters used by Diambra et al. (2013) are also used as a starting point: A = 0.75, C = 0.0025, k_d = 1.5 and k_r = - 0.5. The values selected for the other parameters are presented in Table 6.6 and will be further analysed in the next sections. Initially, the load direction at the padeye was taken as θ_a = 30°, which is approximately perpendicular to the final orientation of the anchor observed in the centrifuge tests. The effect of the loading direction will be analysed later in this chapter.

Macro-element analyses covering the whole drainage domain (drained, partially drained, and undrained) is carried out by varying the parameter K, which can be related to loading rates, as shown previously in section 6.3. The smaller the value of K the closer the response is to drained conditions. On the other hand, the higher the value of K the closer the response is to undrained conditions.

Figure 6.21 shows the force-displacement curves for all drainage regimes, while Figure 6.22 shows the stress paths of the representative soil element. The force-displacement curves show that, for nearly-drained conditions, the anchor capacity is approximately 1150 kN, whereas for nearly-undrained conditions the capacity is approximately 3000 kN.

The peak capacities are presented in a backbone curve in Figure 6.23 and detailed in Table 6.7. As expected for dilative soils, the nearly-undrained capacities for higher values of K are higher than the nearly-drained capacities for lower values of K. The ratio between undrained and drained capacity, $T_{p(un)}/T_{p(dr)}$ = 3.6 from the macro-element model is significantly overestimated in relation to the ratio of 2.2 reported by Chow et al. (2020), as shown in Figure 6.23a. Such a difference occurs due to the significant underestimation of the drained capacity, $T_{p(dr)}$, which is 1374 kN for the centrifuge tests and 811 kN for the macro-element model.

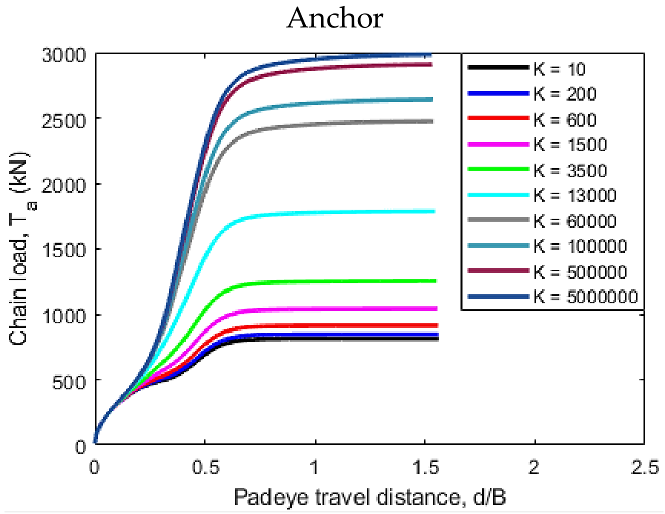

Figure 6.21 – Force-displacement curves for different values of *K*, with *A* = 0.75 and *C* = 0.0025.

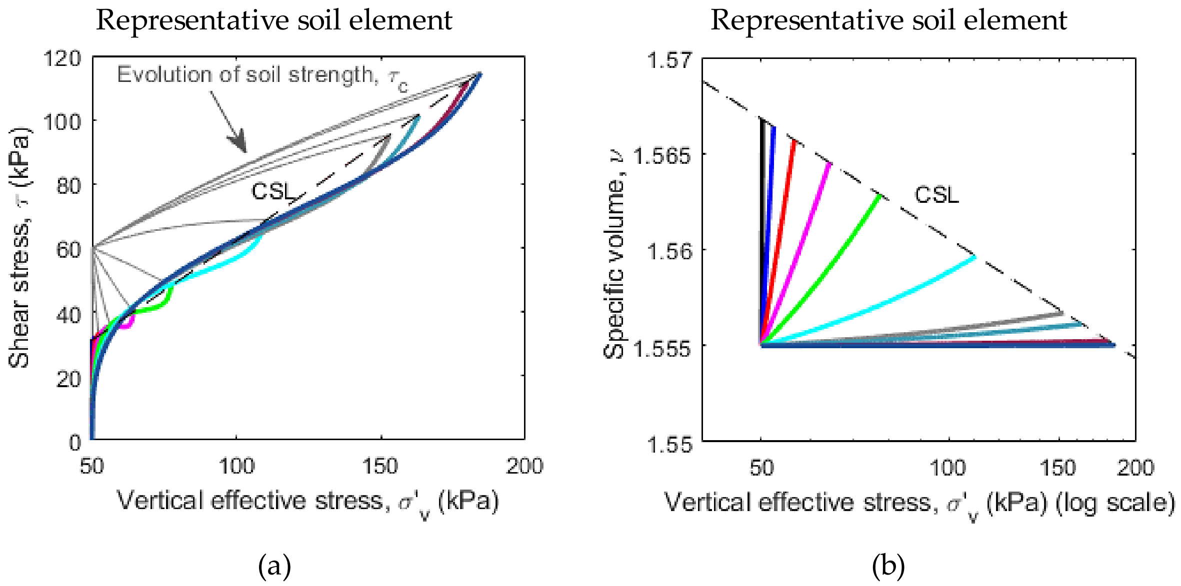

(a) (b)

Figure 6.22 – Representative soil element for different values of *K*, with *A* = 0.75 and *C* = 0.0025.

Table 6.7 – Anchor capacities from macro-element model for different values of *K*, with *A* = 0.75 and *C* = 0.0025.

K	Anchor peak capacity T_p (kN)	$T_p/T_{p(dr)}$
10	811.12	1.00
200	845.99	1.04
600	913.00	1.13
1500	1040.26	1.28
3500	1253.38	1.55
13000	1787.23	2.20
60000	2475.59	3.05
100000	2641.51	3.26
500000	2910.37	3.59
50000000	2986.60	3.68

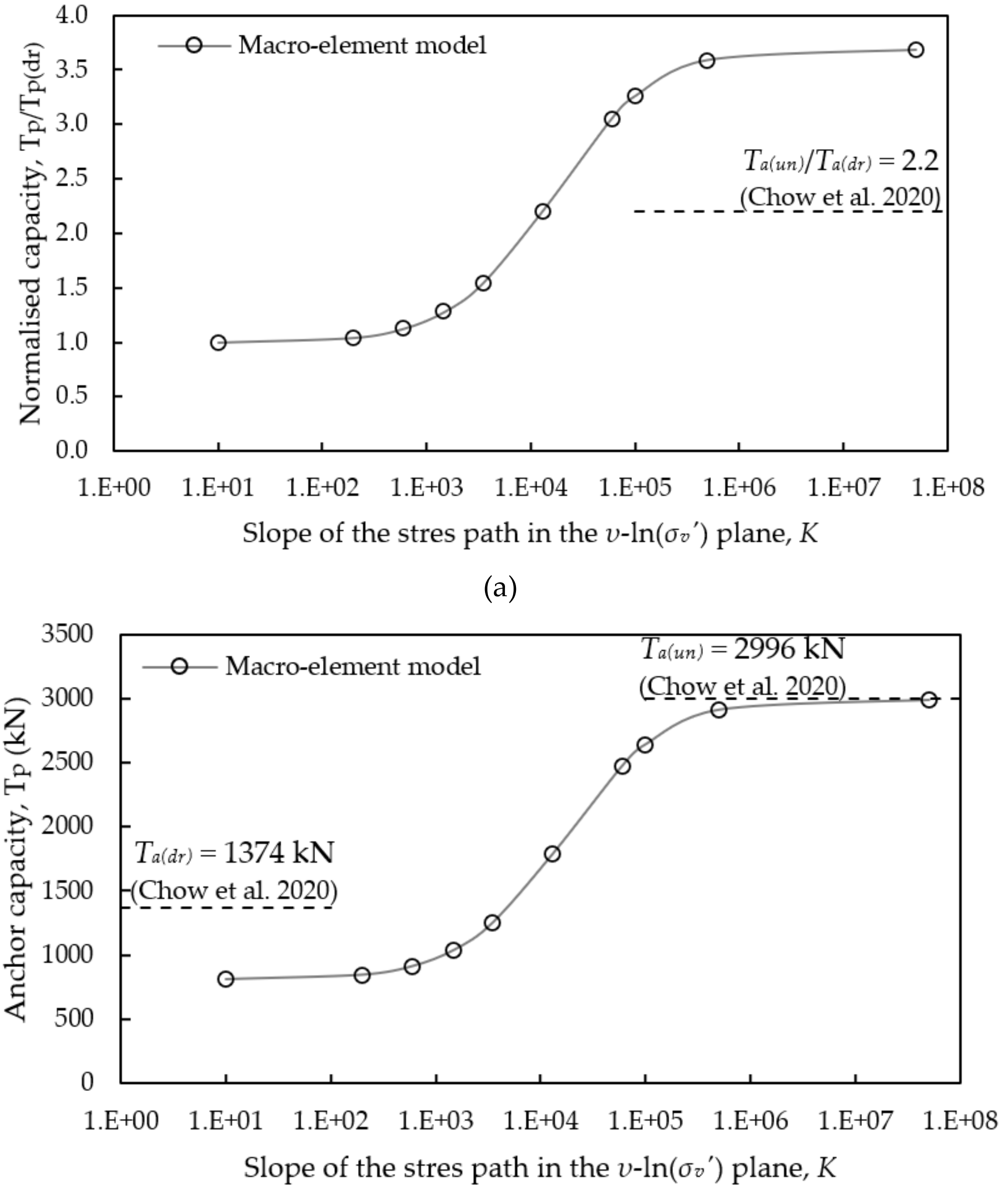

(a)

(b)

Figure 6.23 – Anchor capacities from macro-element analyses as a function of *K*, with *A* = 0.75 and *C* = 0.0025: (a) capacities T_p normalised by drained capacity $T_{p(dr)}$ and (b) capacities T_p given in absolute (not normalised) values.

In order to obtain better agreement between the capacities from the macro-element model and those from the centrifuge tests, the effect of certain soil parameters is analysed in the next section.

6.4.3.3. *Selection of shear parameters for the soil model*

As shown previously in Table 6.6, there are four parameters governing the shear behaviour of the soil: *A*, *C*, k_d and k_r. In the previous chapter, it was shown that, when using the same values for these soil parameters as in Diambra et al. (2013) as a starting point, only the parameters *A* and *C* had to be modified in order to provide good agreement with the experimental results. Using the same rationale, initially the effect of parameters *A* and *C* is analysed. Parameters k_r and k_d assume the same values used by Diambra et al. (2013) for Hostun sand, which are very similar to the parameters used by Gajo & Muir Wood (1999) and Corti et al. (2016) for the same type of sand.

Figure 6.24 and Figure 6.25 show a parametric analysis of parameters *A* and *C*, respectively, for drained and undrained behaviour. Initially, the aim is to match the peak capacity only. Other aspects will be further analysed later.

It can be seen that parameters *A* and *C* have a similar effect on anchor behaviour. For both *A* and *C*, the increase of value of the parameter decreases the peak capacity under drained conditions, while the final post-peak capacity is the same for all values. Under undrained conditions, the final capacity does not depend on the values adopted for *A* and *C*, but the shape of the curve changes. For smaller values of *A* and *C*, a sort of 'loading plateau' is observed at around 50% of the peak load, as circled in red in Figure 6.24b. This type of plateau for such high load levels has not been observed in the centrifuge tests carried out by Chow et al. (2020) and is a result of the kinematic stability of the anchor being reached before the maximum soil strength, as will be shown in detail in section 6.4.3.4. Therefore, the parameters are selected such that this shape is avoided.

Since both parameters *A* and *C* have similar effect on the force-displacement response of the anchor, modification of only one of them is necessary to reproduce the desired behaviour. The parameter *A* therefore assumes the same value as used by Diambra et al. (2013) [$A = 0.75$], and the value of parameter *C* is selected such that the 'loading plateau' is prevented under undrained conditions. Although $C = 0.0001$ provides a better match with the drained capacity from the centrifuge test, the peak capacity for $C = 0.0002$ is also similar to that observed in the centrifuge test, therefore this value is selected to provide a better shape of the curve under undrained conditions and avoid the 'loading plateau' which is still slightly observed for $C = 0.0001$.

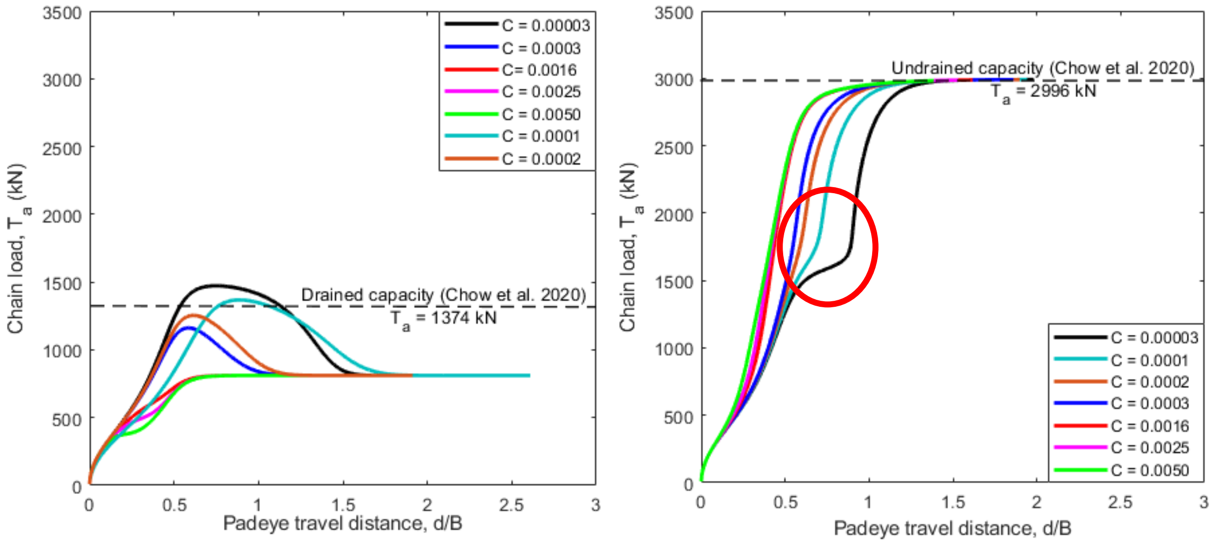

(a) (b)

Figure 6.24 – Parametric analysis: effect of parameter *C* (constant *A* = 0.75) on (a) drained and (b) undrained anchor behaviour.

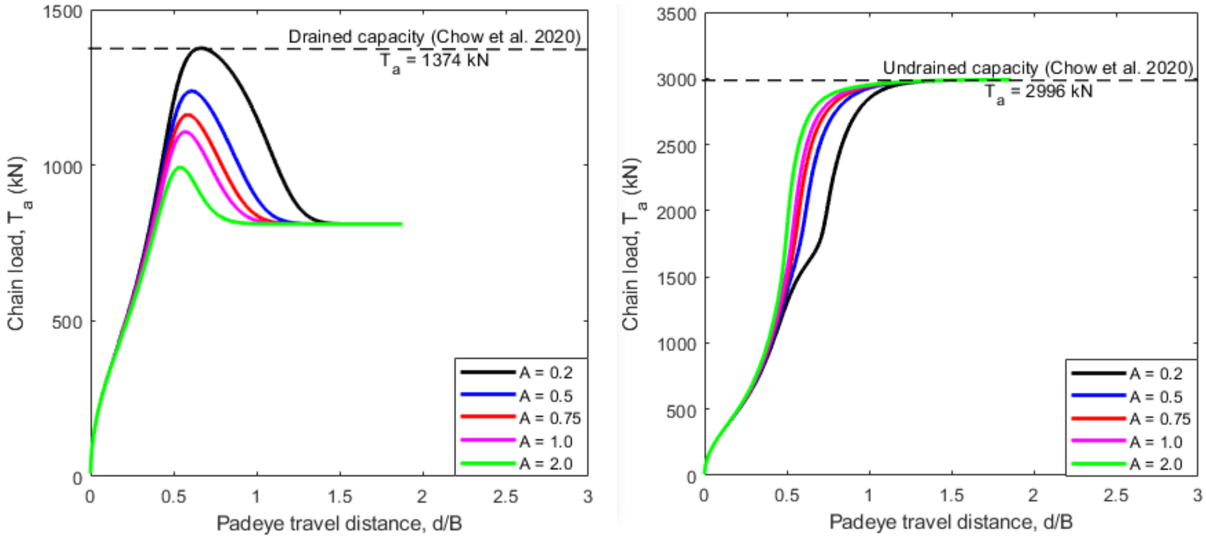

(a) (b)

Figure 6.25 – Parametric analysis: effect of parameter *A* (constant *C* = 0.0025) on (a) drained and (b) undrained anchor behaviour.

With a new value of parameter *C* (0.0002), much better agreement is obtained between the macro-element capacities with the centrifuge tests, as shown in Figure 6.26 and detailed in Table 6.8. The drained anchor capacity is now 1264 kN, which is only 8.7% lower than the value from the centrifuge test (1374 kN). The ratio between undrained and drained capacity is now 2.37, which is 7.2% higher than the ratio of 2.2 from the centrifuge tests (Figure 6.26a). Such difference is due to the underestimation of the drained capacity, as shown in Figure 6.26b.

The back-bone curve in Figure 6.26a is fitted with the relationship previously presented in Equation (6.7). Good agreement is obtained with $A_1 = 1.00$, $A_2 = 2.37$, $K_{50} = 3 \times 10^4$ and $p = 1.15$. The values of K that mark the transition between partially drained to drained and undrained are $K_{dr} = 3\text{x}10^3$ and $K_{un} = 5\text{x}10^5$, respectively.

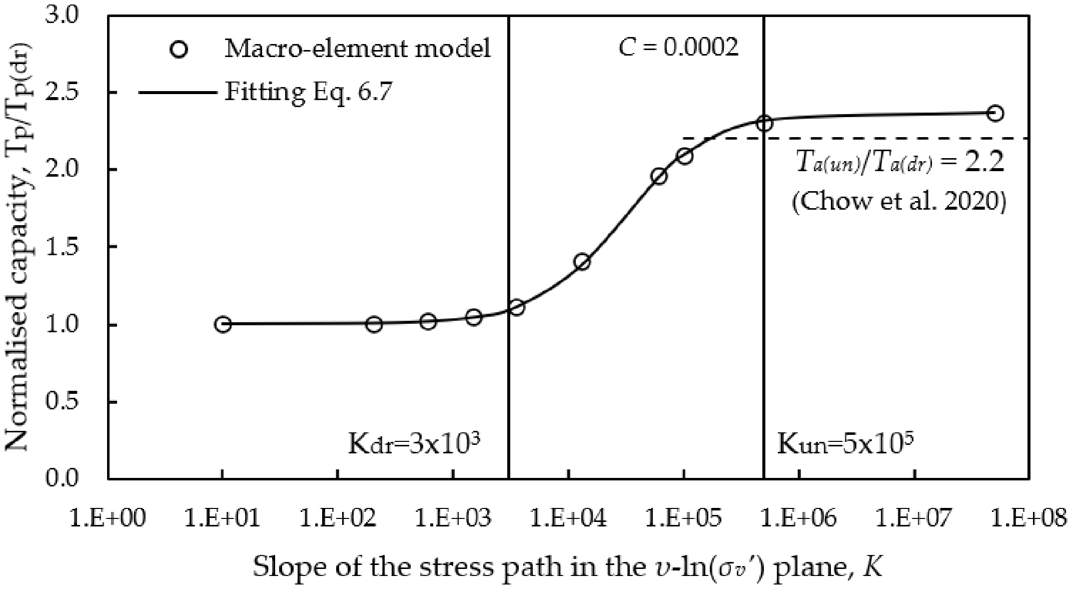

(a)

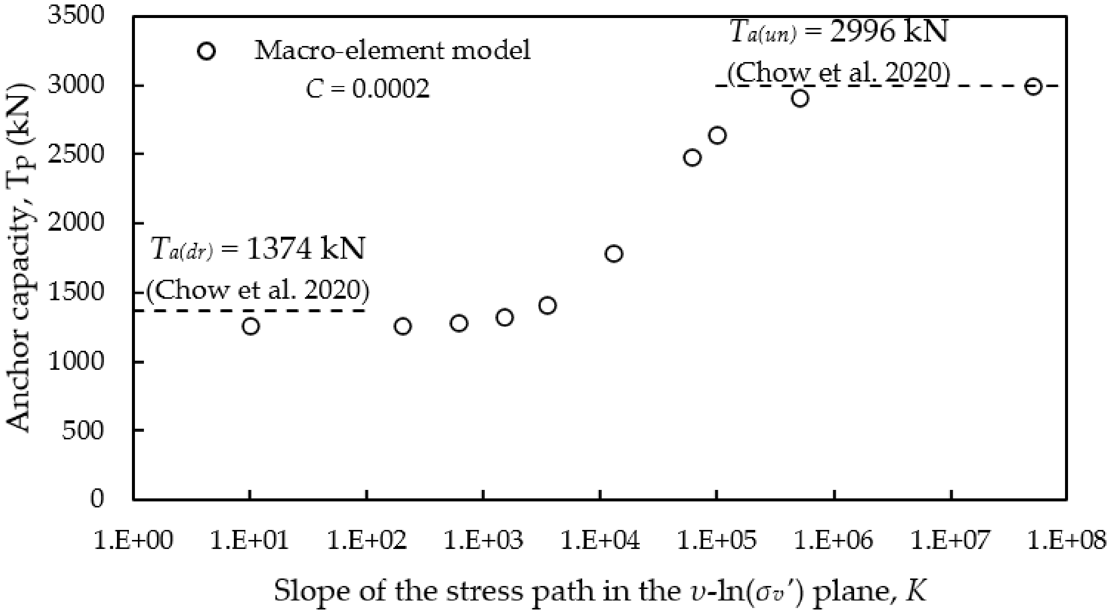

(b)

Figure 6.26 – Anchor capacities from macro-element analyses as a function of K, with $A = 0.75$ and $C = 0.0002$.

Table 6.8 – Anchor capacities from macro-element model for different values of K, with A = 0.75 and C = 0.0002.

K	T_p (kN)	$T_p/T_{p,dr(ref)}$	$V^* = K/\Omega$
10	1264	1.00	0.06
200	1266	1.00	1.20
600	1288	1.02	3.60
1500	1331	1.05	9.00
3500	1410	1.12	21.00
13000	1788	1.41	78.00
60000	2478	1.96	360.00
100000	2644	2.09	600.00
500000	2914	2.30	3000.00
5000000	2990	2.37	300000.00

The force-displacement curves for the whole drainage domain are presented in Figure 6.27a and compared with the centrifuge tests by Chow et al. (2020) in Figure 6.27b. Although the capacities are well captured by the macro-element, the displacements plotted in the horizontal axis are not comparable, since they are computed in a different way. While the macro-element analyses in Figure 6.27a present the total travel distance of the padeye (d_a), as previously explained in Equation (3.16), for the centrifuge tests the displacement of the chain measured at the pulley (d) was measured. The chain distance d measured at the pulley can be significantly higher than the travel distance of the padeye, since it includes chain displacements that do not necessarily move the anchor padeye, e.g. chain tightening and cutting through the soil. In fact, during the centrifuge test, the chain displacement between d/B = 0 and d/B = 2 was reported to be mainly due to the chain cutting through the soil. During this initial stage, little displacement of the anchor was observed, as shown in Chow et al. (2020). In the same study, significant displacement of the chain line due to cutting through the sand was also observed between d/B = 3 and d/B = 4.

Another aspect that plays a role in the difference between chain displacement d and travel distance of the padeye (d_a) is the constant reorientation of the load direction at the anchor padeye. In the macro-element analyses, the direction of the load was assumed to be θ_a = 30°, while in the centrifuge tests it was shown to vary between approximately 90° and 25°. The effect of loading direction will be analysed further in this chapter.

The complexity of the chain mechanisms is accurately captured in clays through the well-established chain solution by Neubecker & Randolph (1995). In sands, on the other hand, no well-established solution has been proposed to date.

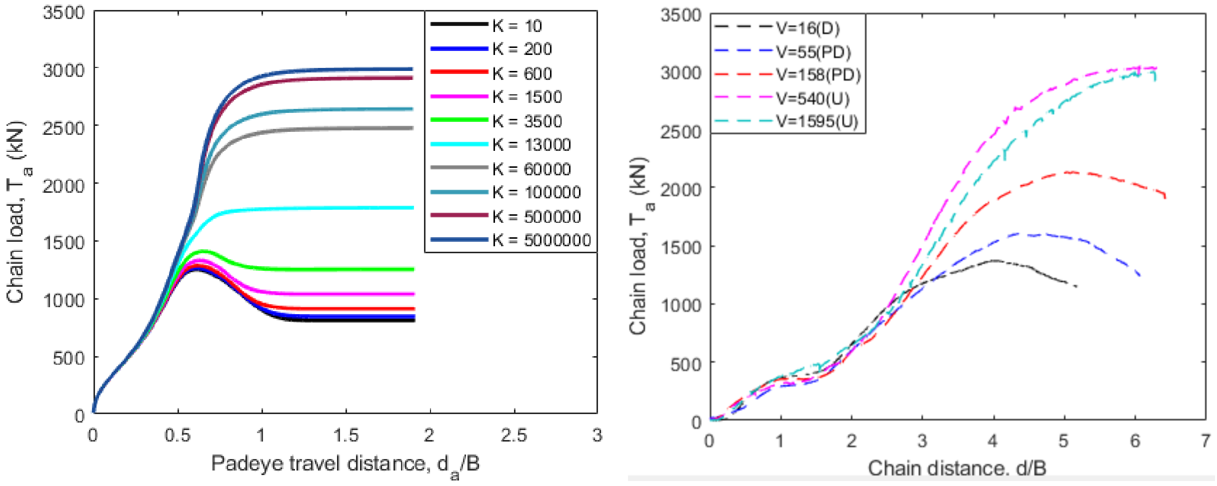

(a) (b)

Figure 6.27 – Force-displacement curves for different values of K with A = 0.75 and C = 0.0002 – (a) macro-element model, (b) centrifuge tests by Chow et al. (2020).

Since the effect of the chain is not included in the analyses presented in this chapter, the following results are presented in a normalised form, i.e. divided by the respective (chain or padeye) displacement at peak for drained conditions. For now, the macro-element analyses for the whole drainage domain is presented. The relationship to the centrifuge tests will be introduced later in this chapter through a conversion procedure from the parameter K to the non-dimensional velocity V^*.

Analysis of the representative soil element (Figure 6.29) compares the stress paths for C = 0.0025 (Diambra, 2010; Diambra et al., 2013) and C = 0.0002. For easier visualisation, only the stress paths for $K = 5\text{x}10^6$ (undrained) and K = 1500 (with significantly less pore pressure generation, i.e. nearly-drained) are shown. A peak in shear stress can be observed for C = 0.0002 under nearly-undrained conditions, whereas for C = 0.0025 no peak in shear stress was observed. A lower value of C, therefore, accentuates the effect of the current drained shear strength τ_c. If the value of *C* is very low, the effect of picnotropy (i.e. the dependency on soil density) is not captured.

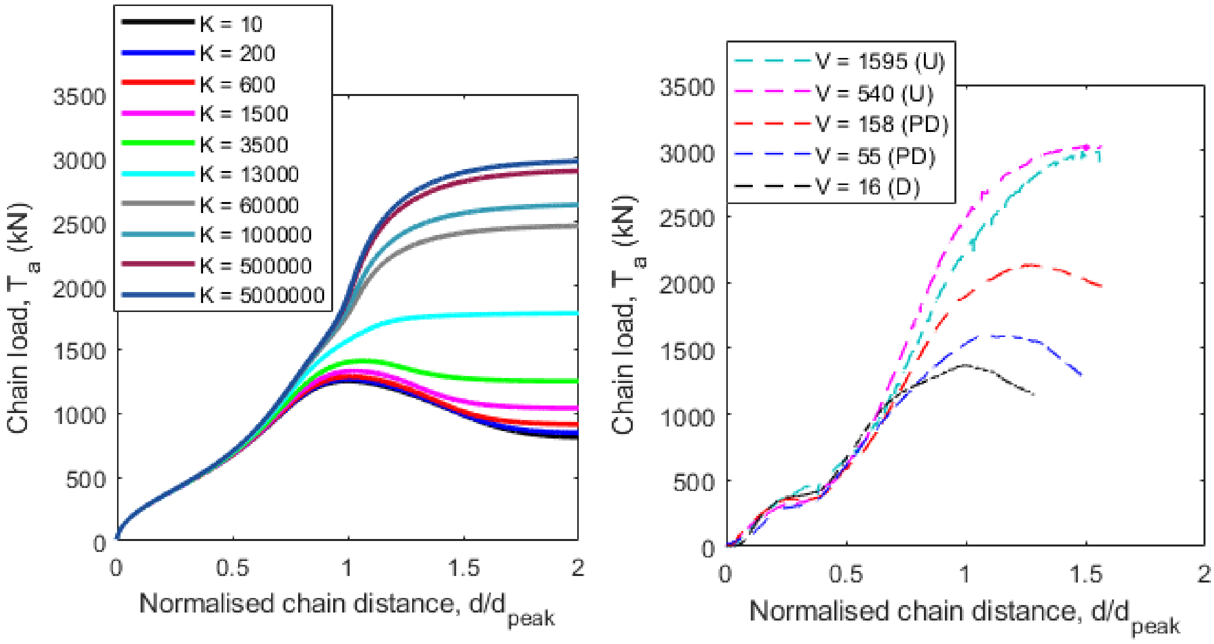

(a) (b)

Figure 6.28 – Force-displacement curves for different values of *K* with *A* = 0.75 and C = 0.0002 normalised by peak distance for drained conditions – (a) macro-element model, (b) centrifuge tests by Chow et al. (2020).

The peak in shear stress of the representative soil element explains the peak in anchor capacity, since there is a direct relationship between the load acting on the anchor and the shear stress of the soil element, as shown in the previous chapter (Table 5.6).

For the undrained case ($K = 5\text{x}10^6$), the shape of the stress path is similar for both values of *C*, which in turn results in a similar shape of the force-displacement curves. However, for *C* = 0.0025 the force-displacement curve presents a stiffer initial behaviour, since the stress path moves faster to higher stress levels and consequently the soil is stronger earlier than for the case with *C* = 0.0002.

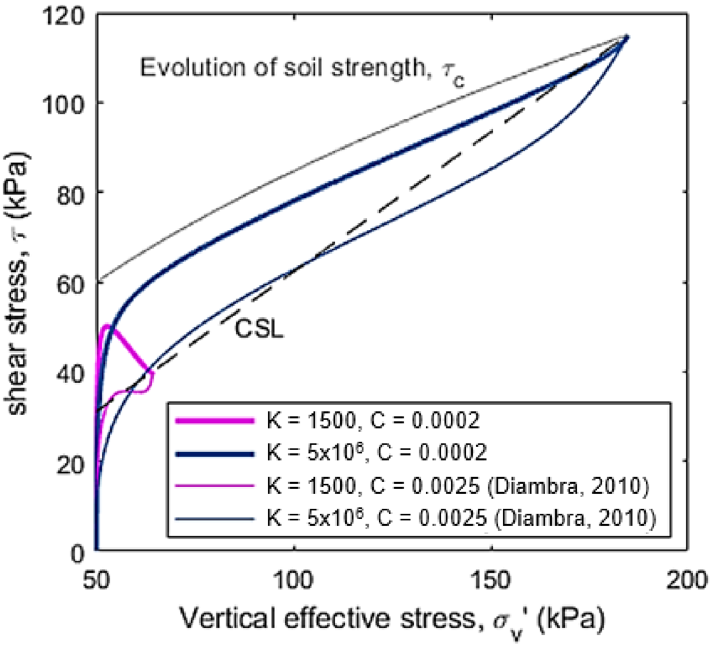

Figure 6.29 – Representative soil element for different values of *K* and *C*.

6.4.3.4. Selection of parameters for the anchor model

The capacity factors N_v, N_h and N_m for the macro-element model with changing strength τ_c were previously defined in Equations (4.1) through (4.3), similarly to the definition for a constant soil strength in Chapter 3 [see Equations (3.6) through (3.8)]. In the literature, capacity factors for sands are defined in a different way [$N_\gamma = F_u / (A_p\ \sigma_v')$, where F_u is the ultimate (normal or tangential) load and A_p is the area of the plate], i.e. divided by the vertical effective stress instead of the shear strength of the soil as in this thesis. The conversion from the capacity factors defined in the literature to the capacity factors as defined in this thesis results in $N_v = 14$ (converted from Merifield & Sloan, 2006) and $N_h = 3$ (converted from Chow et al., 2018a) for an embedment ratio of 5. In absence of data for rotational capacity factors N_m in the literature, a value of 3 selected in Chapter 3 for clays was used.

The parameters m, n and q that control the shape of the loading surface f also assume constant values, as previously shown in section 3.5.2. The plastic potential parameters ξ, χ and ω also assume the values recommended in Chapter 3, $\xi = 1.6$, $\chi = 1.1$ and $\omega = 1.5$. Although for some macro-element analyses a different value of ω was used, 1.5 was shown to provide satisfactory results for most cases, hence it is used as an initial value in this chapter. It follows that only the hardening parameter R_0 needs to be calibrated.

Whereas for the undrained model without a representative soil element in Chapter 3 the hardening parameter R_0 controlled solely the initial stiffness of the force-displacement curve (see Figure 3.6), in the model with a representative soil element it plays a much more relevant role. In this case, R_0 affects the relationship between the strength of the representative soil element and the mobilisation of anchor strength ρ_c through Equation (4.33), since $\rho_c = \tau/\tau_c$ and ρ_c depends on R_0 [through Equation (3.10)]. It follows that the shear stress is related to the hardening parameter R_0 through the expression in (6.13), which means the higher R_0, the higher the shear stress τ for a given displacement $[w^2 + u^2 + (B\beta)^2]^{1/2}$. This implies that, for higher values of R_0, the peak in shear stress τ occurs for a smaller anchor displacement. If the value of R_0 is too small, the "kinematic stability" of the anchor can be reached significantly earlier than the peak in shear stress of the representative soil element, in which case a post peak capacity higher than the point of kinematic stability would occur.

$$\frac{\tau}{\tau_c} = 1 - e^{-R_0\,[w^2+u^2+(B\,\beta)^2]^{1/2}} \tag{6.13}$$

The kinematic stability of the anchor is reached when the anchor aligns with the loading direction, i.e. sliding and rotational motion no longer occur. At this point, tangential and moment loads are equal zero ($H = M = 0$).

The loading path followed by the anchor for three values of R_0 (0.5, 1.5 and 5.0) and the strength surface of the anchor are depicted in Figure 6.30. The strength surface F (ρ_c = 1) in grey represents the final size of the loading surface f (not shown in the figure for better visualisation), which expands or contracts as the mobilisation of anchor capacity/soil strength ρ_c increases or decreases, respectively. It can be seen that, for $R_0 = 0.5$, the kinematic stability is reached long before the maximum shear strength of the soil, hence the loading path in red keeps moving upwards (i.e. in the positive direction of V/V_M) as the loading surface expands towards the strength surface in grey.

The effect of R_0 on the relationship between shear stress and anchor resistance is illustrated in Figure 6.31. When the kinematic stability of the anchor is reached before the current strength of the representative soil element is at peak conditions, the strength of the element continues to increase after the kinematic stability has been reached. This means that the anchor capacity will continue to increase due to the increase in soil strength. This occurs, in this case, for $R_0 = 0.5$ and $R_0 = 1.5$, as shown in Figure 6.31b. On the other hand, if the value of R_0 is higher ($R_0 = 5$), the kinematic stability coincides with the maximum strength of the representative soil element, therefore the maximum capacity of the anchor is the same as the point of kinematic stability.

The suppression of an early kinematic peak comes at the expense of a reduced anchor displacement, as observed in Figure 6.31b and in line with Equation (6.13).

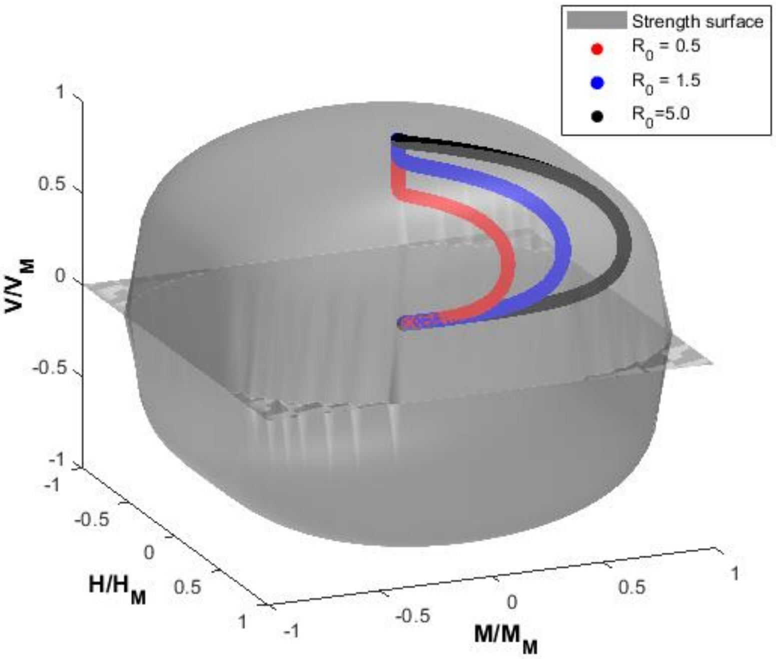

Figure 6.30 – Effect of parameter R_0 on the loading path of the anchor for $R_0 = 0.5$, 1.5 and 5.0.

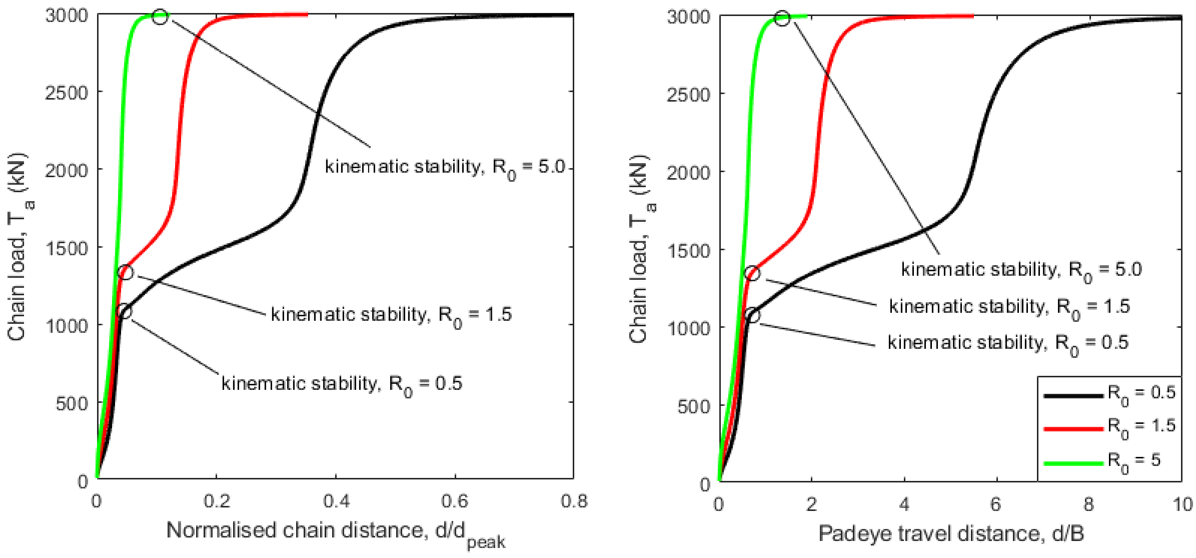

(a) (b)

Figure 6.31 – Effect of parameter R_0 on the relationship between anchor and representative soil element.

*6.4.3.5. Relationship between K and normalised velocities V**

Although the *K*-model introduced previously has advantages in comparison with the decoupled model – such as significantly less time demanded for simulation and reduced number of parameters required – the slope of the stress path *K* must be related to the non-dimensional velocity of the anchor (V^*). In the macro-element analyses presented in Figure 6.14, *K* was related to the rate of vertical displacement of the anchor, v_z. It was shown that the values of *K* can be converted to the non-dimensional velocity by means of a conversion factor Ω given by the ratio between *K* and V^*. In this analysis, V^* is related to the chain displacement on the actuator (i.e. the velocity *v* used for the calculation of V^* is the chain displacement at the actuator), as this was the displacement measured during the centrifuge tests by Chow et al. (2020). The angle of anchor pull with the horizontal (θ_a) is assumed constant. An angle of 30° was selected as it is close to the final rotation of the anchor observed in the centrifuge tests.

The anchor capacities for different values of *K* were shown in Figure 6.26. The ratio between the mid-inclination K_{50} from Equation (6.5) and the mid-velocity V_{50} obtained from the centrifuge tests ($V_{50} = 180$ from Figure 6.17) can be used as a conversion factor Ω from *K* to V^*. The ratio $\Omega = K_{50}/V_{50} = 3 \times 10^4 / 180 = 1.67 \times 10^2$ is used as a conversion factor. The anchor capacities predicted by the macro-element model can then be presented as a function of the converted non-dimensional velocity V^*, as presented in Table 6.9 and depicted in Figure 6.32. It is worth noting that, although the mid-inclination K_{50} differs from case to case, it can be obtained quickly, as a set of 10 macro-element analyses from drained to undrained behaviour takes less than 5 minutes to complete.

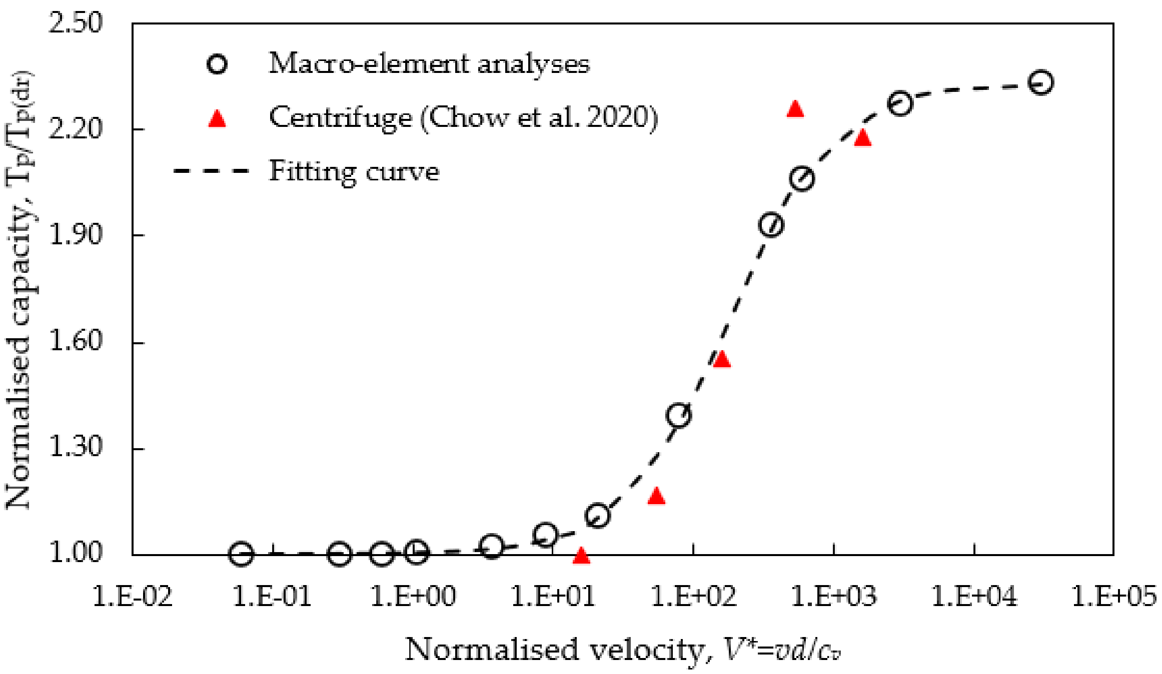

Figure 6.32 – Anchor capacities from macro-element analyses as a function of normalised velocities, V^*.

Table 6.9 – Summary of macro-element results and conversion from K to normalised velocity V^*.

K	T_p (kN)	$T_p/T_{p,dr(ref)}$	$V^* = K/\Omega$	$T_{p,exp}$ (kPa) centrifuge	Ratio $T_a/T_{a,epx}$
2667	1379	1.09	16.00	1374	1.00
9167	1623	1.28	55.00	1606	1.01
26333	2121	1.40	158.00	2134	0.99
90000	2602	2.06	540.00	3106	0.84
265833	2613	2.07	1595.00	2996	0.95

Overall the capacities obtained from the macro-element simulations provide good agreement with the results from the centrifuge tests. Most simulated peak capacities lie within a 5% difference, except for the test with $V^* = 540$ (which seems to be off the fitting curve), for which the difference is 16%. The reasons for such a deviation of this test from the back-bone curve is out of the scope of this study. The force-displacement curves obtained from the macro-element model are compared with the centrifuge data in Figure 6.33. The results agree fairly well both in terms of anchor capacity as well as in terms of normalised displacement. The ratio between simulated and measured capacity is shown in Table 6.9.

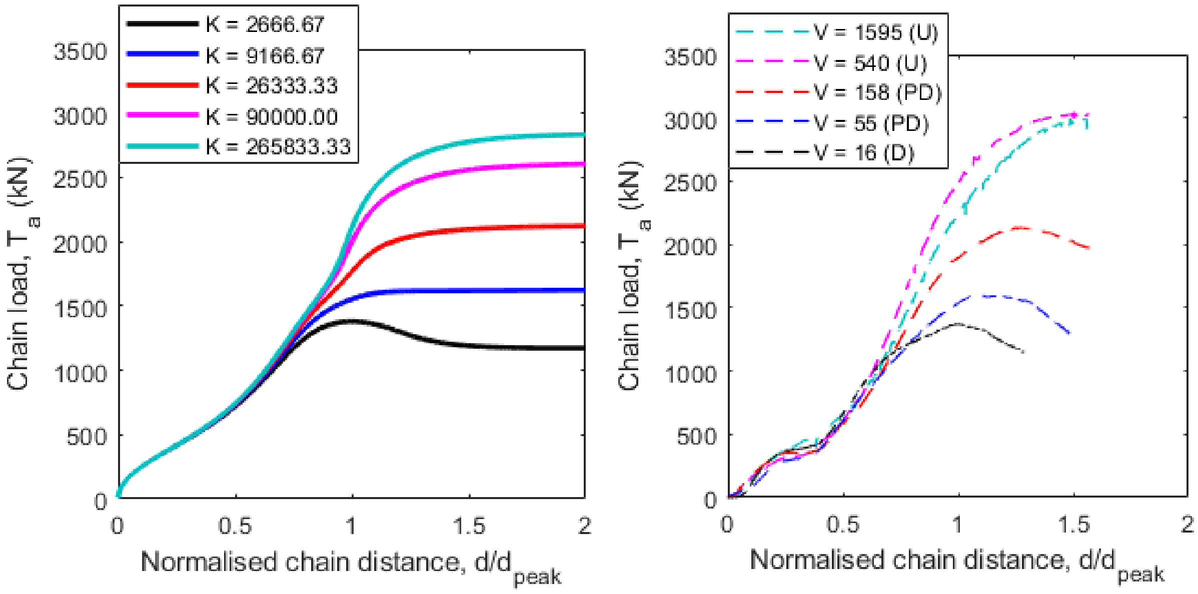

(a) (b)

Figure 6.33 – Force-displacement curves for equivalent values of K and V: (a) macro-element model, (b) centrifuge tests by Chow et al. (2020).

Figure 6.34 displays the behaviour of the representative soil element for the values of K associated with the normalised velocities V^*. An interesting observation is that although the normalised velocity for drained conditions $V_{dr} = 16$ is equivalent to $K = 2667$ from the proposed conversion procedure, such a value of the slope of the stress path does not provide fully-drained conditions, as approximately -22 kPa of excess pore pressure are generated during shearing of the soil element. For $K = 265833.33$, on the other hand, fully undrained conditions are obtained, since the stress-volumetric plot in green on Figure 6.34b exhibits nearly zero volumetric deformation.

That occurs because the ratio between the values of K that mark the transition to undrained and drained behaviour, $K_{un}/K_{dr} = 5\text{x}10^5/3\text{x}10^3 = 166.67$, is higher than the ratio between the normalised velocities $V_{un}/V_{dr} = 540/16 = 34$, which means that horizontal range of the back-bone curve is different when plotted in terms of K with respect to when presented in terms of V^*. By using K_{50}/V_{50} as a conversion factor, it is ensured that the conversion provides good results near the mid-point of the drainage domain. However, for macro-element analyses in the nearly-drained and nearly-undrained zone, some error might appear due to the different scales of K or V^*. In spite of that, the effect of the different scale in *K* and *V** is not significant in terms of anchor capacity. While the converted value of $K = 2666.67$ for drained conditions provided an anchor capacity of $T_{p(dr)} = 1380$ kN, a fully-drained macro-element analysis with $K = 10$ would provide a drained capacity of 1264 kN, which is only 9% lower than the capacity obtained from the conversion method.

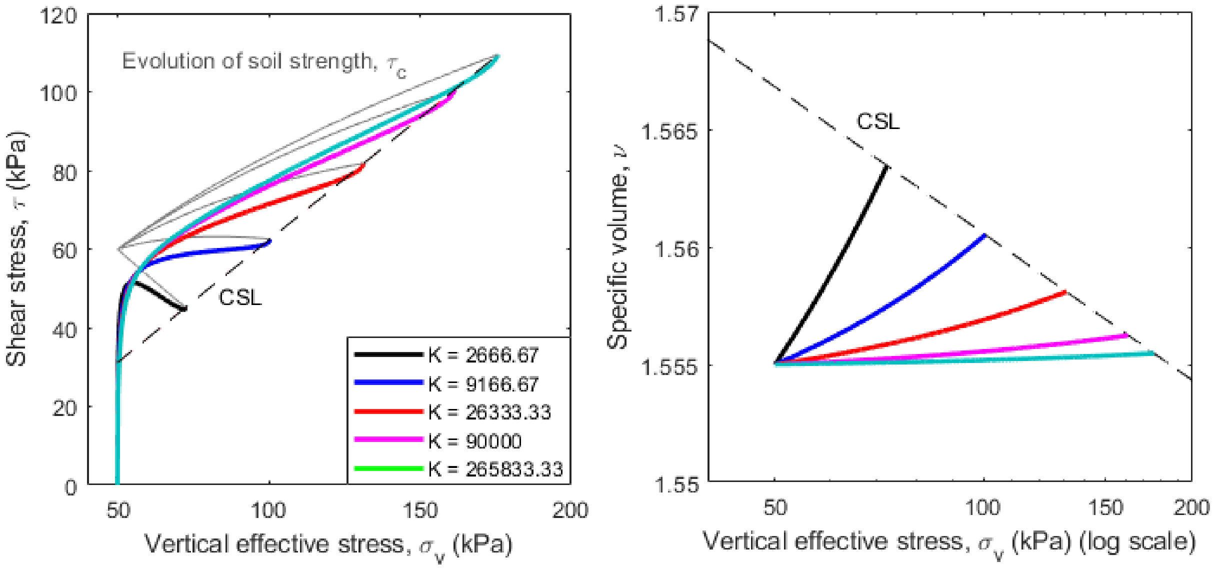

(a) (b)

Figure 6.34 – Response of representative soil element for values of *K* associated with normalised velocities *V**: (a) stress path, (b) stress-volumetric behaviour.

Furthermore, a closer look into Figure 6.17 reveals that the point $V = 540$ and $T_p/T_{p(dr)} = 2.26$ seems to be off the curve and to not follow the trend in the other points. If this point is disregarded, a different fitting curve with $V_{50} = 300$ would provide better agreement with the centrifuge data, as depicted in Figure 6.35. If $V_{50} = 300$ is used, the conversion factor Ω is $K_{50}/V_{50} = 3 \times 10^4 / 300 = 100$. In that case, the drained velocity $V_{dr} = 16$ is equivalent to $K = 16 \times 100 = 1600$, for which the drained capacity is 1336 kN (similar to 1374 kN from the drained centrifuge test). The capacities obtained with the new conversion factor Ω still compare well with the results from the centrifuge tests, as shown in Figure 6.36. In this case, the pore pressure generated during the nearly-drained test is -15 kPa (Figure 6.37), as opposed to -22 kPa with the previous conversion factor of $\Omega = 180$. A more detailed analysis of the pore pressure generation will be presented in a later section.

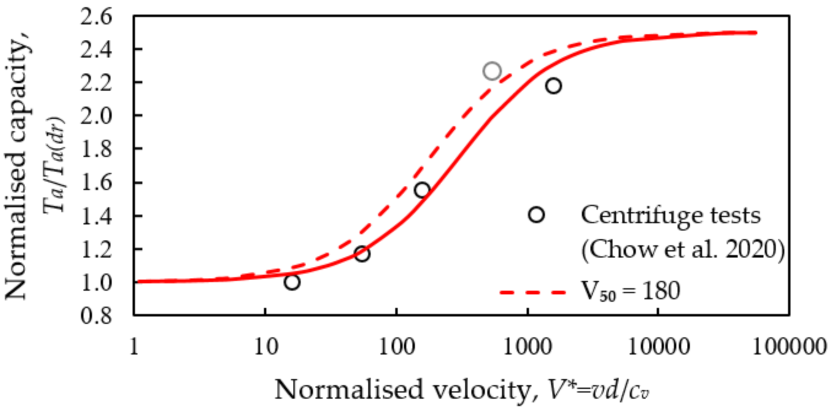

Figure 6.35 – Effect of V_{50} on fitting curve.

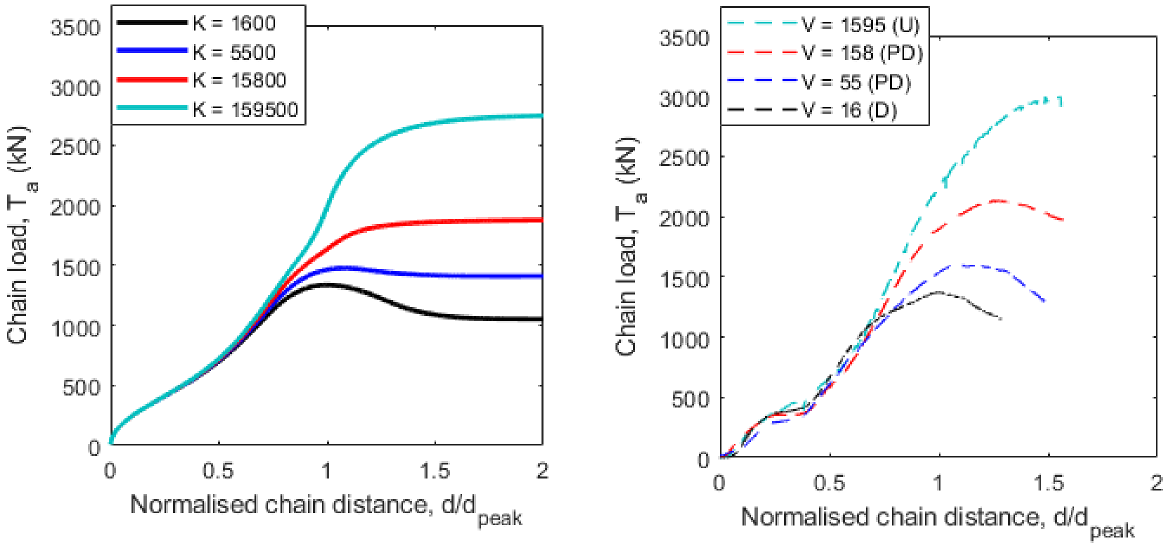

(a) (b)

Figure 6.36 – Force-displacement curves for equivalent values of *K* and *V**, considering a conversion factor $\Omega = 100$: (a) macro-element model, (b) centrifuge tests by Chow et al. (2020).

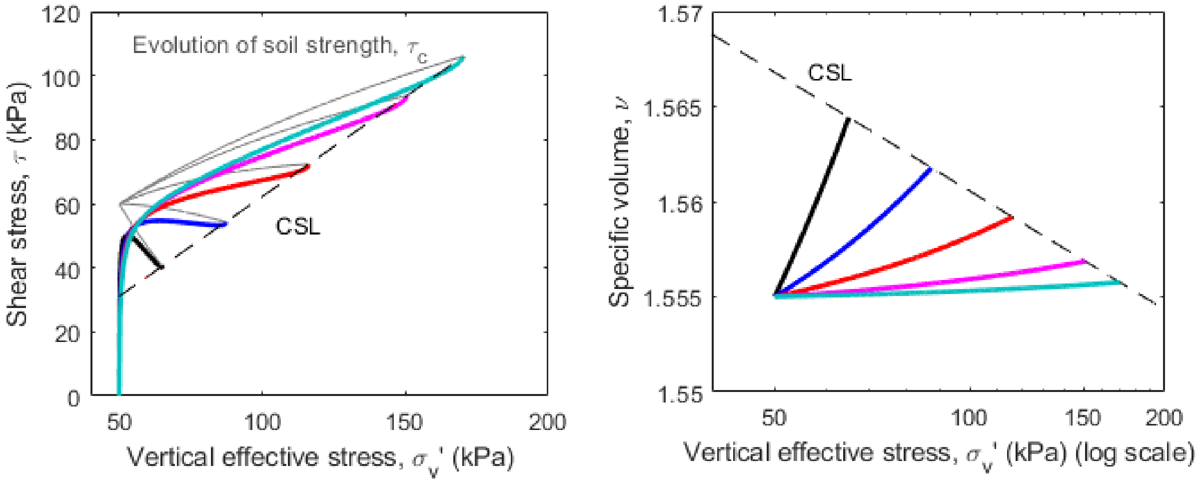

(a) (b)

Figure 6.37 – Response of representative soil element for values of *K* associated with normalised velocities *V**, considering a conversion factor $\Omega = 100$: (a) stress path, (b) stress-volumetric behaviour.

6.4.3.6. *Discussion on V_{un}, V_{dr} and V_{50}*

As shown previously in this chapter, the ratio between K_{50} and V_{50} can be used as a conversion factor from the slopes of the stress path K and the normalised velocities V^*. However, the selection of the parameter V_{50} = 180 for the centrifuge tests was only possible because the centrifuge data were available beforehand. The same applies for the velocities that mark the transition between drained and undrained (V_{dr} = 16 and V_{un} = 540 for the centrifuge tests carried out by Chow et al., 2020). Selecting appropriate values of V_{50} based on previous studies can be challenging, as these might depend on the experimental set-up, soil properties and anchor shape.

For shallow foundations, for example, Finnie & Randolph (1994) found V_{dr} = 0.01 and V_{un} = 30 for circular plates in sand and silt. Stewart & Randolph (1991) found that a sharper transition from drained to undrained is observed for penetrometer tests in comparison with shallow plate foundations. This was confirmed by Watson & Suemasa (2000)[2], who found V_{dr} = 0.2 and V_{un} = 20 for penetrometer tests. Bransby & Ireland (2009) reported significantly lower values V_{dr} = 0.00001 and V_{un} = 0.01 for pipeline upheaval buckling tests in sand, although these tests were carried out at 1**g** conditions, hence with much greater dilation potential.

From calibration chamber penetration tests, Kim et al. (2010) found values of V_{dr} = 0.05 and V_{un} = 1 for mixtures of Jumunjin sand and kaolin clay. Oliveira et al. (2011) reported values of V_{dr} = 1 and V_{un} = 70 for mini-CPT tests in silty tailings.

Overall, the values of V_{un} and V_{dr} are highly dependent on the type of test, therefore reference values are rather difficult to be drawn. Oliveira et al. (2011) mentioned that the values of V_{dr} and V_{un} are highly dependent on the coefficient of consolidation (c_v) that is considered. This is also discussed by Bransby & Ireland (2009) and Silva et al. (2006), who showed that the operative c_v during deformation was not estimated correctly for PCPT tests in clay.

Furthermore, the normalised velocity V^* can be given in terms of distinct displacements: vertical or horizontal displacement of the anchor's padeye or mid-point, total displacement of the anchor's padeye or mid-point, or even the chain displacement at the actuator, which is one of the most used methods, as the measurement is quite straightforward and does not require any

---

[2] Originally described as unpublished work in House et al. (2001). Data obtained from House et al. (2001).

special visualisation technique. The choice of type of displacement to be used for calculating the non-dimensional velocity V^* affects the values of V_{dr}, V_{50} and V_{un} (as previously shown in Figure 6.15), as chain displacements tend to be much higher than the actual displacement of the anchor due to chain slack, cutting-through and evolution of anchor rotation.

Given that a wide range of velocities V_{dr} and V_{un} have been reported in the literature for different applications, the mid-velocity V_{50}, which is necessary to convert the values of K to actual non-dimensional velocities V^*, is also rather difficult to be determined without running a few centrifuge tests. In particular, the normalised velocities obtained from the centrifuge tests of Chow et al. (2020) are significantly higher than those reported in other studies, as shown in Table 6.10. It seems that the values $V_{dr} = 16$ and $V_{un} = 540$ are higher than those reported in the literature by a factor of the centrifuge acceleration (50**g**). However, the reasons for such differences are due to possible dilation effects or differing failure mechanisms, which depends on the structure being analysed (Chow, 2021, *personal communication*; Chow et al., 2022, *forthcoming*). In this thesis, the calibration of the conversion factor Ω relied on such values of normalised velocities V^* (in particular on the mid-velocity V_{50}). It is worth noting, though, that different values of normalised velocities from the centrifuge tests would not affect the validity of the model, as these would only affect the value of the conversion factor Ω between K and V^*.

Table 6.10 – Comparison between normalised velocities from different studies.

Reference	Application	V_{dr}	V_{un}
Finnie & Randolph (1994)	Shallow foundations	0.01	30
Watson & Suemasa (2001)	Penetrometer tests	0.2	20
Kim et al. (2010)	Calibration chamber penetration tests	0.05	1
Bransby & Ireland (2009)	Pipeline upheaval	0.00001	0.01
Oliveira et al. (2011)	Mini-CPT	1	70
Chow et al. (2020)	Plate anchors	16	540

Given the difficulty in obtaining values of V_{dr}, V_{50} and V_{un}, so far, the proposed macro-element model still relies on the determination of V_{un} for the calibration of the operative critical state parameter Γ (as shown in section 6.4.3.1) and on V_{50} for the conversion between values of K and

V^* (as shown in section 6.4.3.5). The development of methods that quantify the influence of different soil properties and e.g. experimental set-up on such values would enable simpler application of the model. Additional studies similar to those by Robinson (2019), for example, which quantified the influence of e.g. soil properties and strain levels on the changes in soil strength with the rate of loading, would be of significantly value. In addition to that, the account of dilation effects in the formulation of the normalised velocity, as proposed by Palmer (1999) and Lauder et al. (2012) might also contribute to a unified approach for the determination of representative velocities V_{dr}, V_{50} and V_{un}. Furthermore, other studies similar to the centrifuge tests carried out by Chow et al. (2020) can provide more insights on how soil properties, testing set-up, loading conditions and anchor geometry can affect the normalised velocities on studies involving anchors.

6.4.3.7. *Effect of angle of pull*

In this section, the effect of different load directions θ_a (the angle of pull with the horizontal at the anchor padeye) is analysed. As shown previously, the effect of the chain connected to the anchor padeye is not considered in the macro-element model for sands, as no well-established chain equations for sands have been developed to date. The macro-element simulations considered a constant load direction $\theta_a = 30°$ at the padeye, which is approximately normal to the final orientation of the anchor observed in the centrifuge tests.

Figure 6.38 shows the effect of θ_a on the anchor orientation. It can be observed that, initially, the anchor orientation for a load direction of 60° agrees well with the centrifuge test for drained conditions. After a peak plate rotation of 42° is reached, the anchor rotates back towards final orientation, since it becomes "easier for the mooring line to further cut through the sand than for the anchor to continue to rotate" (Chow et al., 2020). As expected, the anchor rotation is not captured by the macro-element model, as this behaviour is dependent on the evolution of the shape and orientation of the chain at the padeye during the test.

The force-displacement curves obtained from the macro-element model are compared with the results from the centrifuge tests by Chow et al. (2020) (Figure 6.39). Even though the capacities and the shape of the curves are similar, the displacements are significantly higher than those observed from the centrifuge tests. This might be an indication that most of difference in anchor displacement compared to the chain line displacement is attributed to the chain cutting through the soil and tightening of the initial slack, rather than the change in load direction at the padeye caused by the chain.

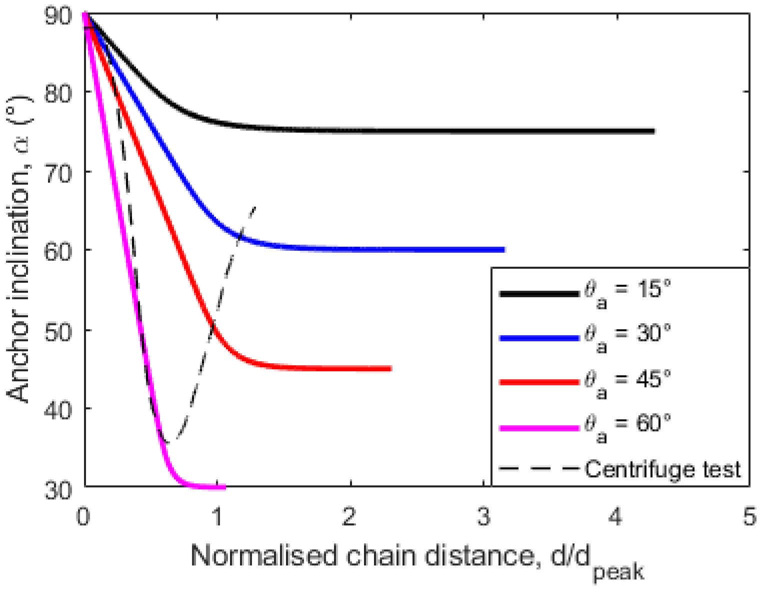

Figure 6.38 – Effect of direction of loading on anchor orientation for drained conditions.

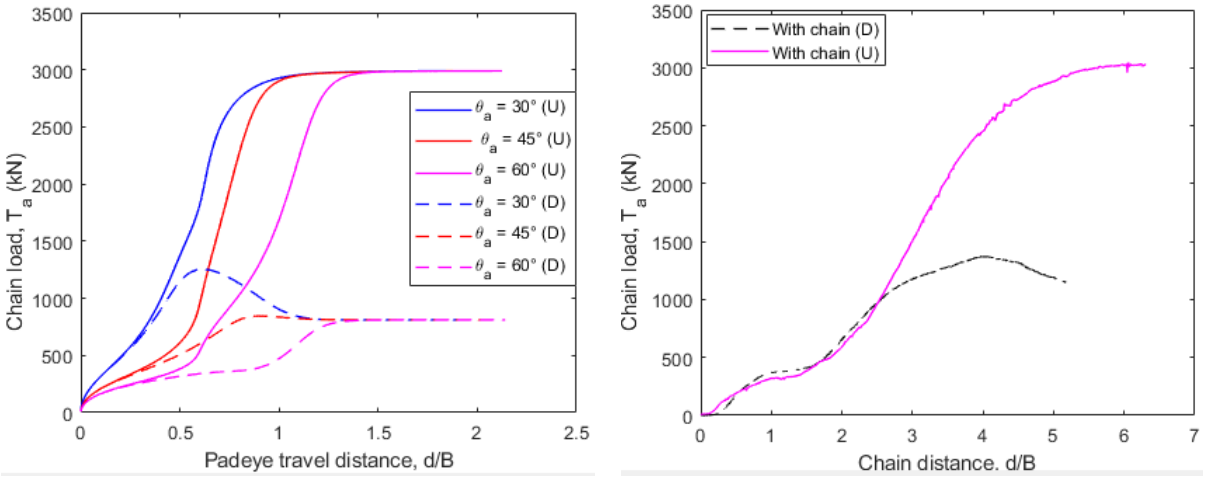

(a) (b)

Figure 6.39 – Effect of direction of loading on force-displacement curves for drained and undrained conditions.

6.4.3.8. Effect of changing vertical total stress

So far in this thesis, all macro-element analyses have considered that the vertical total stress σ_v on the representative soil element (equal to the vertical total stress at the depth of the anchor's mid-point at a certain horizontal distance from the anchor) remained constant during anchor pull. While this assumption is evident for the analyses involving purely horizontal displacement such as those in Chapter 5, the effect of changing vertical stress as the anchor loses embedment is less obvious and shall be assessed.

Constant vertical stress σ_v implies that the weight of soil above the anchor's mid-point does not change. For that assumption to be correct, the soil heave above the anchor must be the same as the loss of embedment of the anchor, i.e. the soil above the anchor must be lifted up on the surface due to the anchor vertical displacement. On the other hand, changing vertical stress σ_v by considering that the loss of embedment of the anchor centre of gravity results in an equal reduction in the soil column above implies that no heave occurs on the mudline.

Centrifuge tests carried out by O'Loughlin & Barron (2012) on vertically loaded vertical strip anchors in dense sand showed that, before the peak load is reached, the soil movements are localised and do not reach the surface. After the peak load has been reached, however, the soil movements extend from the anchor to the surface, causing heave of the mudline as observed in Figure 6.40. It is worth noting that the anchor heave observed in those tests seems to be significantly smaller than the vertical displacement of the padeye, but somewhat comparable to the vertical displacement of the mid-point of the main plate. For this reason, the change in vertical total stress σ_v in this section is assumed to follow the loss of embedment of the anchor's centre, according to Equation (6.14).

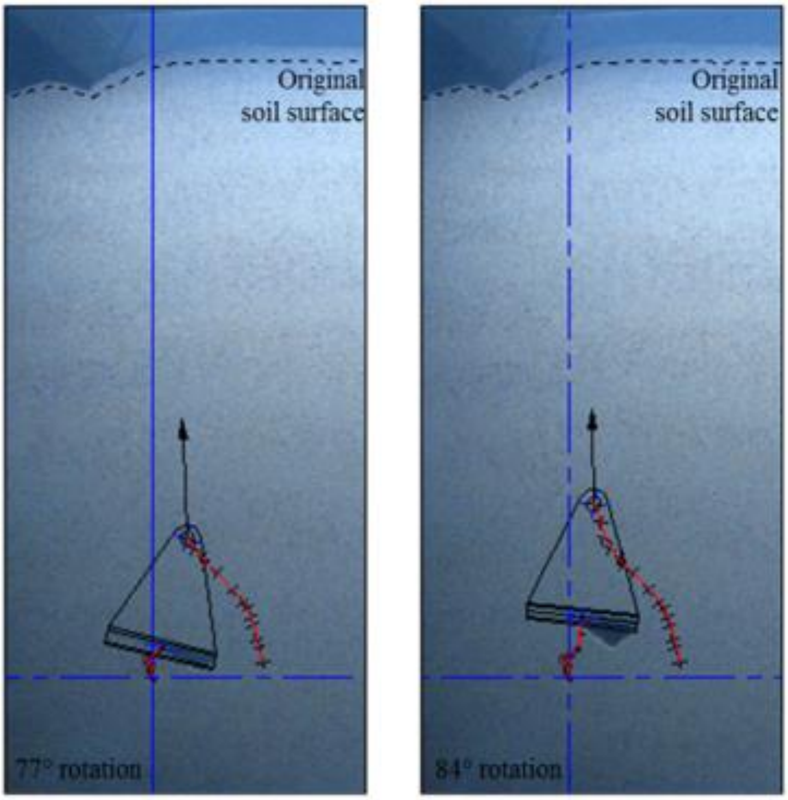

Figure 6.40 – Soil heave due to anchor movement at two stages post peak load (O'Loughlin & Barron, 2012).

$$\dot{\sigma}_v = -\gamma' \, \dot{z} \tag{6.14}$$

where γ' is the effective unit weight of the soil and z is the vertical displacement of the anchor centre of gravity.

Macro-element simulations of the plate anchor tested by Chow et al. (2020) are carried out considering such change in vertical total stress. The results for the anchor resistance are presented in Figure 6.41a and compared with macro-element simulations with constant vertical stress in Figure 6.41b. Initially, results for the whole displacement domain are presented. It can be observed that changing the vertical stress with anchor's vertical displacement has little effect on the force-displacement behaviour. Although a slight reduction in post-peak capacity for nearly-drained cases is observed, the peak capacity is not affected.

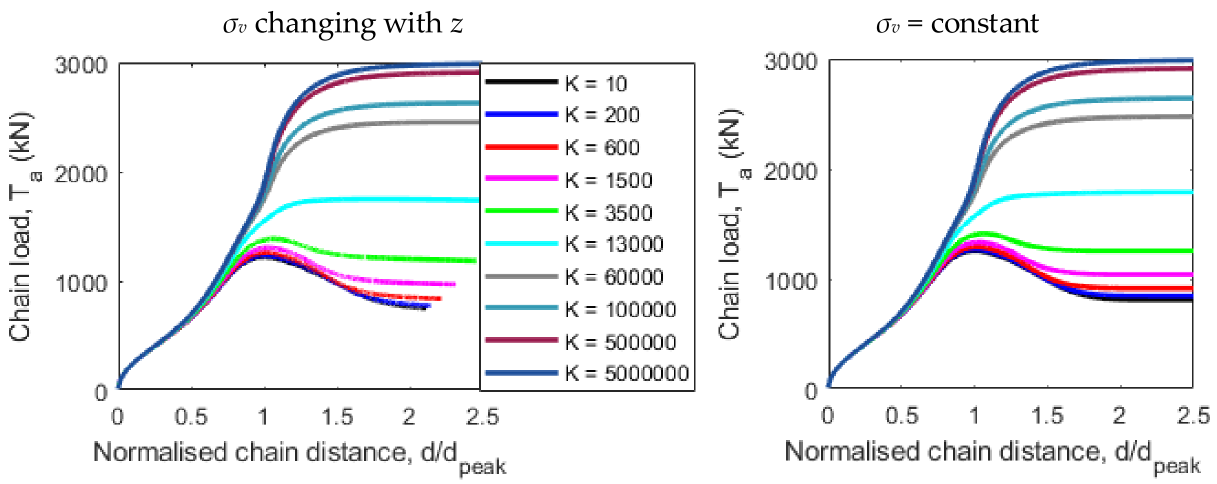

(a) (b)

Figure 6.41 – Comparison of force-displacement curves: (a) accounting for changes in total vertical stress; (b) assuming constant total vertical stress.

The stress-volumetric path of the representative soil element in Figure 6.42 provides insight on how the change in effective stresses might change with anchor displacement. In most cases, the stress path "bends" to the left due to a reduction in vertical effective stress caused by the change in total stress. For the drained case ($K = 10$ in black solid line), for example, for which normally no excess pore pressure is generated, the stress path is expected to be vertical if the total vertical stress is assumed constant (e.g. in Figure 6.22). However, if the change in vertical effective stress is accounted for, a reduction in vertical effective stress can be observed. Particularly for the drained case in Figure 6.42, a difference of approximately -5 kPa in pore pressure is observed due to the loss of embedment of the anchor.

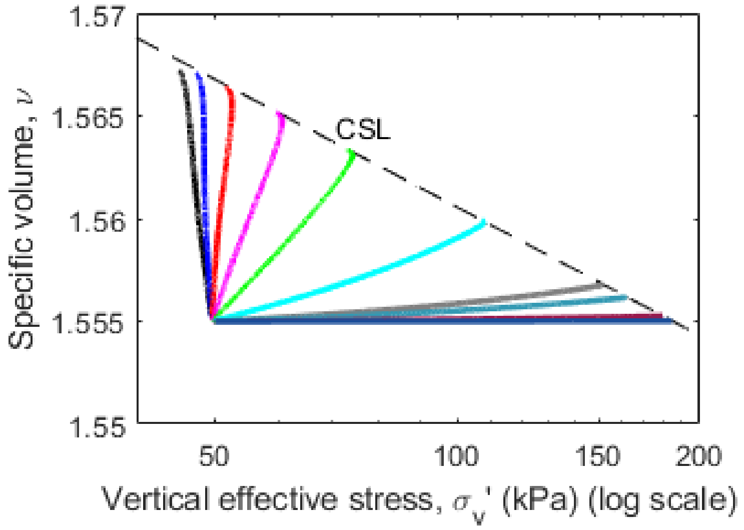

Figure 6.42 – Response of representative soil element accounting for changes in total vertical stress.

The results of macro-element simulations with *K* values equivalent to the non-dimensional velocities *V** of Chow et al. (2020)'s centrifuge tests are presented in Figure 6.43. Even though the pore pressure plotted in the graphs represent different measurements, the results are fairly similar. The evolution of pore pressure generation for the representative soil element (Figure 6.43a) reproduces the pore pressure representative of the whole soil mass around the anchor, while the plot in Figure 6.43b displays the pore pressure measured locally by a transducer attached to the anchor plate. Nonetheless, both graphs show minimal pore pressure generation up to $d/d_{peak} \approx 0.5$ (if the noise in the centrifuge test measurements are ignored) followed by significant increase in (negative) pore pressure up to a point where the pressure stabilises and reaches a plateau.

Although direct comparison between the pore pressure results is rather difficult, the same trends were observed in both plots of Figure 6.43, which is an indication that the pore pressure generated in the representative soil element is in accordance with the pore pressure generation in the bulk of soil during the centrifuge tests.

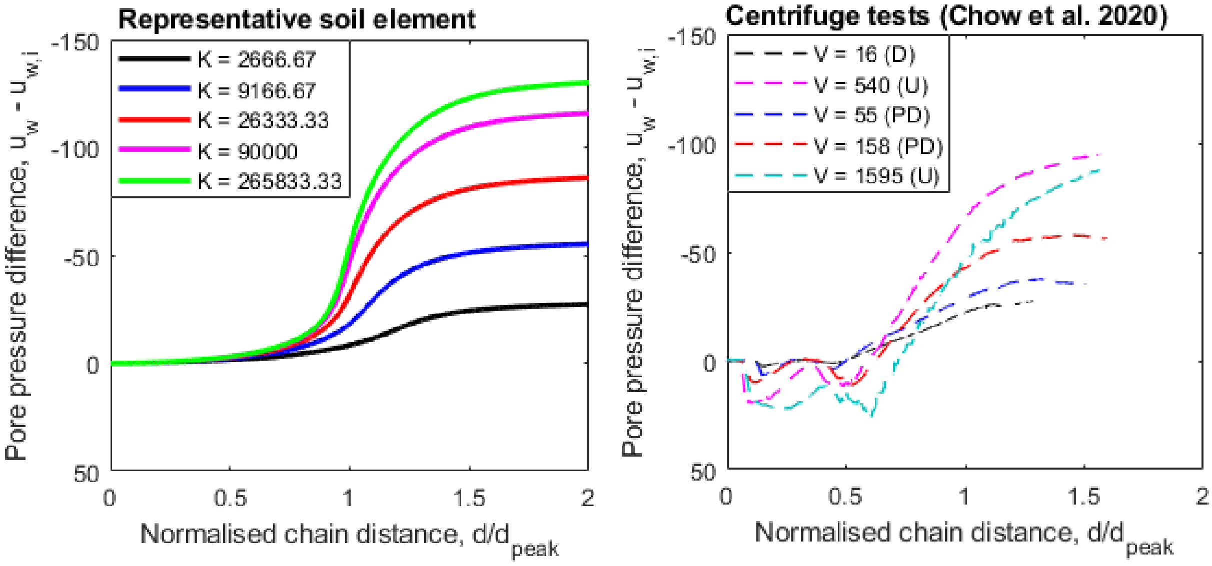

(a) (b)

Figure 6.43 – Pore pressure generation for different loading rates (a) in the representative soil element; (b) on the anchor during centrifuge tests.

6.5. Further validation without the chain effect

Further validation of the macro-element model is carried out through the comparison with centrifuge tests in which the chain effect is not significant. In experimental set-ups in which the anchor is loaded vertically, the line displacement is approximately the same as the travel distance of the anchor padeye (Blake et al., 2011). Barron (2014) carried out drained centrifuge tests on a strip anchor (width B = 0.6 m and length L = 4.2 m) initially installed in Congleton sand under vertical loading. The anchor was loaded vertically at the padeye, which was located at e_n/B = 0.25 from the anchor centre. In the absence of further characterisation of the Congleton sand and given the similarities with the UWA silica sand (as shown in Table 6.11), some soil properties were assumed to be the same as in the previous section for the simulation of Chow et al. (2020)'s centrifuge tests.

Table 6.11 – Characterisation of Congleton sand and UWA silica sand.

Description	Congleton	Reference	UWA sand	Reference
Specific gravity, G_s	2.67*	-	2.67	Chow et al. (2019)
Mean particle size d_{50} (mm)	0.14	O'Loughlin & Barron (2012)	0.18	Chow et al. (2019)
Minimum dry density, ρ_{min} (kg/m^3)	1461	O'Loughlin & Barron (2012)	1497	Chow et al. (2019)
Maximum dry density, ρ_{max} (kg/m^3)	1763	O'Loughlin & Barron (2012)	1774	Chow et al. (2019)
Unit weight, γ (kN/m^3)	17.05	Barron (2014)	20.53	Chow et al. (2020)
Critical state friction angle, φ_{cs}	32.0°	O'Loughlin & Barron (2012)	31.9°	Chow et al. (2019)
Relative density, D_R	91 ± 2 %	Barron (2014)	82 %	Chow et al. (2020)
Initial void ratio, υ	1.501**	-	1.555	Calculated
Slope of CSL, λ	0.009*	-	0.009	Chow et al. (2019)
Operative Γ	1.601*	-	1.601	Calibrated

* Data from Congleton sand not available. Values from UWA silica sand used instead.

** Calculated assuming G_s = 2.67 from UWA silica sand

Most soil and anchor parameters used for the macro-element analyses have the same values as in the previous sections for the simulation of centrifuge tests of Chow et al. (2020) in the previous sections (see Table 6.6 for soil and anchor parameters) except for the plastic potential parameter ω and the normal capacity factor N_v. The plastic potential parameter $\omega = 1.5$ used previously in Chapter 3 as well as in this chapter provides good agreement with the centrifuge test of Barron (2014), though a smaller value ($\omega = 1.2$) provides a better fit with the experimental curve, as shown in Figure 6.44a. A capacity factor (N_v) of 9.0 for strip anchors in sand (Khatri & Kumar, 2011) was used instead of $N_v = 14$ for rectangular anchors used previously in this chapter. The vertical velocity of the actuator in the centrifuge tests was 1 mm/s, which gives a non-dimensional velocity $V^* = 3.63$ (assuming a coefficient of consolidation $c_v = 4.93 \cdot 10^{-4}$ m^2/s as for UWA silica sand in water and a diameter of an equivalent circle with same area $D = 1.79$ m). Although normalised velocities for drained and undrained (V_{dr} and V_{un}) seem to vary a lot depending, for instance, on the experimental set-up, displacement considered for the calculation of the velocity v and type of soil and comparison with other cases must be made with caution, the normalised velocity of 3.63 is lower than the drained velocity $V_{dr} = 16$ from Chow et al. (2020). Hence, fully-drained behaviour was assumed for the macro-element analysis, with $K = 10$.

Comparison between the macro-element analysis and the centrifuge test by Barron (2014) is presented in Figure 6.44. Good agreement is observed between the curves, both in terms of anchor capacity and anchor displacement. While the peak capacity from the centrifuge test is $T_p = 1054$ kN, the capacity obtained from the macro-element model $T_p = 1040$ kN, which is less than 2% smaller. Moreover, the peak capacity is reached at d/B = 2.06 in the centrifuge tests and at d/B = 1.92 in the macro-element analysis, which gives less than 7% difference.

These observations indicate that, when simulated under the same conditions, both anchor capacity and anchor displacements can be accurately captured by the macro-element model. This reinforces the conclusion from the previous section that the chain effects cause a considerable difference in the line displacement measured at the actuator in comparison with the actual distance travelled by the anchor padeye. In an experimental set-up for which the line displacement and padeye travel distance are similar, the macro-element model is able to accurately capture the anchor displacements.

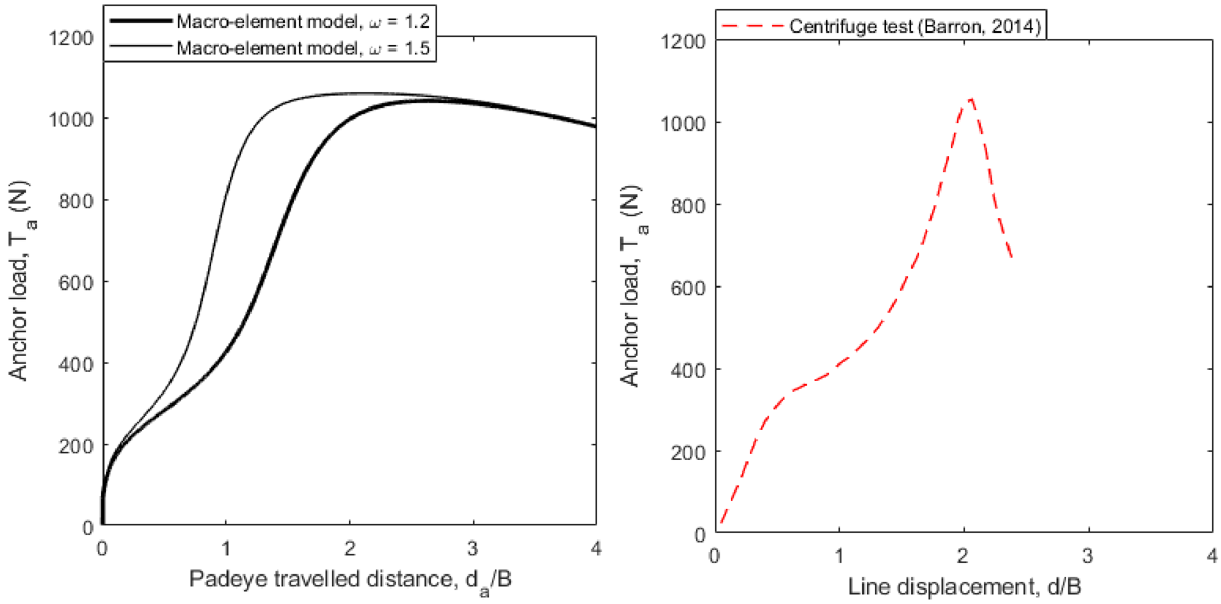

(a) (b)

Figure 6.44 – Force-displacement curves for a vertically-installed strip anchor subjected to vertical loading: (a) macro-element model, (b) centrifuge test (Barron, 2014).

6.6. Discussion, summary of procedures and difficulties

This section summarises the main procedures for the use of the macro-element model to account for different loading rates in sand. A summary of strong points, uncertainties and difficulties is also presented.

Firstly, the experimental conditions, soil properties and anchor geometry have to be defined, as these are input quantities to the model:

- Soil properties: unit weight (γ), friction angle at critical state (φ_{cs}), slope of the critical state line (λ), initial void ratio (v_0);
- Anchor geometry: width (B), length (L), parallel and normal eccentricities (e_p and e_n, respectively);
- Experimental conditions: initial embedment depth (Y), initial anchor orientation (β), load direction with the horizontal at the padeye (θ_a).

Secondly, the parameters for the soil shear model and those for the anchor model are selected or calibrated:

- Parameters for the shear model of the soil: A, C, k_d, k_r (from Severn-Trent model) and Γ for the operative critical state line. Of these, only the parameters C and Γ require calibration, as the values of A, k_d and k_r obtained from the literature seem to be adequate for the sands analysed in this chapter. The parameter C can be calibrated by matching the capacity of a drained centrifuge test (or an accurate FE analysis), as shown previously in Figure 6.24, while the parameter Γ can be calculated using the procedure detailed in 6.4.3.1. The undrained capacity ($T_{p(un)}$) from a centrifuge test (or a reliable FE analysis) is required for the application of the procedure.
- Model parameters of the anchor: 3 normalised capacities (N_v, N_h and N_m) governing size of the failure surface, 3 shape parameters of the loading and strength surfaces (m, n, q), 3 parameters defining the plastic potential surface (ξ, χ and ω) and 1 hardening parameter (R_0) are required as inputs to the macro-element model. Of these, the normalised capacities (N_v, N_h and N_m) and the shape parameters of the loading and strength surfaces (m, n, q) can be obtained from the literature. Two of the three plastic potential parameters and two plastic potential parameters (ξ and χ) assume the constant values suggested in Chapter 3 (1.6 and 1.1, respectively), hence only ω requires calibration to match the peak capacity as well as the respective displacement at peak. However, using a standard value of $\omega = 1.5$ as suggested in Chapter 3 seems to produce reasonable results (as shown in Figure 6.44), therefore this value can be used for an initial estimation of the force-displacement response. The parameter $R_0 = 5$ was the same for both for the tests of Chow et al. (2020) and Barron (2014), which ensures the kinematic stability is not reached before the full soil strength is mobilised, as shown previously in Figure 6.30.

With these procedures, simulations for several values of K (i.e. from drained to undrained, including several partially drained simulations) can be carried out. Since each simulation takes less than 20 seconds to complete, 10 analyses can be performed in less than 4 minutes. The value of K at the mid-point (K_{50}) between drained and undrained capacity can then be determined by plotting the anchor capacities for each value of K in a back-bone-like curve, as previously shown in Figure 6.26.

The next step is to relate the values of *K* to non-dimensional velocities V^*, and this is where the main challenge of the model resides. Conversion from *K* to V^* requires the determination of the non-dimensional velocity at the mid-point (V_{50}), such that the conversion factor $\Omega = K_{50}/V_{50}$ can be established. Due to the lack of more published data on V_{50} for plate anchors in the literature, currently this can only be determined if the results from a few centrifuge tests are available. The determination of representative normalised velocities from simple laboratory testing, as shown in Lauder et al. (2012) and Robinson (2019), shall be further investigated in future research, as this would significantly simplify the application of the model. Currently, the values of V_{50}, V_{dr} and V_{un} for other applications, such as (cone) penetration tests and shallow foundations was shown to be highly variable and dependent on experimental set-up and loading conditions.

The proposed macro-element model, therefore, does not eliminate completely the necessity of a good set of centrifuge tests. Further developments on relating the normalised velocities to simple element tests could potentially eliminate the need of centrifuge tests. The main value of the model applied for different loading rates in sands is that, after calibrated for a certain number of tests (probably 3 or 4), it can be further used to extrapolate the results for different conditions, such as anchor geometry, soil density, initial depth and loading rates, in a very short simulation time.

6.7. Conclusions

This chapter applied the macro-element model presented in Chapter 4 to sandy soils subjected to different loading rates. The main conclusions, including strong points and difficulties in the use of the model, are summarised below.

- The macro-element model is able to capture the change in anchor capacity due to different loading rates in sands by means of a simplified approach in which the stress path is assumed to follow a straight line towards the operational critical state line in the v-σ_v' plane.
- Anchor displacements obtained from the macro-element model are not comparable to the centrifuge tests by Chow et al. (2020), as the model does not include the effect of chain slack, chain cutting through the soil and evolution of load orientation due to the

chain mechanism, whereas the centrifuge tests measured the line displacement at the actuator. Furthermore, the load direction at the padeye (θ_a) was assumed as constant in the macro-element model, whereas in the centrifuge tests this angle varied due to the chain mechanisms. The implementation of a well-established chain solution that relates the load direction at the padeye (θ_a) with the load direction at mudline (θ_0) would possibly lead to accurate prediction of the anchor displacement, as it was shown that for a case where the chain does not play an important role (i.e. comparison with centrifuge test from Barron, 2014), the anchor displacements are well captured by the model.

- The parameters for soil model used by Diambra et al. (2013), which are similar to the values used by Gajo & Muir Wood (1999) and Corti et al. (2016) seem to be adequate, except for parameter C which requires calibration. The same values of parameters A, k_d and k_r were used both for the centrifuge tests of Chow et al. (2020) and Barron (2014), which suggests that these parameters may be assumed as constant for any macro-element analysis in sands.
- Calibration of the operative critical state line is essential to obtain results that are in line with experimental data. If parameters of CSL of the soil obtained from element tests are used, significant differences to centrifuge tests are observed. This is because while the conventional critical state line is defined with element tests while in reality not all elements around the anchor reach critical state conditions at the same time, as the phenomenon is highly non-linear. Furthermore, the critical state line obtained from element testing depends on the testing conditions, and can present high scatter (e.g. Chow et al., 2019). It is worth noting that calibration of the operational CSL requires the undrained capacity of the anchor, which can be challenging to obtain in sands due to its high permeability.
- Conversion from values of K to non-dimensional velocities V^* depends on the value of the non-dimensional velocity V_{50} for the mid-point between drained and undrained capacities, which to date is not vastly available in the literature. Undrained, drained and mid-velocities (V_{un}, V_{dr} and V_{50}, respectively) for other applications (e.g. shallow foundations, penetration tests) can be found in the literature, but such values are highly dependent on the type of test. Even for similar tests (e.g. cone penetration tests), the values of V_{un} and V_{dr} reported in the literature vary significantly, depending on the study.

Using values of V_{50} reported in the literature to derive the conversion factor from K to V^*, therefore, must be done with caution, even if the studies from which V_{50} was derived had similar experimental set-ups and loading conditions as the case of interest. In that sense, a few centrifuge tests are recommended in order to obtain V_{50}, such that an appropriate conversion factor $\Omega = K_{50}/V_{50}$ can be derived. The parameter K_{50} relative to the mid-point of anchor capacities can be quickly obtained by running a series of macro-element simulations, which can be done in only a few minutes.

- Including the effect of changing total vertical stress does not make a significant difference in the results in terms of anchor capacities, but it does provide the advantage that the change in pore pressure of the representative soil element accounting for the loss of embedment can be obtained. While the evolution of pore pressure on the representative soil element cannot be directly related to pore pressure measurements obtained through pore pressure transducers attached to the anchor (as the positions of soil element and transducer are different), a qualitative comparison to verify the trend can be of interest.
- When results from the macro-element model are compared with a case in which the chain effects are not important (e.g. anchor subjected to vertical loading), good agreement with a centrifuge test is observed not only in terms of anchor capacity, but also in terms of anchor displacement. That reinforces the indication that the macro-element is able to reproduce both anchor capacity and displacement accurately, provided the comparison is made under the same conditions. In that sense, the inclusion of a chain solution for sands in the macro-element model would be of great value, as direct comparison with the line displacement measured in centrifuge tests could be carried out.

CHAPTER 7. Summary & conclusions

This thesis focused on the development of a macro-element model that was able to reproduce the response of plate anchors embedded in both granular and cohesive soils, subjected to different loading conditions. Initially, an improved macro-element model for plate anchors in clay loaded under monotonic conditions was proposed, aiming at improving the prediction of anchor displacement during keying as well as anchor response at small displacements (Chapter 3). The macro-element model was expanded to account for the evolution of soil strength due to changes in effective stress caused by pore pressure generation and dissipation (i.e. consolidation) in Chapter 4. The new consolidation-dependent macro-element model combined the macro-element for the anchor under undrained conditions, with two models for the surrounding soil: a consolidation model and a shear model. The response of the bulk soil surrounding the anchor was reproduced by a representative soil element, for which the evolution of soil strength was accounted for. For each step of load, unload or maintained load in the incremental model, the strength of the representative soil element was accounted for in the macro-element model of the anchor.

The performance of the newly proposed model was assessed through comparison with centrifuge tests in cohesive and in granular soils (Chapters 5 and 6, respectively). The macro-element simulations in cohesive soils were compared with two studies: one involving long-term cyclic and maintained loading in a circular plate embedded vertically into the soil and loaded horizontally, and the other one involving different times of soil consolidation during maintained loading in square anchors embedded vertically in the soil and subjected to an eccentric vertical load.

The conclusions drawn from the work described in the previous chapters are summarised below.

7.1. Macro-element model for undrained conditions

The macro-element model for plate anchors in clay was proposed in Chapter 3, using the previously published model of Cassidy et al. (2020) as a starting point. The improvements to that model included a non-associated plastic potential and a strain-hardening rule into the plasticity theory framework. The main findings were:

- The macro-element results were compared with LDFE simulations and centrifuge tests with PIV measurements. The model was shown to be an effective tool to predict force-displacement, rotation and trajectory of plate anchors, covering different anchor geometries, soil properties and loading conditions.
- The non-associated plastic potential significantly improved the prediction of anchor trajectory, avoiding the re-embedment of the anchor observed from simulations with an associated plastic potential. The addition of a non-associated plastic potential required three new parameters, of which two seem to assume constant values ($\xi = 1.6$, $\chi = 1.1$) for all cases. The third plastic potential parameter requires calibration for each case, but one specific value seems to work for most cases ($\omega = 1.5$) and is, therefore, recommended for an initial assessment or starting value during calibration. This value also seemed to capture the effect of different installation methods, but further understanding is required on this matter.
- The strain-hardening rule required an additional parameter (R_0), which controls the initial part of the force-displacement curve. For most cases, $R_0 = 2.5$ produced satisfactory results, however when installation effects were analysed, a much smaller value ($R_0 = 0.3$) provided much better agreement with results from centrifuge tests. The relationship between the hardening parameter R_0 and installation effects is unknown and requires further investigation.
- The macro-element model was expanded to provide insights into the effect of anchor kinematics during cyclic loading. The extended approach suggested that anchor's capacity decrease occurs not only due to changes in soil's conditions, but also to the particular evolution of anchor's kinematics due to anchor re-orientation to find the path of least resistance towards the strength surface F.

7.2. Macro-element model accounting for changes in soil strength

A new macro-element modelling framework aiming to capture the evolution of soil strength was proposed in Chapter 4. The framework included a soil element that represents the whole soil volume around the anchor. The soil element was assumed to be subjected to simple shearing conditions when the anchor is loaded or unloaded, and to consolidation when the anchor is subjected to a maintained (sustained) loading.

The shearing model of the representative soil element is based on the critical state plasticity theory, similarly to the Severn-Trent model proposed by Gajo & Muir Wood (1999). The model used in this thesis had some differences with respect to the loading conditions in the original Severn-Trent model (direct simple shear conditions with constant total stress instead of triaxial conditions), as well as the use of a different formulation for the state parameter, which modified the mathematical formulation of the model, although most essential features remained the same. The consolidation model followed the formulation proposed by Singh & Chatterjee (2018), which consists of a hyperbolic dissipation of pore water pressure with time.

The compatibility between anchor and soil models was given by one equation, which stated that the mobilisation of anchor capacity ρ_c was equal to the mobilisation of soil shear strength (τ/τ_c). Furthermore, it was assumed that the soil strength given by the macro-element model controlled the normal (V_M), tangential (H_M) and rotational (M_M) capacities of the anchor, which govern the size of the anchor's capacity surface.

An optional dependency of the anchor's hardening parameter (R_0) on the current strength of the soil (τ_c) to improve the prediction of anchor displacement when significant changes in soil strength occur was proposed. In addition, a memory surface analogous to that proposed by Corti et al. (2016) was introduced, for which the soil behaviour is stiffer during repeated loading compared with virgin loading and where the original hardening modulus is reestablished once the soil reaches a virgin state. Both additions to the macro-element model are optional refinements that come at the cost of two new parameters.

7.3. Application of new macro-element model to cohesive soils under maintained and long-term cyclic loading

The new modelling framework proposed in Chapter 4 was applied to cohesive soils under combined long-term cyclic and maintained loading in Chapter 5. The macro-element results were compared to a set of centrifuge tests carried out by Zhou et al. (2020), which involved episodes of long- term cyclic and maintained loading on circular plates installed vertically and loaded horizontally, in a way that the anchor only underwent horizontal displacements – i.e. no rotation and no vertical displacements. From these macro-element simulations, the main conclusions were:

- A one-dimensional model significantly simplifies the problem and reduces the number of parameters that require calibration. The parameters related to the plastic potential as well as the sliding and rotational capacities are some of the parameters that are eliminated in a one-dimensional loading scenario. Another advantage of such a loading scenario is that, since no changes in anchor kinematics take place, the variation of anchor capacity is caused solely by the changes in soil strength, which allows the evolution of soil strength to be known and the soil parameters to be calibrated.
- Using the values used by Diambra et al. (2013) as an initial point, only two out of four parameters related to the shear model of the representative soil element were modified to provide good agreement with the centrifuge tests. The two parameters governing the consolidation model were calibrated with centrifuge tests. One hyperbolic stiffness parameter (C) was calibrated with two monotonic tests, to match anchor capacity. One parameter controlling the pore pressure generation (A) as well as two parameters controlling the pore pressure dissipation (a and T_{50}) were calibrated with a centrifuge test involving long-term cyclic loading. The calibration was done by matching the post- cyclic capacity of the anchor
- The influence factor I_σ which controls the stress transfer from the anchor to the representative soil element was calibrated with a centrifuge tests involving an episode of long-term maintained loading. Once again, the calibration was done by matching anchor capacity at a monotonic stage after the episode of maintained loading. Selecting

an appropriate position of the macro-element model (i.e. an appropriate distance between the soil element and the anchor centreline) is essential, since the influence factor depends on this distance. An element distant 0.7 *D* from the circular anchor was shown to be suitable for this loading scenario.

The macro-element model was also verified with another loading scenario involving anchor rotation and both normal and sliding displacements. The macro-element model was used to simulate a set of centrifuge tests involving an initial undrained loading stage, followed by different durations of a maintained loading and then by a final undrained loading stage (Blake et al., 2011). The main conclusions were:

- Using the parameters reported by Diambra et al. (2013) as a starting point, only one out of four parameters related to the shear model required calibration, as opposed to two parameters in the one-dimensional case. While in the one-dimensional case the parameters *C* governing the hyperbolic stiffness relationship and *A* controlling pore pressure generation were modified, for the loading scenario in Blake et al. (2011) only the parameter *C* assumed a different value.
- The influence factor I_σ used for this loading scenario was relative to a square loaded area distant 0.7*B* from the centre of the anchor, which is in line with the representative element distant 0.7*D* from the circular anchor in the one-dimensional loading scenario. The influence of the influence factor I_σ in the three-dimensional loading scenario was much less pronounced than in the one-dimensional case, as the variation of anchor capacity after long-term maintained loading did not vary significantly when different values I_σ were assumed.
- The mechanism of stress transfer from the anchor to the representative soil element differs depending on the loading scenario. For a one-dimensional loading scenario, the additional stress taken by the representative soil element is horizontal, hence this stress can be easily converted to a vertical stress (and considered in the macro-element model) by means of multiplying the horizontal stress by K_0. For a three-dimensional loading scenario that involves anchor rotation, the additional stress transferred from the anchor to the representative soil element is inclined due to anchor rotation during the application of load. Therefore, stress rotation from an inclined to a vertical orientation is

done by Mohr's circle. To that end, the macro-element must be able to capture anchor rotation with reasonable accuracy. Comparison of anchor rotation with a previous study (Song et al., 2006) suggested that the rotational behaviour is well captured by the macro- element model.

- For the three-dimensional case, the macro-element simulations with constant value R_0 provides the same result as the simulation with R_0 varying with the current soil strength τ_c and with a memory surface. This is because the soil strength does not vary significantly for this testing condition, as opposed to the one-dimensional case, where the long-term cyclic loading caused significant variation of soil strength.

Overall, the macro-element simulations provided good agreement with all centrifuge tests in both loading scenarios. The main challenge seems to be the dependency of the model calibration on a few centrifuge tests. For the one-dimensional centrifuge tests by Zhou et al. (2020), the calibration of the parameters required centrifuge results from monotonic, cyclic and maintained loading. Once the parameters related to these loading conditions were calibrated, the model was verified against more complex situations involving a combination of maintained and cyclic loading and monotonic stages. For the three-dimensional case by Blake et al. (2011), a calibration-and-challenging approach was not possible, since in order to obtain adequate values of the consolidation parameters a and T_{50}, the results of the centrifuge tests were needed. Comparison with additional tests involving different loading scenarios (e.g. cyclic loading) would be of interest for further verification of the model, but such tests are not available in the literature.

7.4. Application of new macro-element model to granular soils under different loading rates

The new modelling framework was applied to granular soils in Chapter 6. Results from macro- element simulations were compared with two sets of centrifuge tests: one involving a vertically-installed plate anchor subjected to inclined loading at different rates (Chow et al., 2020) and one involving a vertically-installed anchor subjected to vertical loading under drained conditions (Barron, 2014).

For the tests involving different loading rates, initially a general approach in which decoupled stages of shear and consolidation (similar to the approach used for the one-dimensional case in Chapter 5) was used to simulate partially-drained conditions. However, the high computational time required to complete these simulations led to the development of a simplified approach, in which the stress path of the representative soil element in the stress-volumetric plane (υ-σ_v') was assumed to be a straight line with slope *K* and the intersection with the critical state line is the same as that for the decoupled model. From an initial assessment with a hypothetical situation (involving the rectangular anchor from Cassidy et al. (2012)), the *K*-model was shown to provide similar results to the decoupled model, hence the *K*-angle model was adopted for the remaining analyses in Chapter 6. Besides being considerably faster than the coupled model, the *K*-angle model also has the advantage of decreasing the number of parameters that require calibration. Since the soil consolidation is not directly considered (i.e. the consolidation stages are accounted for by the inclination of the stress path), the two consolidation parameters a and T_{50} are no longer used in the *K*-angle model. Furthermore, the influence factor I_σ is not required in the simplified modelling approach.

The main conclusions are summarised below:

- An operative critical state line is necessary to accurately capture the response of plate anchors in sand. Macro-element analyses showed that, when the critical state line obtained from element testing is used, significant differences to centrifuge tests are observed. This is because while the conventional critical state line is defined with element tests while in reality not all elements around the anchor reach critical state conditions at the same time. The operative critical state line represents the state for which the anchor exhibits indefinite displacement with no changes in chain load.
- The calibration procedure proposed for the representative soil element involved calibrating the hyperbolic stiffness parameter C with a drained monotonic test and calibrating the intercept of the critical state line Γ through a simple procedure described in section 0. The calibration procedure of Γ is carried out by assuming that the slope of the critical state line is the same as that for the normal consolidation line (λ) and that, at peak conditions, the mobilisation of capacity is nearly 1 (i.e. $\rho_c \approx 1$) and the anchor load T_a is purely normal to the anchor (i.e. $V = T_a$). For the calibration of Γ, the anchor's

undrained capacity ($T_{p(un)}$) is required, which can be challenging in centrifuge tests in granular soils due to the high permeability of such soils. In Chow et al. (2020)'s studies, that was achieved by using methocel as the pore fluid instead of water, which slows consolidation due to the high viscosity of the fluid.

- While the K-model has important advantages in comparison with the decoupled model, the parameter K does not have a direct physical meaning. However, it controls the amount of drainage that is allowed during anchor loading, similarly to the anchor's velocity of pull. It follows that converting K to the normalised V^* is essential to give a physical significance to the former parameter. A conversion factor from K to V^* was proposed, such that values of K divided by the conversion actor yield values of normalised velocity V^*. The conversion factor is given by the ratio between K_{50} and V_{50}. K_{50} is the mid-value of K in the drainage domain, K_{50} (i.e. the value of K for the mid-value between drained and undrained capacity), which can be easily obtained through a series of macro-element simulations covering drained, partially-drained and undrained analyses. V_{50} is the mid-value of the normalised velocity V^* in the drainage domain, which cannot be easily determined. Given the lack of data on V_{50} for anchors in the literature, it is uncertain whether its values vary within a narrow range. Consequently, a small number of centrifuge tests is required to obtain the value of V_{50} and then to yield the conversion factor between K and V^*. When V_{50} could be established, the conversion from K to V^* by means of the proposed conversion factor gave good results, and the back-bone curve of normalised capacity versus normalised velocity obtained from macro-element simulations agreed well with the results from centrifuge tests.
- The chain displacement was not captured by the macro-element model in the loading scenario of Chow et al. (2020)'s tests due to the lack of a well-established chain solution for sands in the literature. When the displacements are normalised by the displacement at peak for drained conditions, the macro-element results are similar to those from the centrifuge tests. In a loading scenario that involves purely vertical loading (for which the anchor padeye's displacement is similar to the chain displacement), much more accurate results were obtained by the macro-element model in comparison with the centrifuge test results.

7.5. Summary

Overall, the macro-element modelling framework proposed in this thesis is a useful tool to predict the behaviour of plate anchors with different geometries embedded in different types of soil, under different loading conditions and different drainage responses. Several simulations can be carried out in a short period, since most simulations take less than a minute to complete. Even for the case with several episodes of long-term cyclic loading (e.g. Test 4 in Chapter 5), the analysis was completed in less than 20 minutes. For monotonic loading, the analyses are usually complete in less than 20 seconds, whereas FE simulations can take many hours (e.g. 40 hours for each 3D FE analysis carried out by Tian et al. (2015)).

However, in most cases the macro-element analysis does not eliminate the necessity of a few centrifuge tests. In particular for those cases that involve long-term cyclic loading, the calibration of parameters governing pore pressure generation and dissipation are essential, as long-term operations can lead to high changes in soil strength.

7.6. Future research

As discussed throughout the thesis, some aspects related to both anchor kinematics and soil response require further research, as described below.

7.6.1. Chain solution for sands

While a well-established chain solution for clays was introduced by Neubecker & Randolph (1995) and used in several studies, a chain solution for sands that relates the load direction at mudline to the direction of load at the padeye is not found in the literature. Because of that, the chain displacement, which is usually the displacement measured in centrifuge tests, cannot be verified through the macro-element model. While the displacement of the anchor padeye can be accurately captured by the model in situations that involve only vertical loads at the padeye, significant differences between padeye displacement and chain distance are observed in loading scenarios that involve the chain tightening and cutting through the soil (e.g. reverse catenary chain profile).

An accurate model for chain in sands that is capable of capturing the evolution of the chain angle at padeye (θ_a) as a function of anchor displacement, chain angle at mudline (θ_0) and soil strength would improve the prediction of anchor displacement, as the macro-element model gives accurate displacements when a suitable chain solution is employed – as observed in Chapter 3, in which the chain solution of Neubecker & Randolph (1995) was used.

7.6.2. Long-term cyclic loading in three-dimensional conditions

Macro-element analyses involving long-term cyclic loading in one-dimensional conditions (i.e. with anchor displacements in one direction only) were carried out in Chapter 5 and compared with centrifuge tests. The anchor kinematics do not play an important role in the results, since no rotation and no displacements parallel to the anchor plane occur in this loading scenario. The macro-element analyses in section 3.6 suggested that anchor capacity can decrease during episodes of cyclic loading due to anchor kinematics, whereas the soil strength was shown to increase in long-term cyclic loading operations in section 5.2. In a situation that involves both changes in anchor kinematics (i.e. anchor rotation and displacements in both normal and tangential directions), it is uncertain whether anchor the decrease in anchor capacity due to kinematics is more or less important than the increase in anchor capacity due to increase in soil strength. Even though the macro-element results presented in section 5.4 suggested that, for long-term cyclic loading, the variation of soil strength is more important than the changes in anchor kinematics, which leads to an increase in anchor capacity, those results were not validated with experimental data due to the lack of published results. It is suggested, therefore, that further research on long-term partial drainage and consolidation effects during cyclic loading is done through centrifuge tests with set-ups that cause anchor displacements in both vertical and horizontal directions, as well as anchor rotations. With such experiments, it is expected that the combined effect of consolidation with anchor kinematics can be investigated in more detail.

7.6.3. Determination of normalised velocity V_{50}

As discussed in Chapter 6, the normalised velocity V_{50} is necessary to convert the slopes of the stress path, K, to normalised velocities, V^*. Since the study of Chow et al. (2020) is the only one in the literature that analysed loading rate effects in plate anchors, no conclusions can be drawn with respect to how sensitive V_{50} is to different soil types, experimental set-ups, equipment used, among other aspects. The matter of velocities that marks the response of cone penetration tests from partially drained to drained (V_{dr}) and to undrained (V_{un}) was studied by several researchers, as previously discussed in section 6.4.3.6. However, significant discrepancies were observed in the values of V_{dr} and V_{un} among studies. The values obtained in all studies on penetration tests as well as in shallow foundations are significantly smaller than those reported by Chow et al. (2020) for plate anchors. Therefore, a study about the effect of soil characteristics and loading conditions/experimental set-up on the values of V_{50} would increase the confidence on the macro-element model results, since the value of V_{50} governs the conversion from the slope of the stress path, K, to normalised velocities, V^*. A unified approach accounting for e.g. dilation effects in sand (as in Lauder et al., 2012) and soil properties (as in Robinson, 2019) on the normalised velocities, in such a way that these values can be determined from simple laboratory testing, would simplify the application of the model and would potentially eliminate or reduce the need of centrifuge tests for model calibration.

7.6.4. Use of the macro-element framework to other geotechnical applications

Even though the modelling framework combining a macro-element governing the evolution of anchor kinematics with two models to describe the shear and consolidation response of the soil, the framework may also be used for other geotechnical applications.

Instead of a macro-element for anchors, for example, the modelling framework could combine a macro-element for e.g. drag-embedded anchors, pipeline and cable ploughing, as well as monopiles, suction caissons or shallow foundations, with a model that captures the evolution of soil conditions during operation. Particularly for this thesis, direct simple shear condition given by a Severn-Trent-like model was selected as representative of the soil behaviour during anchor loading, but for other structures another loading condition of the soil might be more appropriate. The macro-element model for the geotechnical structure and the soil model are merely modelling ingredients that can be changed and adapted to specific situations. Likewise, the ingredients of the soil model used for anchors (e.g. formulation of state parameter, flow rule, hardening, etc.) can be easily modified to better reproduce certain behaviours of interest.

In that sense, the author believes that the model proposed in this thesis can inspire researchers to apply macro-element modelling to other geotechnical structures under complex conditions that induce significant changes in soil characteristics, such as strength and stiffness.

References

Aghazadeh Ardebili, Z., Gabr, M., & Rahman, M. (2016). Uplift capacity of plate anchors in saturated clay: analyses with different consitutive models. *International Journal of Geomechanics, 16*(2), 04015053.

Akinmusuru, J. O. (1978). Horizontally Loaded Vertical Plate Anchors in Sand. *Journal of the Geotechnical Engineering Division, 104*(2), 283-286.

Al Heib, M., Emeriault, F., & Nghiem, H.-L. (2020). On the use of 1g physical models for ground movements and soil-structure interaction problems. *Journal of Rock Mechanics and Geotechnical Engineering, 12*, 197-211.

American Petroleum Institute. (2015). *API Recommended Practice - 2SK design and analysis of stationkeeping systems for floating structures.* API.

Andersen, K. (2015). Cyclic soil parameters for offshore foundation design. In V. Meyer (Ed.), *Frontiers in Offshore Geotechnics III* (pp. 5-82). London: CRC Press.

Andersen, K., Allard, M., & Hermstad, J. (1994). Centrifuge model tests of a gravity platform on very dense sand; II: Interpretation. *7th International Conference on Behaviour of Offshore Structures (BOSS 94)* (pp. 255-282). Cambridge: Mass. Proc. (1).

Atkinson, J. (2000). Non-linear stiffness in routine design. *Géotechnique, 50*(5), 487-508.

Aubeny, C. (2018). *Geomechanics of Marine Anchors.* Boca Raton, USA: Taylor & Francis Group.

Aubeny, C., & Chi, C. (2010). Mechanics of drag embedment anchors in a soft seabed. *Journal of Geotechnical and Geoenvironmental Engineering, 136*(1), 57-68.

Aubeny, C., & Chi, C. (2014). Analytical model for vertically loaded anchor performance. *Journal of Geotechnical and Geoenvironmental Engineering, 140*(1), 14-24.

Augusteijn, N., & Buitendijk, M. (2021, February 18). *Boskalis: Kincardine is a prelude to more floating wind projects*. Retrieved from Project Cargo Journal: https://www.projectcargojournal.com/offshore/2021/02/18/boskalis-kincardine-is-a-prelude-to-more-floating-wind-projects/?gdpr=accept

Barron, B. (2014). *An investigation into the keying behaviour and the capacity of plate anchors in sand.* Institute of Technology Sligo: MSc Thesis.

BBC. (2021, July 28). *'Most powerful' tidal turbine starts generating electricity off Orkney*. Retrieved from BBC: https://www.bbc.com/news/uk-scotland-north-east-orkney-shetland-57991351

Beard, B. (1980). *Holding capacity of plate anchors.* Port Hueneme, California, USA: Naval Construction Battalion Center.

Been, K., & Jefferies, M. G. (1985). A state parameters for sands. *Geotechnique, 35*(2), 99-112.

Blake, A., O'Loughlin, C., & Gaudin, C. (2011). Setup following keying of plate anchors assessed through centrifuge tests in kaolin clay. In S. Gourvenec, & D. White (Ed.), *Frontiers in Offshore Geotechnics II* (pp. 705-710). Perth, Australia: CRC Press/Balkema.

Blake, A., O'Loughlin, C., & Gaudin, C. (2015). Capacity of dynamically embedded plate anchors as assessed through field tests. *Canadian Geotechnical Journal, 52*, 87-95.

Bobei, D., Lo, S., Wanatowski, D., Gnanendran, C., & Rahman, M. (2009). Modified state parameter for characterizing static liquefaction of sand with fines. *Canadian Geotechnical Journal, 46*, 281-295.

Boussinesq, M. (1885). *Application des potentieles a l'etude de l'equilibre et du mouvement des solides elastiques.* Paris: Gauthier-Villars.

Bransby, F., & O'Neill, M. (1999). Drag anchor fluke soil interaction in clays. *Proceedings of the 7th International Symposium on Numerical Models in Geomechanics*, (pp. 489-494). Graz, Austria.

Bransby, M., & Ireland, J. (2009). Rate effects during pipeline upheaval buckling in sand. *Proceedings of the Institution of Civil Engineers, 162*(GE5), 247-256.

Brinkgreve, R. (2021, March 3). *The Soft-Soil and Soft-Soil Creep Model.* Retrieved from Virtuosity Blog - Infrastructure Insights: https://blog.virtuosity.com/the-soft-soil-and-soft-soil-creep-model

Brown, D. (2005). Mooring Systems. In S. K. Chakrabarti (Ed.), *Handbook of Offshore Engineering* (pp. 663-708). Amsterdam: Elsevier.

Brown, M. J., Davidson, C., Cerfontaine, B., CIantia, M., Knappet, J., & Brennan, A. (2020). Developing Screw Piles for Offshore Renewable Energy Application. In S. Haldar, P. S., & R. Ghanekar (Eds.), *Advances in Offshore Geotechnics - Proceedings of ISOG 2019* (pp. 101-119). Singapore: Springer.

Burd, H., Taborda, D., Zdravkovic, L., Abadie, C., Byrne, B., Houlsby, G., . . . Potts, D. (2020). PISA design model for monopiles for offshore wind turbines: application to a marine sand. *Géotechnique, 70*(11), 1048-1066.

BW Ideol. (2021, 04 June). *BW Ideol's second demonstrator - Hibiki.* Retrieved from BW Ideol: https://www.bw-ideol.com/en/japanese-demonstrator

Byrne, B., Houlsby, G., Burd, H., Gavin, K., Igoe, D., Jardine, R., . . . Zdravkovic, L. (2020). PISA design model for monopiles for offshore wind turbines: application to a stiff glacial clay till. *Géotechnique, 70*(11), 1030-1047.

CarbonBrief. (2017). *CarbonBrief.* Retrieved October 18, 2017, from https://www.carbonbrief.org/daily-brief/wind-power-overtakes-coal-first-time-uk-china-invest-361bn-clean-power-2020

Cassidy, M. J., Gaudin, C., Randolph, M. F., Wong, P. C., Wang, D., & Tian, Y. (2012). A plasticity model to assess the keying of plate anchors. *Geotechnique, 62*(9), 825-836.

Cerfontaine, B., Davidson, C., Brown, M., Knappett, J., Sharif, Y., Higgins, K., . . . Osman, A. (2021). Centrifuge Testing of Large Screw Pile Geometries for Offshore Applications. In Y. A. K.G. Higgins (Ed.), *Piling 2020: Proceedings of the Piling 2020 Conference.* London: ICE.

Cerfontaine, B., Knappett, J., Brown, M., & Bradshaw, A. (2019). Effect of soil deformability on the failure mechanism of shallow plate or. *Computers and Geotechnics, 109*, 34-45.

Cerfontaine, B., Knappett, K., Brown, M., Davidson, C., & Sharif, Y. (2020). Optimised design of screw anchors in tension in sand for renewable energy applications. *Ocean Engineering, 217*, 108010.

Chen, W., & Randolph, M. (2007). External radial stress changes and axial capacity for suction caissons in soft clay. *Geotechnique, 57*(6), 499-511.

Chow, S., Bienen, B., Randolph, M., & Roy, A. (2022). Rapid soil-structure interactions in saturated sand. *Proceedings of the 20th International Conference on Soil Mechanics and Geotechnical Engineering* (Forthcoming paper, to be presented). Sydney, Australia: ICSMGE.

Chow, S., Diambra, A., O'Loughlin, C., Gaudin, C., & Randolph, M. (2020). Consolidation effects on monotonic and cyclic capacity of plate anchors in sand. *Geotechnique, 70*(8), 720-731.

Chow, S., Le, J., Forsyth, M., & O'Loughlin, C. (2018). Capacity of vertical and horizontal plate anchors in sand under normal and shear loading. In A. McNamara, S. Divall, R. Goodey, N. Taylor, S. Stallebrass, & J. Panchal (Ed.), *9th International Conference on Physical Modelling in Geotechnics (ICPMG 2018)* (pp. 559-564). London: Taylor & Francis Group.

Chow, S., O'Loughlin, C., Corti, R., Gaudin, C., & Diambra, A. (2015). Drained cyclic capacity of plate anchors in dense sand: Experimental and theoretical observations. *Geotechnique Letters, 5*(2), 80-85.

Chow, S., O'Loughlin, C., Gaudin, C., & Lieng, J. (2018). Drained monotonic and cyclic capacity of a dynamically installed plate anchor in sand. *Ocean Engineering, 148*, 588-601.

Chow, S., O'Loughlin, C., Gaudin, C., Knappett, J., Brown, M., & Lieng, J. (2017). An Experimental Study of the Embedment of a Dynamically Installed Anchor in Sand. *Offshore Site Investigation Geotechnics 8th International Conference Proceeding* (pp. 1019-1025). London: Society for Underwater Technology.

Chow, S., O'Loughlin, C., Zhou, Z., White, D., & Randolph, M. (2020). Penetrometer testing in a calcareous silt to explore changes in soil strength. *Géotechnique, 70*(12), 1160-1173.

Chow, S., Roy, A., Herduin, M., Heins, E., King, L., Bienen, B., O'Loughlin, C., Gaudin, C., Cassidy, M. (2019). *Characterisation of UWA superfine silica sand.* Perth, Australia: Oceans Graduate School.

Chung, S., Randolph, M., & Schneider, J. (2006). Effect of penetration rate on penetrometer resistance in clay. *Journal of Geotechnical and Geoenvironmental Engineering, 132*(9), 1188-1196.

Ciavaglia, F., Carey, J., & Diambra, A. (2017). Time-dependent uplift capacity of driven piles in low to medium density chalk. *Géotechnique Letters, 7*(1), 90-96.

Clewes, B., & Micheel, L. (2007). Deck space shortage no barrier to deepwater pile installation. *Offshore Engineer, 32*(4), 141-146.

Colreavy, C., O'Loughlin, C., & Randolph, M. (2016). Experience with a dual pore pressure element piezoball. *International Journal of Physical Modelling in Geotechnics, 16*(3), 101-118.

Correia, A. (2011). *A pile-head macro-element approach to seismic design of monoshaft supported bridges.* Pavia, Italy: PhD Thesis, European School for Advanced Studies in Reduction of Seismic Risk (ROSE School).

Corti, R., Diambra, A., Muir Wood, D., Escribano, D., & Nash, D. F. (2016). Memory surface hardening model for granular soils under repeated loading conditions. *Journal of Engineering Mechanics, 142*(12), 04016102.

Craig, R. (2004). *Craig's Soil Mechanics* (7th ed.). London: Spon Press.

Cremer, C., Pecker, A., & Davenne, L. (2001). Cyclic macro-element for soil-structure interaction: material and geometrical non-linearities. *International Journal for Numerical and Analytical Methods in Geomechanics, 25*, 1257-1284.

Dafalias, Y. F. (1986). Bounding surface plasticity. I: Mathematical foundation and hypoplasticity. *Journal of Engineering Mechanics ASCE, 112*(9), 966-987.

Das, B. (1978). Model tests for uplift capacity of foundations in clay. *Soils and Foundations, 18*(2), 17-24.

Das, B. (1980). A procedure for estimation of ultimate uplift capacity of foundations in clay. *Soils and Foundations, 20*(1), 77-82.

Das, B. (1990). *Earth anchors.* Amsterdam: Elsevier.

Das, B., & Seeley, G. (1975). Break-out resistance of shallow horizontal anchors. *Journal of Geotechnical Engineering Division, 101*(9), 999-1003.

Dean, E. T. (2010). *Offshore Geotechnical Engineering: Principles and Practice.* London: Thomas Telford Ltd.

Diab, B., & Tahan, N. (2005). Offshore Installation. In S. K. Chakrabarti (Ed.), *Handbook of Offshore Engineering* (pp. 1055-1126). Amsterdam: Elsevier.

Diambra, A., Ibraim, E., Russell, A. R., & Muir Wood, D. (2013). Fibre reinforced sands: from experiments to modelling and beyond. *International Journal for Numerical and Analytical Methods in Geomechanics, 37*, 2427-2455.

DNV. (2014). *DNV-OS-J101: Design of Offshore Wind Turbine Structures.* Norway: Det Norske Veritas.

DNV-GL. (2017). *DNVGL-RP-E302 - Design and installation of plate anchors in clay.* DNV-GL.

Douglas, D. J., & Davis, E. H. (1964). The movements of buried footings due to movement and horizontal load and the movement of anchor plates. *Geotechnique, 14*(2), 115-132.

Dove, P., Tre, H., & Wilde, B. (1998). Suction embedded plate anchor (SEPLA): a new anchoring solution for ultra-deepwater mooring. *Deep Offshore Technology Conference.* New Orleans: Deep Offshore Technology Conference.

Drucker, D. (1958). The definition of an inelastic material. *Journal of Applied Mechanics, 26*, 101-106.

Durakovic, A. (2020, December 9). *First Kincardine Floating Giant Heads to Scotland*. Retrieved from OffshoreWind.biz: https://www.offshorewind.biz/2020/12/09/first-kincardine-floating-giant-heads-to-scotland/

Elkhatib, S. (2006). *The behaviour of drag-in plate anchors in soft cohesive soils.* PhD Thesis: The University of Western Australia.

Elkhatib, S., & Randolph, M. (2005). The effect of interface friction on the performance of drag-in plate anchors. *Proceedings of the 5th International Symposium on Frontiers in Offshore Geotechnics (ISFOG)* (pp. 171-177). Perth, Australia: ISFOG.

Equinor. (2019). *What We Do*. Retrieved from Equinor: https://www.equinor.com/en/what-we-do/floating-wind.html

Esrig, M., Kirby, R., Bea, R., & Murphy, B. (1977). Initial development of a general effective stress method for the prediction of axial capacity for driven piles. *Proceedings of 9th Offshore Technology Conference* (p. OTC 2943). Houston, Texas: OTC.

European Union. (2020). *Flotant Project*. Retrieved from https://flotantproject.eu/

Evans, S. (2019, September 20). *Carbon Brief.* Retrieved September 01, 2021, from https://www.carbonbrief.org/analysis-record-low-uk-offshore-wind-cheaper-than-existing-gas-plants-by-2023

Finnie, I., & Randolph, M. (1994). Punch-through and liquefaction induced failure of shallow foundations on calcareous sediments. *Proceedings of BOSS'94: behaviour of offshore structures* (pp. 217-230). Oxford, UK: Pergamon.

Flessati, L., di Prisco, C., & Callea, F. (2020). Numerical and theoretical analyses of settlements of strip shallow foundations on normally consolidated clays under partially drained conditions. *Géotechnique*(DOI: 10.1680/jgeot.19.P.348), Ahead of Print.

Floatgen. (2018, September 19). *France's first offshore wind turbine produces electricity*. Retrieved from Floatgen: https://floatgen.eu/en/actualites/frances-first-offshore-wind-turbine-produces-electricity

Floatgen. (2020, January 14). *Floatgen acheives a total of 6 GWh of power production in 2019*. Retrieved from Floatgen: https://floatgen.eu/en/actualites/floatgen-achieves-total-6-gwh-power-production-2019

Gajo, A., & Muir Wood, D. (1999). Severn-Trent sand: a kinematic-hardening constitutive model: the q-p formulation. *Geotechnique, 49*(5), 595-614.

Gaudin, C., O'Loughlin, C. D., Randolph, M. F., & Lowmass, A. (2006). Influence of the installation process on the performance of suction embedded plate anchors. *Geotechnique, 56*(6), 381-391.

Gaudin, C., O'Loughlin, C. D., Randolph, M. F., Cassidy, M. J., Wang, D., Tian, Y., & Hambleton, J. P. (2014). Advances in offshore and onshore anchoring solutions. *Australian Geomechanics Journal, 49*(4), 59-71.

Gaudin, C., Simkin, M., White, D., & O'Loughlin, C. (2010). Experimental investigation into the influence of a keying flap on keying of plate anchors. *20th International Offshore and Polar Engineering Conference.* Beijing, China: International Society of Offshore and Polar Engineers.

Gaudin, C., Tian, M. J., Randolph, M. F., Wang, D., & O'Loughlin, C. D. (2015). Design and performance of suction embedded plate anchors. In V. Meyer (Ed.), *Frontiers in Offshore Geotechnics III* (pp. 863-868). London: CRC Press.

Gerdes, J. (2021, June 21). *Energy Monitor*. Retrieved September 05, 2021, from https://energymonitor.ai/tech/renewables/why-floating-turbines-will-unlock-offshore-wind-energys-full-potential

Golightly, C. (2018). Offshore Wind Foundation Engineering: Fixed and Floating Structures. *Presentation at HR Wallingford UK.* Wallingford, UK.

Gottardi, G., & Butterfield, R. (1995). The displacement of a model rigid surface footing on dense sand under general planar loading. *Soils and Foundations, 35*(3), 71-82.

Gottardi, G., Houslby, G., & Butterfield, R. (1999). Plastic response of circular footings on sand under general planar loading. *Geotechnique, 49*(4), 453-469.

Gourvenec, S. (2018). The role of centrifuge modelling in capturing whole-life responses of geotechnical infrastructure to optimize design. In A. McNamara, S. Divall, R. Goodey, N. Taylor, S. Stallebrass, & J. Panchal (Eds.), *Physical Modelling in Geotechnics, Volume 1: Proceedings of the 9th Proceedings of the 9th International Conference on Physical Modelling in Geotechnics* (pp. 51-75). London: CRC Press / Balkema.

Gourvenec, S., & Randolph, M. (2010). Consolidation beneath circular skirted foundations. *International Journal of Geomechanics, 10*(1), 22-29.

Gourvenec, S., Vulpe, C., & Murphy, T. (2014). A method for predicting the consolidated undrained bearing capacity of shallow foundations. *Géotechnique, 64*(3), 215-225.

GWEC. (2017). *Global Wind Statistics 2016.* Brussels: Global Wind Energy Council.

GWEC. (2021). *Global Wind Report.* Global Wind Energy Council.

Haigh, S., Eadington, J., & Madabhushi, S. (2012). Permeability and stiffness of sands at very low effective stresses. *Géotechnique, 62*(1), 69-75.

Han, C. (2016). *Performance of plate anchors under sustained loading.* PhD Thesis: University of Western Australia.

Han, C., & Liu, J. (2020). A review on the entire installation process of dynamically installed anchors. *Ocean Engineering*, 107173.

Han, C., Wang, D., Gaudin, C., O'Loughlin, C., & Cassidy, M. (2016). Behaviour of vertically loaded plate anchors under sustained uplift. *Géotechnique, 66*(8), 681-693.

Heurlin, K., Resseguier, S., Melin, D., & Nilsen, K. (2015). Comparison between FEM analyses and full-scale tests of fluke anchor behavior in silty sand. In V. Meyer, *Frontiers in offshore geotechnics III* (pp. 875-880). Leiden, The Netherlands: CRC Press/Balkema.

Houlsby, G., & Cassidy, M. (2011). A simplified mechanically based model for predicting partially drained behaviour of penetrometers and shallow foundations. *Géotechnique Letters, 1*(3), 65-69.

House, A., Oliveira, J., & Randolph, M. (2001). Evaluating the coefficient of consolidation using penetration tests. *International Journal of Physical Modelling in Geotechnics, 1*(3), 17-26.

Hu, Y., & Randolph, M. (1998). A practical numerical approach for large deformation problems in soil. *International Journal for Numerical and Analytical Methods in Geomechanics, 22*(5), 327-350.

Hu, Y., & Song, Z. (2008). Large deformation FE analysis of plate anchor keying in clay. *Proceedings of the 12th International Conference of International Association for Computer Methods and Advances in Geomechanics (IACMAG)*, (pp. 3299-3309). Goa, India.

Huisman, M. (2021, August 23). *Shh! Silent piling in progress.* Retrieved from Heerema: https://www.heerema.com/insights/shh-silent-piling-in-progress

Ideol. (2016, December 13). *Floatgen's anchors have been delivered*. Retrieved from BW Ideol: https://www.bw-ideol.com/en/actualites/floatgens-anchors-have-been-delivered

IEA. (2019). *World Energy Outlook.* International Energy Agency.

Ilamparuthi, K., Dickin, E., & Muthukrisnaiah, K. (2002). Experimental investigation of the uplift behaviour of circular plate anchors embedded in sand. *Canadian Geotechnical Journal, 39*, 648-664.

Itoh, M. (2019). *Overview of NEDO's Offshore Wind Power Technology Development.* Kitakyushu, Japan: NEDO.

James, R., & Ros, M. (2015). *Floating Offshore Wind: Market and Technology Review.* Carbon Trust.

Jardine, R. (1992). Some observations on the kinematic nature of soil stiffness. *Soils and Foundations, 32*(2), 111-124.

Jardine, R., & Standing, J. (2012). Field axial cyclic loading experiments on piles driven in sand. *Soils and Foundations, 52*(4), 723-736.

Kay, S., Gourvenec, S., Paix, E., & Alderlieste, E. (2021). *Intermediate Offshore Foundations.* London, UK: CRC Press (Taylor & Francis Group).

Khatri, V., & Kumar, J. (2011). Effect of anchor width on pullout capacity of strip anchors in sand. *Canadian Geotechnical Journal, 48*(3), 511-517.

Kim, K., Prezzi, M., Salgado, R., & Lee, W. (2010). Penetration rate effects on cone resistance measured in a calibration chamber. In P. Robertson, & P. Mayne (Ed.), *Proceedings of 2nd International Symposium on Cone Penetration Testing (CPT 10)*, (pp. 1-8). Huntington Beach, CA, USA.

Knappett, J. A., Brown, M. J., Aldaikh, H., Patra, S., O'Loughlin, C. D., Chow, S. H., . . . Jieng, J. T. (2015). A review of anchor technology for floating renewable energy devices and key design considerations. In V. Meyer (Ed.), *Frontiers in Offshore Geotechnics III* (pp. 887-892). London: CRC Press.

Koschinski, S., & Ludemann, K. (2013). *Development of noise mitigation measures in offshore wind farm construction.* Germany: Federal Agency for Nature Conservation.

Ladanyi, B., & Johnston, G. H. (1974). Behavior of Circular Footings and Plate Anchors Embedded in Permafrost. *Canadian Geotechnical Journal, 11*(4), 531-553.

Lam, N.-S., & Housby, G. (2005). The theoretical modelling of asuction caisson foundation using hyperplasticity theory. *Proceedings of International Symposium of Frontiers in Offshore Geotechnics (ISFOG)* (pp. 417-423). Perth, Australia: Taylor & Francis.

Lambe, T., & Whitman, R. (1969). *Soil Mechanics.* New York: John Wiley & Sons.

Lankhorst Offshore. (2021, July 19). *WindFloat Atlantic Floating Wind Turbine Moorings*. Retrieved from Lankhorst Offshore: https://www.lankhorstoffshore.com/about-us/news-events/windfloat-atlantic-floating-wind-turbine-moorings

Lauder, K., Brown, M., Bransby, M., & Gooding, S. (2012). Variation of tow force with velocity during offshore ploughing in granular materials. *Canadian Geotechnical Journal*, 1244-1255.

Lehane, B., & Jardine, R. (2003). Effects of long-term pre-loading on the performance of a footing on clay. *Géotechnique, 53*(8), 689-695.

Li, Z., Kotronis, P., Escoffier, S., & Tamagnini, C. (2015). Macroelement modelling for single vertical piles. *Proceedings of 6th International Conference on Earthquake Geotechnical Engineering* (pp. 1-9). Christchurch, New Zealand: ISSMGE.

Lieng, J. T., Hove, F., & Tjelta, T. I. (1999). Deep Penetrating Anchor: Subseabed deepwater anchor concept for floaters and other installations. *International Symposium on Offshore Polar Engineering (ISOPE)* (pp. 613-619). Brest, France: ISOPE.

Liu, H. (2012). Recent Study of Drag Embedment Plate Anchors in China. *Journal of Marine Science and Application, 11*, 393-401.

Liu, H., Liu, C., Yang, H., Li, Y., Zhang, W., & Xiao, Z. (2012). A novel kinematic model for drag anchors in seabed soils. *Ocean Engineering, 49*, 33-42.

Manzari, M. T., & Dafalias, Y. F. (1997). A critical state two-surface plasticity model for sands. *Geotechnique, 47*(2), 255-272.

Martin, C., & Houslby, G. (2000). Combined loading of spudcan foundations on clay: laboratory tests. *Geotechnique, 50*(4), 325-338.

Martins, T. (2020). Offshore anchoring systems with torpedo piles. *SNAME 25th Offshore Symposium.* Houston, Texas, USA: OnePetro.

Medeiros, C. (2002). Low Cost Anchor System for Flexible Risers in Deep Waters. *Proceedings of the 34th Annual Offshore Technology Conference* (pp. OTC-14151-MS). Houston, Texas: Offshore Technology Conference.

Merifield, R., & Sloan, S. (2006). The ultimate pullout capacity of anchors in frictional soils. *Canadian Geotechnical Journal, 43*, 852-868.

Merifield, R., Lyamin, A., & Sloan, S. (2006). Three-dimensional lower-bound solutions for the stability of plate anchors in sand. *Geotechnique, 56*(2), 123-132.

Merifield, R., Lyamin, A., Sloan, S., & Yu, H. (2003). Three-dimensional lower bound solutions for stability of plate anchors in clay. *Journal of Geotechnical and Geoenvironmental Engineering, 129*(3), 243-253.

Merifield, R., Sloan, S., & Yu, H. (2001). Stability of plate anchors in undrained clay. *Géotechnique, 51*(2), 141-153.

Muir Wood, D. (2004). *Geotechnical Modelling* (1st ed.). Oxfordshire: Spoon Press.

Muir Wood, D. (2009). *Soil Mechanics: A One-Dimensional Introduction.* Cambridge: Cambridge University Press.

Muir Wood, D., Belkheir, K., & Liu, D. (1994). Strain softening and state parameter for sand modelling. *Geotechnique, 44*(2), 335-339.

Murff, J., Randolph, M., Elkhatib, S., Kolk, H., Ruinen, R., Strom, P., & Thorne, C. (2005). Vertically loaded plate anchors for deep water applications. *Proceedings of 5th*

International Symposium on Frontiers Offshore Geotechnics (ISFOG) (pp. 31-48). Perth, Australia: ISFOG.

Murray, E., & Geddes, J. (1987). Uplift of anchor plates in sand. *Journal of Geotechnical Engineering, 113*(3), 202-215.

Murray, E., & Geddes, J. (1989). Resistance of passive inclined anchors in cohesionless medium. *Geotechnique, 39*(3), 417-431.

Neely, W., Stuart, J., & Graham, J. (1973). Failure loads of vertical anchors in sand. *Journal of the Geotechnical Engineering Division, 99*(9), 669-685.

Neubecker, S. R., & Randolph, M. F. (1995). Profile and frictional capacity of embedded anchor chains. *Journal of Geotechnical Engineering, 121*(11), 797-803.

Ng, C. (2014). The state-of-the-art centrifuge modelling of geotechnical problems at HKUST. *Journal of Zhejiang University-SCIENCE A (Applied Physics & Engineering), 15*(1), 1-21.

Nova, R., & Montrasio, L. (1991). Settlements of shallow foundations on sand. *Geotechnique, 41*(2), 243-256.

Oliveira, J., Almeida, M., Motta, H., & Almeida, M. (2011). Influence of penetration rate on penetrometer resistance. *Journal of Geotechnical and Geoenvironmental Engineering, 137*(7), 695-703.

O'Loughlin, C. D., Richardson, M. D., Randolph, M. F., & Gaudin, C. (2013). Penetration of dynamically installed anchors in clay. *Geotechnique, 63*(11), 909-919.

O'Loughlin, C. D., White, D. J., & Stanier, S. A. (2015). Novel Anchoring Solutions for FLNG - Opportunities Driven by Scale. *Offshore Technology Conference.* Houston: Offshore Technology Conference.

O'Loughlin, C., & Barron, B. (2012). Capacity and keying response of plate anchors in sand. *Offshore Site Investigation and Geotechnics: Integrated Geotechnologies - Present and future* (pp. 649-656). London: Society for Underwater Technology (SUT).

O'Loughlin, C., & Barron, B. (2012). Capacity and keying response of plate anchors in sand. *Offshore Site Investigation and Geotechnics: Integrated Technologies - Present and Future* (pp. 649-655). London, UK: OnePetro.

O'Loughlin, C., Blake, A., Richardson, M., Randolph, M., & Gaudin, C. (2014). Installation and capacity ofdynamically embedded plate anchors as assessed through centrifuge tests. *Ocean Engineering, 88*, 204-213.

O'Loughlin, C., Lowmass, A., Gaudin, C., & Randolph, M. (2006). Physical modelling to assess keying characteristics of plate anchors. *6th Physical Modelling in Geotechnics* (pp. 659-665). London: Taylor & Francis Group. doi:10.1201/NOE0415415866.ch94

O'Loughlin, C., Randolph, M., & Richardson, M. (2004). Experimental and Theoretical Studies of Deep Penetrating Anchors. *Proceedings of Offshore Technology Conference* (pp. OTC-16841-MS). Houston, Texas: Offshore Technology Conference.

O'Neill, M., Bransby, F., & Randolph, M. (2003). Drag anchor fluke–soil interaction in clays. *Canadian Geotechnical Journal, 40*, 78-94.

Orbital Marine. (2021). *Orbital Marine Power Launches O2: World's Most Powerful Tidal Turbine*. Retrieved from Orbital Marine: https://orbitalmarine.com/orbital-marine-power-launches-o2/

Osman, A. S., & Bolton, M. D. (2004). A new design method for retaining walls in clay. *Canadian Geotechnical Journal, 41*, 451-466.

Osman, A., & Bolton, M. (2006). Ground movement predictions for braced excavations in undrained clay. *Journal of Geotechnical and Geoenvironmental Engineering, 132*(4), 465-477.

Page, A., Grimstad, G., Eiksund, G., & Jostad, H. (2018). A macro-element pile foundation model for integrated analyses of monopile-based offshore wind turbines. *Ocean Engineering, 167*, 23-35.

Passini, L. d., Schnaid, F., & Salgado, R. (2017). Experimental Study of Shaft Resistance of Model Piles in Fluidized and Nonfluidized Fine Sand. *Journal of Offshore Mechanics and Arctic Engineering, 139*(5), 1-12.

Ponniah, D., & Finlay, T. (1988). Cyclic behaviour of plate anchors. *Canadian Geotechnical Journal, 25*(2).

Power Technology. (2021, January 25). *Pelamis, World's First Commercial Wave Energy Project, Agucadoura*. Retrieved from Power Technology: https://www.power-technology.com/projects/pelamis/

Principle Power. (2021, February 14). *New giants at sea*. Retrieved from Principle Power: https://www.principlepower.com/projects/windfloat-atlantic

Randolph, M., & Gourvenec, S. (2011). *Offshore Geotechnical Engineering.* Oxon: Spon Press.

Renewable UK. (2020). *Renewable UK*. Retrieved September 06, 2021, from https://www.renewableuk.com/page/WindEnergy

Richardson, M. D. (2008). *Dynamically Installed Anchors for Floating Offshore Structures.* PhD Thesis: The University of Western Australia.

Richardson, M., O'Loughlin, C., & Randolph, M. (2005). The geotechnical performance of deep penetrating anchors in calcareous sand. *Proceedings of the International Symposium on Frontiers in Offshore Geotechnics (ISFOG)* (pp. 357-363). Perth, Australia: ISFOG.

Richardson, M., O'Loughlin, C., Randolph, M., & Gaudin, C. (2009). Setup Following Installation of Dynamic Anchors in Normally Consolidated Clay. *Journal of Geotechnical and Geoenvironmental Engineering, 135*(4), 487-496.

Robinson, S. (2019). *Rate effect behaviour of different clays from high speed triaxial element testing.* School of Science and Engineering. Dundee, Scotland: University of Dundee.

Roscoe, K., & Schofield, A. (1957). Discussion on stability of short pier foundations in sand. *British Welding Journal, 4*(1), 12-19.

Rowe, R. K., & Davis, E. H. (1982). The behaviour of anchor plates in clay. *Geotechnique, 32*(1), 9-23.

Rowe, R., & Davis, E. (1982). The behaviour of plate anchors in sand. *Geotechnique, 32*(1), 25-41.

Russell, A. R., & Khalili, N. (2004). A bounding surface plasticity model for sands exhibiting particle crushing. *Canadian Geotechnical Journal, 41*, 1179-1192.

Rystad Energy. (2020, October). *Energy Voice.* Retrieved September 05, 2021, from https://www.energyvoice.com/renewables-energy-transition/wind/uk-wind/274960/uk-renewable-energy-capacity-double-2026/

Santamarina, J., & Cho, G. (2001). Determination of Critical State Parameters in Sandy Soils—Simple Procedure. *Geotechnical Testing Journal, 24*(2), 185-192.

Sarkar, J., Tajnin, R., Islam, S., Sarkar, G., & Rokonuzzman, M. (2018). Pure horizontal, vertical and moment capacity of plate anchors in sand. *4th International Conference on Civil Engineering for Sustainable Development (ICCESD 2018).* Khulna, Bangladesh.

Sauven, J. (2017, September 26). Wind power is now cheaper than nuclear – the energy revolution is happening. *The Guardian.*

Schofield, A. N., & Wroth, C. P. (1968). *Critical state soil mechanics.* London: MGraw-Hill.

Shelton, J. (2007). Omni-Max anchor development and technology. *Proceedings of Oceans Conference* (pp. 1-10). Vancouver, Canada: IEEE.

Silva, M., White, D., & Bolton, M. (2006). An analytical study of the effect of penetration rate on PCPTs in clay. *International Journal of Numericaland Analytical Methods in Geomechanics, 30*(6), 501-527.

Singh, S. (1998). *Behavior of plate anchors in soft saturated clay under monotonic and cyclic loading.* PhD Thesis: Anna University Chennai, India.

Singh, S., & Ramaswamy, S. (2008). Effect of shape on holding capacity of plate anchors buried in soft soil. *Journal of Geomechanics and Geoengineering, 3*(2), 157-166.

Singh, V., & Chatterjee, S. (2018). Elastoplastic consolidation above and beneath strip anchors under uplift forces. *Marine Georesources and Geotechnology, 36*(5), 505-514.

Skau, K., Grimstad, G., Page, A., Eiksund, G., & Jostad, H. (2018). A macro-element for integrated time domain analyses representing bucket foundations for offshore wind turbines. *Marine Structures, 59*, 158-178.

Song, Z., Hu, Y., & Randolph, M. (2008). Numerical simulation of vertical pullout of plate anchors in clay. *Journal of Geotechnical and Geoenvironmental Engineering, 134*(6), 866-875.

Song, Z., Hu, Y., O'Loughlin, C. D., & Randolph, M. F. (2009). Loss in anchor embedment during plate anchor keying in clay. *Journal of Geotechnical and Geoenvironmental Engineering, 135*(10), 1475-1485.

Song, Z., Hu, Y., Wang, D., & O'Loughlin, C. (2006). Pullout capacity and rotational behaviour of square anchors in kaolin clay and transparent soil. *Proceedings of the International Conference on Physical Modelling in Geotechnics* (pp. 1325-1331). Hong Kong: ISMGE.

Stanier, S., & White, D. (2019). Enhancement of bearing capacity from consolidation: due to changing strength or failure mechanism? *Géotechnique, 69*(2), 166-173.

Stewart, D. (1992). *Lateral loading of piled bridge abutments due to embankment construction.* The University of Western Australia: PhD Thesis.

Stewart, D., & Randolph, M. (1991). A new site investigation tool for the centrifuge. *Proceedings of the Centrifuge 91 Conference*, (pp. 531-538). Boulder, Colorado, USA.

Suzuki, Y., & Lehane, B. (2015). Cone penetration at variable rates in kaolin-sand mixtures. *International Journal of Physical Modelling in Geotechnics, 15*(4), 209-219.

Taylor, R. (2005). Centrifuges in modelling: principles and scale effects. In R. Taylor (Ed.), *Geotechnical Centrifuge Technology* (pp. 20-34). Glasgow: Blackie Academic and Professional.

Terzaghi, K., & Peck, R. (1967). *Soil Mechanics in Engineering Practice* (2nd edition ed.). New York: John Wiley and Sons.

Tian, Y., & Cassidy, M. (2008). Modelling of pipe-soil interaction and its application in numerical simulation. *International Journal of Geomechanics, 8*(4), 213-229.

Tian, Y., Gaudin, C., & Cassidy, M. (2014). Improving plate anchor design with a keying flap. *Journal of Geotechnical and Geoenvironmental Engineering, 140*(5).

Tian, Y., Gaudin, C., Randolph, M., & Cassidy, M. (2015). Influence of padeye offset on bearing capacity of three-dimensional plate anchors. *Canadian Geotechnical Journal, 52*(6).

Tsuha, C., Foray, P., Jardine, R., Yang, Z., Silva, M., & Rimoy, S. (2012). Behaviour of displacement piles in sand undercyclic axial loading. *Soils and Foundations, 52*(3), 393-410.

Vardanega, P., & Bolton, M. (2016). Design of geostructural systems. *Journal of Risk and Uncertainty in Engineering Systems, Part A: Civil Engineering, 2*(1), 04015017.

Vardanega, P., Kolody, E., Pennington, S., Morrison, P., & Simpson, B. (2012). Bored pile design in stiff clay. I: codes of practice. *Proceedings of the Institution of Civil Engineers, 165*(4), 213-232.

Vryhof. (2021). *Stevshark Rex - Holding power in the most extreme conditions.* Vryhof.

Wang, D., Gaudin, C., & Randolph, M. (2013). Large deformation finite element analysis investigating the performance of anchor keying flap. *Ocean Engineering, 59*, 107-116.

Wang, D., Hu, Y., & Randolph, M. (2011). Keying of Rectangular Plate Anchors in Normally Consolidated Clays. *Journal of Geotechnical and Geoenvironmental Engineering, 137*(12), 1244-1253.

Wang, H., Yuan, W., & Jia, F. (2015). A macro element method to improve computational efficiency in large-scaled nonlinear analysis. *Computers, Materials and Continua, 47*(1), 31-43.

Watson, P. G., Gaudin, C., Senders, M., & Randolph, M. F. (2006). Installation of suction caissons in layered soil. *International Conference on Physical Modelling in Geotechnics* (pp. 685-691). Hong Kong: International Conference on Physical Modelling in Geotechnics.

Watson, P., Suemasa, N., & Randolph, M. (2000). Evaluating Undrained Shear Strength Using the Vane Shear Apparatus . *Proceedings 10th International Offshore and Polar Engineering Conference (ISOPE)* (pp. 485-493). Washington, USA: ISOPE 2000.

Wilde, B., Treu, H., & Fulton, T. (2001). Field testing of suction embedded plate anchors. *11th International Offshore and Polar Engineering Conference (ISOPE). 2*, pp. 544-551. Cupertino, USA: 11th International Offshore and Polar Engineering Conference (ISOPE).

Wiser, R., Rand, J., Seel, J., Beiter, P., Baker, E., Lantz, E., & GIlman, P. (2021). Expert elicitation survey predicts 37% to 49% declines in wind energy costs by 2050. *Nature Energy, 6*, 555-565.

Wong, P., Gaudin, C., Randolph, M., Cassidy, M., & Tian, Y. (2012). Performance of suction embedded plate anchors in permanent mooring applications. *Proceedings of the 22nd international offshore and polar engineering conference* (pp. 640-645). Rhodes, Greece: International Society of Polar and Offshore Engineers.

Yang, M., Aubney, C. P., & Murff, J. D. (2012). Behaviour of suction embedded plate anchors during keying process. *Journal of Geotechnical and Geoenvironmental Engineering, 138*(2), 174-183.

Yin, Z.-Y., Teng, J.-C., Li, Z., & Zheng, Y.-Y. (2020). Modelling of suction bucket foundation in clay: From finite element analyses to macro-elements. *Ocean Engineering, 210*, 107577.

Yu, H. S. (1998). CASM: A unified state parameter model for clay and sand. *International Journal for Numerical and Analytical Methods in Geomechanics, 22*, 621-653.

Yu, L., Liu, J., Kong, X., & Hu, Y. (2011). Numerical study on plate anchor stability in clay. *Géotechnique , 61*(3), 235-246.

Yu, L., Zhou, Q., & Liu, J. (2015). Experimental study on the stability of plate anchors in clay under cyclic loading. *Theoretical and Applied Mechanics Letters, 5*, 93-96.

Zhang, D., Phoon, K., Huang, H., & Hu, Q. (2015). Characterization of model uncertainty for cantilever deflections in undrained clay. *Journal of Geotechnical and Geoenvironmental Engineering, 141*(1), 04014088.

Zhang, W., Zhou, Z., Pradhan, D., Wang, P., & Jin, H. (2022). Design considerations of drag anchors in cohesive soil for floating facilities in the South China sea. *Marine Structures, 81*, 103101.

Zhang, Y., Andersen, K., & Jeanjean, P. (2019). Cyclic p-y curves in clays for offshore structures. Houston, Texas: Offshore Technology Conference (OTC).

Zhang, Y., Andersen, K., Jeanjean, P., Karlsrud, K., & Haugen, T. (2020). Validation of monotonic and cyclic p-y framework by lateral pile load tests in stiff, overconsolidated clay at the Haga site. *Journal of Geotechnical and Geoenvironmental Engineering, 146*(9), 04020080.

Zhang, Y., Andersen, K., Klinkvort, R., Jostad, H., Sivasithamparam, N., Boylan, N., & Langford, T. (2016). Monotonic and cyclic p-y curves for clay based on soil performance. Houston, Texas: Offshore Technology Conference (OTC).

Zhou, Z., O'Loughlin, C. D., White, D. J., & Stanier, S. A. (2020). Improvements in plate anchor capacity due to cyclic and maintained loads combined with consolidation. *Géotechnique, 70*(8), 732-749.

Zhou, Z., White, D., & O'Loughlin, C. (2019). An effective stress framework for estimating penetration resistance accounting for changes in soil strength from maintained load, remoulding and reconsolidation. *Géotechnique, 69*(1), 57-71.

Zimmermann, E., Smith, M., & Shelton, J. (2009). Efficient Gravity Installed Anchor for Deepwater Mooring. Houston, Texas: Offshore Technology Conference.